CONSTITUTIVE MODELING OF POLY(ETHYLENE TEREPHTHALATE)

THESIS

Presented in Partial Fulfillment of the Requirements for the Degree Master of Science in the Graduate School of The Ohio State University

By

Shyam Venkatasubramaniam

Graduate Program in Mechanical Engineering

The Ohio State University

2014

Master's Examination Committee:

Dr. Rebecca Dupaix, Advisor

Dr. Brian Harper

Abstract

The ability to accurately computationally predict the end properties of Poly(Ethylene Terephthalate) (PET) based components is of immense use to the packaging industry to reduce product development and lifecycle costs. One activity being undertaken prominently by the industry is the development of PET bottles to maximize the shelf life of beverage-filled bottles.

This thesis deals with the development of a material model of PET for use in finite element simulation of blow molding. The mechanical behavior of PET is highly non-linear with temperature dependence, strain-rate dependence, molecular weight (Inherent Viscosity – IV) dependence, strain-state dependence and the tendency when induced by strain to crystallize.

Uniaxial compression experiments were conducted on PET samples to characterize the temperature, strain-rate and IV dependence of stress-strain characteristics. The temperature range for the tests was 363K to 383K, the (true) strain rates used were 0.1/s and 1/s and the IVs of samples used were 0.80, 0.86, 0.92 and 0.98.

The Dupaix-Boyce (DB) model (Dupaix, 2003) is a complex physically-based material model which can capture the viscoelastic, hyperelastic and plastic aspects of polymer mechanical behavior. This model was fit to the compression test results. Furthermore, uniaxial tension tests were conducted to check the predictive capability of the compression fit DB model in tension. The model under-predicted stress in tension and a different set of constants had to be used to fit the initial portion of the DB model stress strain results to the experimental curves. The temperature range for the tension tests was the same as for the compression tests while the strain rates used were 0.05/s, 0.1/s and 0.425/s engineering strain rate. The IVs used were 0.80, 0.92 and 0.98.

A major observation from the uniaxial tension tests was the inability of the DB model to capture drastic strain hardening associated with strain-induced crystallization. This hardening occurred at very large strains in uniaxial tension and not compression. The onset of this hardening and the magnitude of stress increase were highly dependent on the temperature and strain-rate. An algebraic model to capture this strain hardening was developed to be used with the DB model. The results from the modified model were studied and discussed.

Dedication

This document is dedicated to my parents and grandparents.

Acknowledgments

I thank my advisor, Dr. Rebecca Dupaix for the opportunity to conduct this work under her. She has been a great advisor, guide, supervisor and mentor. I express immense gratitude for the wonderful learning and research experience I have had under her without having to worry about funding. I thank Dr. Brain Harper for agreeing to be on my M.S. thesis committee.

I thank my lab-mate Danielle Mathiesen for her support, especially during my work with Abaqus simulations, Marissa Gill and Brian Neilon for supporting me with experimental testing activities, Kevin Wolf and Chad Bivens from the machine shop for their support in sample preparation, Dr. Jose Castro of Integrated Systems and Engineering and his group members Rachmat Mulyana and Seung-Hyun Ko for their role in the injection molding of samples and DSC and lab alumnus Gurucharan Chandrasekaran whose thesis has been a reference for me.

I thank my parents Bhuvana amma and Hari appa and my grandparents Rajam paati, Lakshmi paati, Thathappa and Nalla thatha for always being there for me.

Finally, I thank my friends Rahul, Sudharshan, Neeraj, Anirudh, Revathi, Santhosh, Hari Babu, Jagan, Sripad, Aswin and many others who made my life here easy and fun.

Vita

May 2010 .....B.E. Mechanical Engineering, College of Engineering Guindy (Anna University), Chennai, India

September 2010 to September 2011 .....Graduate Engineer Trainee, Ashok Leyland Limited, Chennai, India

September 2011 to June 2013 .....Deputy Manager - Testing, Product Development, Ashok Leyland Limited, Chennai, India

August 2013 to present .....Graduate Research Associate under Dr. Rebecca Dupaix, Department of Mechanical Engineering, The Ohio State University

Fields of Study

Major Field: Mechanical Engineering

Table of Contents

List of Tables

List of Figures

Chapter 1: Introduction and Literature Review

1.1 Mechanical Behavior of Poly(Ethylene Terephthalate)

Poly(Ethylene Terephthalate) (PET) finds widespread use in the packaging industry, primarily as bottles and containers for beverages and food, as stretched films in solar cells and as drawn synthetic fibers. It is a thermoplastic polyester which is semi-crystalline in its structure. The excellent moisture barrier properties of PET in conjunction with its light weight, sufficient temperature resistance and impact strength make it an ideal material for use as soft drink container bottles.

A variety of manufacturing processes are available to make products out of PET and stretch-blow molding is the primary process used to make soft drink bottles. Other processes include hot-drawing for fibers and films and thermoforming for trays and other products.

PET mechanically has a glassy behavior at lower temperatures, until a temperature called the Glass Transition temperature (Tg). This glassy behavior is characterized by a high modulus of elasticity and brittleness. Beyond Tg, the behavior shifts from glassy to rubbery and is characterized by a significant reduction in the modulus of elasticity. This

softening is highly temperature dependent and decreases with temperature. In this state, PET can be drawn to very large strains. The behavior is also dependent on the rate of draw, with stiffening observed with increasing rate of draw. Thus, the behavior can be characterized as a combination of linear elastic, viscoplastic and hyperelastic, with each characteristic affected by temperature, draw ratio and Inherent Viscosity (IV), which is a measure of the molecular weight of the polymer molecule.

The aforementioned manufacturing processes take advantage of the rubbery behavior of PET by heating it above Tg to shape the polymer and cooling it below Tg to lock the shape in place. PET also undergoes a phenomenon called strain-induced crystallization which causes an increase in stiffness, density and a reduction in gas permeability. This property can be used to advantage in increasing the shelf life of beverages held in PET bottles.

The extremely non-linear behavior of PET poses a challenge in developing a material model of PET for use in finite element simulation. Simulation plays a major role in predicting material behavior during processing and predicting the end product characteristics while saving on tooling and associated development costs and time.

1.2 Purpose of this work

The purpose of this work is to characterize the mechanical behavior or PET through compression and tension experiments and fit the Dupaix-Boyce material model to describe the temperature, strain-rate and IV dependent material behavior of PET for use in finite element simulation of blow molding.

1.3 Summary of this work

Compression tests were initially conducted on cylindrical specimens cut from preforms. The stress strain characteristics from these experiments showed a dip in medium strains which was irregular, inconsistent and could not be captured when attempted to fit with the Dupaix-Boyce (DB) model. Compression tests were repeated with non-hollow discs cut from specimens injection molded from PET pellets. These experiments gave consistent results without the dip, which deemed the hollow specimens unsuitable for compression tests because of the possibility of other deformation modes. The DB model was fit to these results. A good fit was achieved. Tension tests were then conducted first using standard tensile bars, then using small rectangular bars after finite element and experimental comparison of results from both so that they yield similar stress-strain curves. Tests were then continued with small bars, which could reach higher final strains within the constraints of the testing environmental chamber. A different set of constants could fit the DB model the initial portion of the stress strain curves from the tension tests

beyond which significant strain hardening was observed which could not be captured by the model. This hardening did not occur in compression and suggested the possibility of occurrence of strain-induced crystallization. This strain hardening was characterized and the Dupaix-Boyce model was modified to allow the capture of this hardening in uniaxial tensile testing simulation. The results are also compared with that obtained by simulation using the Elasto-Visco-Plastic (EVP) material model.

This thesis is written in the following sequence: Chapter 1 describes the introduction and literature review for this work, which primarily consists of experimental characterization of the mechanical behavior of PET with temperature, strain-rate and IV dependence, constitutive modeling background, strain-induced crystallization and the EVP model. Chapter 2 describes the compression testing setup, procedure and analysis of test results. Chapter 3 describes the Dupaix-Boyce (DB) constitutive model which is used as the primary model in this work. Chapter 4 describes the fitting of compression experiment data to the Dupaix-Boyce model for different temperatures, strain-rates and IVs. Chapter 5 describes tension test procedures, results and the fitting of the model to capture tension test results, including the inability to capture drastic strain hardening due to strain induced crystallization. Chapter 6 compares tension and compression test results in terms of true stress versus true strain and stretch invariants. Chapter 7 describes the EVP model and discusses the simulation results obtained from the EVP model with the Dupaix-Boyce model. Chapter 8 describes the development and implementation of the

crystallization module to capture strain hardening due to crystallization in uniaxial tensile tests. Chapter 9 concludes the thesis and discusses possible future work.

1.4 Literature review

Significant research activity has been done previously by different groups to characterize the mechanical behavior of PET.

1.4.1 Mechanical behavior of PET

Jabarin (1984) conducted orientation studies on PET through simultaneous bi-axial tensile tests to determine the relationship between physical properties of PET with molecular weight (related to Inherent Viscosity, I.V.) and molecular orientation. Mechanical properties were found to be strongly related to strain-rate, draw ratio, IV and orientation temperature, and very strongly related to the degree of orientation. The degree of orientation was found to be dependent on IV, stretch ratio and temperature. Birefringence studies also indicated the existence of strain-induced crystallization of PET. The extent of this crystallization and the molecular structure upon crystallization were found to be dependent on strain-rate and orientation. Measured value of birefringence was directly related to orientation. Orientation was found to be towards the direction of greatest stretching in unequal biaxial stretching, decreasing with temperature

and increasing with strain rate. Also, orientation was higher with increasing IV for lower strain rates and became independent of IV at higher strain rates.

Chandran and Jabarin (1993) studied the characteristics of the stress strain curves during biaxial stretching experiments. They found the stress-strain curves in sequential biaxial drawing to be concave upward under lower strain rate and higher temperature which changed to convex upward at higher strain rates and lower temperatures and also when the first stretch exceeded a critical draw ratio, which indicates strain induced crystallization during drawing in the first direction. Stress was also found to increase with increasing strain rate and decrease with increasing temperature.

Zaroulis and Boyce (1997) conducted differential scanning calorimetry (DSC) tests on amorphous PET in conjunction with uniaxial and plane strain compressive tests in the glassy and glass transition regions of PET. The test results were found to be highly dependent on temperature, strain rate and orientation. DSC results indicated that strain hardening observed could be because of molecular orientation and not strain induced crystallization at lower temperatures during uniaxial deformation. However, during plane strain deformation, both orientation and crystallization were observed with strain-hardening. It could not be determined if crystallization occurred during deformation or during annealing post deformation.

Llana and Boyce (1999) studied experimentally the stress-strain behavior of PET under large strain uniaxial and plane strain deformation above the glass transition region and studied the crystallographic texture evolution by Wide Angle X-Ray Diffraction (WAXD). From the uniaxial test results, the stress-strain characteristics were found to have four distinct regions. The initial stress response is stiff, followed by a roll-over indicating the start of plastic flow. This is followed by a steady increase in stress with respect to strain, known as the initial strain hardening. Finally, there is a dramatic rise in stress at large strains. All these segments of the curve were found to be strain-rate dependent until when the deformation can considered to be isothermal. At higher strain rates, the deformation is more adiabatic, which causes thermal softening. In the plane strain results, the initial stiffness increased with strain rate and the onset of dramatic hardening decreased with the same. Also, higher temperature caused softening of the stress-strain characteristics. Another observation was the reduction in recovered strain with increase in temperature. The initial flow stress was observed to be higher for plane strain compression and the strain hardening was also observed to be much higher. The DSC aspects of this work have been discussed below in the section on crystallization.

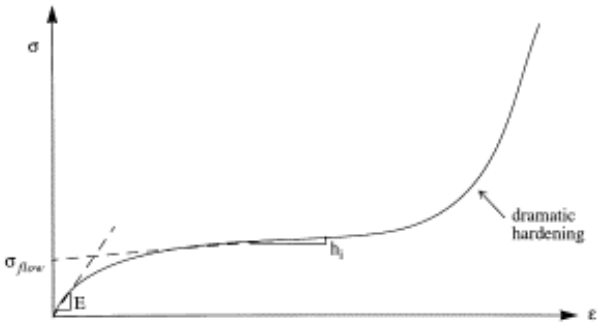

Figure 1.1 Stress vs Strain sample curve for PET (Boyce, Socrate and Llana, 2000)

1.4.2 Constitutive Modeling of PET

The behavior of PET at high temperature was a combination of different characteristics - linear elastic at initial small strains, non-linear visco-elastic in the medium strains and hyperelastic with dramatic strain hardening at higher strains. Each of these individual characteristics are also temperature and strain rate dependent. Amorphous polymer chains do not have crosslinks like rubbery materials. Instead they have physical entanglements which can slip during drawing by a process called reptation (de Gennes, 1979). Capturing these physical phenomena in a mathematical model poses a challenge to the engineer.

Modeling the glassy-rubbery behavior of polymers started as a one-dimensional model developed by Haward and Thackray (1968) which used the Eyring flow model and rubber elasticity theory and included yield and strain hardening.

Buckley et al (1995) developed a three-dimensional model which split the net stress output from the model to be the summation of stresses caused by individual sections of the model. The individual sections of the model here comprised of bond distortion modeled with linear elasticity and Eyring viscous flow and a conformational change part modeled using the Edwards-Viglis entropy function. Fitting of this model to biaxial experimental data was published by Buckley et al (1996). This model captured the characteristics of the stress strain curve well except in conditions of low strain rates and higher temperatures. This model did not include the effect of chain reptation.

Reptation was included in a model developed by Adams et al (2000) which extended the model of Buckley et al (1995) but the model fit to biaxial data with varying strain rate had not been discussed. Hence, the strain rate dependence of this model is unknown.

As mentioned before, PET shows hyperelastic characteristics at large strains. To capture this, hyperelastic material modeling ought to be discussed. The early hyperelastic models were described by Treloar (1943), Mooney (1940), Rivlin (1948) and Ogden (1972). These models were phenomenological in nature were primarily based on the development of an expression for strain energy, which when differentiated with respect to strain would provide an expression relating stress and strain.

Newer hyperelastic models where developed based on a more physical interpretation of deformation and one of the more popular models were developed Arruda and Boyce

(1993a and 1993b). They proposed an 8-chain model which was based on the deformation of a unit cell of the material constructed to be a unit cube with eight chains attached to the corners of the cube from the center. This model is based on the physics of the problem rather than being phenomenological and was able to capture the strain state dependence of stress very well.

Boyce, Socrate and Llana (2000) developed a constitutive model that broke down the total stress output to be a sum of the stress caused by intermolecular interactions and by molecular orientation. Each of these parts were described by a three dimensional spring to represent elasticity and a dashpot to represent plasticity. For the intermolecular interaction resistance, the spring was linear elastic which was active in the initial stretches. Plastic flow was set to start after the stress exceeded a particular value. The molecular orientation part consisted of a non-linear spring that could capture strain hardening and a dashpot to capture reptation and molecular relaxation.

Dupaix and Boyce (2007) modified this model which could capture the temperature, strain-rate and strain-state dependent behavior of PET and PETG. Since PETG does not undergo crystallization, the strain hardening mechanism from this model is primarily based on molecular orientation. The dashpot section in the molecular orientation portion from the previous model was improved upon to be based on a temperature and strain rate independent parameter called the orientation parameter. This parameter was used to govern the turning off of molecular relaxation after which dramatic strain hardening is

initiated at high strains. This model has been used to capture the behavior of polymers other than PET like PMMA which is amorphous by Palm and Dupaix (2006). Strain induced crystallization is not covered by this model yet it provided good fits for PET behavior based on molecular orientation based strain hardening for experimental compression test data. Fitting was not done for tension data.

Dupaix and Krishnan (2006) extended the Dupaix-Boyce model to account for strain-induced crystallization. They added an additional chain of spring and dashpot to the in parallel to the intermolecular resistance portion of the Dupaix-Boyce model with stiffer properties to reflect the occurrence of crystallization. The occurrence of crystallization was set up to start after a particular level of strain specified by the orientation parameter discussed earlier, and at slower strain rates. The stress output due to intermolecular interaction was a function of the net stress in the non-crystallized and crystallized spring-damper setup. The percentage of crystallinity which was computed with an equation based on the non-isothermal version of the Avrami equation developed by Doufas et al (2000). The Dupaix-Krishnan model, however, did not account for the temperature and strain-rate dependence of crystallization.

In this work, the model from Dupaix (2003) is used. For modeling strain induced crystallization however, a different first – time approach has been attempted.

1.4.3 Strain-induced Crystallization of PET

Llana and Boyce (1999) conducted DSC experiments and under uniaxial compression came out with the following observations. Percentage crystallinity was found to be independent of strain rate and was at around 30% for all strain rates. However, it was highly dependent on temperature and was observed to increase from 14% to 30% at 378K with an increase of just one order of magnitude of the strain rate. Also, at higher strain rates where the deformation becomes adiabatic, the thermal softening observed is associated with a drop in crystallinity. It was observed from the plane strain compression DSC results that crystallization occurred significantly during the deformation, but the increase with increase in strain rate was negligible and increase in temperature. There was also ambiguity with the fact if crystallization took place during strain or during the cool down period. Wide Angle X-Ray Diffraction (WAXD) studies were also conducted to study crystallographic texture and was found to be related to the orientation associated with the particular deformation state like uniaxial, plane strain, etc. WAXD results as to strain rate and temperature dependence of crystallization was consistent with DSC results.

Dupaix and Boyce (2005) compared the stress strain characteristics at similar conditions from PET and its non-crystallizing co-polymer, PETG. The experiments were conducted at temperatures from 25^{o}C to 110^{o}C, strain rates from 0.005/s to 1/s and at uniaxial and plane strain compression. The observation here was that the behavior of both polymers

were similar in most cases, which suggested ruling out of crystallization in causing strain hardening. However, at 90^{o}C plane strain conditions, PET showed stiffer behavior than PETG which suggested beginning of crystallization at highly oriented conditions like plane strain compression thus causing strain hardening.

Misra and Stein (1979) found that crystallization occurred during stretching of amorphous PET only if stretching crossed 80% elongation. Jabarin (1992) conducted similar tests to find out that strain induced crystallization occurred before the stretching reached the strain hardening region of the force-displacement curve.

Ashford et al (2000) studied the prediction of molecular orientation and crystallinity during the drawing of PET. They concluded that during drawing, there is a steady development in orientation while crystallization is inhabited. Crystallization occurs after drawing following first order kinetics with the rate depending on orientation and temperature. This would imply strain hardening occurring during drawing might be caused by orientation. This work suggested development of crystallization during annealing after drawing.

Blundell and team (1996) also characterized using synchrotron radiation the strain induced crystallization at fast draw rates in biaxial stretching. They discussed two competing phenomena during the drawing of PET – Relaxation during drawing versus crystallization which effectively tended to create the effect of crosslinking. Higher

temperatures increased mobility and disorientation while higher draw ratio increased the rate of crystallization.

Blundell and team (2000) studied orientation prior to crystallization during drawing of PET by the recording of Wide angle X-ray scattering data at fast draw rates under biaxial stretching. They characterized molecular orientation in terms of an orientation order parameter. The rate of increase of this parameter decreased with increasing temperature and decreasing strain-rate. The onset of crystallization occurred after the completion of drawing when the strain rate was higher than the rate of chain retraction motion and at slower rates occurred during the deformation itself.

Chaari et al (2003) studied the development of crystallization versus mechanical behavior using WAXD. They conducted uniaxial tensile tests on initially amorphous PET at different strain rates above glass transition temperature up to a stretch of 5 and draw rate of 0.75/s. They concluded that at slower draw rates, crystallization occurred after drawing while at medium draw rates, it occurred during the deformation. At high draw rates, crystallization started during draw and continued after the drawing had ended. At even higher rates, they anticipated the possibility of crystallization starting after deformation as observed by Mahendrasingham et al (1999). With respect to the mechanical properties, Chaari and group could relate strain hardening to the start and growth of crystallization. The stress strain curve was divided into three regions based on the state of the microstructure. The first region was viscoelastic with the polymer chains undergoing

extension in an amorphous matrix. This was followed by nucleation, in which the oriented nuclei behaved as crosslinks. Finally, crystallization initiated, which was linked to strain hardening.

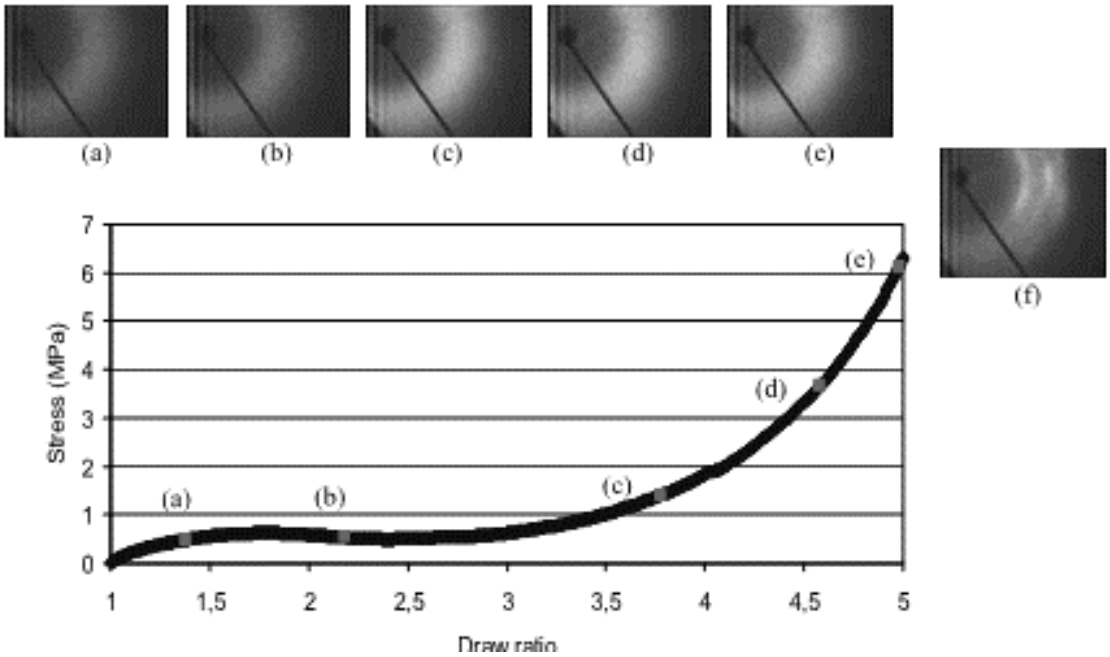

Figure 1.2 PET Tensile stress vs strain at strain rate 0.06/s with corresponding WAXD patterns (Chaari et al, 2003). WAXD pattern (f) is taken minutes post deformation.

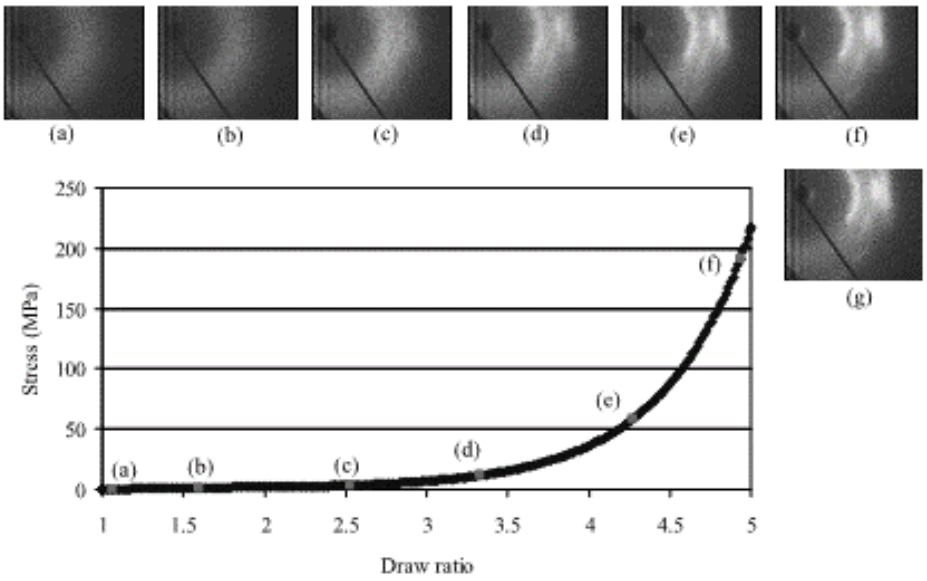

Figure 1.3 PET Tensile stress vs strain at strain rate 0.2/s with corresponding WAXD patterns (Chaari et al, 2003). WAXD pattern (f) is taken minutes post deformation.

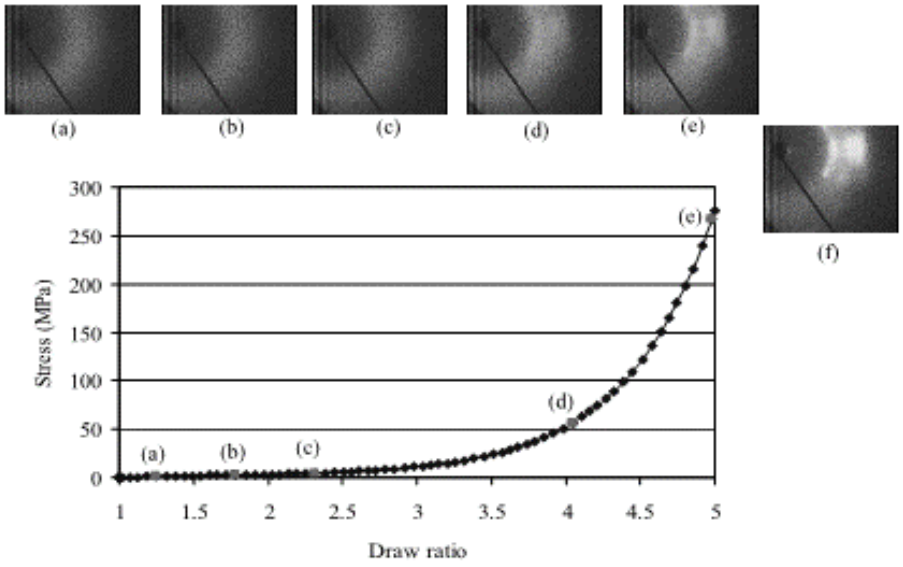

Figure 1.4 PET Tensile stress vs strain at strain rate 0.75/s with corresponding WAXD patterns (Chaari et al, 2003). WAXD pattern (f) is taken minutes post deformation.

1.4.4 Elasto-Visco-Plastic Model background

C G'Sell and JJ Jonas (1979) proposed a one-dimensional visco-plastic model to describe the behavior of polymers in uniaxial tension. This model incorporated temperature and strain rate dependence and could be fit to describe the behavior of PET in uniaxial tension. It also had a provision for the capture of strain hardening at large strains using a hardening modulus.

Mir, Thibault and DiRaddo (2011) developed the C G'Sell model into a generalized three dimensional model using the von Mises yield criterion and also incorporated a strain softening modulus to capture the reduction of stress observed in polymers after a peak stress has been reached. The constitutive equations in this model were used in this thesis to perform numerical integration and predict stress-strain characteristics to be compared with the Dupaix-Boyce model.

1.5 Summary

This chapter discussed the application of PET and introduced various aspects of the mechanical behavior of PET and outlined the scope and summary of this entire work. The mechanical behavior of PET with respect to dependence on temperature, strain-rate, strain-state and inherent viscosity (IV) have been studied by various researchers and a

consistent idea has been put forth by them that decrease of temperature and IV and increase of strain-rate leads to a stiffer behavior. The different approaches of constitutive modeling this highly non-linear behavior of PET were studied from past research. The Dupaix-Boyce model published in 2003 was used as a basis for modeling in this thesis. Finally, this chapter also dealt with the study of literature to understand and characterize the different processes that occur during stiffening of the stress-strain curve of PET which includes molecular orientation and strain-induced crystallization. The underlying mechanisms that define crystallization and orientation were studied.

Chapter 2: Uniaxial Compression Tests

2.1 Introduction

Material testing was conducted to obtain characteristics of PET to which the Dupaix-Boyce model was fit. It was decided to start with uniaxial experiments followed by model fitting after which other deformation modes can be experimentally tested and then validated with the model if required. For this uniaxial testing, compression tests were chosen over tension tests.

2.2 Compression vs Tension Testing

Uniaxial compression testing with a constant true strain-rate had some advantages compared to tension testing. Firstly, higher final strains could be reached in compression within the size limitations of the testing facility. Secondly, compression specimens would usually be smaller than tension bars which means a quicker attainment of uniform testing temperature. Thirdly, compression testing did not require implementation of proper gripping mechanisms to prevent slipping of the specimen. Fourthly, localized necking was not possible in compression which meant the true strain rate throughout the specimen would be uniform. Finally, compression testing required a reduction in draw rate to

maintain a constant true strain rate as opposed to tension testing which required an increase. This meant that the drawing rate can always be set within the limitations of the testing machine irrespective of the final strain. However, compression testing has a disadvantage when compared to tension testing, which is the friction at the specimen-compression platen interface. This friction can play a large role especially at very large strains.

This can be explained by the expression

$$\frac{d\varepsilon}{dt} = \frac{d}{dt}\left(\ln(\frac{L}{L_o})\right) = \frac{1}{L} * \frac{dL}{dt}$$

It can be observed that as L increases $\frac{dL}{dt}$ has to be increased for constant $\frac{d\varepsilon}{dt}$.

2.3 Materials and Methods

2.3.1 Test Samples from Preforms

This work required characterization of (Inherent Viscosity) IV dependence of PET. IV is related to the molecular weight of the polymer, hence higher IVs are associated with more viscosity and stiffer responses. Preforms of the following four IVs 0.80, 0.86, 0.92 and 0.98 were sourced from the sponsor and cut into rings of 8mm thickness as in the pictures below. Using sections cut from preforms seemed to offer a few advantages than molding samples specific to compression.

Since the preforms are the input to the blow molding process and the Dupaix-Boyce model was to be used primarily for blow molding simulation, material characteristics obtained from the preform would accurately serve as the basis to fit the model. Errors associated with the usage of specimens in simulation which would hugely differ in size and shape as the compression samples would be eliminated. Sections of the preform would pretty much be a cylindrical compression specimen but with a hollow and the taper in the preform wall was small enough to be ignored. Also, time and money associated with molding compression specimens could be saved. Finally, the tested samples and the preforms would have the process parameters to be exactly similar to the actual material used. In spite of these advantages, the preform sections were found to be poor compression specimens. This would be described later in the chapter.

The rings cut from the preforms had a height of 8mm along with an outer diameter of 21 mm and an inner diameter of 13.5 mm. A slight taper was present in the preform which was neglected for stress and strain calculation.

Figure 2.1 Whole preform from which sections are cut

Figure 2.2 Cut preform section used as compression specimen

2.3.2 Test Conditions

Three different temperatures of 363K, 373K and 383K which are above the glass transition temperature were chosen for the tests considering the temperature range at which the Dupaix-Boyce model will be used in blow molding simulation. Two different true strain rates of -0.1/s and -1/s were chosen for each of these temperatures to build the

test matrix because these differed by an order of magnitude, yet, fell comfortably within the operating range of the machine.

2.3.3 Experimental Facility

An Instron Universal Testing machine, model Instron 5869, was used to perform the tests. It is a dual column electromechanical testing machine with a maximum load capacity of 50kN and a speed range of 0.001-500 mm/min.

For compression testing, the 50kN load cell was setup for use with compression platens in a temperature control chamber providing the necessary conditions of temperature for the test. The system was controlled by the Instron Bluehill software which is setup to run on a personal computer.

The motion of the cross head was setup for the given height of the specimen so as to allow a constant true strain rate. The rate of compression reduces as compressive travel increases to maintain a constant true strain rate. To enable this, the 'Profiler' module in the control software, Instron Bluehill, was used. A continuous non-linear function input for motion was not supported by Instron Bluehill and hence the required displacement curve was split into a number of blocks of constant displacement rate while ensuring each block remained within the control limits of the machine. Refer to Figure 2.4 and 2.5 for actual time histories of true strain rate and displacement rate. The number of blocks

available to provide program constant true strain rate of 1/s in the machine was only three as seen in figure 2.5. This was because the machine failed to accurately reverse the motion of the compression platen at the set final compressive strain when a higher number of blocks were used. Because of this, stress strain characteristics at the strain rate of 1/s show bumps which occurred as the machine changed its strain rate with each block for a constant overall true strain rate.

Figure 2.3 Instron 5869 testing machine

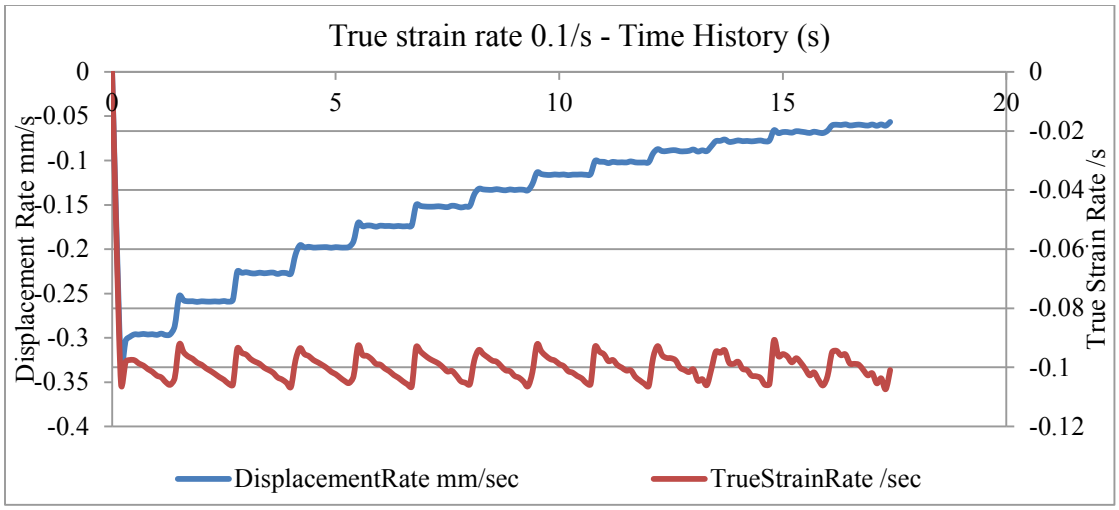

Figure 2.4 Time history of actual true strain rate and displacement rate for overall true strain rate 0.1/s

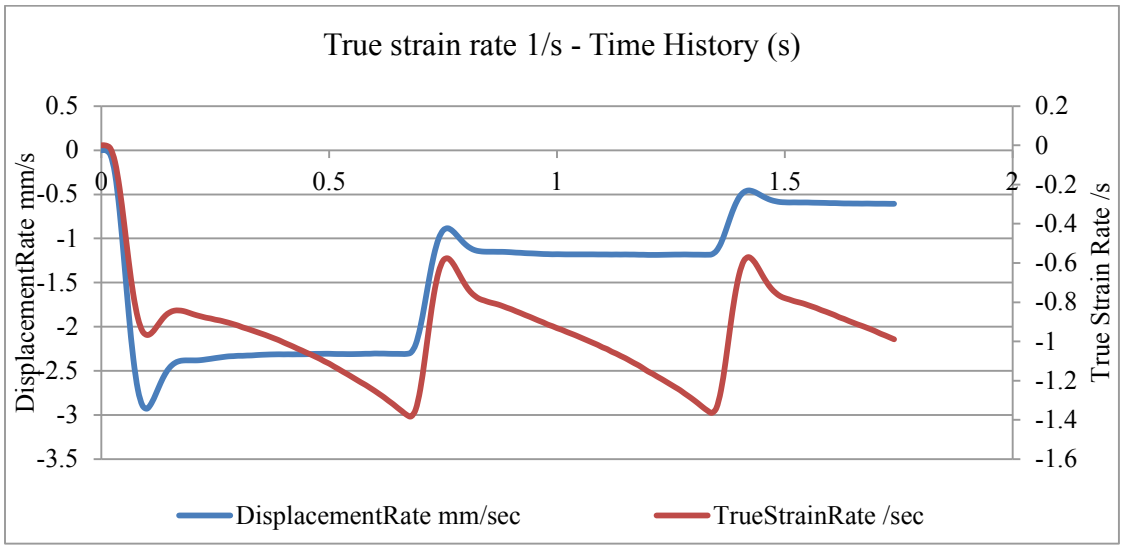

Figure 2.5 Time history of actual true strain rate and displacement rate for overall true strain rate 1/s

2.3.4 Experimental Procedure

The following procedure was followed for the compression experiments. The oven was allowed to equilibrate at the test temperature for an hour. The material samples were initially stored in a dessicant chamber which had a relative humidity of about 40%. This was because the polymer is sensitive to moisture especially if stored for long time periods. The sample to be tested was taken out and its dimensions were measured using a Vernier caliper. WD 40 lubricant was sprayed on the compression platens of the machine and a thin film of Teflon was placed over the surfaces of the platens. The lubricant and sheets are used to prevent friction between the specimen and platen. The sample was placed on the lower platen and allowed to equilibrate at the oven temperature for ten minutes. After equilibration, the compression test was run at constant true strain rate for the given temperature and strain rate to a final engineering strain level of -0.8. The raw time series data of force and displacement was output as a comma separated text file. The test was repeated until sufficient repeatability was established.

For the computation of stress from the recorded force readings, the specimen was assumed to maintain a constant volume throughout the compression process, i.e., the product of cross sectional area with the length was assumed to be a constant. The area computed for a given compression at a point in time is divided into the force at that time to compute the engineering stress at that point in time. The following methodology is used to compute true stress σ_T and true strain ε_T in relation to force F, engineering stress

σ_E, engineering strain ε_E, stretch S, initial length L_0, final length L, change in length ΔL, initial area A_0 and final area A.

$$\sigma_E = \frac{F}{A_0}$$

$$\varepsilon_E = \frac{\Delta L}{L_0}$$

$$S = \frac{L}{L_0} = \frac{L_0 + \Delta L}{L_0} = 1 + \varepsilon_e$$

$$\varepsilon_T = \ln(\frac{L}{L_0})$$

$$\sigma_T = \frac{F}{A} = \frac{F}{A_0} * \frac{L}{L_0} = \sigma_E * S$$

Figure 2.6 Dessicant chamber

2.3.5 Observation from initial samples

Two batches of preforms were acquired from the sponsor. The samples from the first batch turned opaque after a few minutes of equilibration time in the oven. This, however, did not occur in samples which were from the second batch. Further investigation showed that first batch was old and the second fresh. Differential Scanning Calorimetry (DSC) was carried out on these samples from different sources to ascertain the percentage of crystallinity in the sample. DSC did not show a significant difference in the percentage crystallinity of samples from both sources. Moisture absorption over time could have led to the problems with the first batch. All future testing was done with material from the second batch.

Table 2.1 Initial DSC test results

Sample	IV	DSC %Crystallinity	Remarks
Initial11	NA	6.5	Turned opaque (Crystallized) upon equilibration
Later #1	0.80	6.7	Did not crystallize
Later #2	0.98	6.1	Did not crystallize

2.4 Results for compression tests with preforms

The results of the compression tests with the preform sections are given below. The engineering stress versus stretch plots for the temperatures 363K, 373K and 383K and strain rates 0.1/s and 1/s are shown in figures 2.7 to 2.12. Each figure shows the curve at a constant temperature and true strain rate. The four curves in these figures represent the four IVs tested – 0.80, 0.86, 0.92 and 0.98.

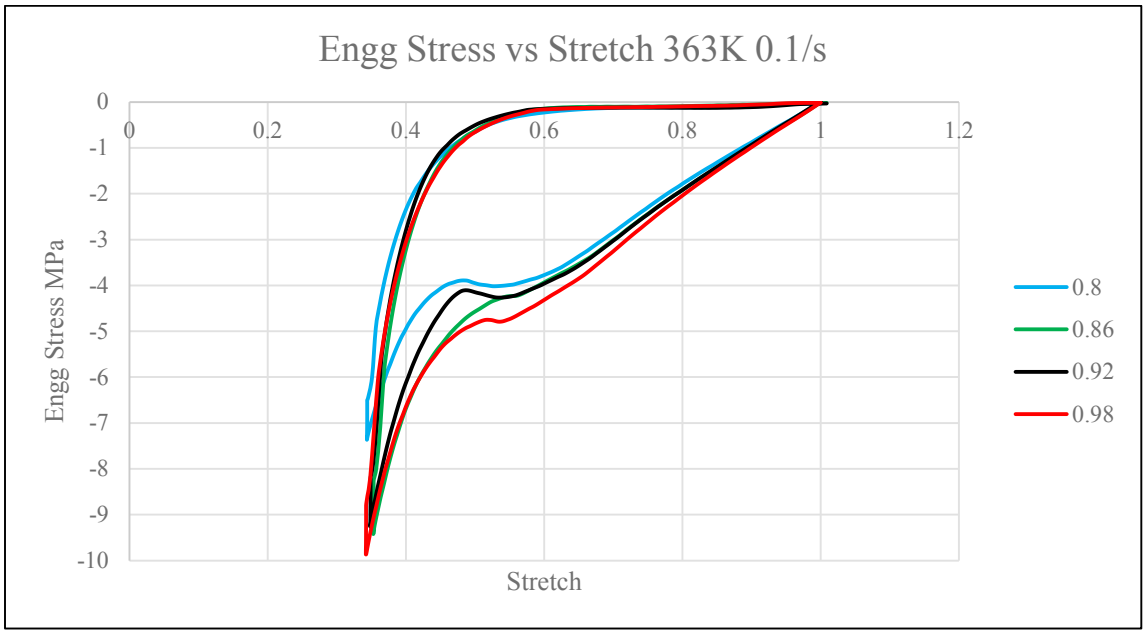

Figure 2.7 Comparison of Stress vs Stretch curves from different samples of same IV at 363K 0.1/s

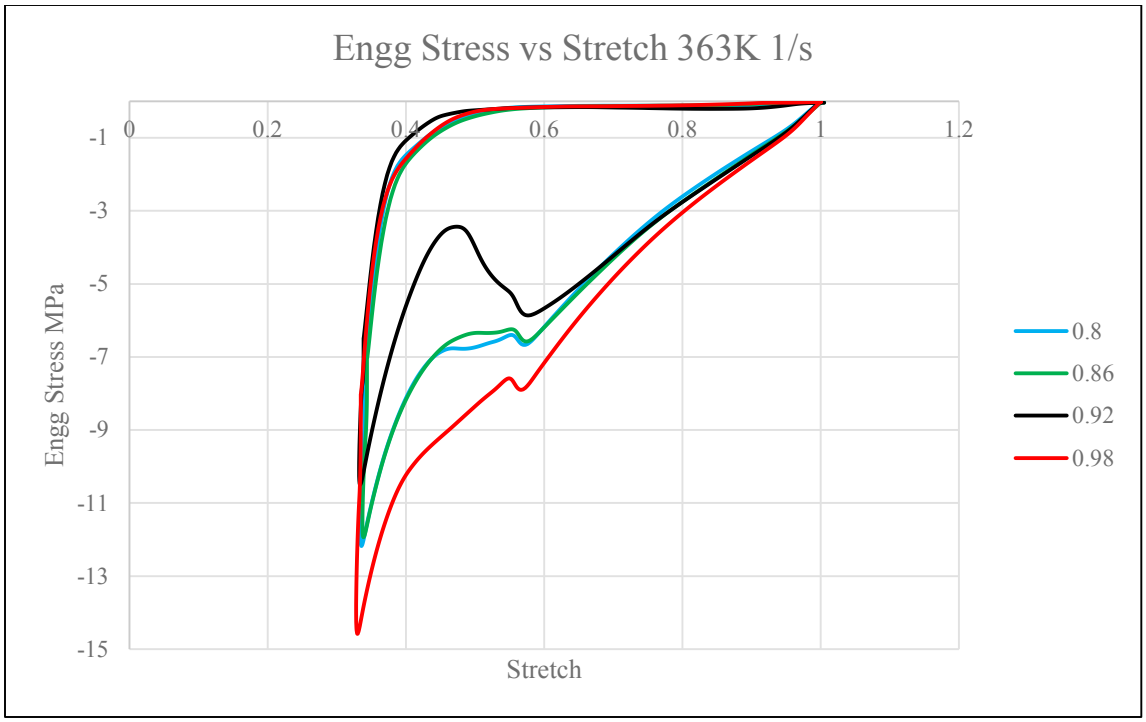

Figure 2.8 Comparison of Stress vs Stretch curves from different samples of same IV at 363K 1/s

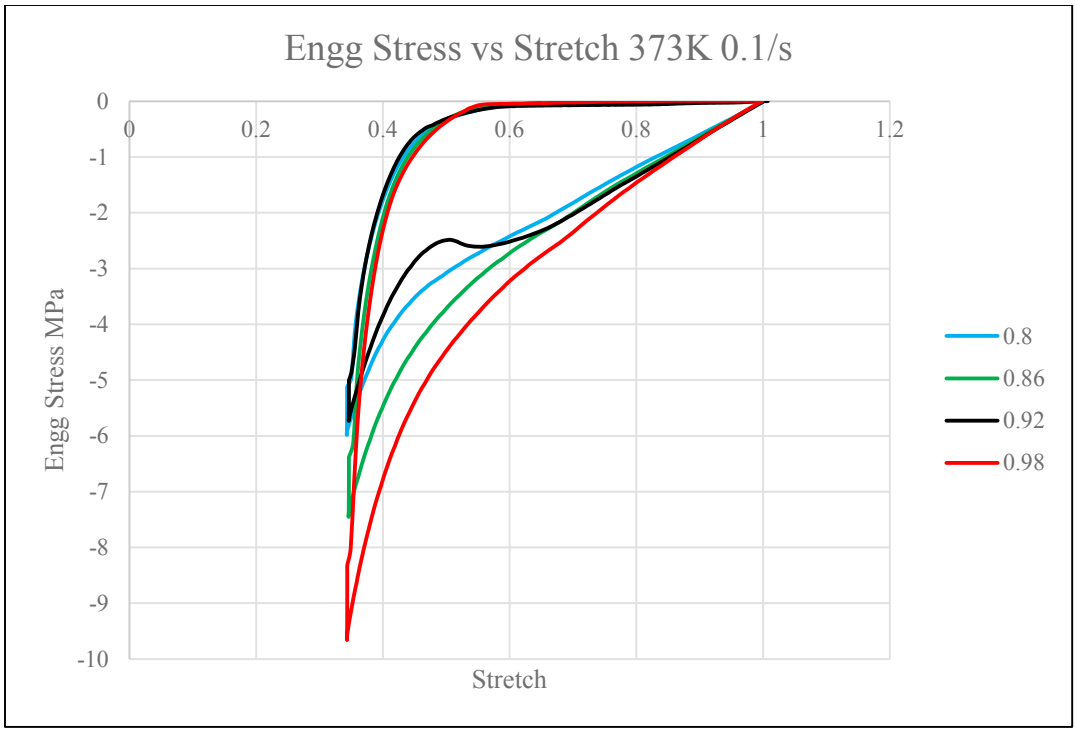

Figure 2.9 Comparison of Stress vs Stretch curves from different samples of same IV at 373K 0.1/s

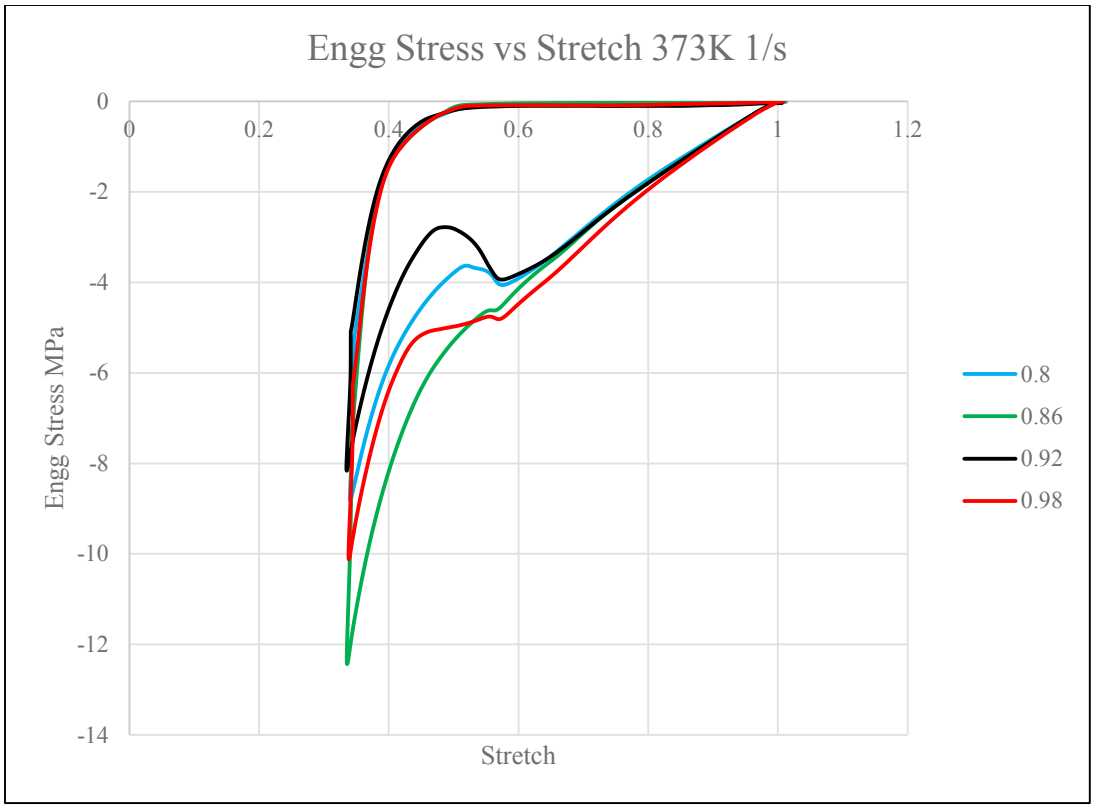

Figure 2.10 Comparison of Stress vs Stretch curves from different samples of same IV at 373K 1/s

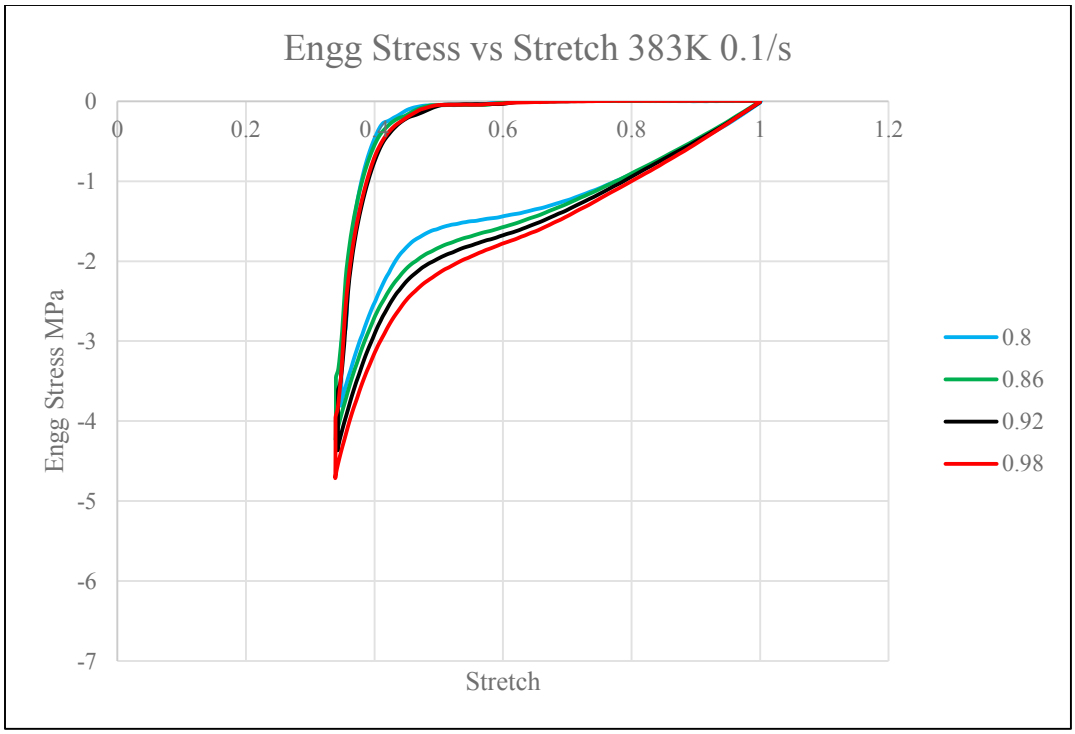

Figure 2.11 Comparison of Stress vs Stretch curves from different samples of same IV at 383K 0.1/s

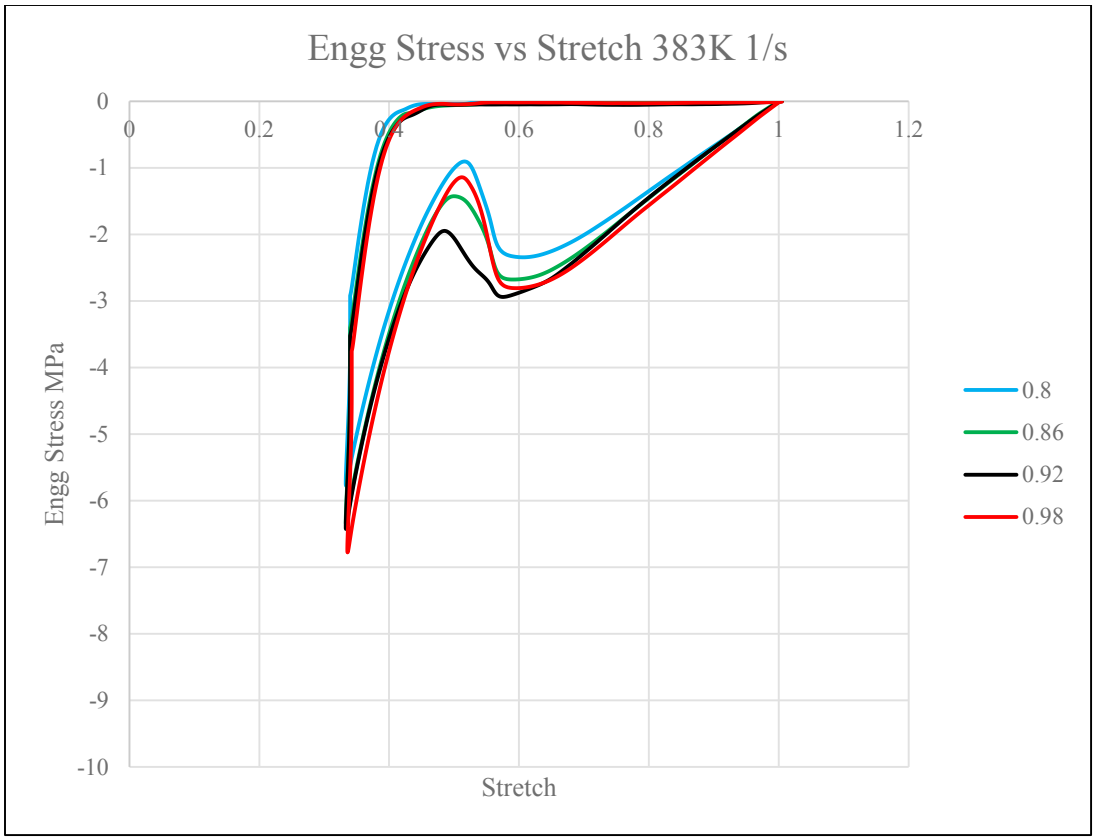

Figure 2.12 Comparison of Stress vs Stretch curves from different samples of same IV at 383K 1/s

2.4.1 Observation from results with preform

The general characteristic of the Engineering Stress vs Stretch curve consisted of a linear relation until a stretch varying from 0.6 to 0.8 was reached, beyond which a dip was observed in the curve. This dip showed significant variations across IVs even in similar conditions of strain rate and temperature as observed in the above plots.

It became necessary to ascertain if this dip was actually because of material behavior or due to external effects like that of friction between the specimen and the platen or unwanted deformation patterns like buckling because of the hollow shape of the specimen.

To ascertain the role of friction on the curves, the tests were repeated without the use of Teflon sheets between the specimen and the platens. No specific pattern could be observed from the results.

Table 2.2 Number of samples showing dip out of 2 tests at similar conditions

		Number of samples showing dip out of 2 trials each	
		Without Teflon sheet	With Teflon sheet
363K 0.1/s	8	1	1
	0.86	1	0
	0.92	0	2
	0.98	1	0
363K 1/s	8	0	2
	0.86	2	0
	0.92	2	2
	0.98	0	0
373K 0.1/s	8	1	2
	0.86	0	2
	0.92	2	2
	0.98	0	2
373K 1/s	8	0	2
	0.86	0	0
	0.92	2	2
	0.98	1	1

Table 2.2 indicates that friction could not have played a major role in causing the dip. Another observation that could be made about the dip was that the samples not showing the dip appeared 'squished' while those showing the dip appeared more uniform. Figure 2.13 shows the stress-stretch characteristics of different samples of the same IV of 0.92, tested at the same temperature and strain rate. In this figure, two samples have exhibited the dip and they don't appear as 'squished' as the other two samples, which have not exhibited this dip.

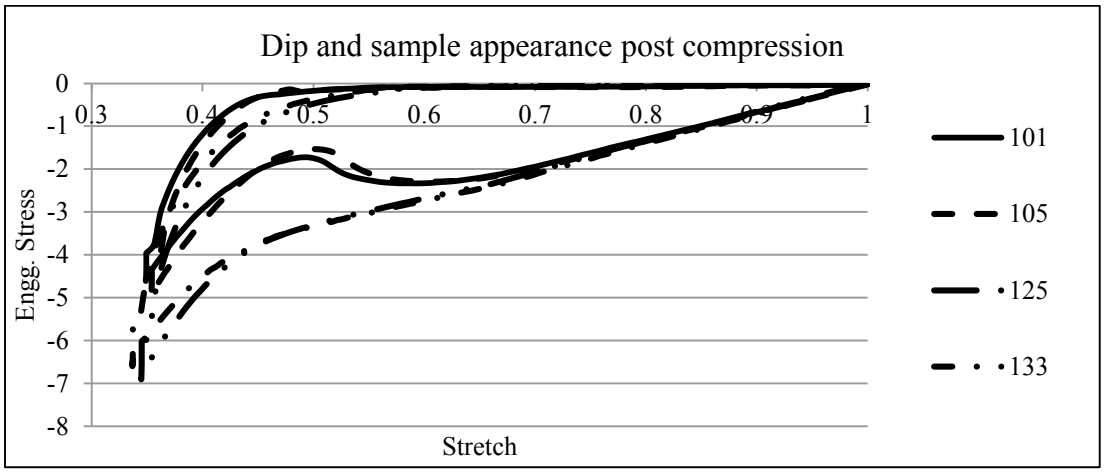

Figure 2.13 Comparison of Stress vs Stretch curves from different samples of same IV at similar conditions

Figure 2.14 Sample appearance after testing

The above observation pointed out to the possibility of the unwanted deformation patterns being caused by the hollow center of the samples. One possibility was that due to the presence of the hole, the specimen during compression tended to close in on the hole through buckling, or bending or undergoing non-uniform deformation rather than maintaining pure uniaxial deformation which was essential for the validity of the test results. In addition, the Dupaix-Boyce model fits to these curves yielded poor fits because the presence of the dips which suggested that the curves obtained may not have been valid compression test results. This necessitated the repeat of tests with regular circular samples without a hole.

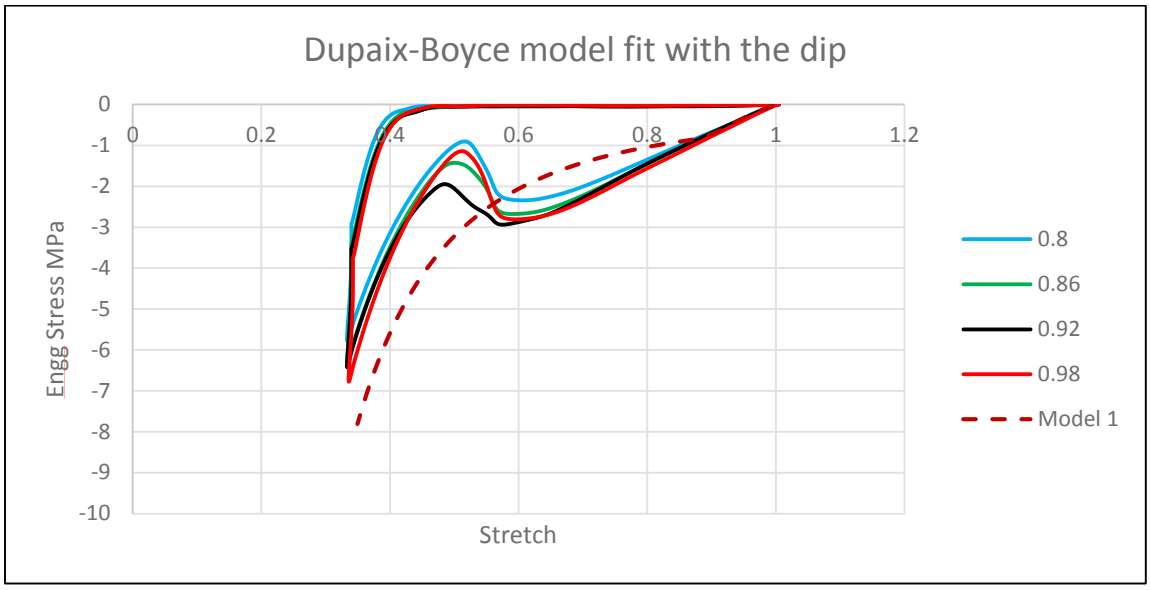

Figure 2.15 Dupaix-Boyce model best fit with the dip at 383K 1/s

Other than the dip, the general observation with the test results was that the material showed stiffer behavior with increase in IV. It can be observed from the above results that IV 0.80 has shown the lowest stress levels and IV 0.98 the highest. IV 0.86 and 0.92 have behaved interchangeably which might suggest that the specific samples used might be closer to each other in mechanical behavior, falling within the scope of random inter-trial differences.

2.5 Repeat of experiments with non-hollow specimens

Pellets of the four different IVs were provided by the sponsor and injection molded at the facility in the Integrated Systems Engineering (ISE) department at OSU. The mold consisted of the shapes as shown in figure 2.16.

Table 2.3 Molding Parameters

Melt Zone Temperature	520°F
Velocity	1.5 inch/s
Packing Pressure	550 psi
Cooling Time	55s
Mold Temperature	80°F
Back Pressure	50 psi
RPM	80

Table 2.4 Actual Packing Pressure used to prevent mis-runs

IV	Packing Pressure psi
0.80	550
0.86	675-700
0.92	700
0.98	500

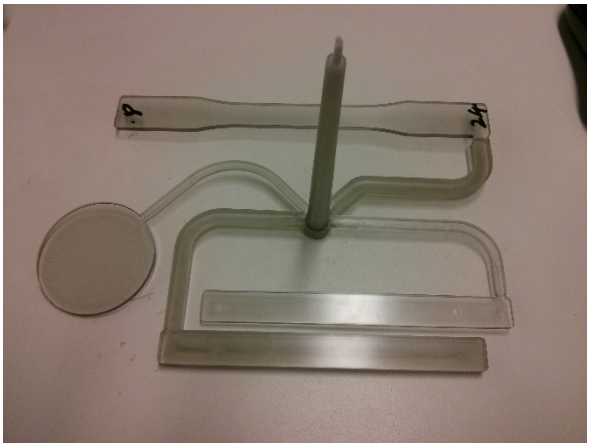

Figure 2.16 Injection molded sample

The mold consisted of a disc and a rectangular bar of 3.5 mm thickness. Small circular discs of diameter 12.5 mm where cut out from the disc for use as compression specimens. The rectangular bar was used as tensile test specimens of gauge length 20mm. A standard tensile bar was available in the mold, but could not be used for tension tests because of size restriction of the environmental chamber. This is discussed in detail in chapter 5.

DSC was conducted on samples from the 4 IVs; their results are given below. Figures 2.17 to 2.20 contain the plots of heat flow vs temperature for each of the four IVs, from which percentage crystallinity have been calculated. It can be seen that the highest IV sample of 0.98 shows higher percentage of crystallinity (Figure 2.20). Physically, samples of that IV appeared considerably less transparent than the other IVs.

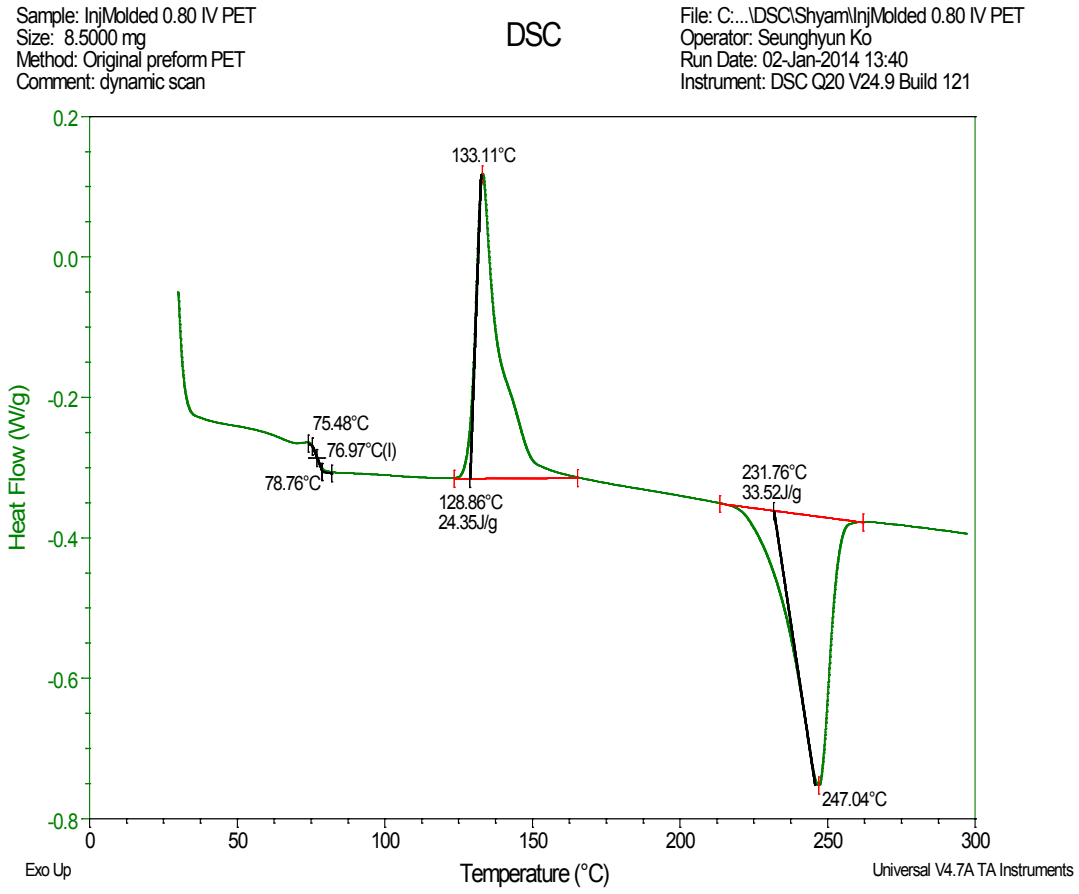

Figure 2.17 DSC result for IV 0.8. Crystallinity computed to be 6.55%

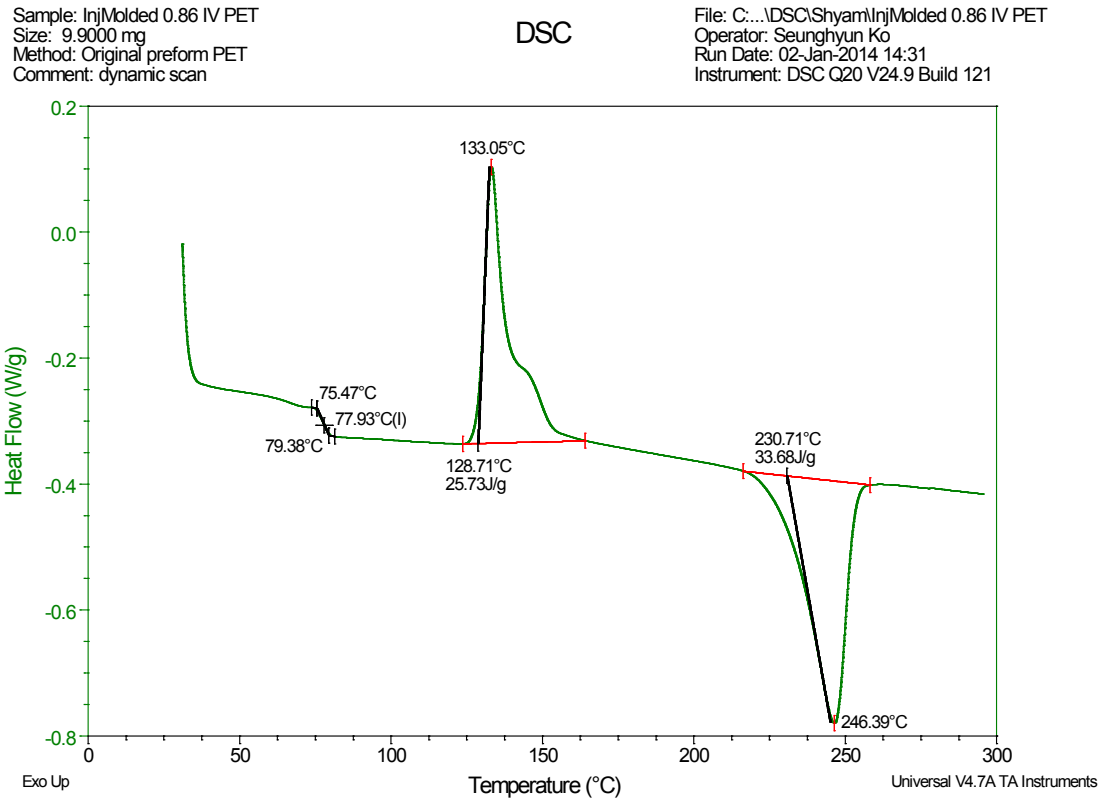

Figure 2.18 DSC result for IV 0.86. Crystallinity computed to be 5.67%

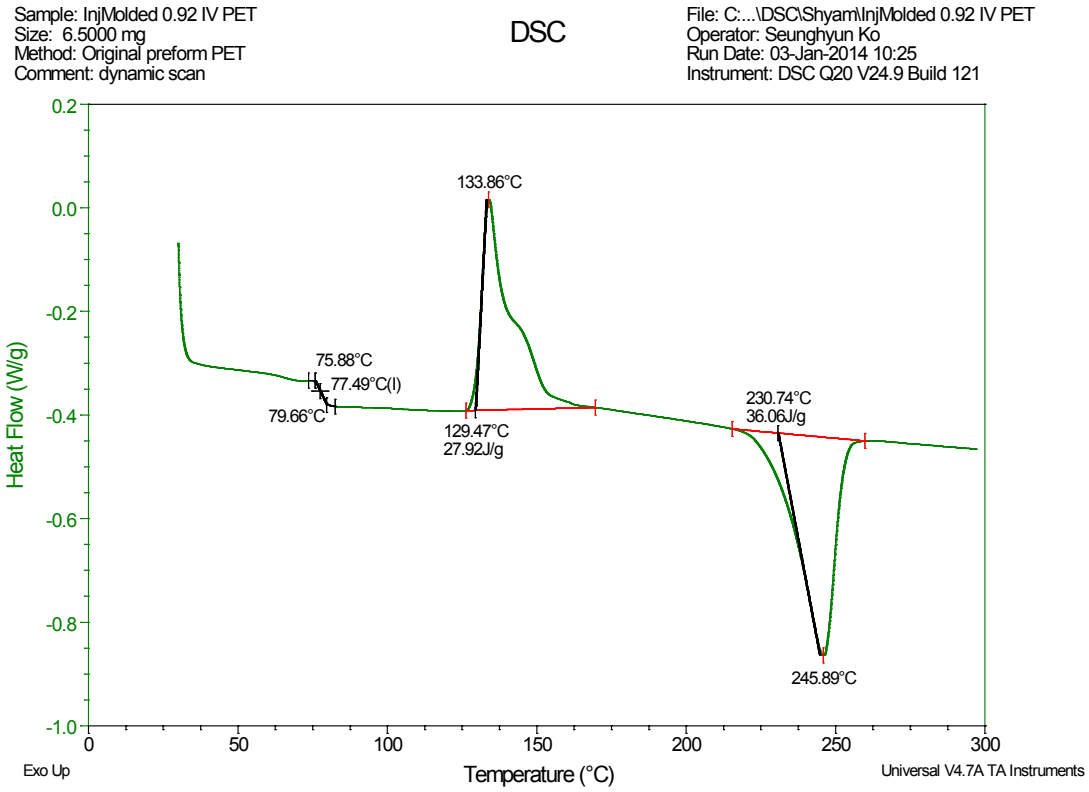

Figure 2.19 DSC result for IV 0.92. Crystallinity computed to be 5.81%

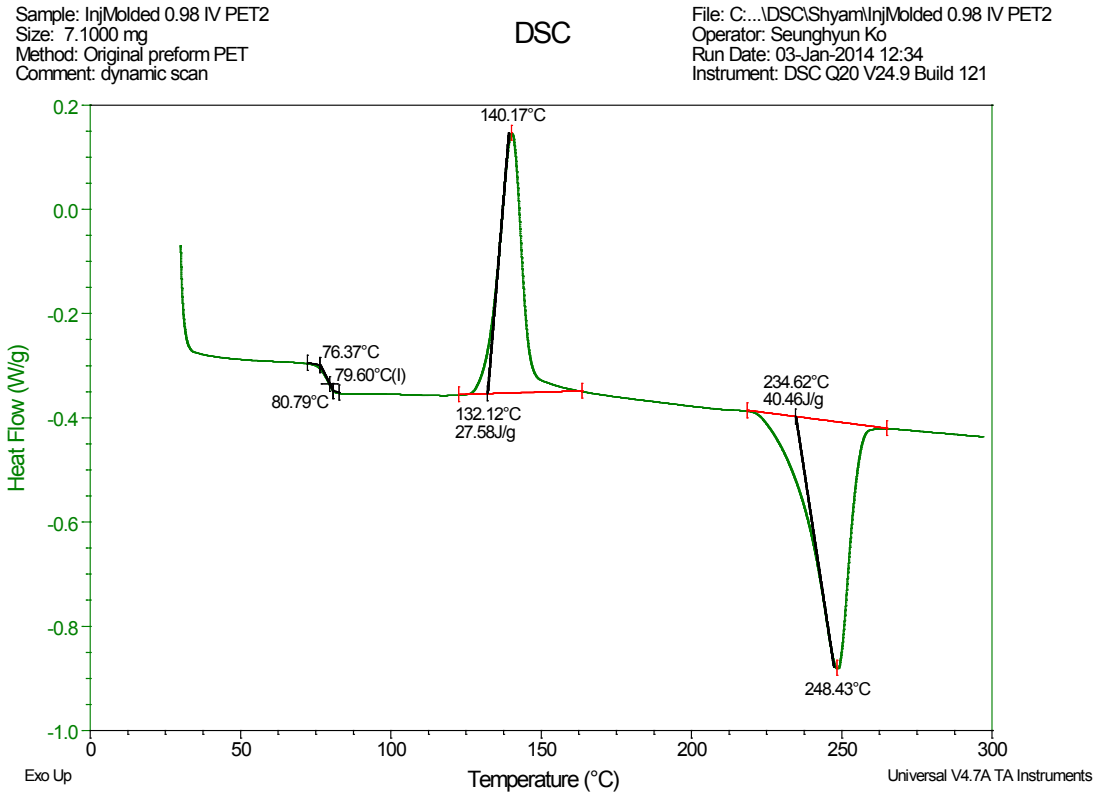

Figure 2.20 DSC result for IV 0.98. Crystallinity computed to be 9.19%

2.5.1 Comparison of Stress-Strain characteristics of hollow and non-hollow specimens

Engineering Stress vs Stretch curves were similar for compression tests on the hollow preform and the non-hollow disc, for a given temperature and strain rate, only up to the point beyond which the dip was observed for the hollow preform. The discs showed a continuous trend of strain hardening where the hollow specimens started to soften with the dip. Plots comparing both types of compression specimens at similar conditions are shown in figures 2.21 – 2.22.

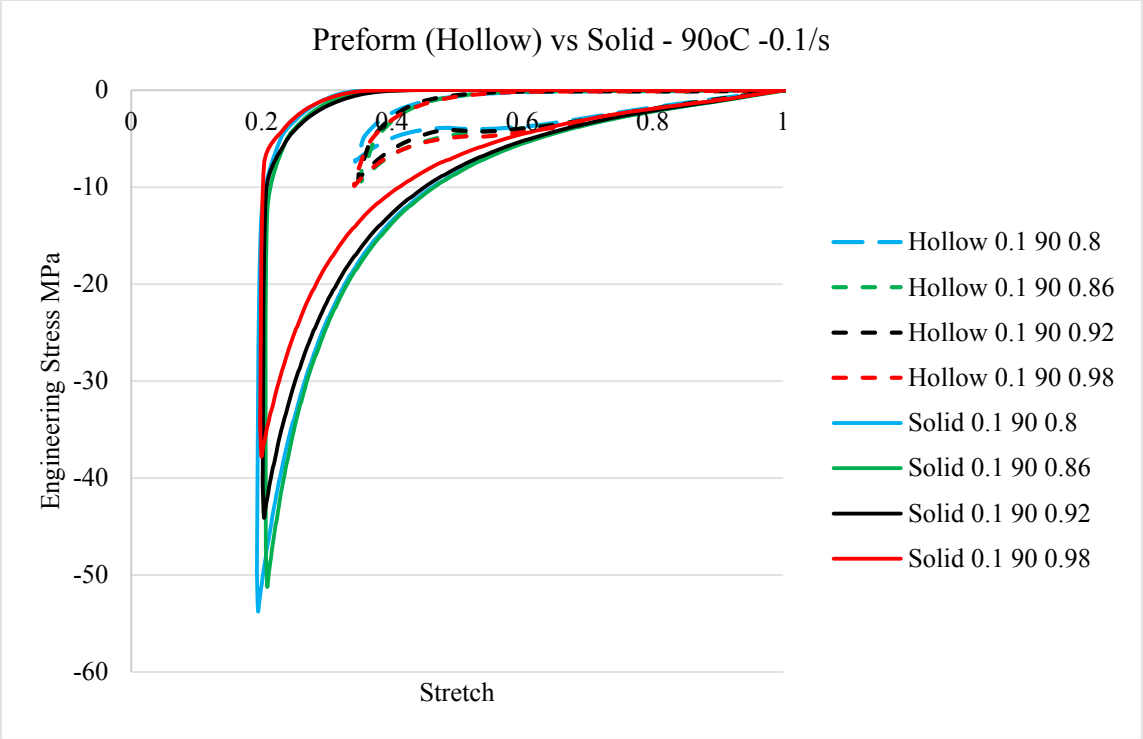

Figure 2.21 Comparison of Stress vs Stretch curves for Hollow and Solid compression specimens. The legend is 'Type StrainRate Temperature IV'.

Figure 2.22 Comparison of Stress vs Stretch curves for Hollow and Solid compression specimens. The legend is 'Type StrainRate Temperature IV'.

The observed results prove that the dip recorded was not a true material characteristic, but a false reading associated with unwanted deformation patterns occurring in the hollow specimen during the course of uniaxial compression. As a result, all experimental data used for fitting a material model was taken from tests with solid disc specimens.

2.6 Experimental Uniaxial Compression Test Results for the non-hollow specimens

2.6.1 IV dependence of Stress vs Stretch characteristics

Figures 2.23 to 2.30 represent the Engineering Stress vs Stretch curves for different IVs at the same conditions of temperature and strain-rate. Published literature indicate that the material shows stiffer characteristics with increase in IV. However, from conducted experiments it can be seen that IVs 0.80, 0.86 and 0.92 show very similar curves - the curves are very close and almost overlaid on each other. IV 0.98 shows softer characteristics than the rest, but this must be attributed to the molding parameters of specimens of this IV as mentioned previously. Also, the specimens of this IV appeared less transparent than the rest because of which readings from this IV were not considered for further analysis.

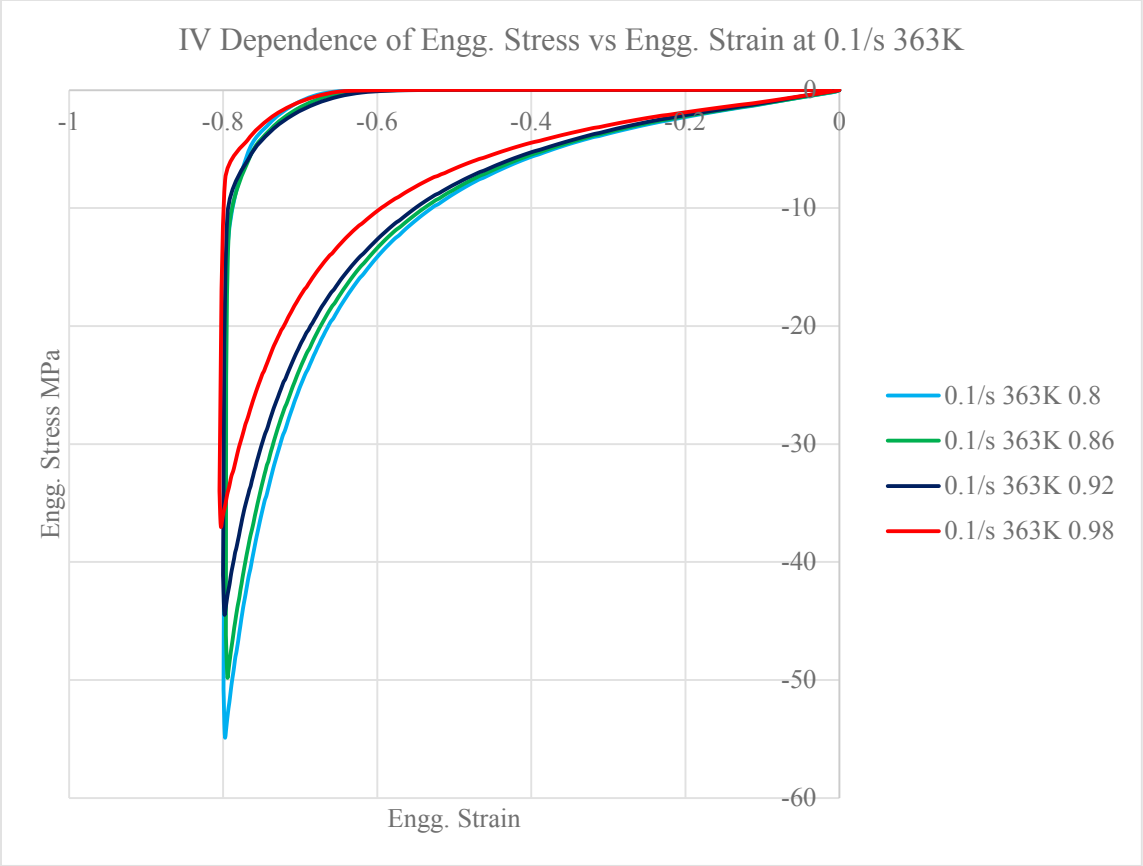

Figure 2.23 IV dependence of Stress vs Strain curves at 0.1/s 363K

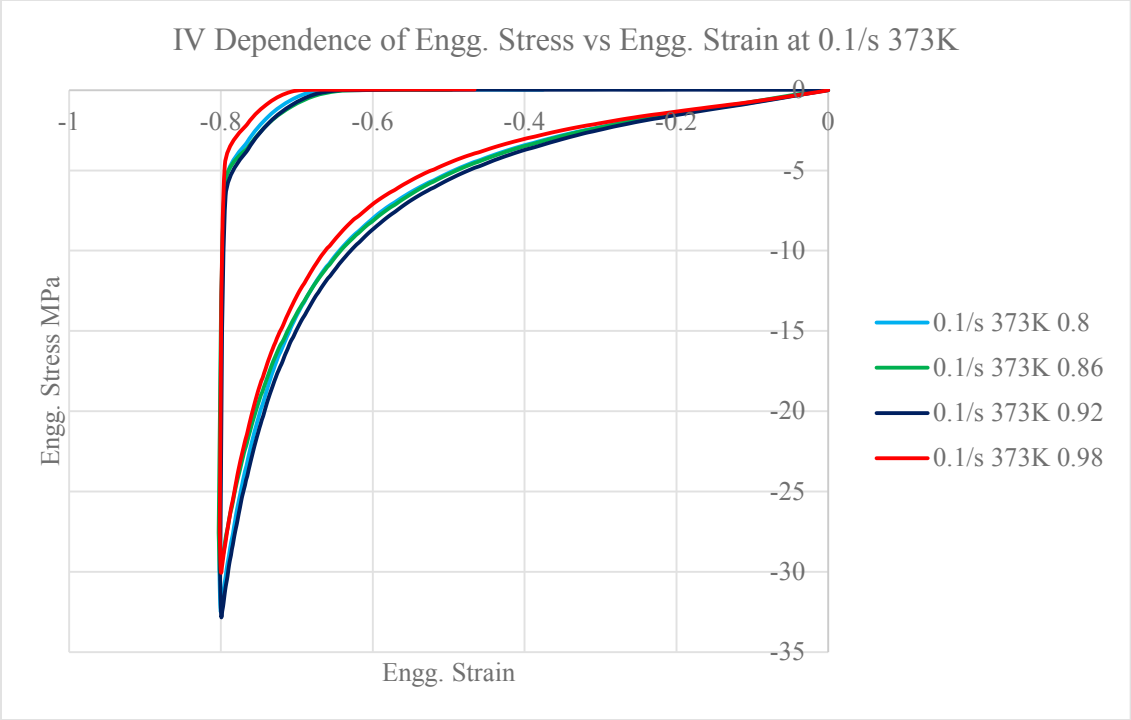

Figure 2.24 IV dependence of Stress vs Strain curves at 0.1/s 373K

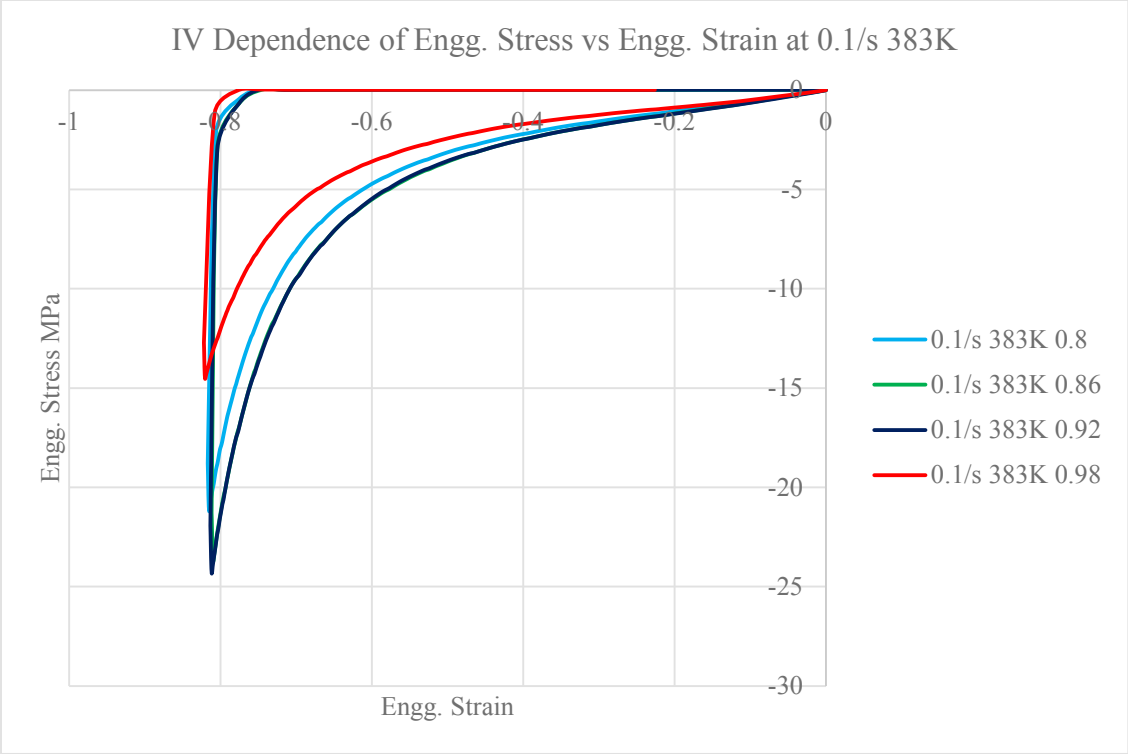

Figure 2.25 IV dependence of Stress vs Strain curves at 0.1/s 383K

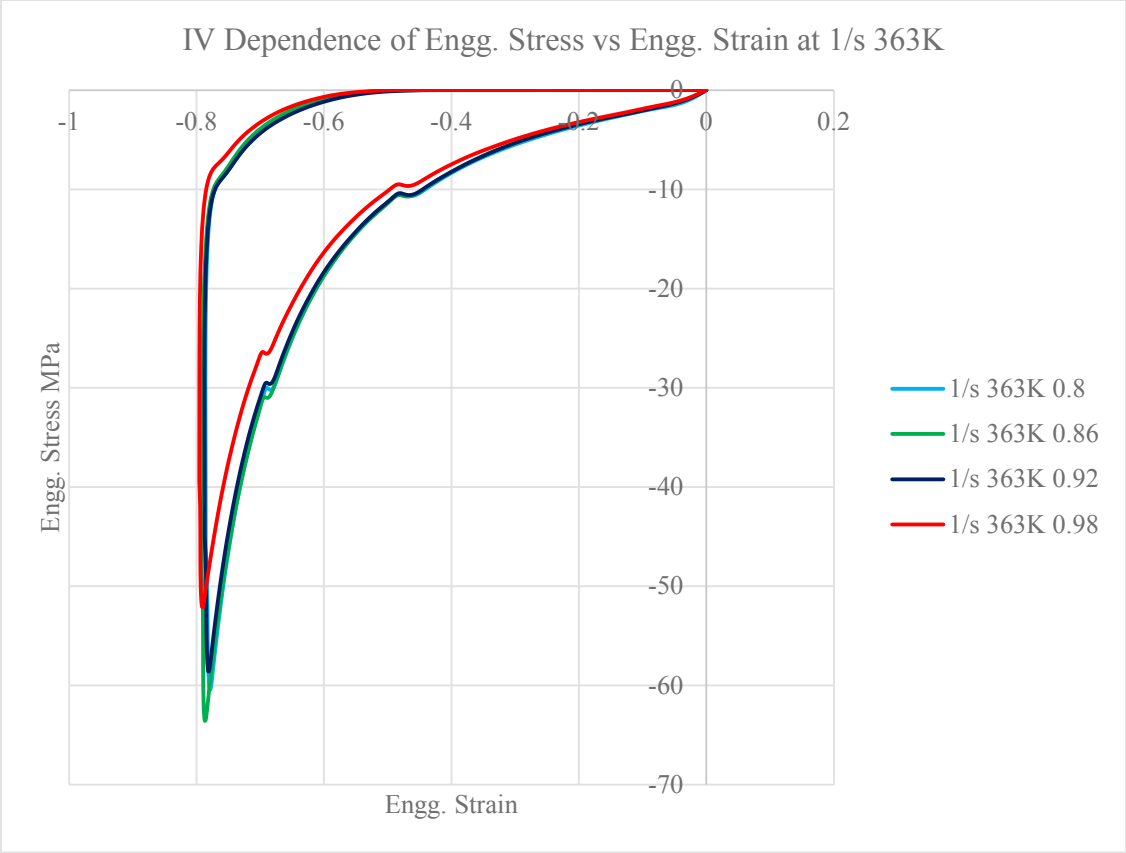

Figure 2.26 IV dependence of Stress vs Strain curves at 1/s 363K

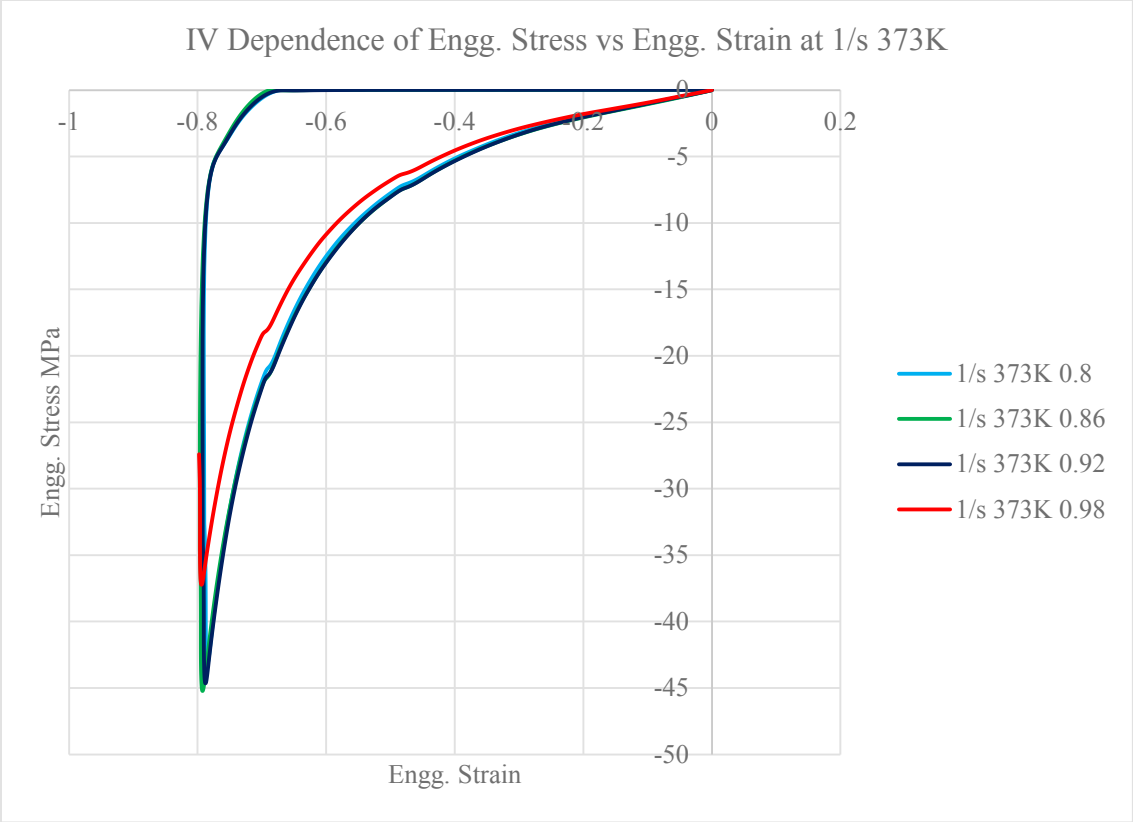

Figure 2.27 IV dependence of Stress vs Strain curves at 1/s 373K

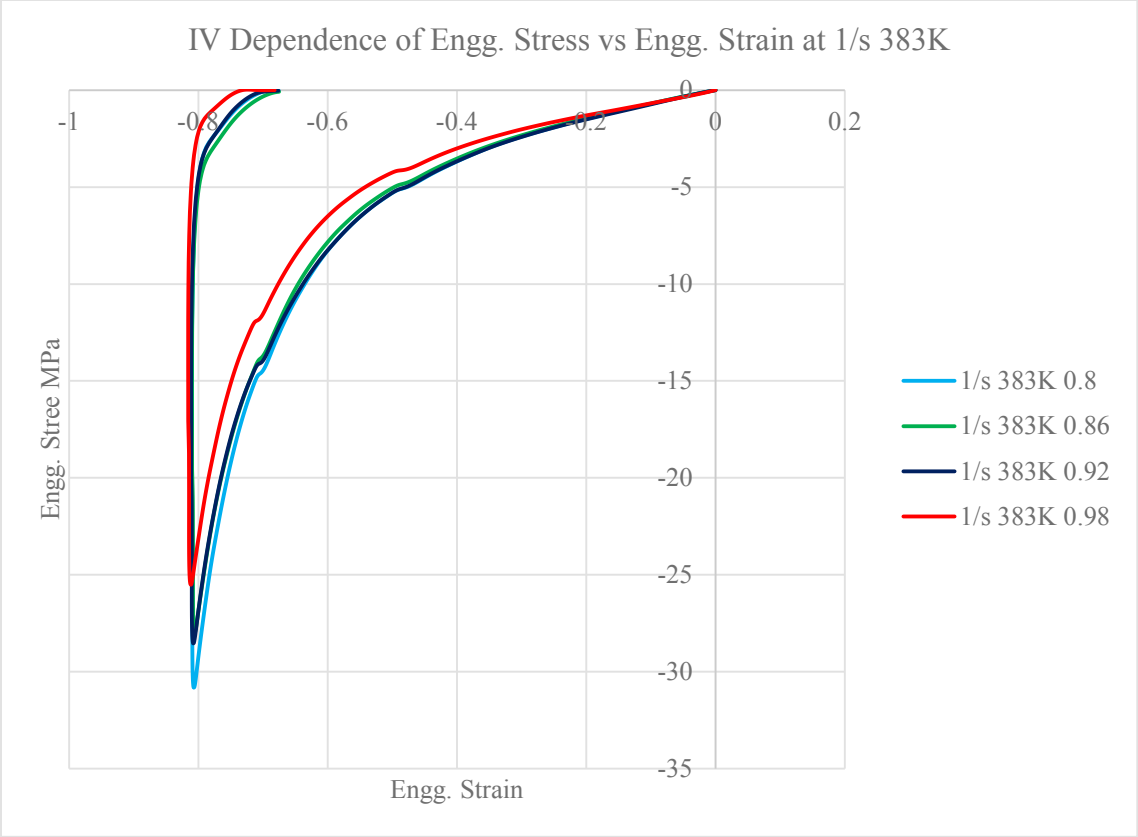

Figure 2.28 IV dependence of Stress vs Strain curves at 1/s 383K

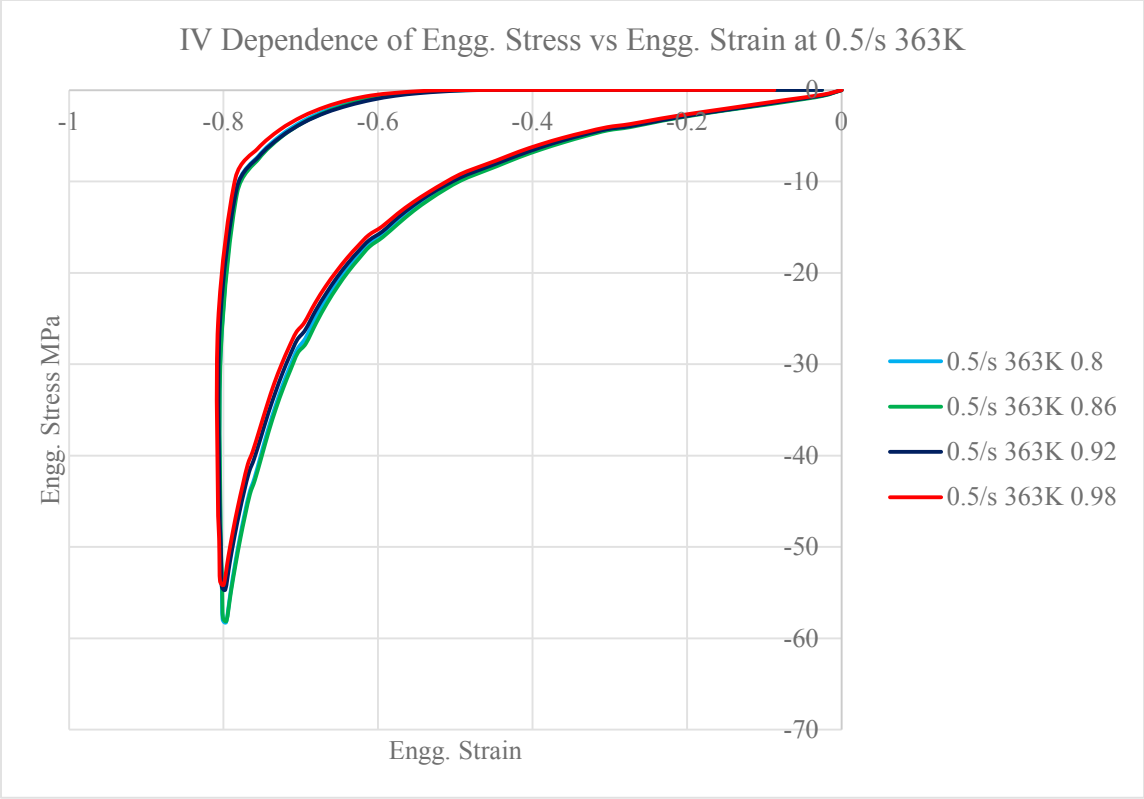

Figure 2.29 IV dependence of Stress vs Strain curves at 0.5/s 363K

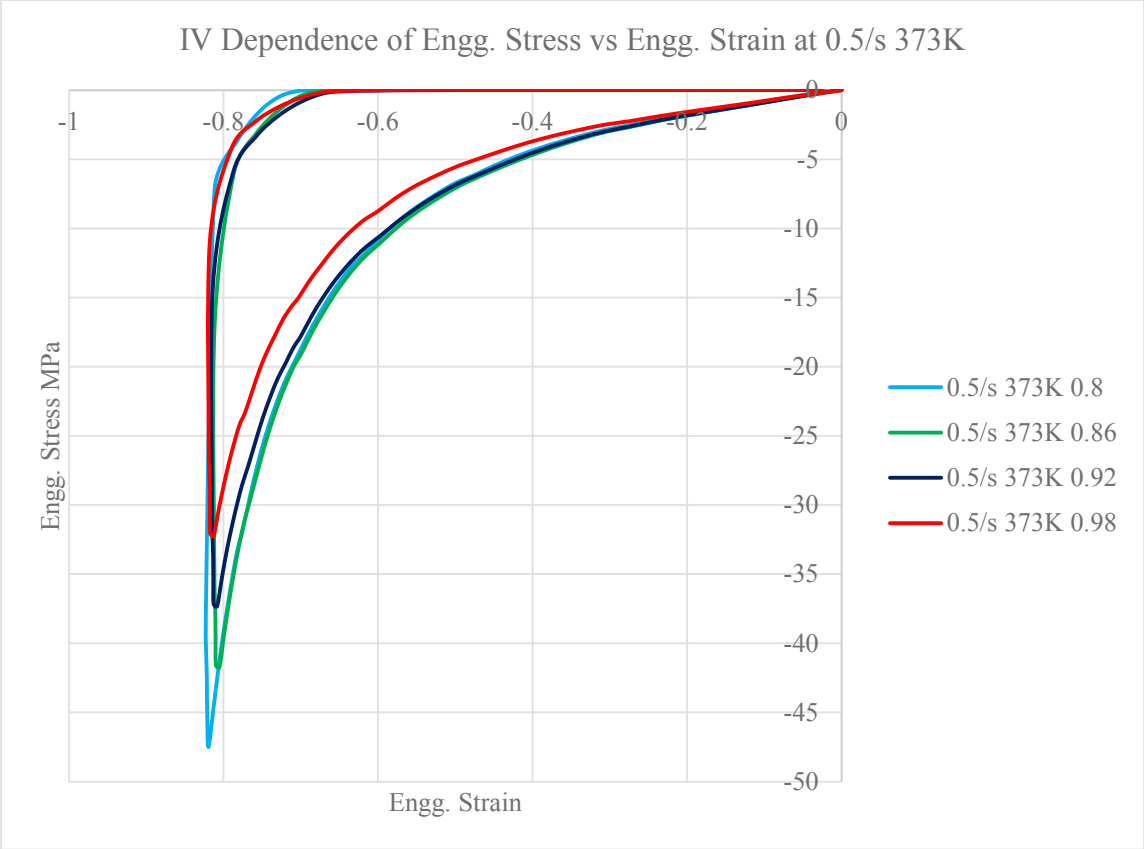

Figure 2.30 IV dependence of Stress vs Strain curves at 0.5/s 373K

2.6.2 Temperature dependence of Stress vs Stretch characteristics

PET becomes softer with increase in temperature. This can be observed in figures 2.31 to 2.38 where the material shows softer characteristics with increase in temperature for a given IV and strain rate.

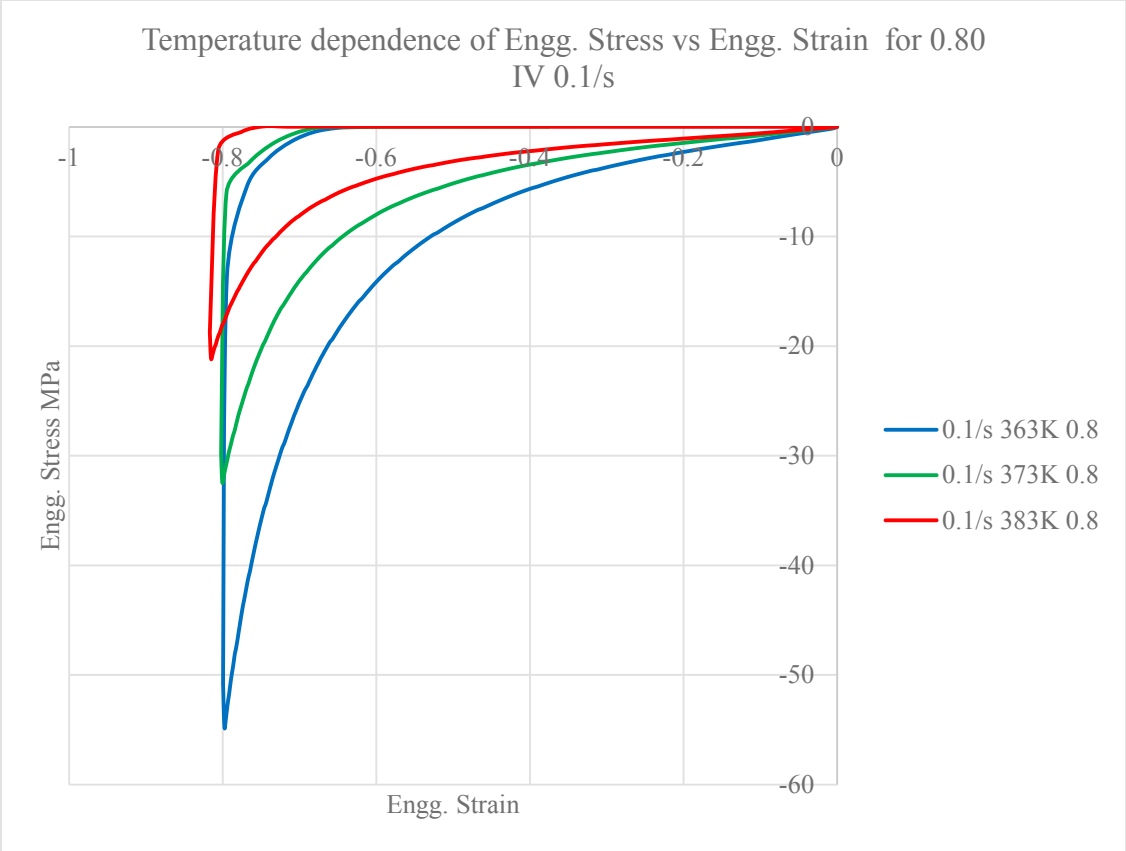

Figure 2.31 Temperature dependence of Stress vs Strain curves at 0.80 IV 0.1/s

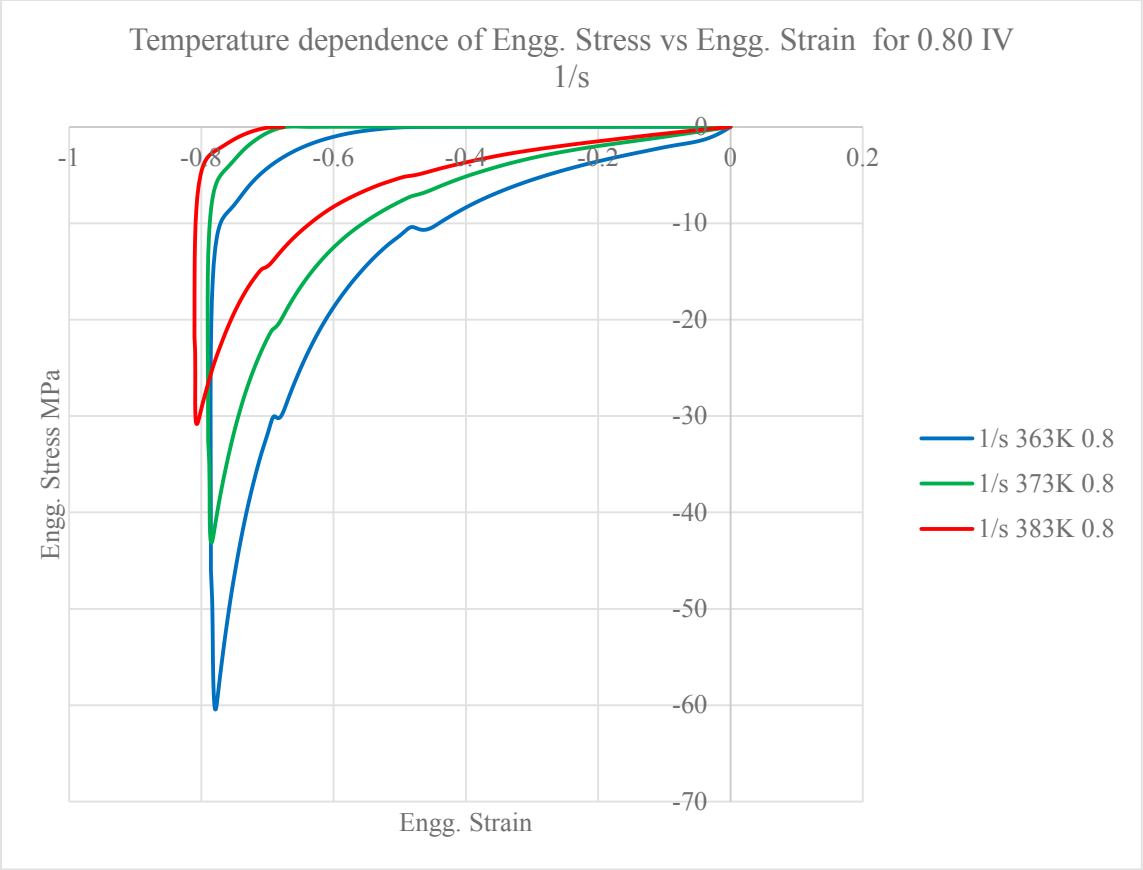

Figure 2.32 Temperature dependence of Stress vs Strain curves at 0.80 IV 1/s

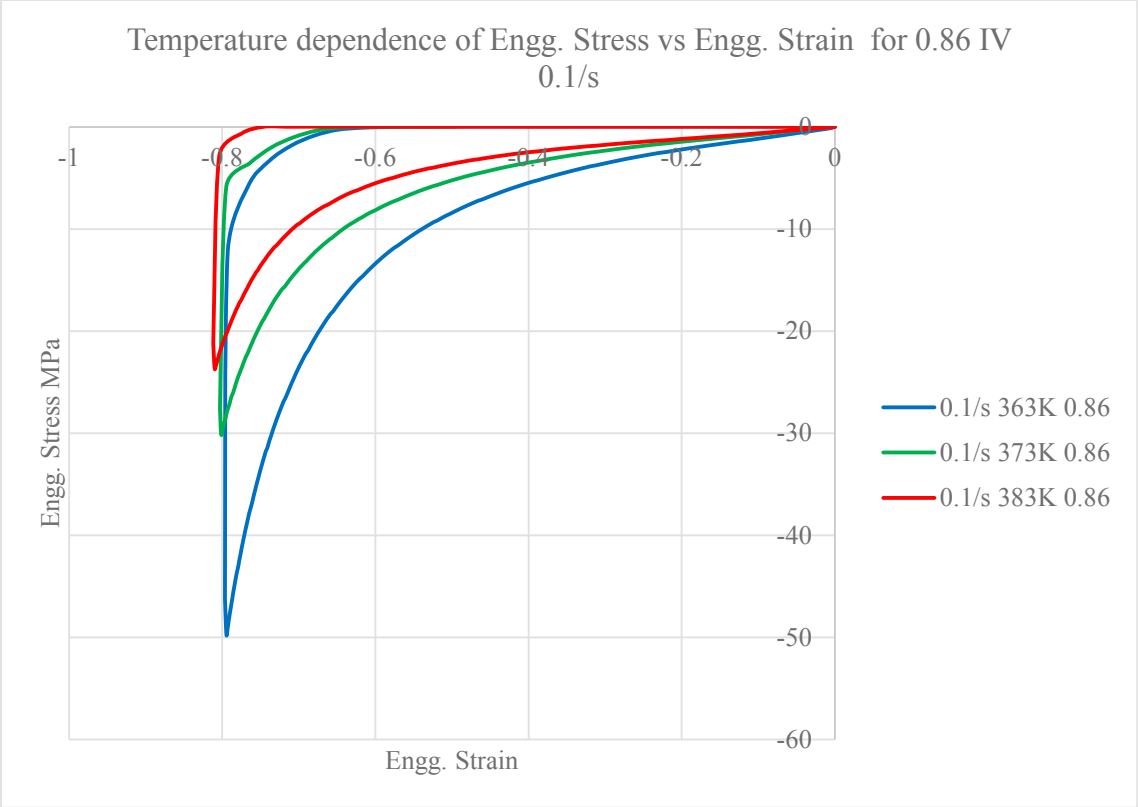

Figure 2.33 Temperature dependence of Stress vs Strain curves at 0.86 IV 0.1/s

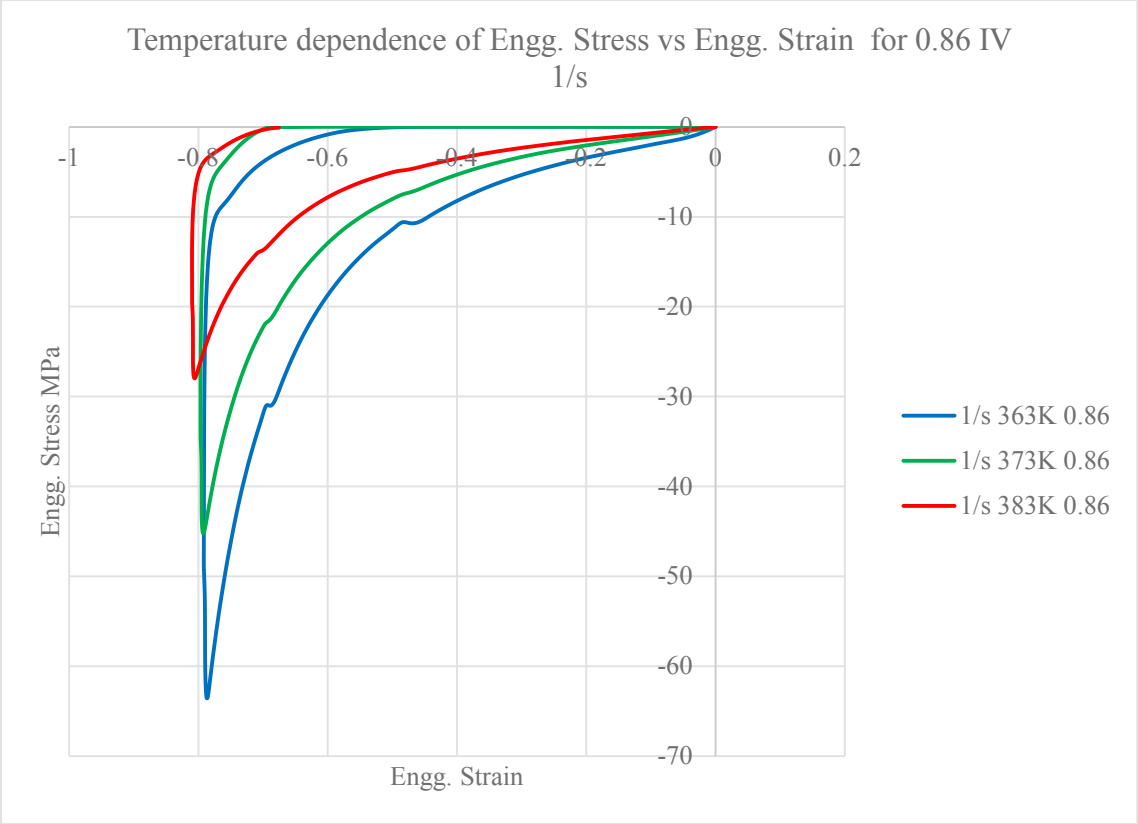

Figure 2.34 Temperature dependence of Stress vs Strain curves at 0.86 IV 1/s

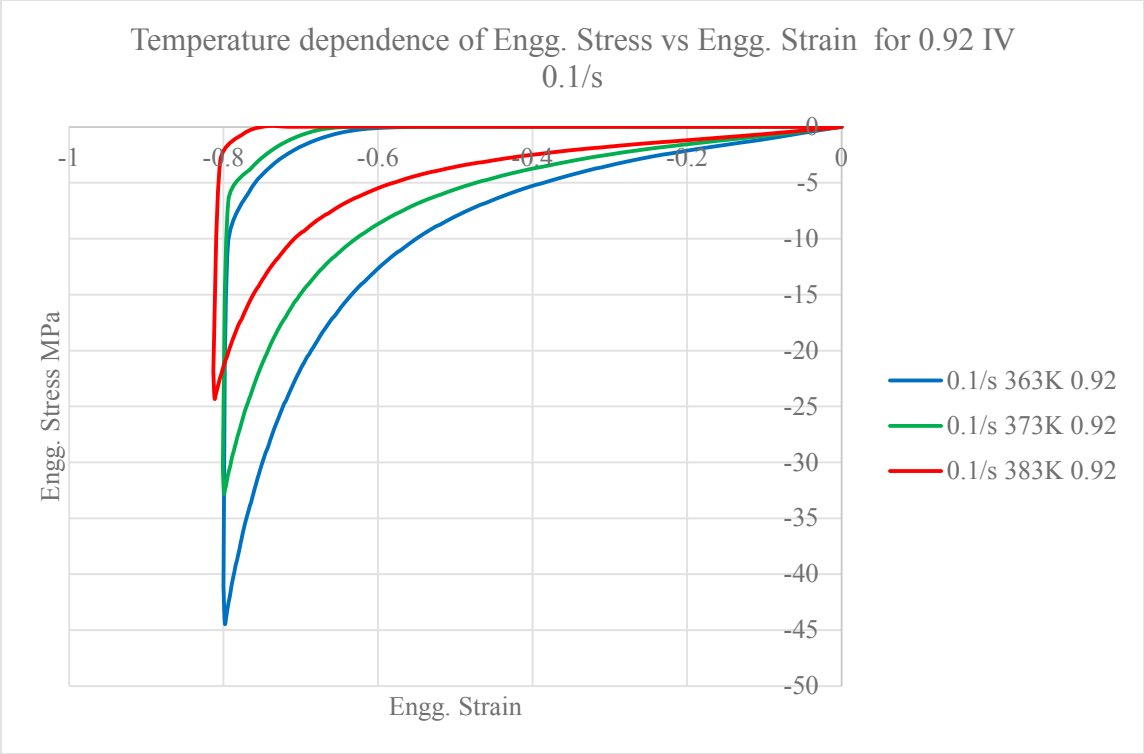

Figure 2.35 Temperature dependence of Stress vs Strain curves at 0.92 IV 0.1/s

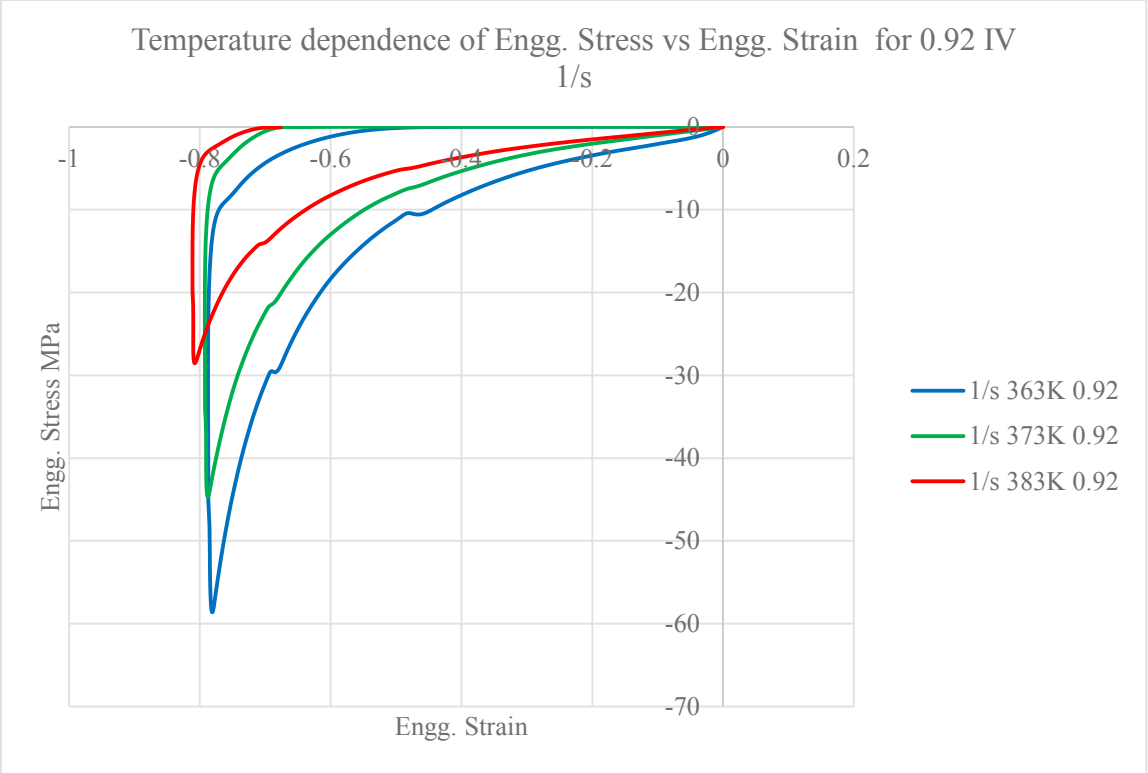

Figure 2.36 Temperature dependence of Stress vs Strain curves at 0.92 IV 1/s

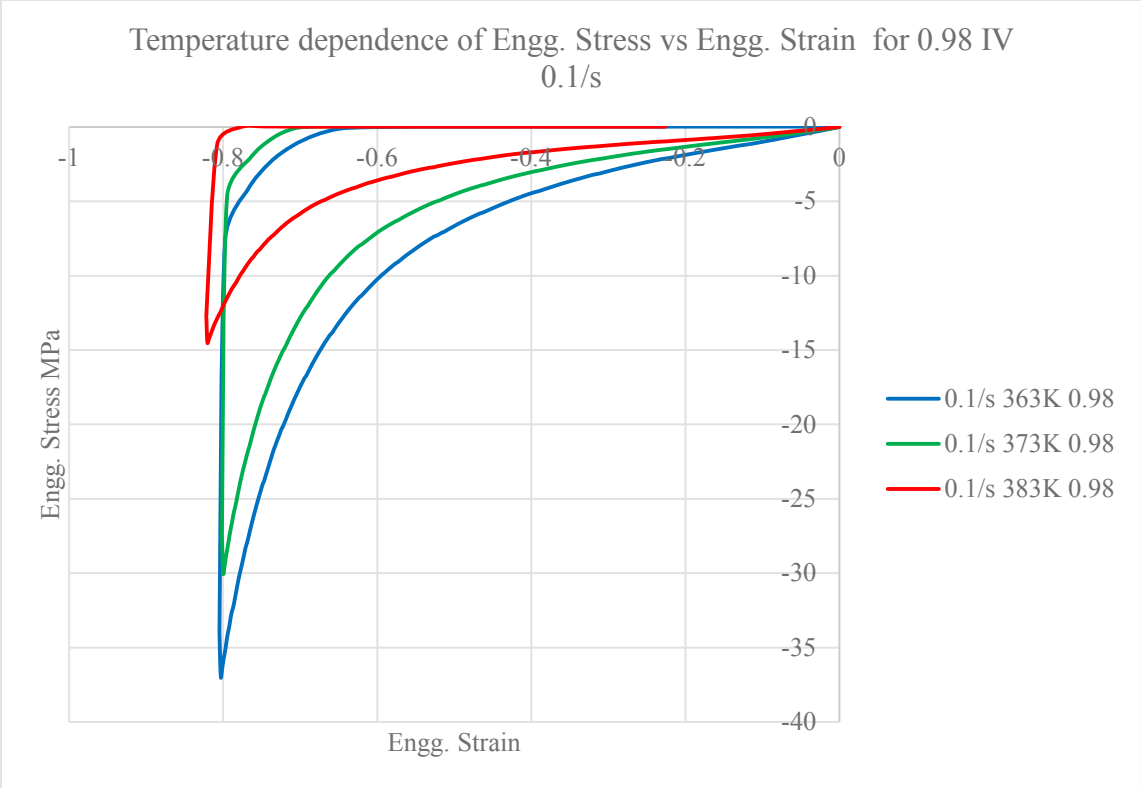

Figure 2.37 Temperature dependence of Stress vs Strain curves at 0.98 IV 0.1/s

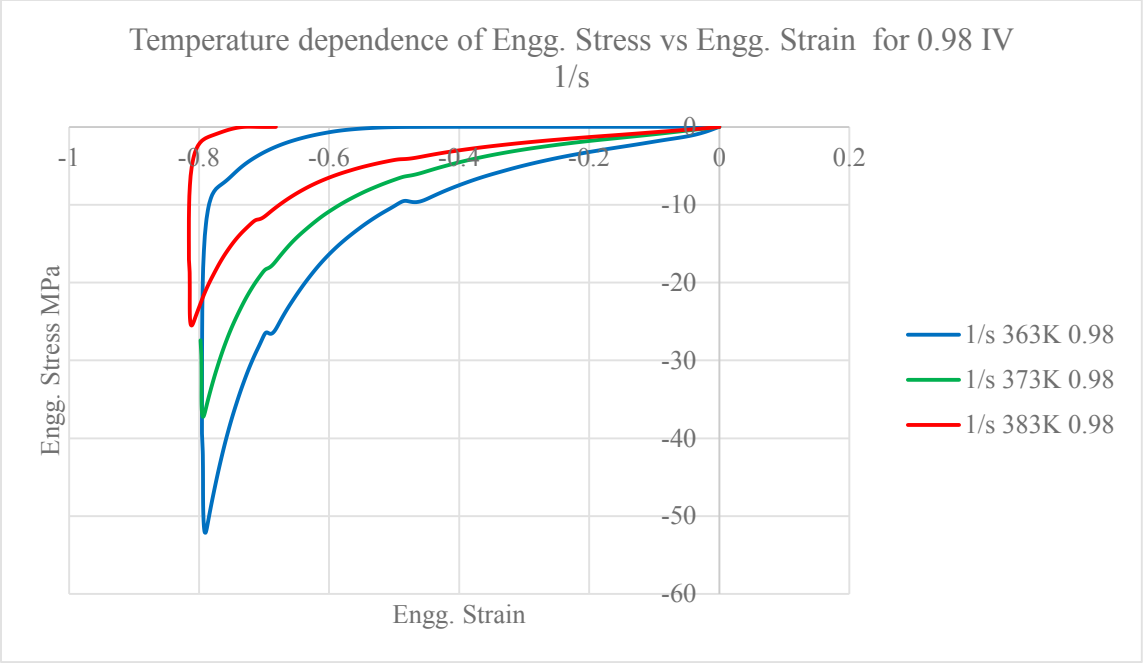

Figure 2.38 Temperature dependence of Stress vs Strain curves at 0.98 IV 1/s

2.6.3 Strain rate dependence of Stress vs Stretch characteristics

PET behavior is viscoelastic in the rubbery region. The material shows stiffer characteristics with increase in draw rate for given IV and temperature. This can be observed in figures 2.39 to 2.50.

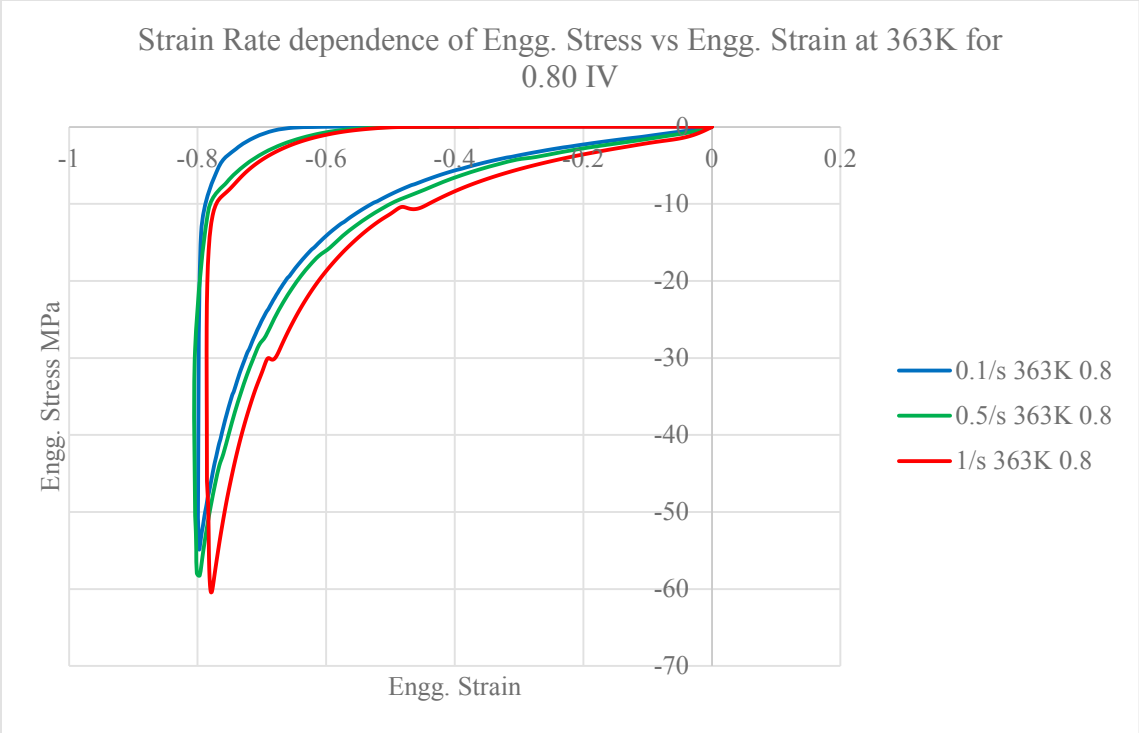

Figure 2.39 Strain Rate dependence of Stress vs Strain curves at 363K 0.80 IV

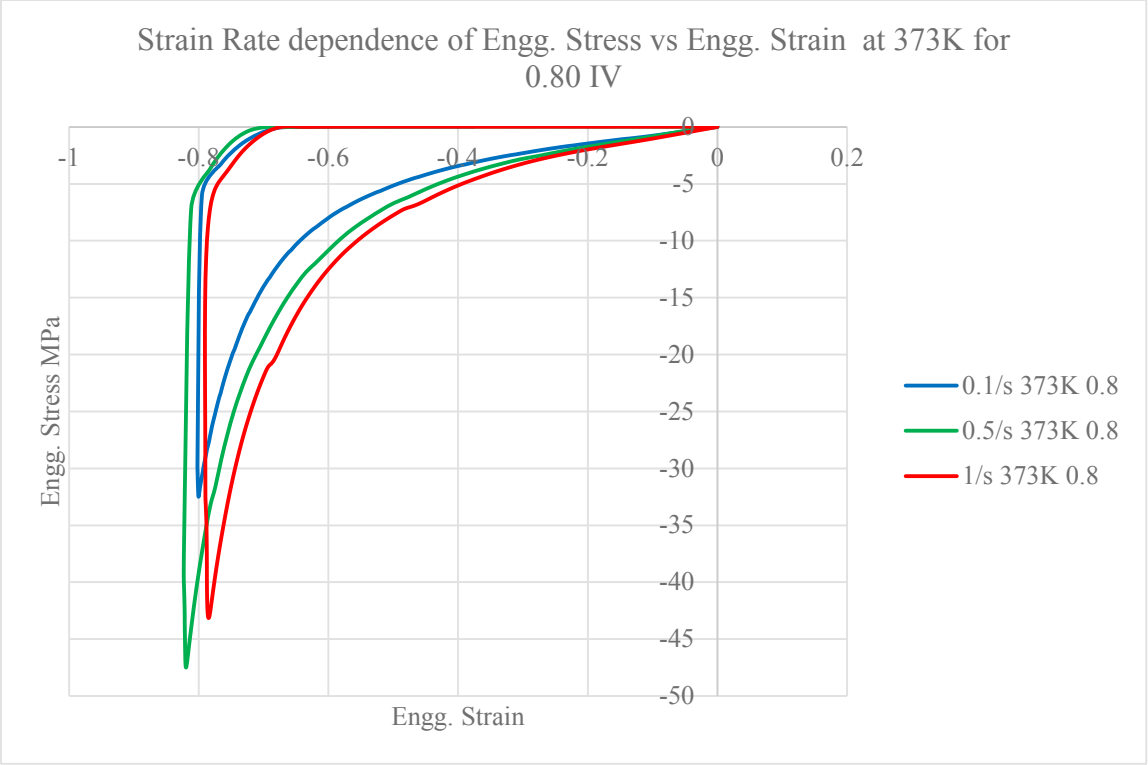

Figure 2.40 Strain Rate dependence of Stress vs Strain curves at 373K 0.80 IV

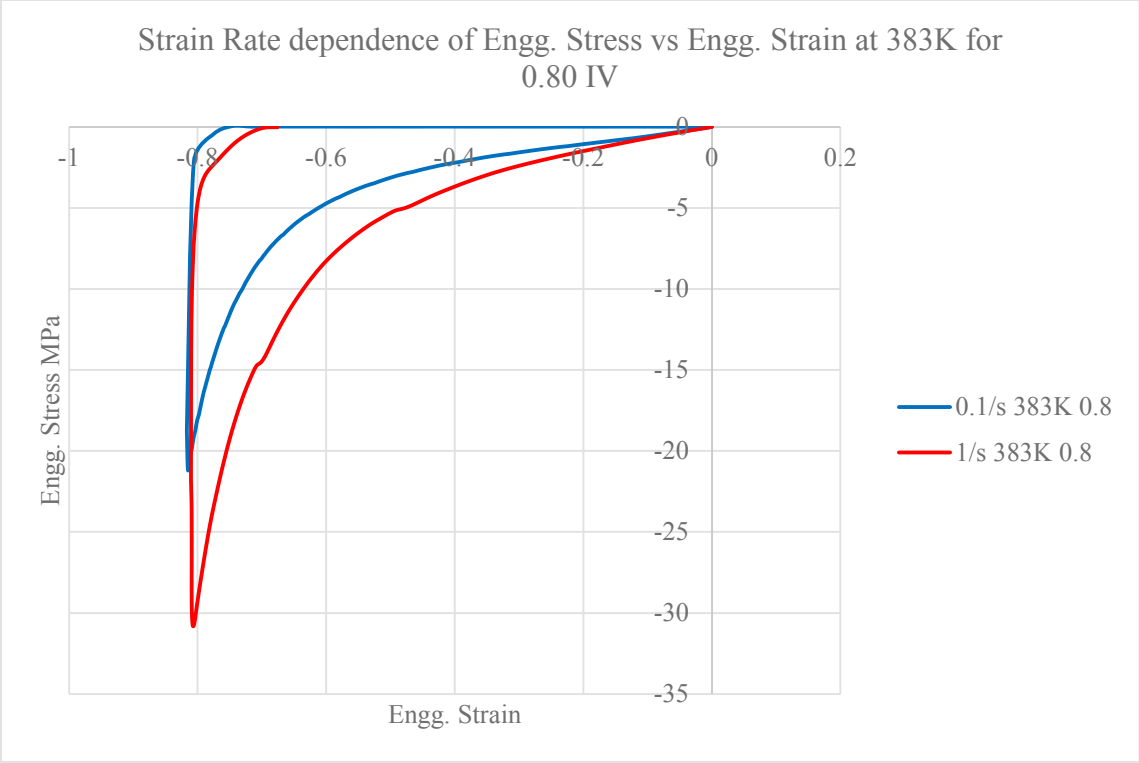

Figure 2.41 Strain Rate dependence of Stress vs Strain curves at 383K 0.80 IV

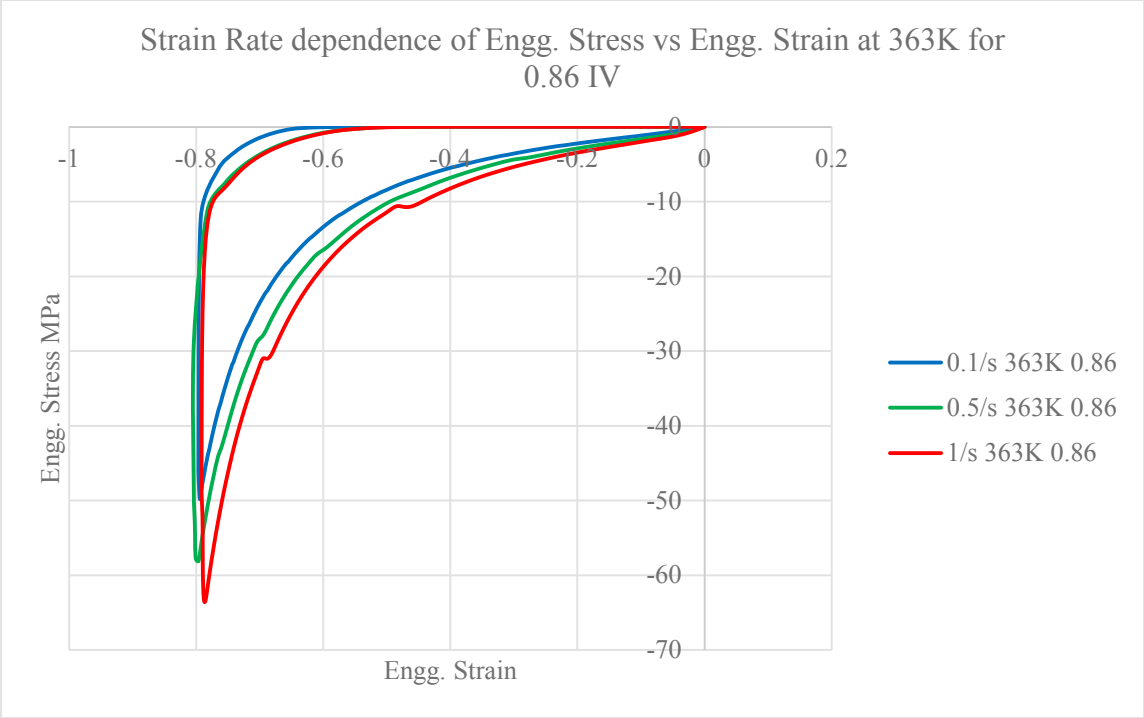

Figure 2.42 Strain Rate dependence of Stress vs Strain curves at 363K 0.86 IV

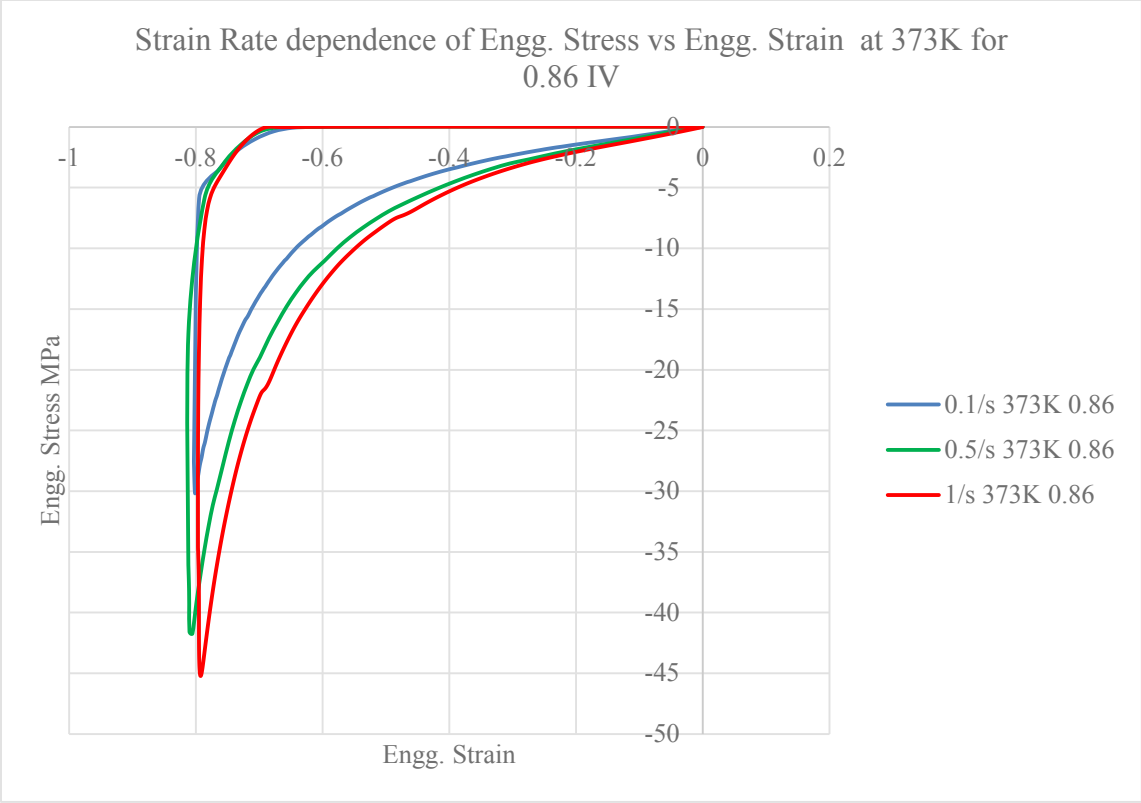

Figure 2.43 Strain Rate dependence of Stress vs Strain curves at 373K 0.86 IV

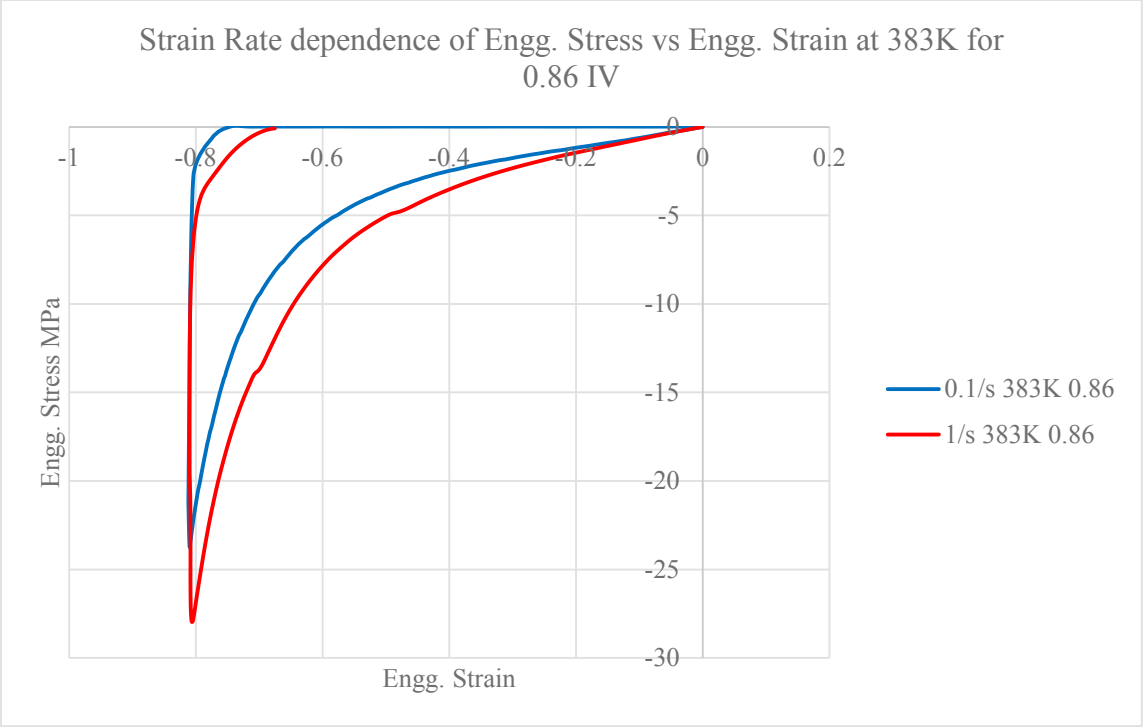

Figure 2.44 Strain Rate dependence of Stress vs Strain curves at 383K 0.86 IV

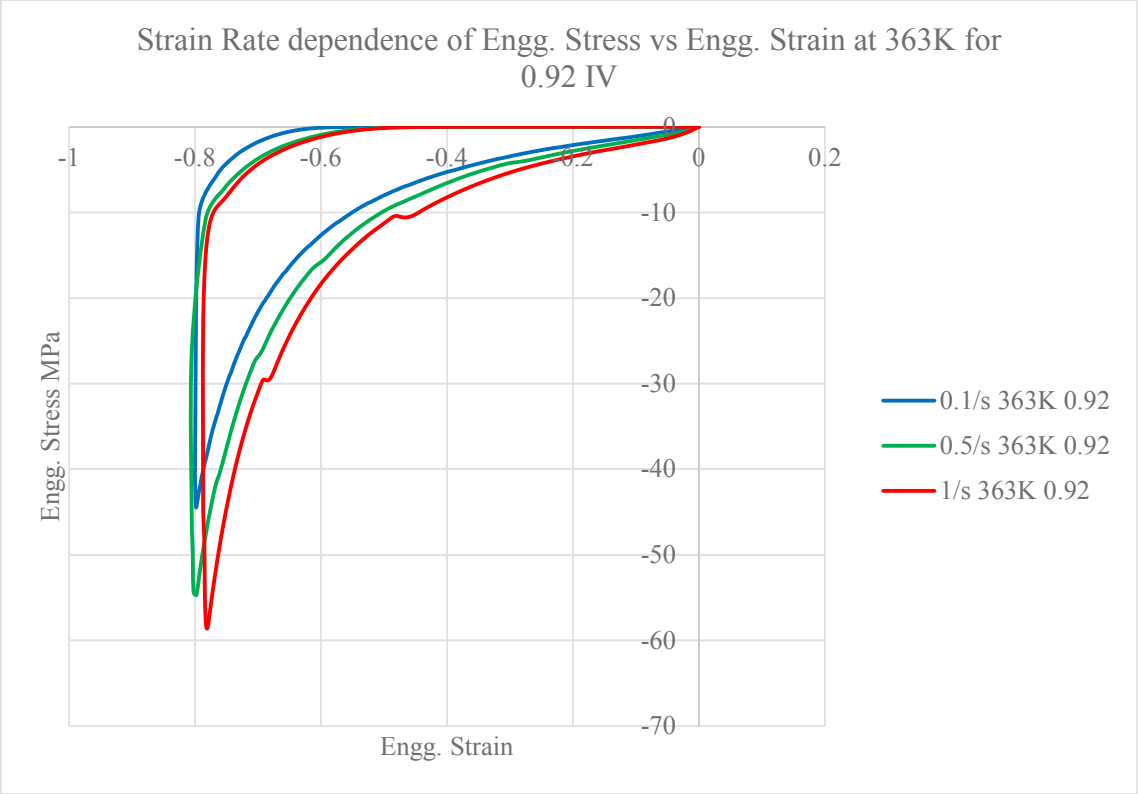

Figure 2.45 Strain Rate dependence of Stress vs Strain curves at 363K 0.92 IV

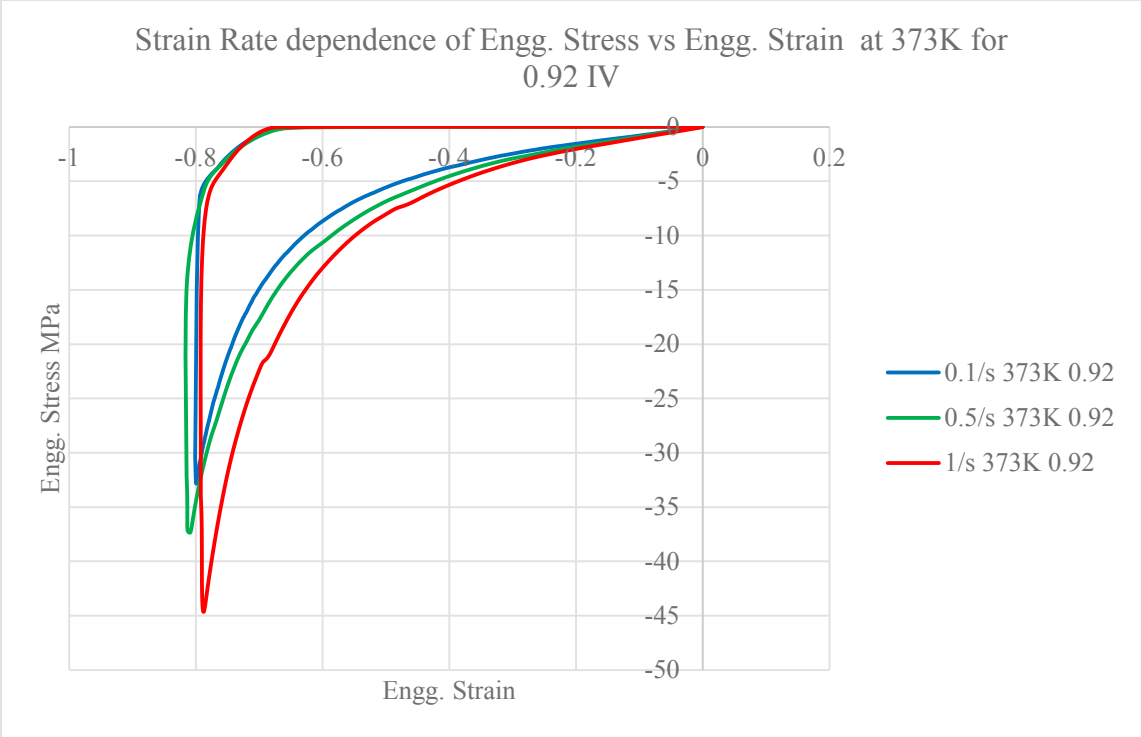

Figure 2.46 Strain Rate dependence of Stress vs Strain curves at 373K 0.92 IV

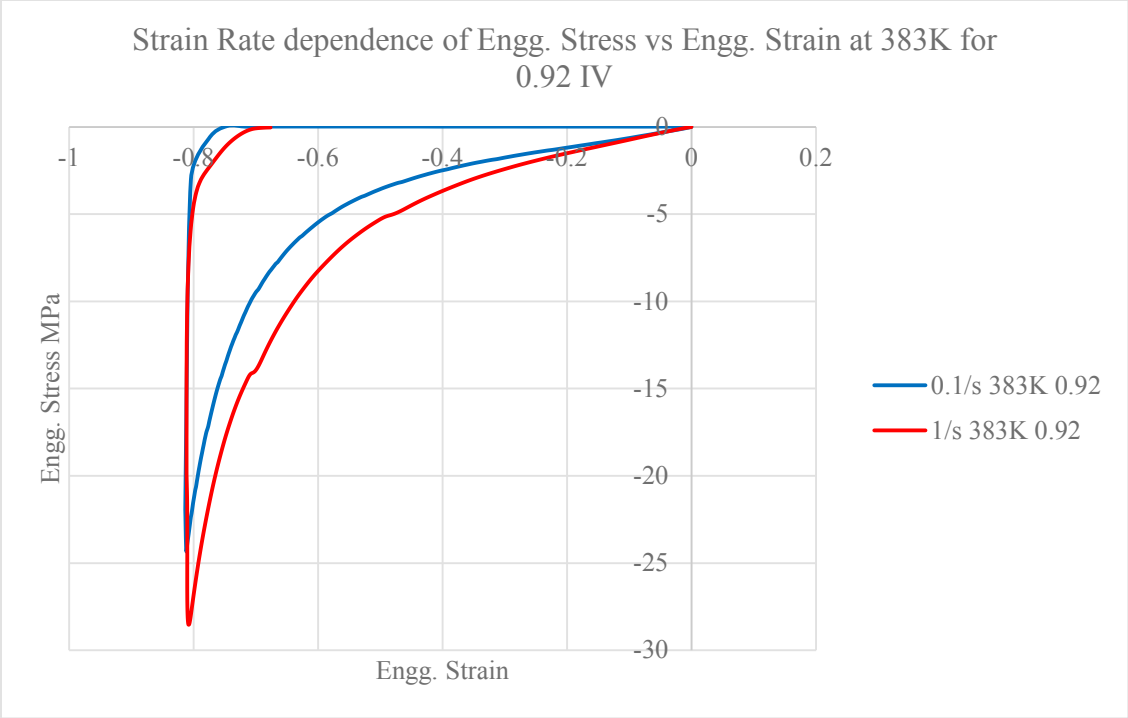

Figure 2.47 Strain Rate dependence of Stress vs Strain curves at 383K 0.92 IV

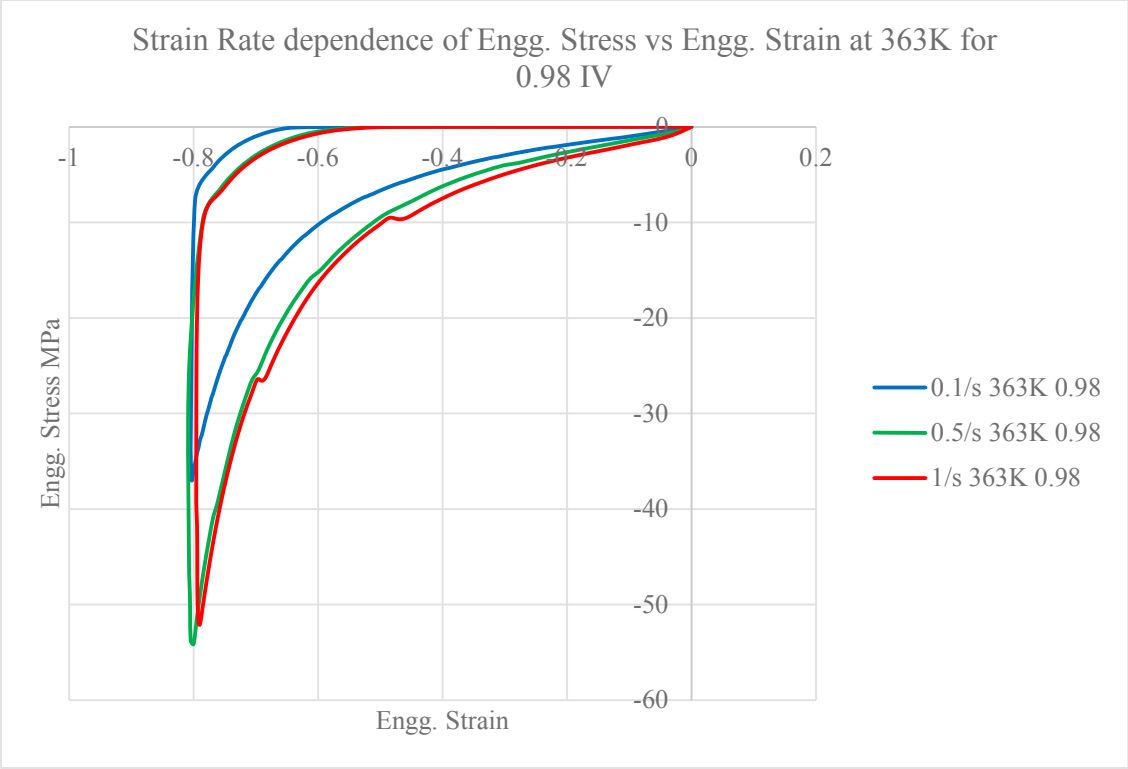

Figure 2.48 Strain Rate dependence of Stress vs Strain curves at 363K 0.98 IV

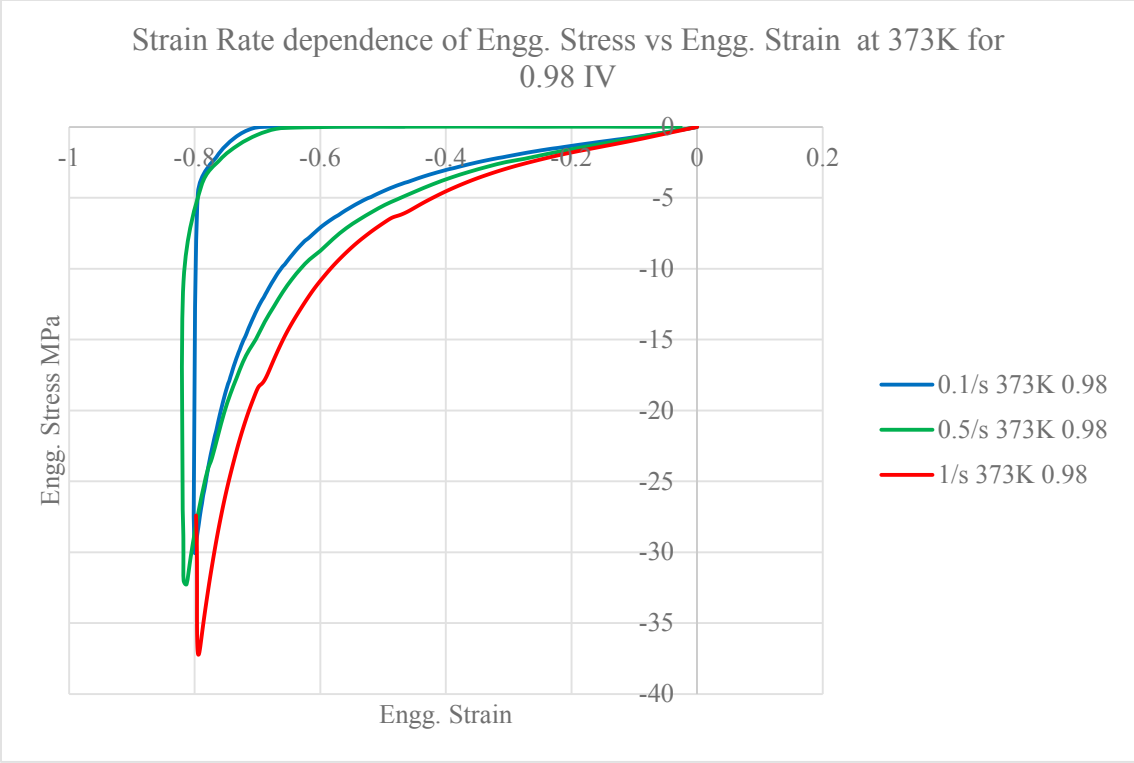

Figure 2.49 Strain Rate dependence of Stress vs Strain curves at 373K 0.98 IV

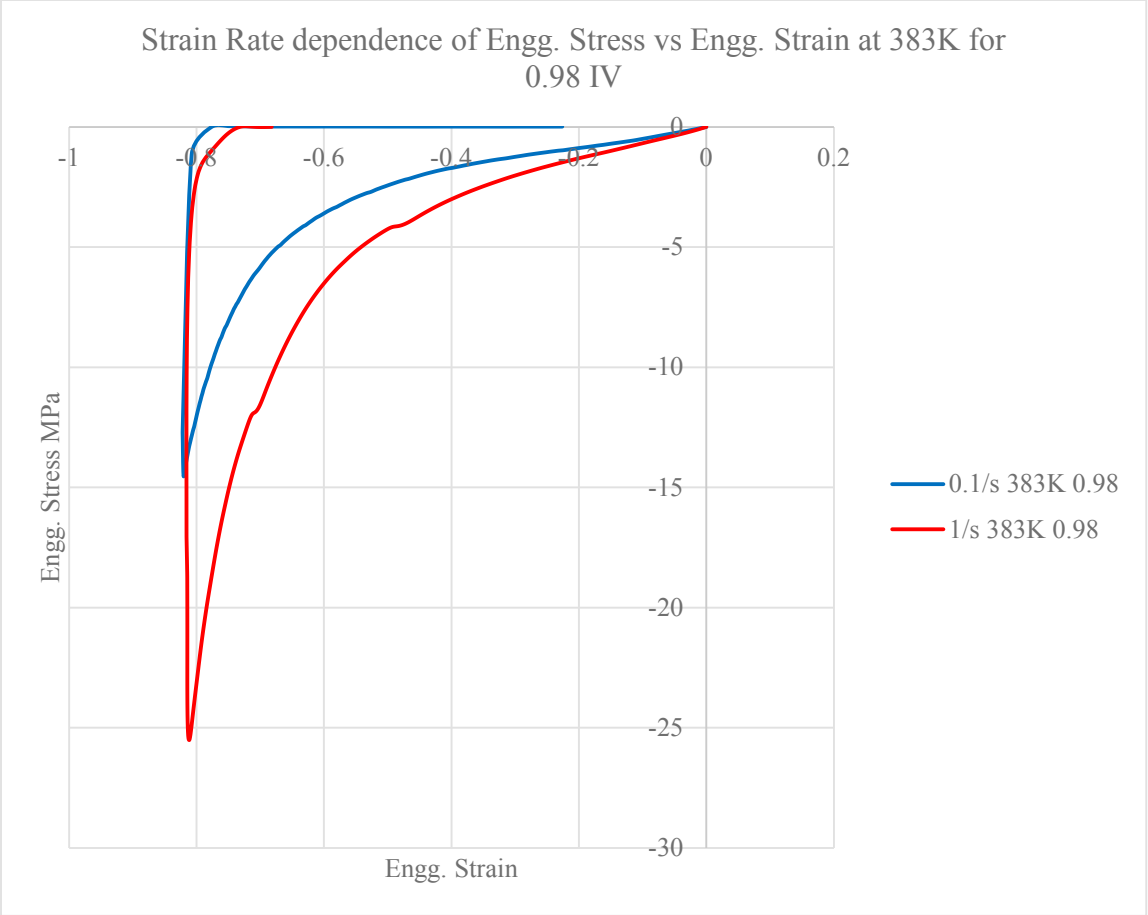

Figure 2.50 Strain Rate dependence of Stress vs Strain curves at 383K 0.98 IV

2.7 Discussion and Conclusions

In the previous compression tests with the hollow specimens, the material showed stiffer behavior as the IV increased, the dip notwithstanding. However, for the compression tests with the non-hollow specimens, IV 0.98 showed significantly softer characteristics as seen in the above plots. It is to be noted that the IV 0.98 molds were less transparent than the other IVs. There was difficulty filling up the full mold during injection of IV 0.98

because of which injection pressure and other process parameters had to be modified before whole molds could be obtained from the machine. This might have affected the end properties of the samples, because of which IV 0.98 was excluded from further analysis. In the averaged curves of the other IVs of 0.80, 0.86 and 0.92, the curves are very similar, and are almost overlaid on each other. Though the fact that the PET becomes stiffer with increasing IVs is published and proven, significant differences were not observed with these experimental results.

Chapter 3: The Dupaix-Boyce Constitutive Model

3.1 Introduction

This chapter describes the Dupaix-Boyce (Dupaix, 2003) constitutive model, which has been used to characterize PET in this work. This model is hyperelastic-viscoplastic in nature and has been formulated using a solid mechanics approach. This model has been developed to capture the near melt-like regime of the deformation and flow of polymers by using an approach which adds viscous effects into an elastic or a hyper-elastic model. It is based on prior developments in solid mechanics in modeling large strain deformation of polymers which is also time dependent (Bergstrom and Boyce 1998, Boyce et al. 2000). The approach and modeling framework is based on the work of Boyce, Socrate and Llana (2000). This model however, does not include the strain-induced crystallization that occurs in PET under certain conditions. In this thesis, the dramatic strain hardening associated with strain-induced crystallization has been modeled separately as a plug-in to the Dupaix-Boyce model. This modification will be discussed in the later chapters.

3.2 Description

The Dupaix-Boyce model considers the constitutive response of a near melt-like polymer to be a sum of the responses due to two different mechanisms resisting deformation – intermolecular forces and network resistance. Intermolecular forces occur between neighboring polymer segments and gives the material its initial stiffness. As strain increases, at a finite level of stress called flow stress, flow initiates in the polymer. Network resistance is caused by stretching and orientation of the polymer chains along the direction of deformation.

Resistance between polymer chains created by intermolecular forces is termed **Network I** and the resistance due to stretching and orientation of the polymer chains in the direction of the applied force is termed **Network N**. Each of these mechanisms is modeled as a system with a spring component and a dashpot component as shown in the following image. The spring represents the elastic component and the dashpot the flow component.

In the equations below, the model constants are in Bold. They are also described in Table 3.1.

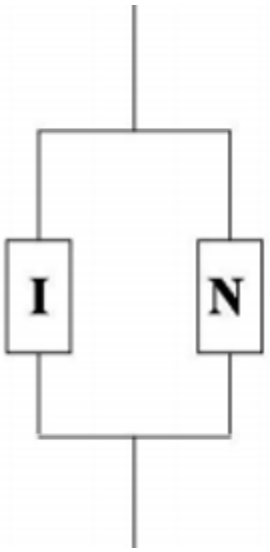

Figure 3.1 The networks of the Dupaix-Boyce Model; I – Intermolecular forces N – Network resistance

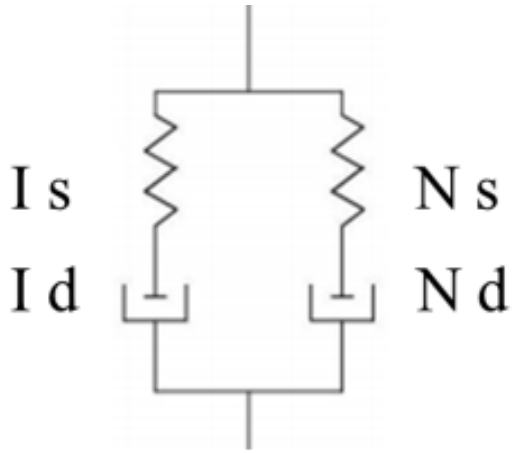

Figure 3.2 The inner elements of each model; s- Spring d – Damper

3.3 Constitutive relation derivation for Intermolecular forces (I)

3.3.1 Multiplicative Decomposition of Deformation Gradient

The deformation gradient in this network is assumed to be multiplicatively composed of an elastic and a plastic component as described by Lee (1969).

$$F_I = F_I^e F_I^p \tag{3.1}$$

Each of the components here are multiplicatively composed of a stretch and a rotation component by polar decomposition.

$$F_I^e = V_I^e R_I^e \tag{3.2}$$

$$F_I^p = V_I^p R_I^p \tag{3.3}$$

The velocity gradient is defined as

$$L_I = \dot{F}_I F_I^{-1} \tag{3.4}$$

Which, when represented by elastic and plastic deformation gradient components becomes

$$L_I = \dot{F}_I^e F_I^{e-1} + F_I^e \dot{F}_I^p F_I^{p-1} F_I^{e-1} = L_I^e + \tilde{L}_I^p \tag{3.5}$$

The plastic velocity gradient additively is composed of a symmetric plastic rate of stretching and an antisymmetric plastic spin given by

$$\tilde{L}_I^p = \tilde{D}_I^p + \tilde{W}_I^p \tag{3.6}$$

$\tilde{W}_I^p$ is set to zero to keep the representation unique.

3.3.2 Elastic (Spring) Characteristics for Network I

A constitutive relation between the plastic rate of stretching $\widetilde{D}_I^p$ and the normalized deviatoric stress for network I N_I is given by

$$\widetilde{D}_I^p = \dot{\gamma}_I^p N_I \tag{3.7}$$

$$N_I = \frac{1}{\sqrt{2\tau_I}} T_I' \tag{3.8}$$

$$\tau_I = [\frac{1}{2} T_I' T_I']^{1/2} \tag{3.9}$$

T_I' is the deviatoric component of Cauchy stress T_I

The Cauchy stress is related to the deformation gradient through the relation

$$T_I = \frac{1}{J_I} \mathcal{L}^e [\ln(V_I^e)] \tag{3.10}$$

Where $\mathcal{L}^e$ is the elasticity tensor and $\ln(V_I^e)$ the Hencky strain defined by Anand (1979). The above equations cover the spring portion of network I.

3.3.3 Plastic Flow (Dashpot) Characteristics for Network I

For the dashpot, the plastic strain rate is modeled to follow a thermally activated process given by the expression

$$\dot{\gamma}_I^p = \dot{\boldsymbol{\gamma}}_{\mathbf{0I}} [-\frac{\boldsymbol{\Delta G}\left(1-\frac{\tau_I}{s}\right)}{k\theta}] \tag{3.11}$$

Where $\dot{\gamma}_I^p$ is the pre-exponential factor, ΔG the free energy barrier to flow, s the shear resistance which is 0.15 times the shear modulus μ, k the Boltzmann constant and θ the absolute temperature.

$$\mu = \frac{1}{2}\left(\boldsymbol{\mu_{gl}} + \boldsymbol{\mu_r}\right) - \frac{1}{2}\left(\boldsymbol{\mu_{gl}} - \boldsymbol{\mu_r}\right)\tanh\left(\frac{5}{\boldsymbol{\Delta\theta}}\left(\theta - \theta_g\right) + \boldsymbol{X_g}\left(\theta - \theta_g\right)\right) \quad (3.12)$$

$$\mu = \frac{3E\boldsymbol{B}}{9B - E} \quad (3.13)$$

Where μ_{gl} is the glassy shear modulus, μ_r the rubbery shear modulus, $\Delta\theta$ the temperature range for glass transition, θ_g the glass transition temperature which is fixed at 350K, X_g the slope outside the glass transition region, μ the shear modulus, B the bulk modulus which is a model constant and E the Youngs modulus. The strain rate dependency of strain rate is incorporated by shifting glass transition temperature with strain rate given by

$$\theta_g = \theta_g^* \ : \dot{\gamma}_I^p < 8.66E - 5$$

$$\theta_g = \boldsymbol{\xi}\log_{10}\dot{\gamma}_I^p + \boldsymbol{\zeta} + \theta_g^* \ : \dot{\gamma}_I^p > 8.66E - 5 \quad (3.14)$$

Where ξ and ζ are the material constants and θ_g^* the reference transition temperature. T_I is the Cauchy stress output from network I.

3.4 Constitutive relation derivation for Network interactions (N)

3.4.1 Multiplicative Decomposition of Deformation Gradient

This resistance of arises due to stretching and orientation of polymer chains along the deformation direction. This is modeled again using a spring and a dashpot similar to network I. However, the spring here is highly non-linear based on the Arruda-Boyce model (Arruda and Boyce 1993 a and b). The equations pertaining to the deformation

gradient is similar to that used for network I, consisting of the multiplicative decomposition of the overall deformation gradient into elastic and plastic deformation gradients.

$$F_N = F_N^e F_N^p \tag{3.15}$$

Each of the components here are multiplicatively composed of a stretch and a rotation component by polar decomposition.

$$F_N^e = V_N^e R_N^e \tag{3.16}$$

$$F_N^p = V_N^p R_N^p \tag{3.17}$$

The velocity gradient is defined as

$$L_N = \dot{F}_N F_N^{-1} \tag{3.18}$$

Which, when represented by elastic and plastic deformation gradient components becomes

$$L_N = \dot{F}_N^e F_N^{e-1} + F_N^e \dot{F}_N^p F_N^{p-1} F_N^{e-1} = L_N^e + \tilde{L}_N^p \tag{3.19}$$

The plastic velocity gradient additively is composed of a symmetric plastic rate of stretching and an antisymmetric plastic spin given by

$$\tilde{L}_N^p = \tilde{D}_N^p + \tilde{W}_N^p \tag{3.20}$$

$\tilde{W}_N^p$ is set to zero to keep the representation unique.

3.4.2 Elastic (Spring) Characteristics for Network N

The constitutive relation between Cauchy stress and deformation gradient is based on the Arruda-Boyce eight-chain rubber elasticity model (Arruda and Boyce 1993 a and b) which is given by:

$$T_N = \frac{1}{J_N}\frac{\boldsymbol{nk\theta}}{3}\frac{\sqrt{\boldsymbol{N}}}{\bar{\lambda}_N}\mathcal{L}^{-1}\left(\frac{\bar{\lambda}_N}{\sqrt{\boldsymbol{N}}}\right)[B_N - \bar{\lambda}_N{}^2 I] \tag{3.21}$$

Where n is chain density, N the number of rigid links between entanglements, $nk\theta$ the rubbery modulus, the inverse Langevin function given by $L(\beta) = \coth(\beta) - (\frac{1}{\beta})$.

The 8-chain rubber elasticity model tries to capture the outcome of stretching and orientation by using a unit cell with 8 identical chains, where the stretch of each individual chain is given by an effective chain stretch $\bar{\lambda}_N$ which is the root mean square of the distortional applied stretch. The inverse Langevin function allows a drastic increase in stress as $\bar{\lambda}_N$ approaches $\sqrt{N}$ which implies that the chain has reached the limit of its extensibility, beyond which stress would increase dramatically.

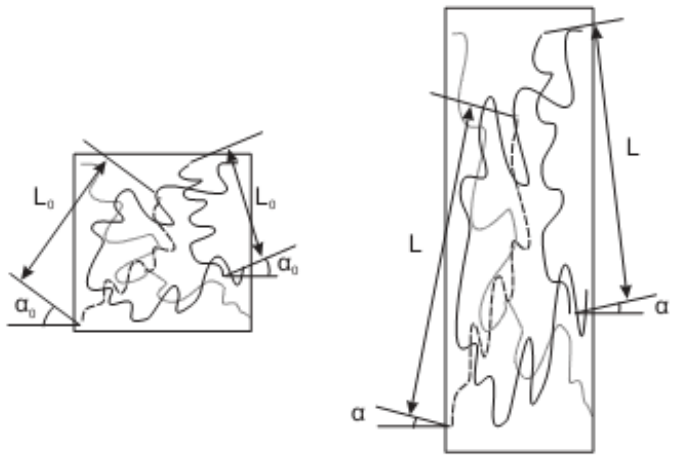

Figure 3.3 Illustration of stretch and orientation of chains in a random network – Undeformed (L) and Deformed (R) (Dupaix 2003)

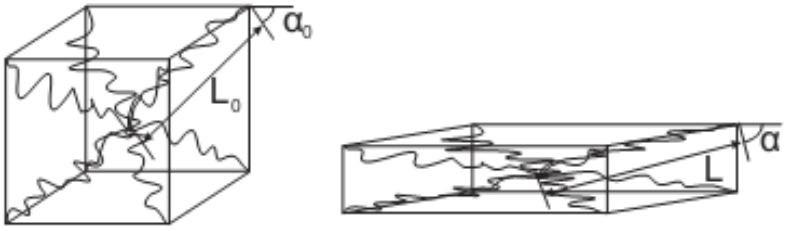

Figure 3.4 8-chain network model- Undeformed (L) and Deformed (R) (Dupaix 2003)

The above mentioned equations cover the spring portion of network N. For the dashpot, the following equations are defined.

$$\widetilde{D}_N^p = \dot{\gamma}_N^p N_N \tag{3.22}$$

$$N_N = \frac{1}{\sqrt{2\tau_N}} T_N' \tag{3.23}$$

$$\tau_N = [\frac{1}{2} T_N' T_N']^{1/2} \tag{3.24}$$

Where $\widetilde{D}_N^p$ is the rate of molecular relaxation and N_N the normalized deviatoric stress.

3.4.3 Plastic Flow (Dashpot) Characteristics for Network N

To capture the rate of relaxation, a parameter called the 'orientation' parameter is created from the geometry of the eight chain model. This parameter is related to the maximum angle formed between a diagonal chain in the eight chain model and one of the principal axes α_{max}. The orientation parameter is equal to $\alpha_{min} = \frac{\pi}{2} - \alpha_{max}$. The rate of relaxation $\dot{\gamma}_N^p$ is described constitutively as shown below.

$$\dot{\gamma}_B^p = \left(\frac{\frac{\alpha_{min}}{\alpha_c} - 1}{\frac{\alpha_0}{\alpha_c} - 1}\right) C(\tau^B)^{\mathbf{1/n}} \tag{3.25}$$

$$C = (h\alpha_{min})^{1/n} \tag{3.26}$$

$$h = \boldsymbol{D}exp\left(-\frac{\boldsymbol{Q}}{\boldsymbol{R\theta}}\right) \tag{3.27}$$

When α_{min} reaches the cutoff orientation parameter $\boldsymbol{\alpha_c}$, $\dot{\gamma}_B^p$ becomes zero which means that plastic flow ceases and stress increases rapidly. This setup allows the capture of rapid strain hardening which is observed at high strains. Q/R, D, n and α_c are model constants. T_N is the Cauchy stress output from network N.

The net stress output from this model will be the sum of Cauchy stresses due to network I and network N.

$$T = T_I + T_N \tag{3.28}$$

Table 3.1 Constants of the Dupaix-Boyce model

Model Constants	Symbol	Description	Network I/N s-spring d-damper
PROPS(1)	μ_{gl}	Shear modulus in glassy region	I s
PROPS(2)	μ_r	Shear modulus in rubbery region	I s
PROPS(3)	$\Delta\theta$	Glassy - rubbery transition temperature interval	I s
PROPS(4)	X_g	Slope wrt. temperature outside transition region	I s
PROPS(5)	ξ	First rate shift factor for glass transition temperature	I s
PROPS(6)	ς	Second rate shift factor for glass transition temperature	I s
PROPS(7)	B	Bulk modulus	I s
PROPS(8)	ΔG	Activation energy for flow to start	I d
PROPS(9)	$\dot{\gamma}_{0I}$	Pre-exponential factor for plastic flow	I d
PROPS(10)	$nk\theta$	Rubbery modulus; n – chain density	N s
PROPS(11)	N	No. of rigid links between entanglements	N s
PROPS(12)	Q/R	Temperature factor for relaxation	N d
PROPS(13)	D	Pre-exponential factor for relaxation	N d
PROPS(14)	$1/n$	Exponent	N d
PROPS(15)	α_c	Flow cutoff angle for Network N	N d

3.5 Summary

The constitutive model used in this thesis, the Dupaix-Boyce model has thus been described in this chapter. The model assumes stress created in a polymer to be the sum of stresses due to intermolecular forces due to interaction between molecules **I** and network level stretch and orientation during deformation **N**. Each of these concepts are modeled to

occur in parallel and each individually consist of an energy storing spring element that causes stress to increase with deformation in series with a dissipative dashpot that captures inelastic deformation. **I** is linear elastic until the yield point when plastic flow begins. The flow rule that governs the yield point is temperature and rate dependence. The flow rule in **N** captures molecular relaxation but his flow cuts off when the deformation increases beyond a certain value and becomes entirely hyperelastic. This allows the model to capture the steep increase of stress at large deformation that is observed in some polymers. This model is fit to capture the behavior of PET as described in the following chapters.

Chapter 4: Dupaix-Boyce Model Fit for Uniaxial Compression Data

4.1 Introduction

This chapter describes the fit of the Dupaix-Boyce constitutive model to the experimental data obtained from the uniaxial compression tests. The Dupaix-Boyce model as described in the previous chapter consists of 15 model constants of which some can be fit based on a physical relation to the experimental data and the rest by trial and error.

4.2 Model Constants

Table 4.1 lists the model constants used in the Dupaix-Boyce model, their usage in individual portions of the networks I and N, and their relation to the physical nature of the problem.

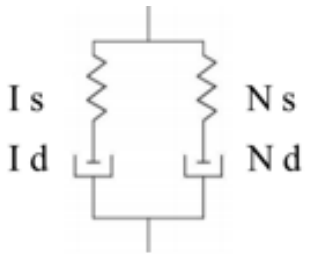

Figure 4.1 Inner elements of the Dupaix-Boyce model

Table 4.1 Description of DB model constants

Model Constants	Symbol	Description	Network I/N s-spring d-damper	Behavior Component
PROPS(1)	μ_{gl}	Shear modulus in glassy region	I s	Initial Elastic Behavior
PROPS(2)	μ_r	Shear modulus in rubbery region	I s	
PROPS(3)	$\Delta\theta$	Glassy - rubbery transition temperature interval	I s	
PROPS(4)	X_g	Slope wrt. temperature outside transition region	I s	
PROPS(5)	ξ	First rate shift factor for glass transition temperature	I s	
PROPS(6)	ς	Second rate shift factor for glass transition temperature	I s	
PROPS(7)	B	Bulk modulus	I s	
PROPS(8)	ΔG	Activation energy for flow to start	I d	Flow Stress
PROPS(9)	$\dot{\gamma}_{0I}$	Pre-exponential factor for plastic flow	I d	
PROPS(10)	$nk\theta$	Rubbery modulus; n – chain density	N s	Resistance Elasticity
PROPS(11)	N	No. of rigid links between entanglements	N s	
PROPS(12)	Q/R	Temperature factor for relaxation	N d	Molecular Relaxation
PROPS(13)	D	Pre-exponential factor for relaxation	N d	
PROPS(14)	$1/n$	Exponent	N d	
PROPS(15)	α_c	Flow cutoff angle for Network B	N d	

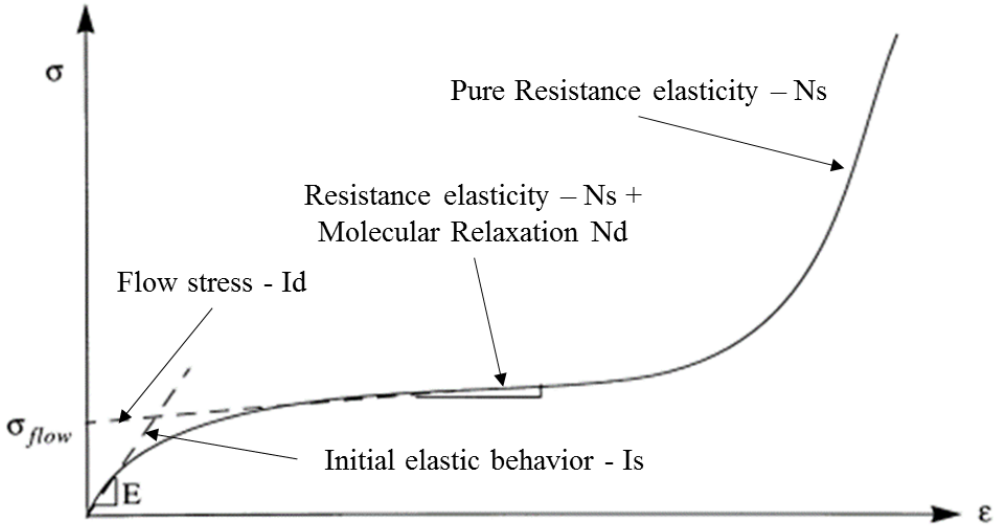

Figure 4.2 Stress Stain curve sections governed by DB model constant sets (Curve from Boyce, Socrate and Llana, 2000)

4.3 Fitting Initial Elastic Behavior in Network I

The initial elastic behavior of a polymer was modeled using a function describing the shear modulus of the material as a function of temperature from the initial glassy state, through the transition temperature to the rubbery state using the equation (3.12). Figure 4.3 depicts this function and the model constants that govern this function.

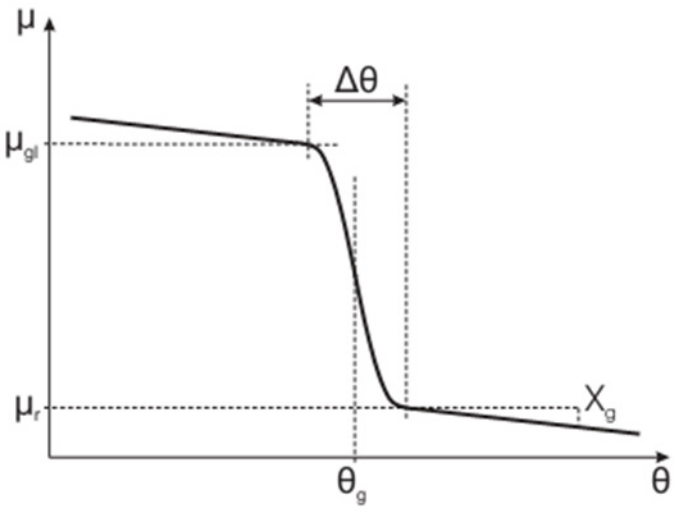

Figure 4.3 Temperature dependence of shear modulus (Dupaix, 2003)

Data from experiments was available for the temperatures 363K, 373K and 383K. Glass transition temperature was set at 350K and the following constants were obtained which fit the above curve representing the temperature dependence of shear modulus to the experimental data. Shear modulus data from the experiments was plotted and overlaid with values obtained from equation (3.12) to arrive at a proper fit for the first 4 constants. This is shown in figure 4.4.

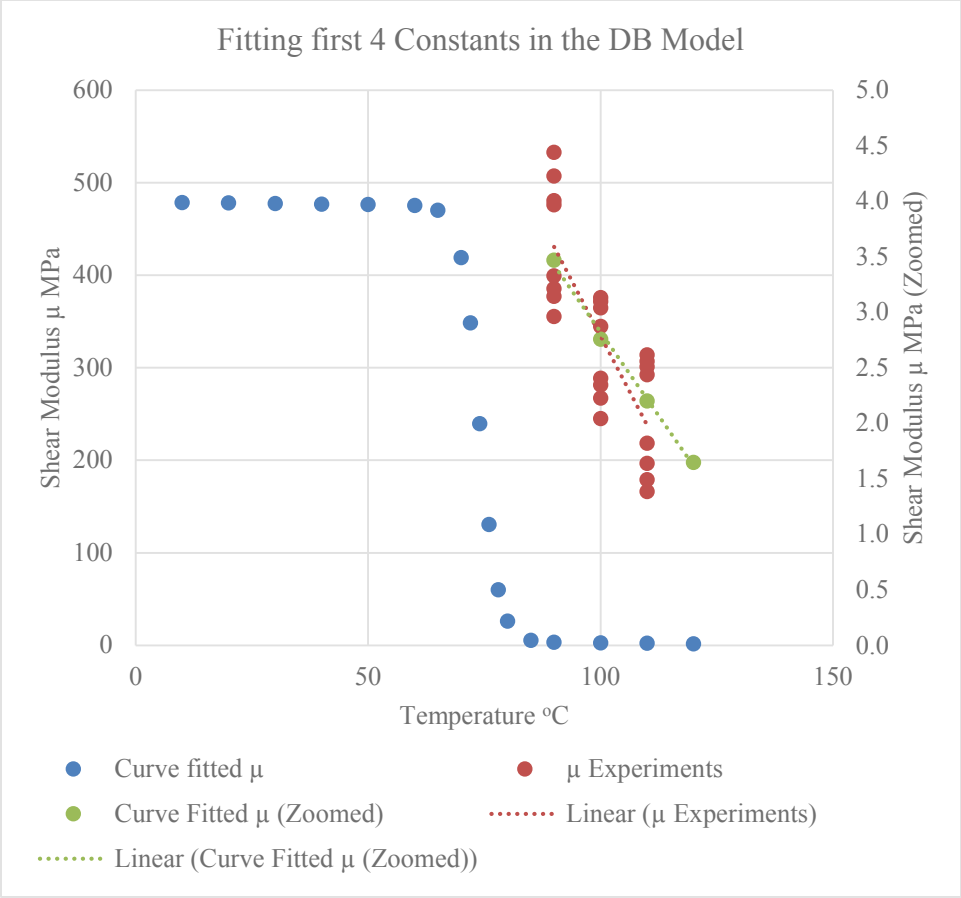

Figure 4.4 Fitting of first 4 constants

Table 4.2 Fitted first 4 constants

Model Constants	Symbol	Fit Value	Unit
PROPS(1)	μ_{gl}	0.475E9	N/m^2
PROPS(2)	μ_r	0.42E7	N/m^2
PROPS(3)	$\Delta\theta$	23	K
PROPS(4)	X_g	-0.62E6	N/m^2

To model strain-rate dependence, an equation of the form of the WLF equation used in temperature-time superposition application was used (See equation 3.14). This equation shifts the glass transition temperature based on a shift factor dependent on the model constants ξ and ζ. The following values provided a good fit for these two constants.

Table 4.3 Model constants fit for strain rate dependence of glass transition temperature

Model Constants	Symbol	Fit Value	Unit
PROPS(5)	ξ	3	K
PROPS(6)	ς	1.2263	K

As the temperature dependence of shear modulus had already been defined in constants 1-4, a temperature independent value of bulk modulus B was to be fit, which along with shear modulus would allow the derivation of the temperature dependent value of Young's Modulus and Poisson's ratio for use in the linear elastic equations of Network I in the Dupaix-Boyce Model. The following value provided a good fit for the Bulk modulus.

Table 4.4 Model constant fit for bulk modulus

Model Constants	Symbol	Fit Value	Unit
PROPS(7)	B	1E6	N/m^2

4.4 Fitting Flow Stress Behavior in Network I

The flow rule for intermolecular resistance (network I) was defined by equation (3.11) which provided the plastic shear strain rate modeled as a thermally activated process. The model constants governing this section were the pre-exponential factor $\dot{\gamma}_{0I}$ and activation energy ΔG. The following values for these constants provided a good fit.

Table 4.5 Model constants fit for Flow Stress Behavior in Network I

Model Constants	Symbol	Fit Value	Unit
PROPS(8)	ΔG	2E12	J
PROPS(9)	$\dot{\gamma}_{0I}$	1.8E-19	1/s

4.5 Fitting Network Resistance Elasticity in Network N

The network elastic resistance, as given in equation (3.21) is modeled using the Arruda-Boyce Hyperelastic (Arruda and Boyce, 1993a) model and relates stress to stretch by relating it to chain stretch of a chain in the 8-chain cube. Two model constants were required for this section, which were $nk\theta$, which relates to chain density and N, which is the number of rigid links between entanglements. The following values were arrived at for these constants by trial and error.

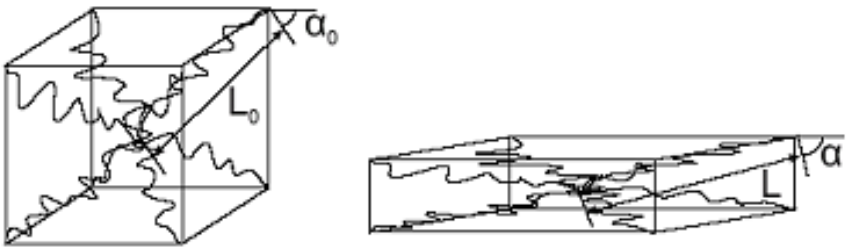

Figure 4.5 Unit cell in the Arruda-Boyce 8-Chain model (Arruda and Boyce, 1993a)

Table 4.6 Model constants fit for Network Resistance Elasticity in Network N

Model Constants	Symbol	Fit Value	Unit
PROPS(10)	$nk\theta$	3E6	N/m^2
PROPS(11)	N	7	-na-

4.6 Fitting Molecular Relaxation in Network N

The molecular relaxation section in network N defines a flow rule depending on the orientation of the molecular chains. This relation is defined by a series of equations (3.25, 3.26 and 3.27) and is set up to switch off plastic flow when the orientation parameter crosses a minimum limit. The values for the model constants used here are provided in the table below.

Table 4.7 Model constants fit for Molecular Relaxation in Network N

Model Constants	Symbol	Fit Value	Unit
PROPS(12)	Q/R	5.335E3	K
PROPS(13)	D	3.2	$((N/m^2)^3 s)^{-1}$
PROPS(14)	$1/n$	4	-na-
PROPS(15)	α_c	5E-2	rad

4.7 Experimental and Dupaix-Boyce Model Results for Uniaxial compression

The following plots show the experimental and Dupaix-Boyce model simulation results for uniaxial compression under different conditions of temperature, strain-rate and IV. It can be observed that the above mentioned values of constants provided simulated results which were very close to the experimental results, without having to change constants over the strain-rate and temperature range of interest.

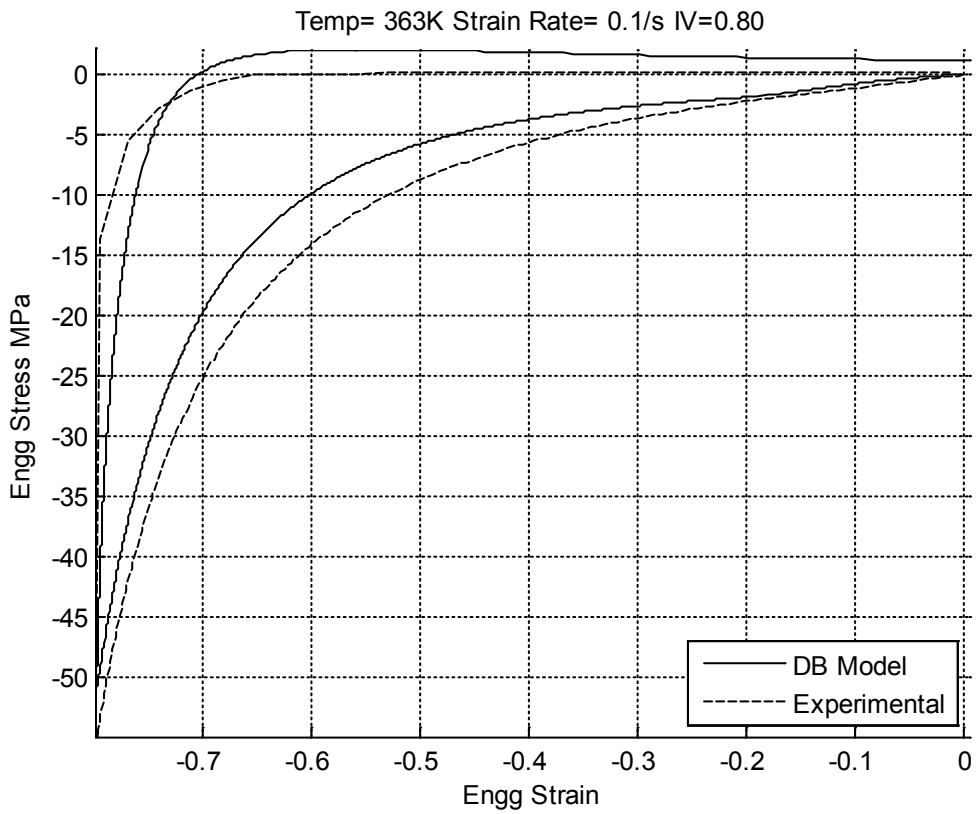

Figure 4.6 DB model fit - Temp 363K SR 0.1/s IV 0.80

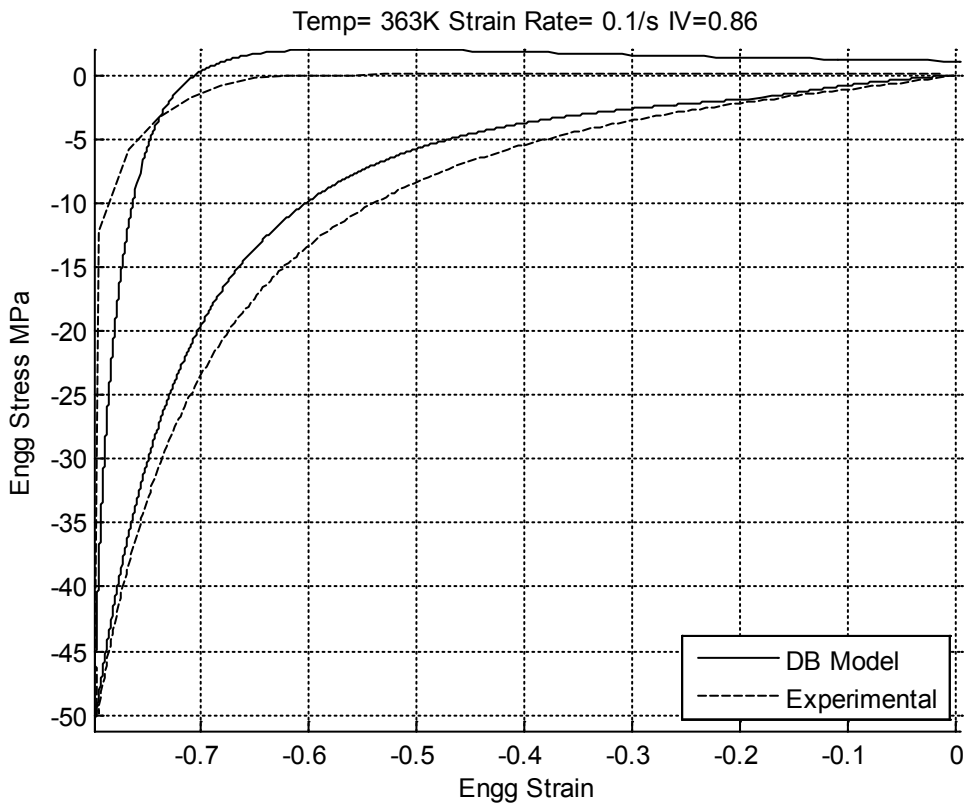

Figure 4.7 DB model fit - Temp 363K SR 0.1/s IV 0.86

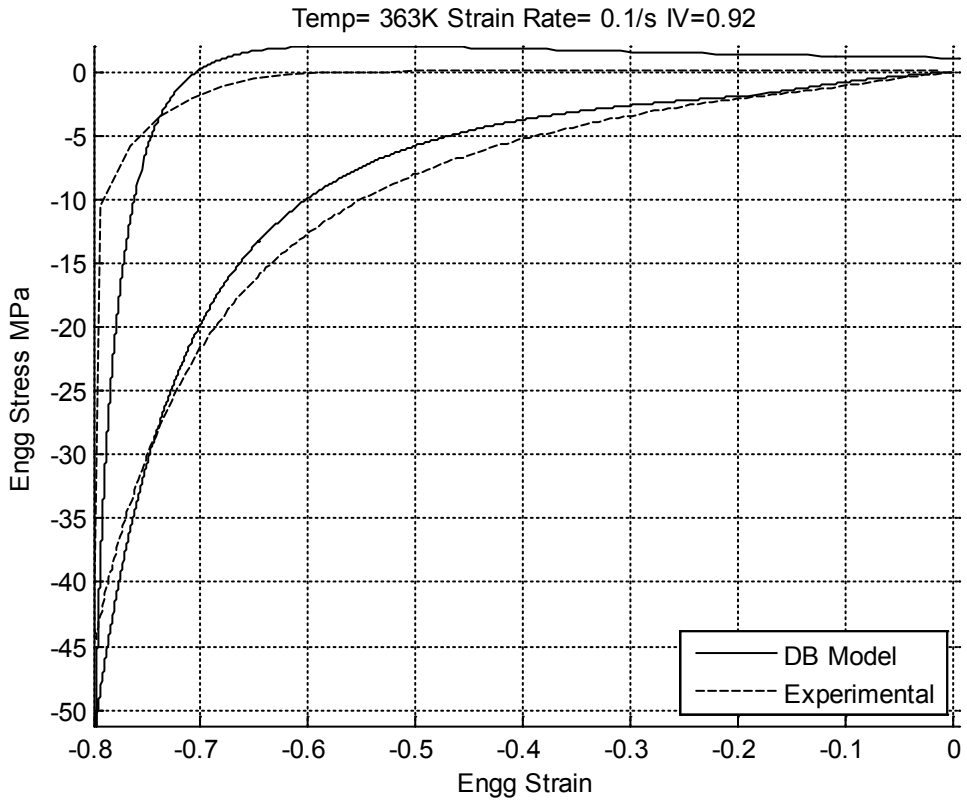

Figure 4.8 DB model fit - Temp 363K SR 0.1/s IV 0.92

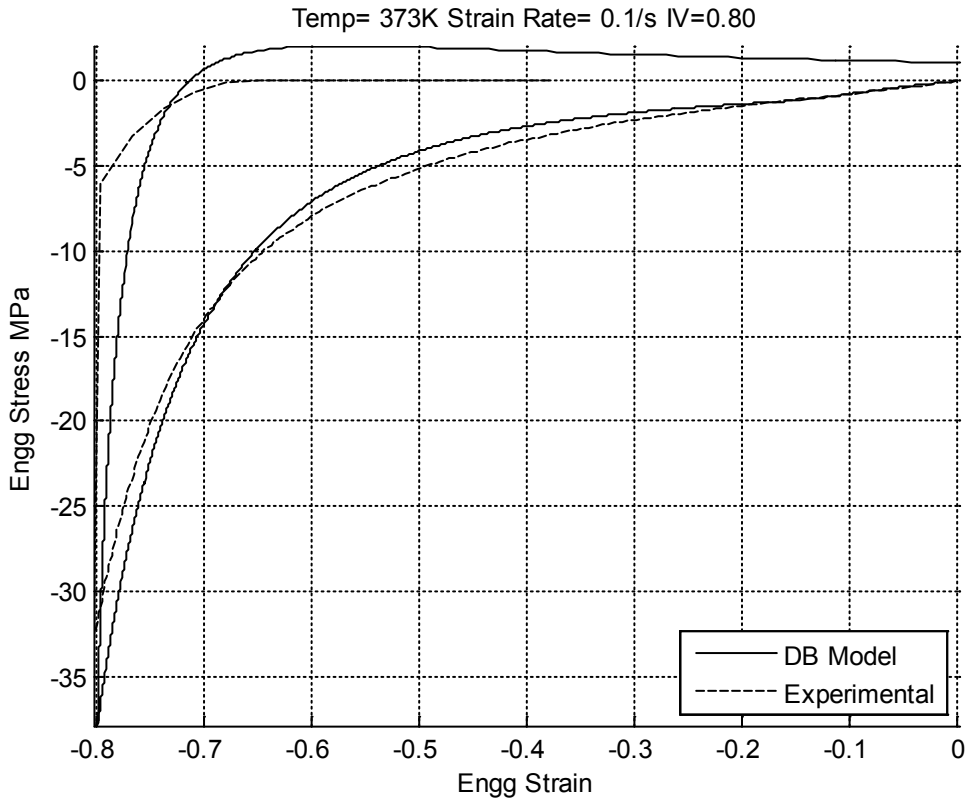

Figure 4.9 DB model fit - Temp 373K SR 0.1/s IV 0.80

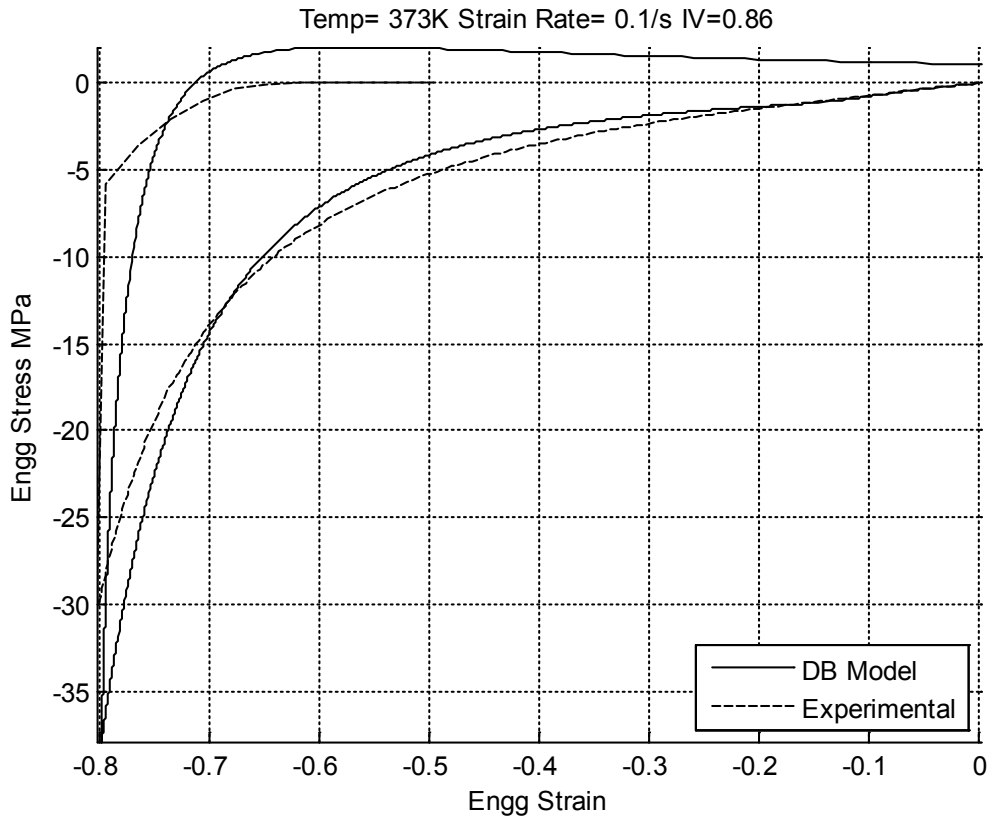

Figure 4.10 DB model fit - Temp 373K SR 0.1/s IV 0.86

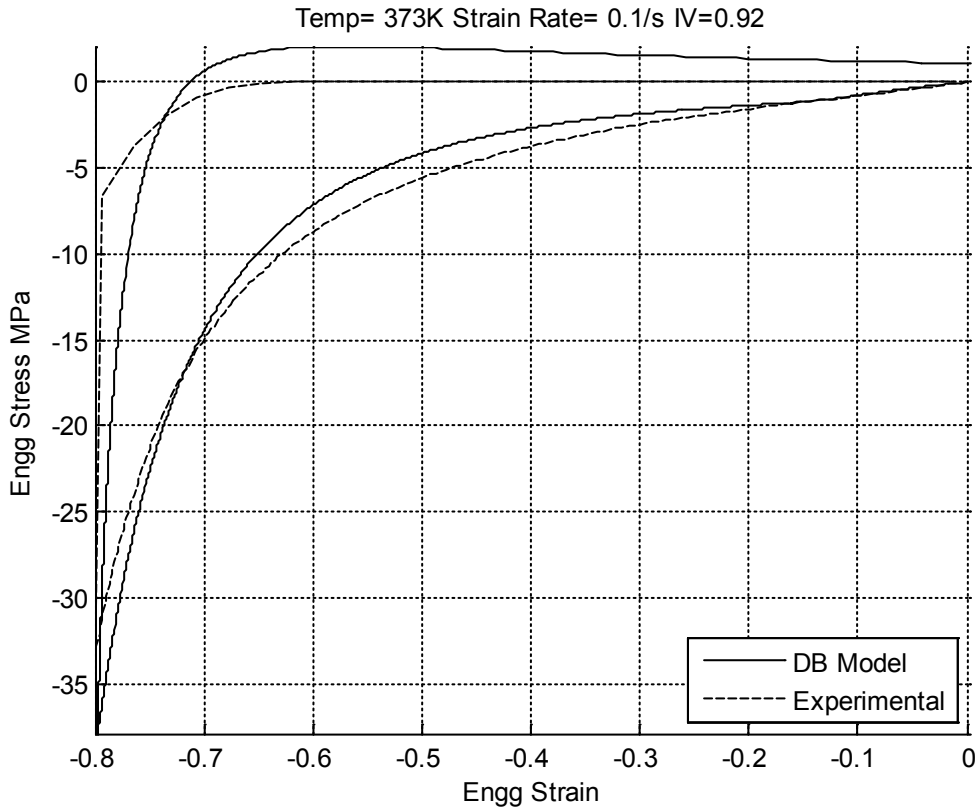

Figure 4.11 DB model fit - Temp 373K SR 0.1/s IV 0.92

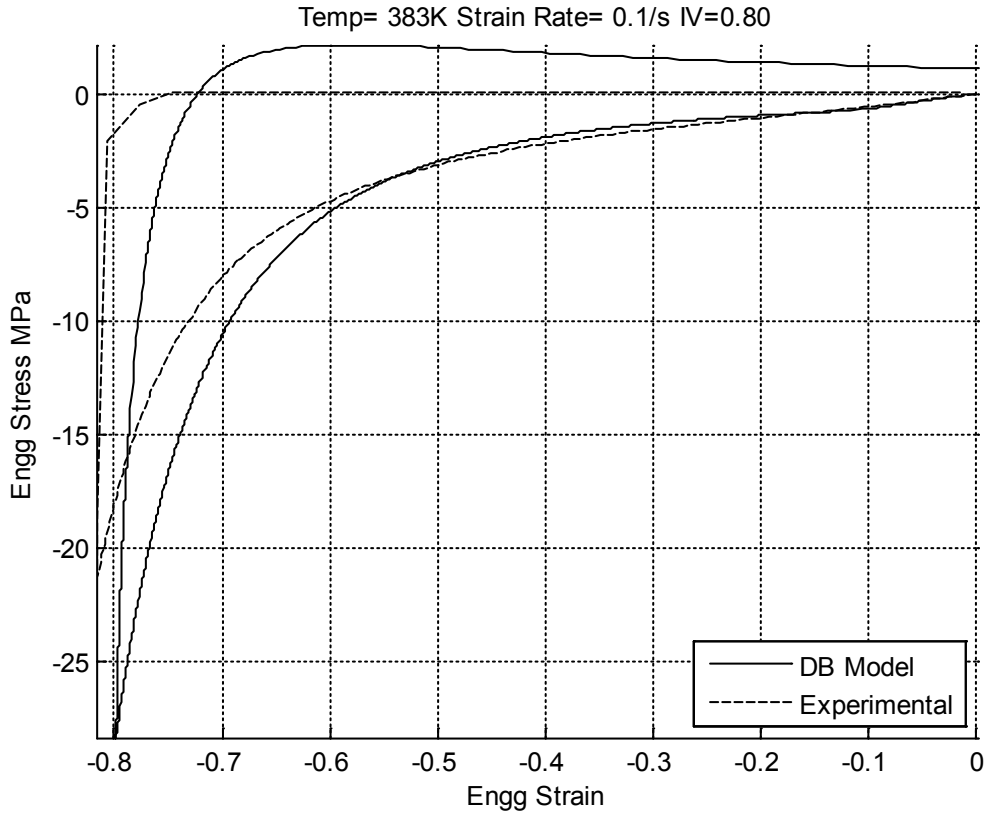

Figure 4.12 DB model fit - Temp 383K SR 0.1/s IV 0.80

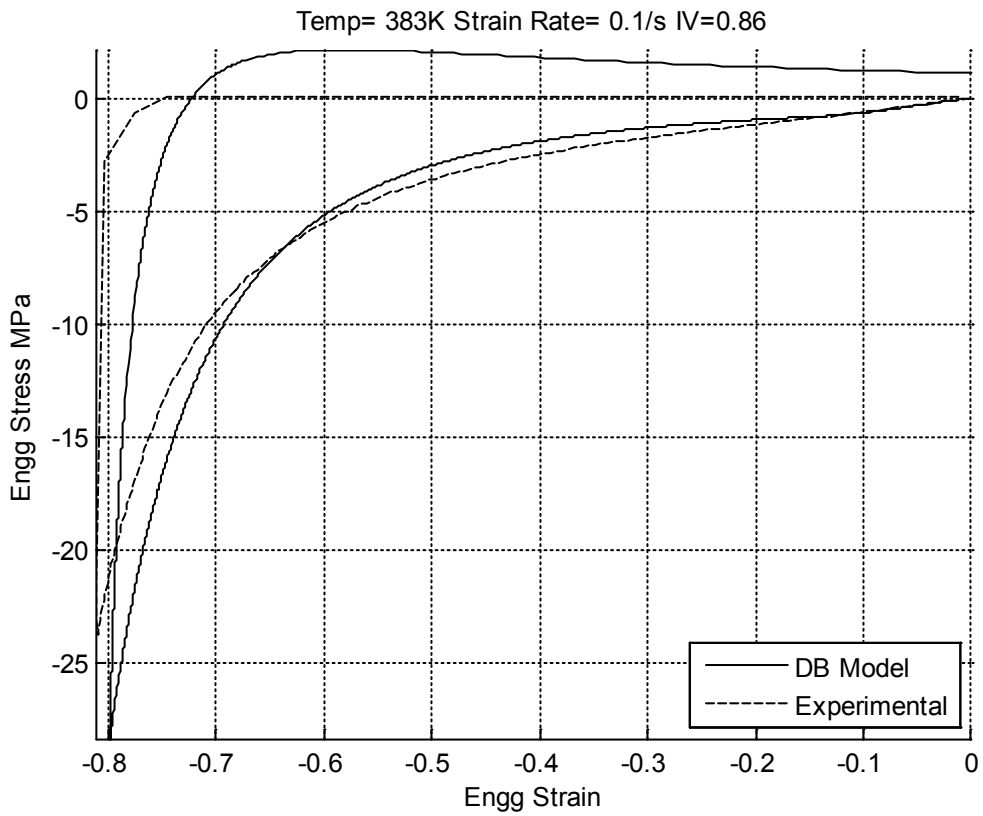

Figure 4.13 DB model fit - Temp 383K SR 0.1/s IV 0.86

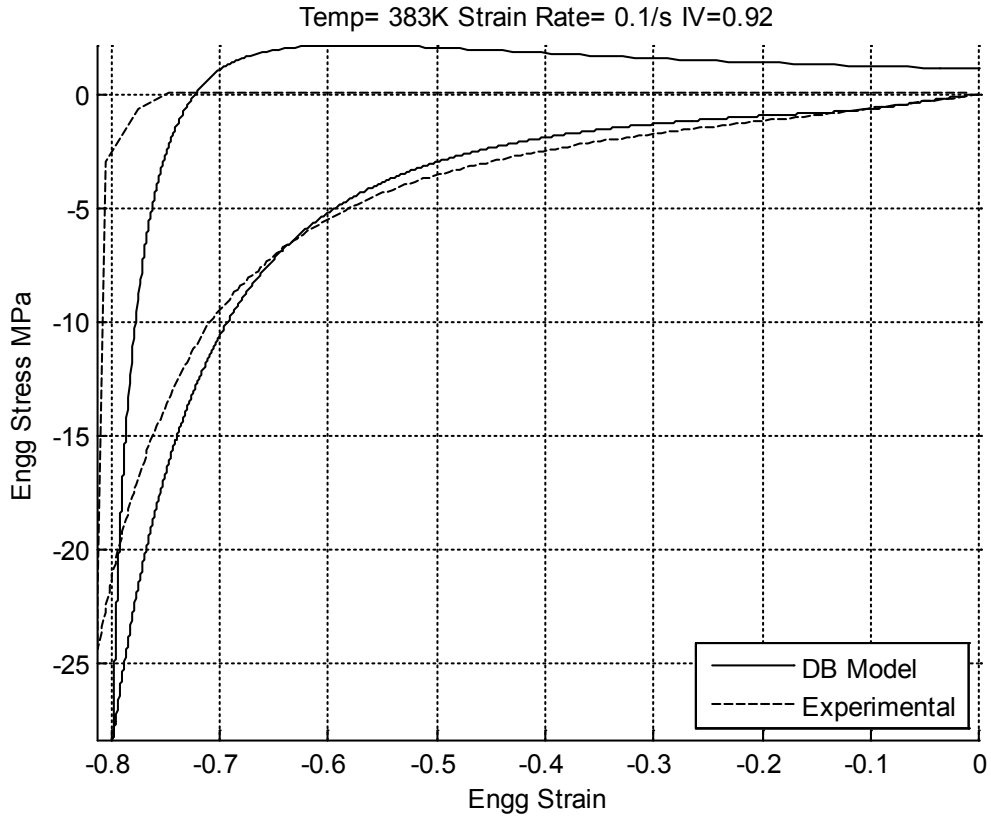

Figure 4.14 DB model fit - Temp 383K SR 0.1/s IV 0.92

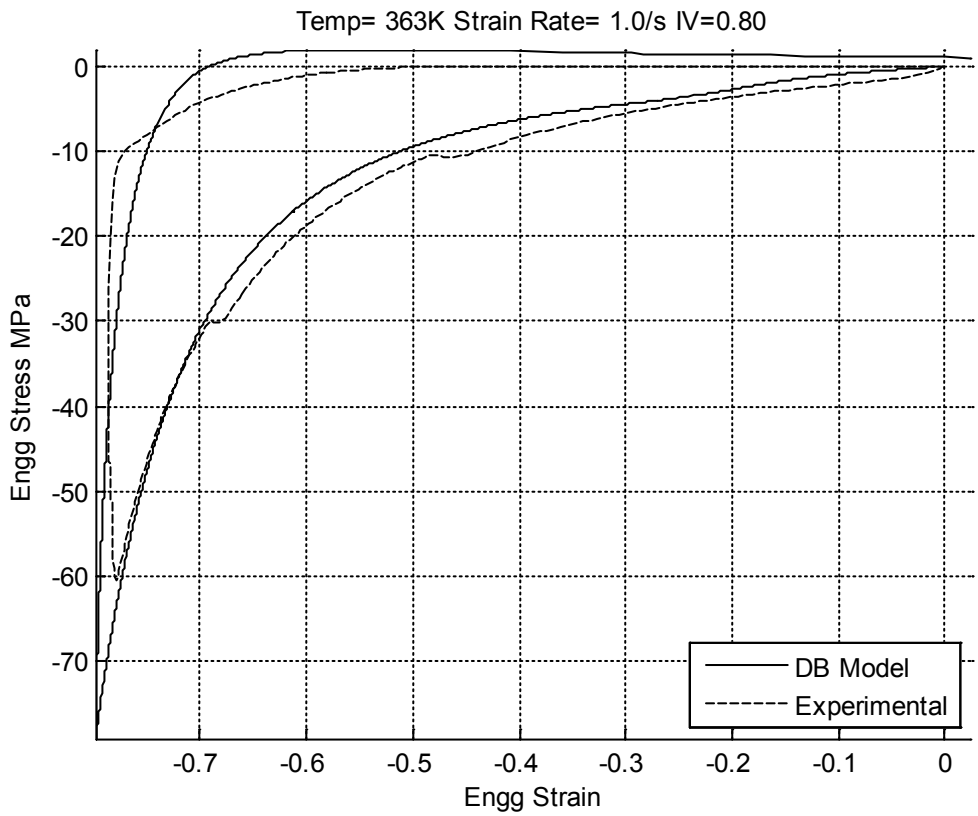

Figure 4.15 DB model fit - Temp 363K SR 1/s IV 0.80

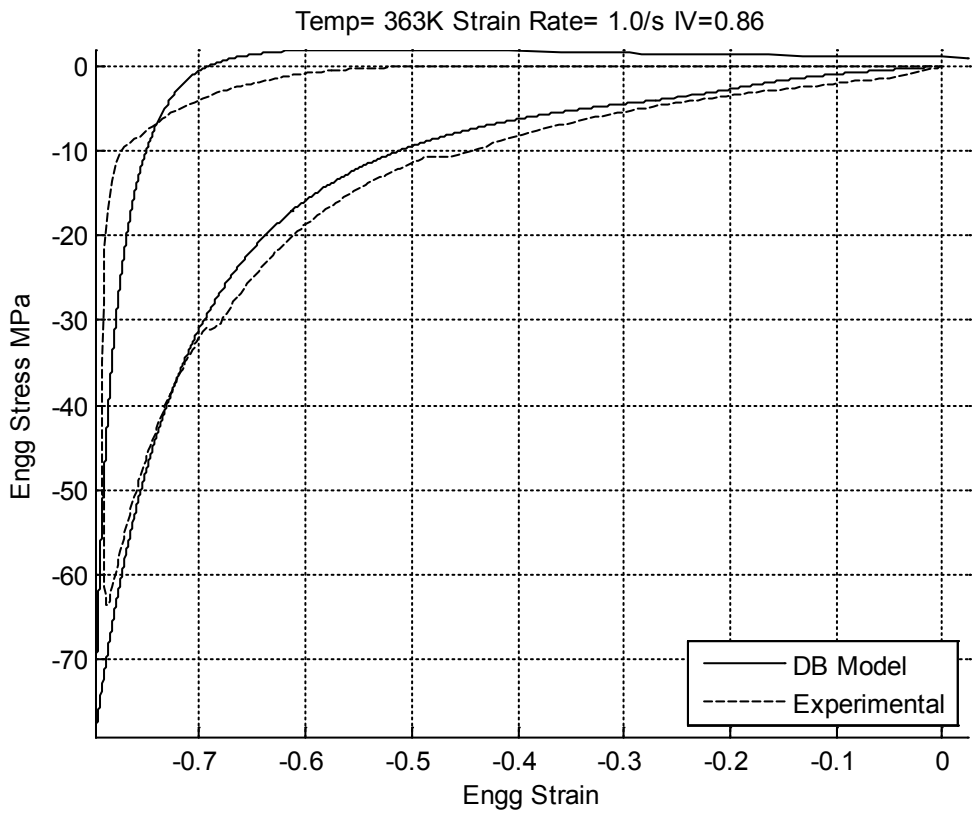

Figure 4.16 DB model fit - Temp 363K SR 1/s IV 0.86

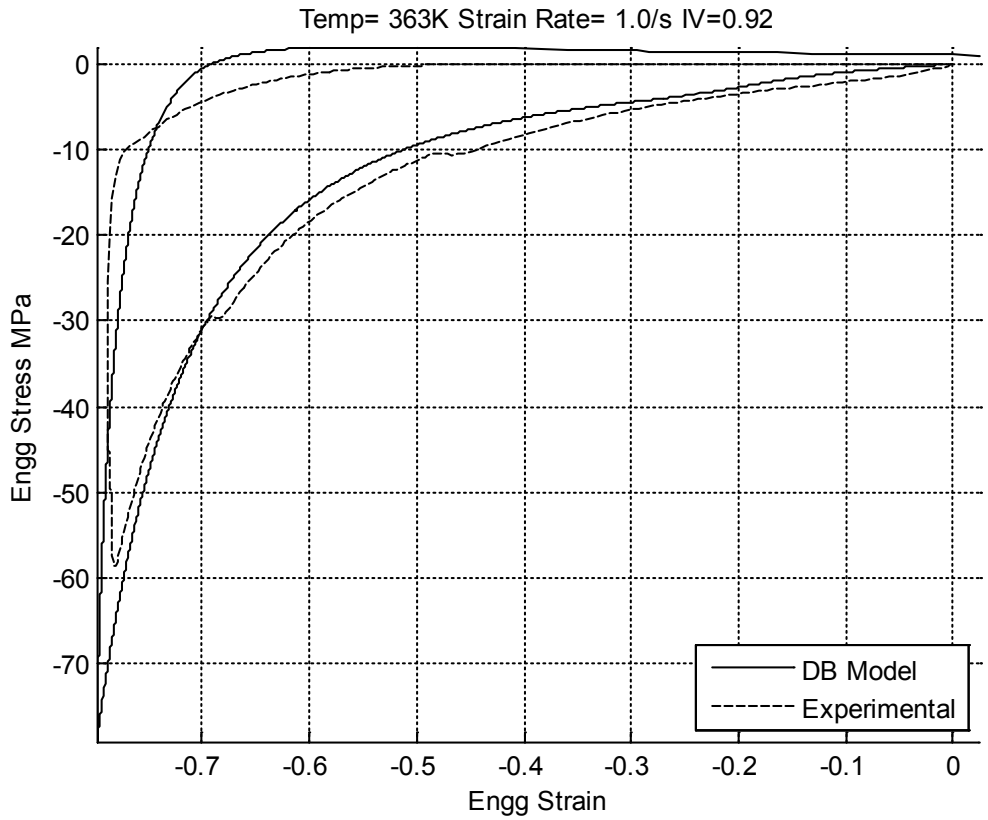

Figure 4.17 DB model fit - Temp 363K SR 1/s IV 0.92

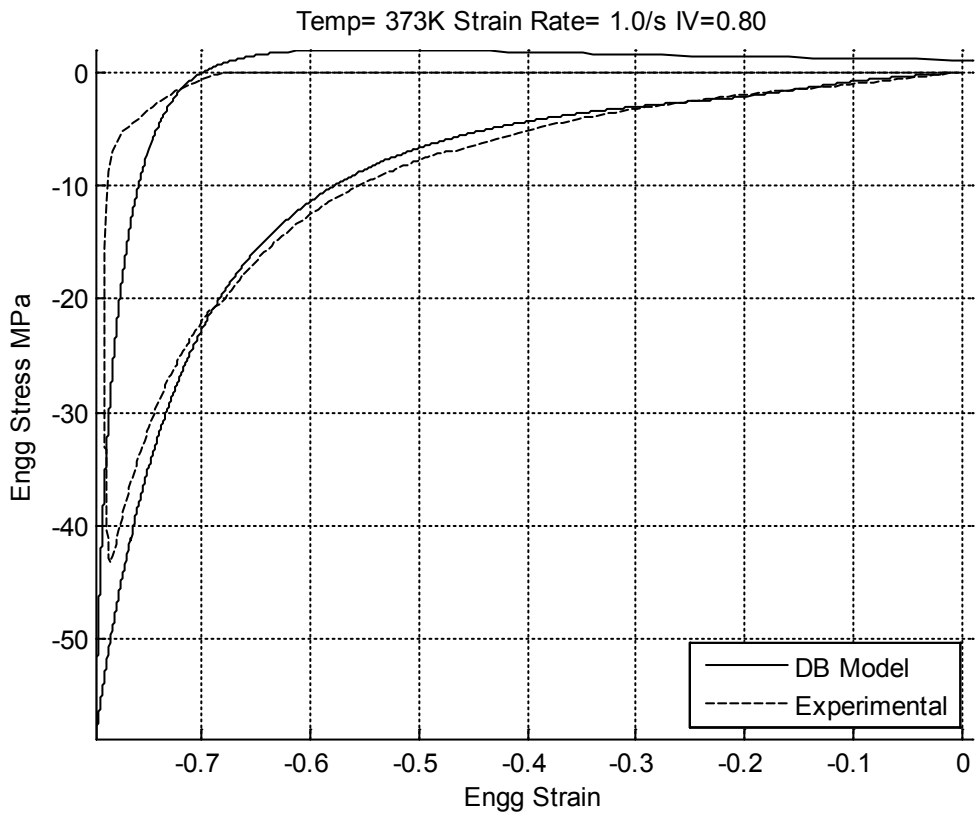

Figure 4.18 DB model fit - Temp 373K SR 1/s IV 0.80

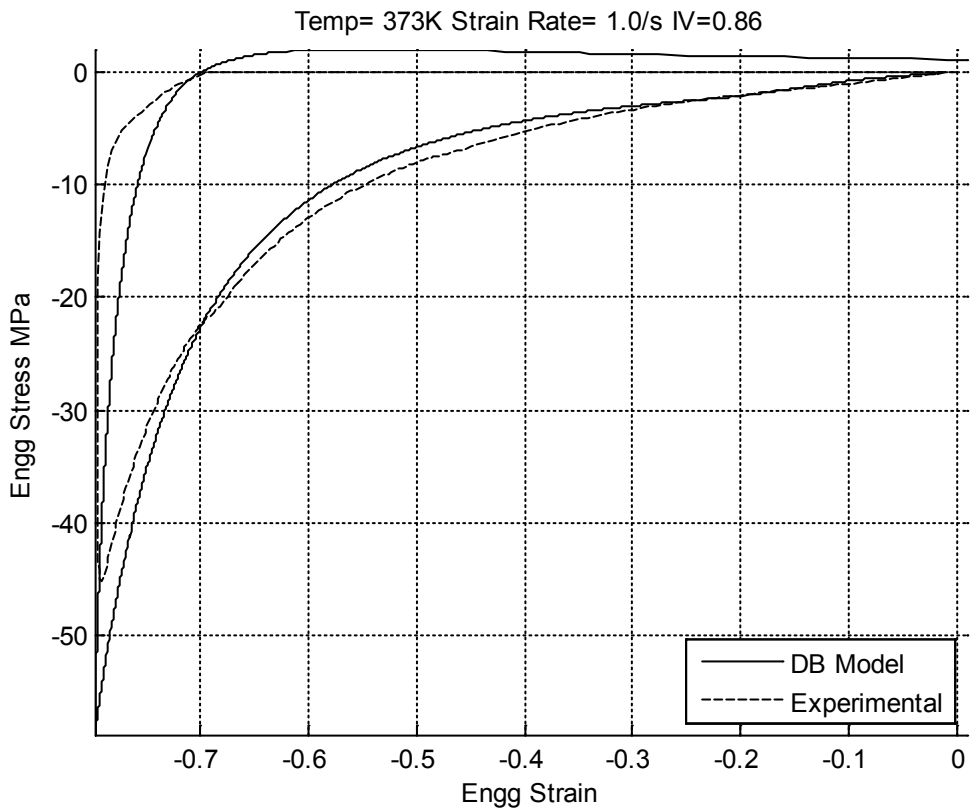

Figure 4.19 DB model fit - Temp 373K SR 1/s IV 0.86

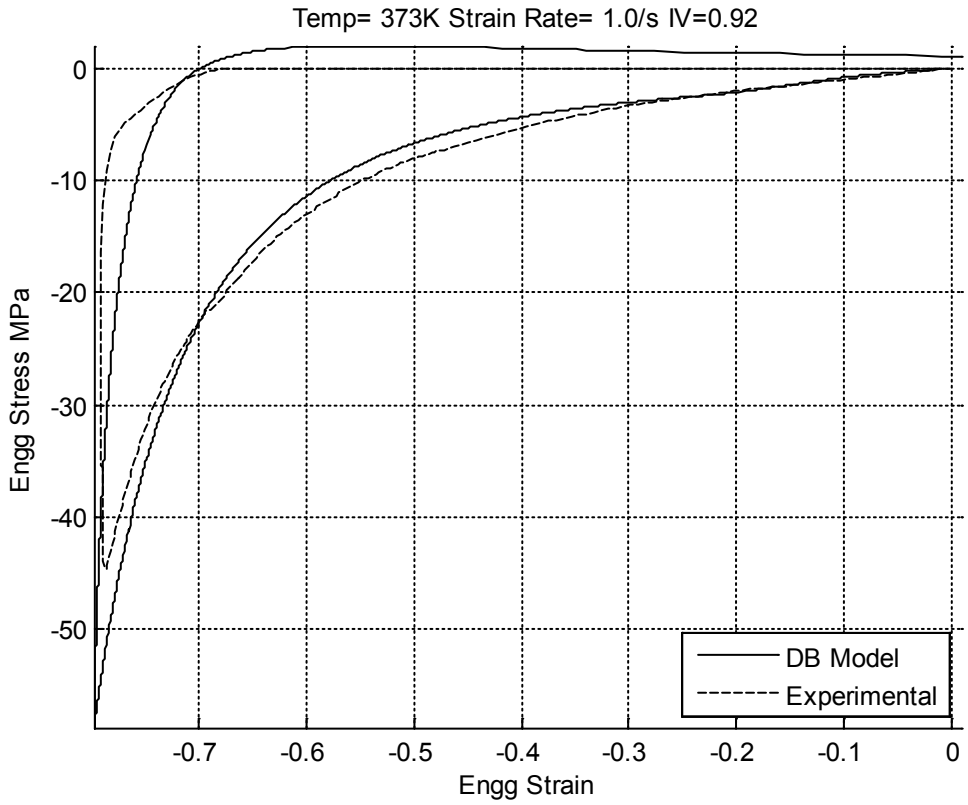

Figure 4.20 DB model fit - Temp 373K SR 1/s IV 0.92

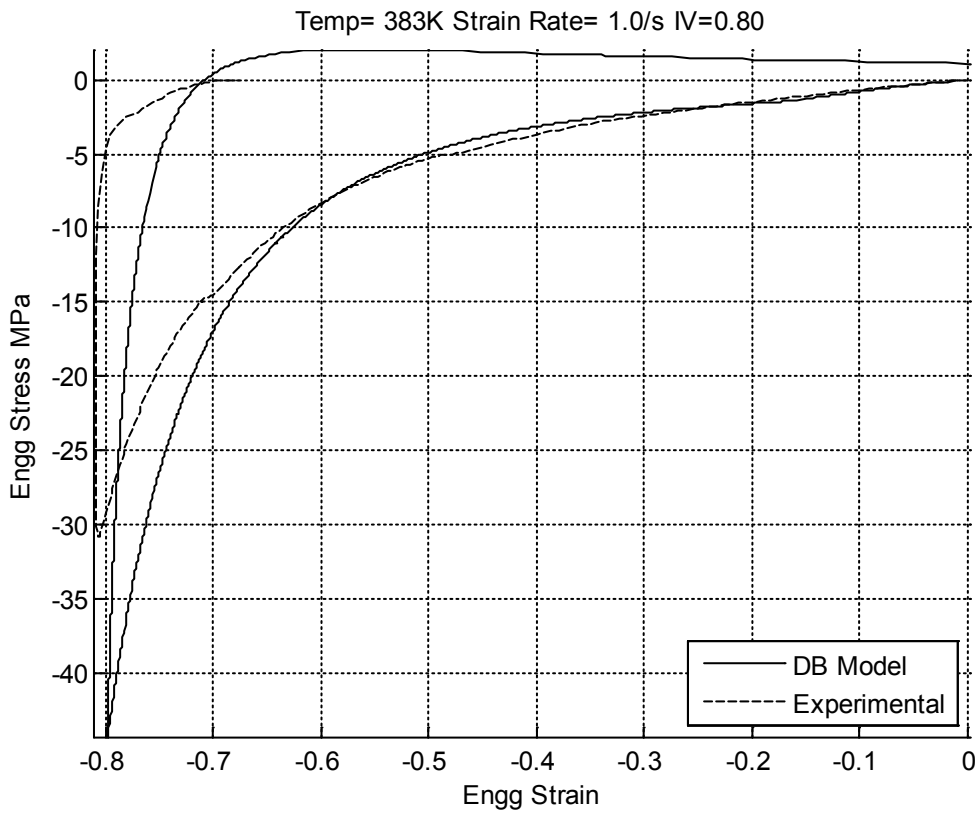

Figure 4.21 DB model fit - Temp 383K SR 1/s IV 0.80

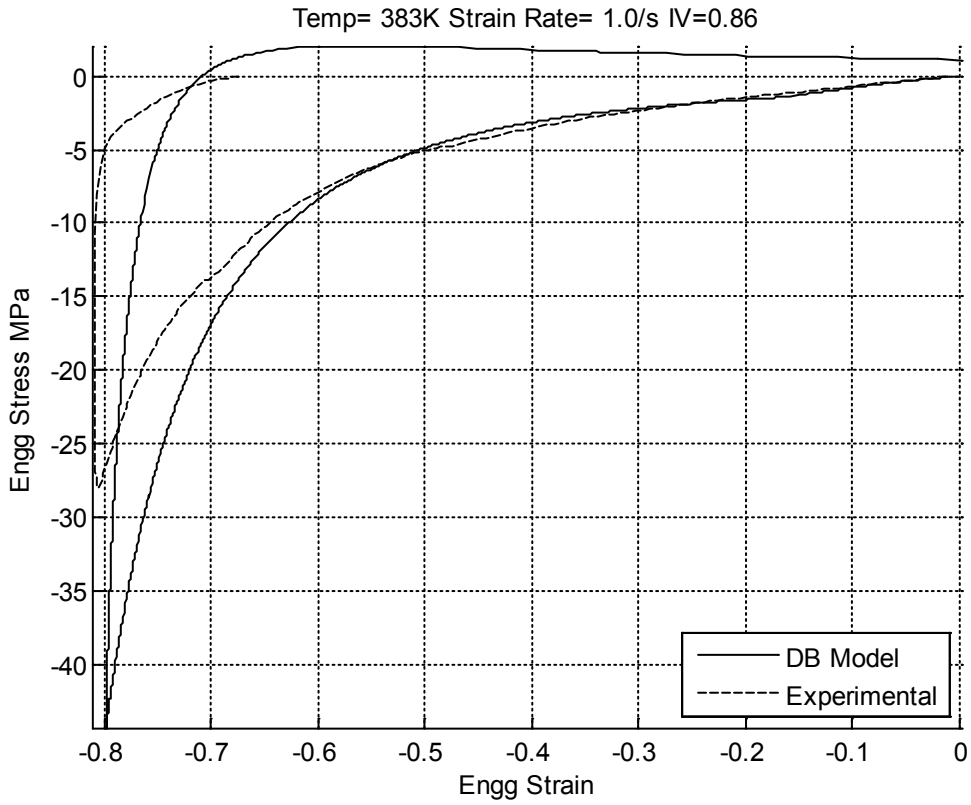

Figure 4.22 DB model fit - Temp 383K SR 1/s IV 0.86

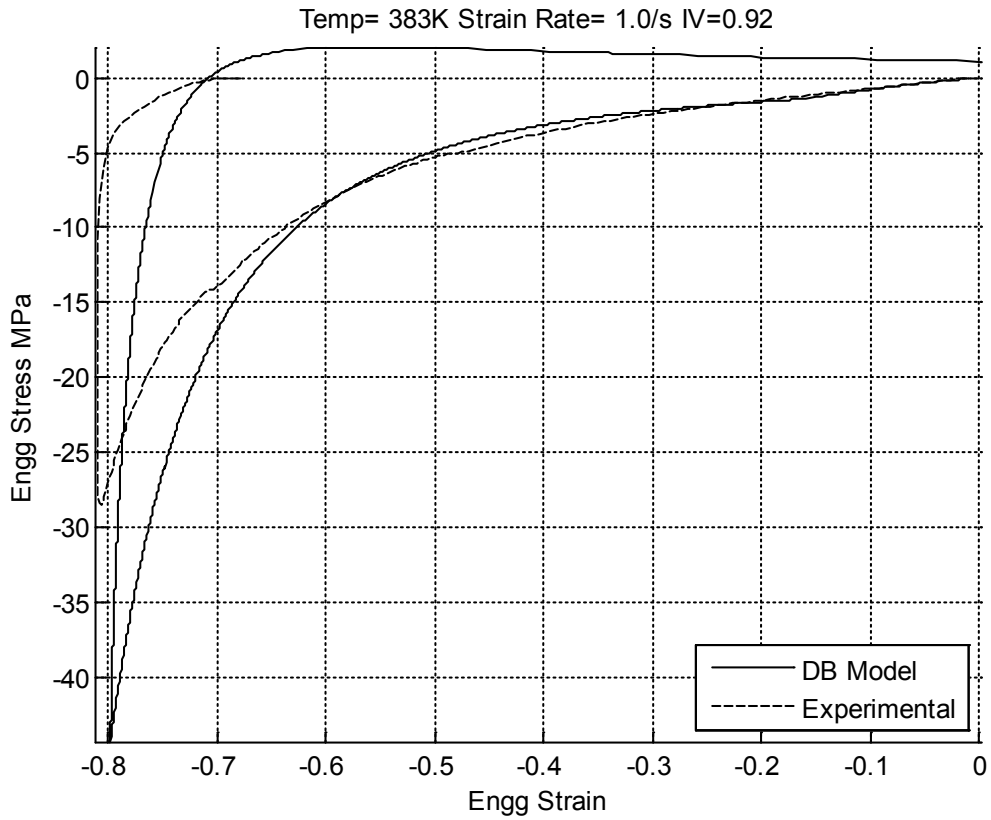

Figure 4.23 DB model fit -Temp 383K SR 1/s IV 0.92

4.7 Conclusion

This chapter described the fitting of the model constants of the Dupaix-Boyce model for compression experimental results with the non-hollow circular specimens. This set of constants gave a very good fit for different temperatures from 363K to 383K and true strain rates of 0.1/s and 1/s without requiring a change of model constants. Close agreement could be observed between both the loading and unloading experimental curves and the curves predicted by the Dupaix-Boyce model. Following successful

compression fits, this process was repeated to fit for experimental uniaxial tensile test results. Minor changes were required to fit the model for the tensile test results because the set of constants used in compression under-predicted the stress in tension. This is described in detail in Chapter 5.

Chapter 5: Uniaxial Tension Tests

5.1 Introduction

Following compression testing and fit of the Dupaix – Boyce model, uniaxial tension experiments were conducted for the primary purpose of determining if the material characteristics were different during tension and also to determine whether the Dupaix-Boyce model fit to the compression data would also simulate tensile characteristics for the same material. The finding from the tensile tests was that the material (PET) showed drastic strain hardening during tension. This strain hardening was extremely high beyond a certain draw ratio and was completely absent in compression testing. The results of these experiments suggested crystallization occurs during tension, which had to be separately modeled and plugged into the Dupaix-Boyce model for it to be captured (see Chapter 8).

5.2 Tensile Testing Procedure

5.2.1 Problems Faced in Tensile Testing

Tension testing ought to be done in similar conditions of temperature and strain rate as compression testing to compare stress and strain parameters. Initial tension tests were attempted with standard ASTM D638 Type 1 sized tensile bars but this posed a few difficulties. Firstly, the size of the standard tensile bars are large relative to the size of the environment chamber, because of which large strain could not be reached by drawing. Secondly, since uniaxial engineering strain rate was directly proportional to the length of the sample for a constant true strain rate, the longer standard bar was limited from reaching higher strain rates because of limitations in the maximum speed of head movement of the testing machine.

A few trials were attempted to do away with the high temperature environmental chamber by dipping the samples in a hot water bath at test temperature followed by instant clamping and testing on the machine. This method did not work because the samples cooled quickly and irregularly along their length thus leading to highly localized tensile strain in some portions of the specimen and no strain at all in other portions. Another major problem was slipping at the grips. Wedge grips were used initially, which failed to hold on to the sample during trials as the samples tended to become thinner with increasing tensile strain. Later, pneumatic grips were used, which managed to hold on to

the specimen with minor slipping at higher uniaxial tensile stress levels. Slipping could not be eliminated completely and can be seen as small bumps in the test result stress-strain plots.

5.2.2 Tensile Testing with Small Bars

Because of the problems associated with size restrictions of the environment chamber and the speed capability of the machine, tensile testing was decided to be done using the small rectangular bars of 3.2mm thickness which were a part of the molded samples. The width of the samples was 13mm and the length 20mm. To verify the validity of these tests performed with non-standard specimens a few tests were conducted at similar temperature and strain rate conditions for specimens of both types, i.e., standard sized tensile bars and the smaller rectangular bars. It could be observed that the Stress vs Strain curve for both type of specimens were almost overlaid on each other until the point when the test with the standard sized specimen had to be stopped. Refer to figure 5.1 for these results. So, it was safe to assume that tensile tests with different size specimens of PET yielded the same stress-strain characteristics for a given strain rate.

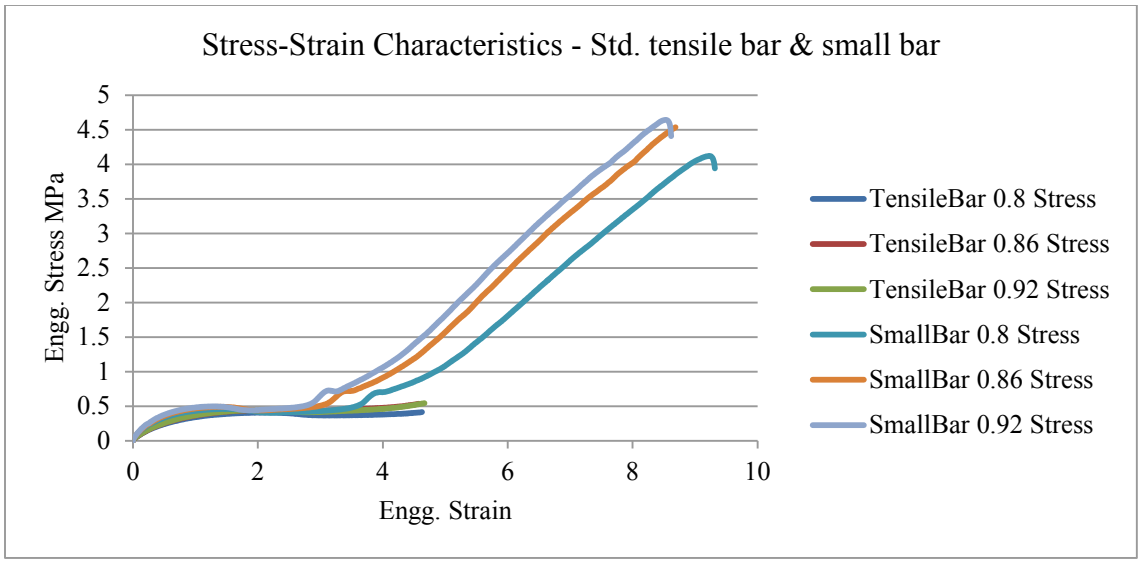

Figure 5.1 Std. Tensile bar vs Small bar - Stress Strain characteristics at 373K 0.1/s

Furthermore, Finite Element simulations were conducted using ABAQUS to verify the validity of using the small rectangular bars for the test. The simulation was conducted using a non-linear material Stress-Strain curve taken from compression experiments, fit to the Arruda-Boyce hyperelastic model in Abaqus and a Poissons ratio of 0.45. Contact interaction properties were also applied to study the effect of the grips of the machine on the specimen.

Tensile simulations yielded a fairly uniform tensile stress throughout the length of the specimen. Contact interactions at the ends were replaced by simple boundary conditions to allow the simulation to run to higher draw ratios. The resulting tensile stress profiles were also uniform. These results allowed the conclusion of tensile test results from the small rectangular bars to be valid. Figure 5.3 shows axial stresses upon gripping while

figure 5.4 shows the same at a small tensile strain. Figure 5.5 shows the axial strain at a higher tensile strain with the grips replaced by boundary conditions to aid convergence of the solution. It can be observed that the axial stress profile is uniform throughout the length of the specimen with a minor variation close to the grips.

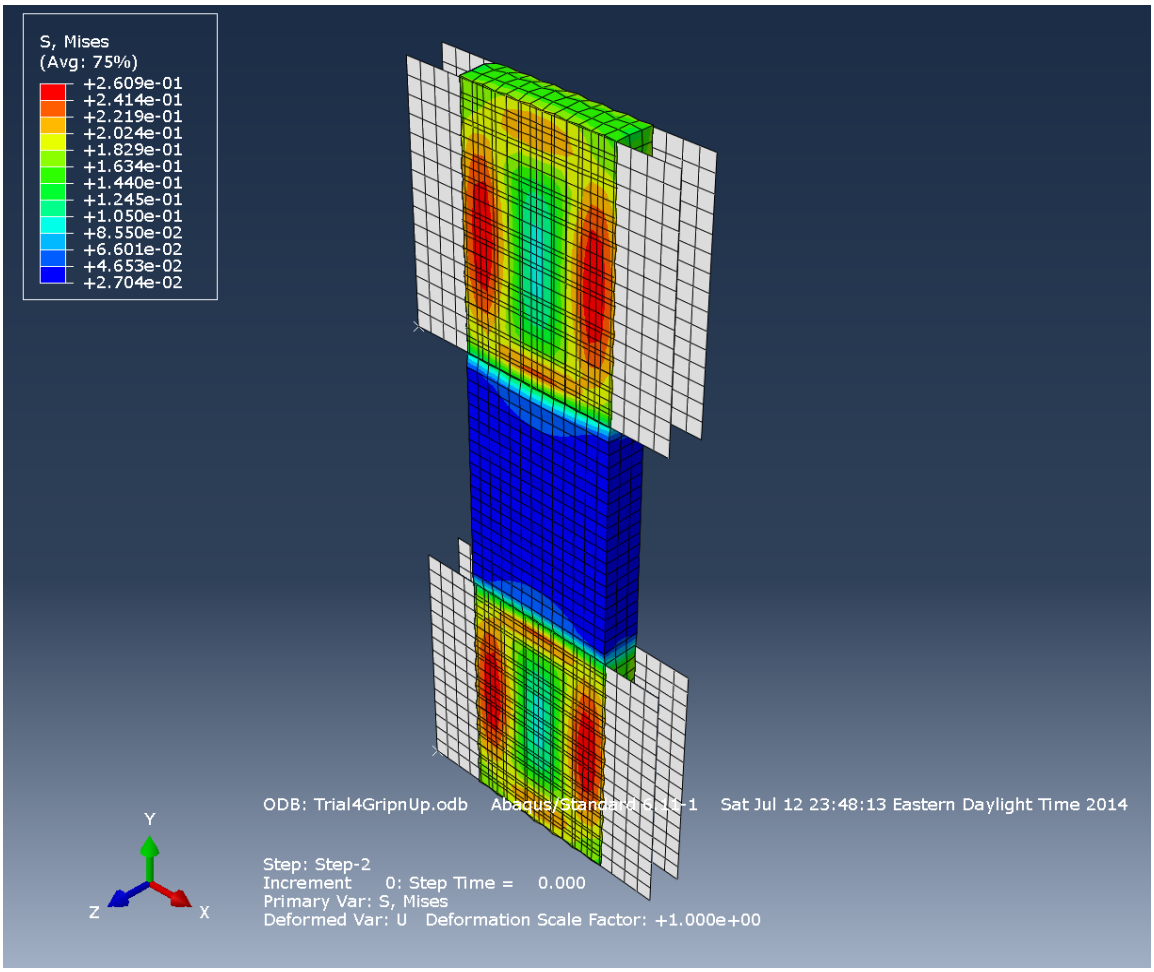

Figure 5.2 Finite element simulation of von-Mises stress upon gripping the small tensile bar

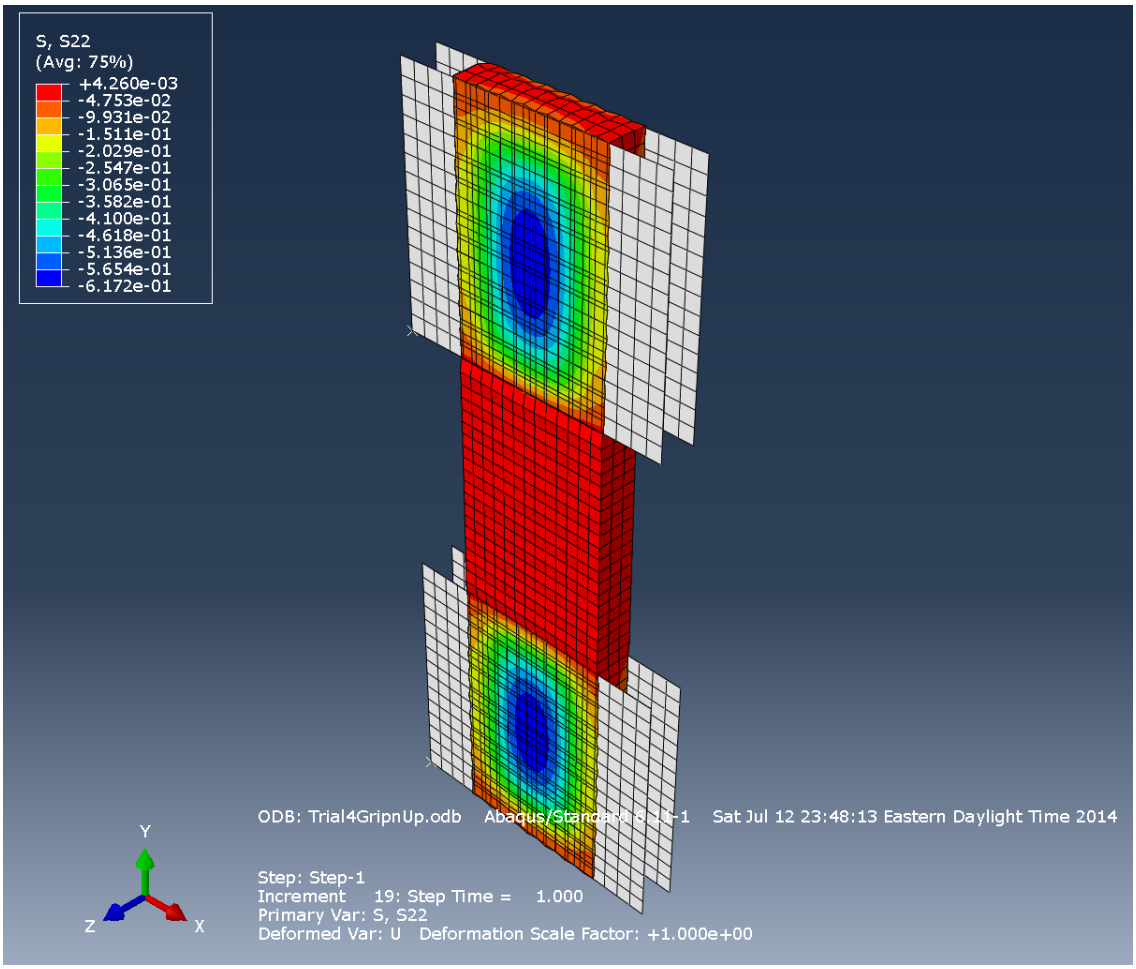

Figure 5.3 Stress in draw direction S22 upon gripping of the small tensile bar

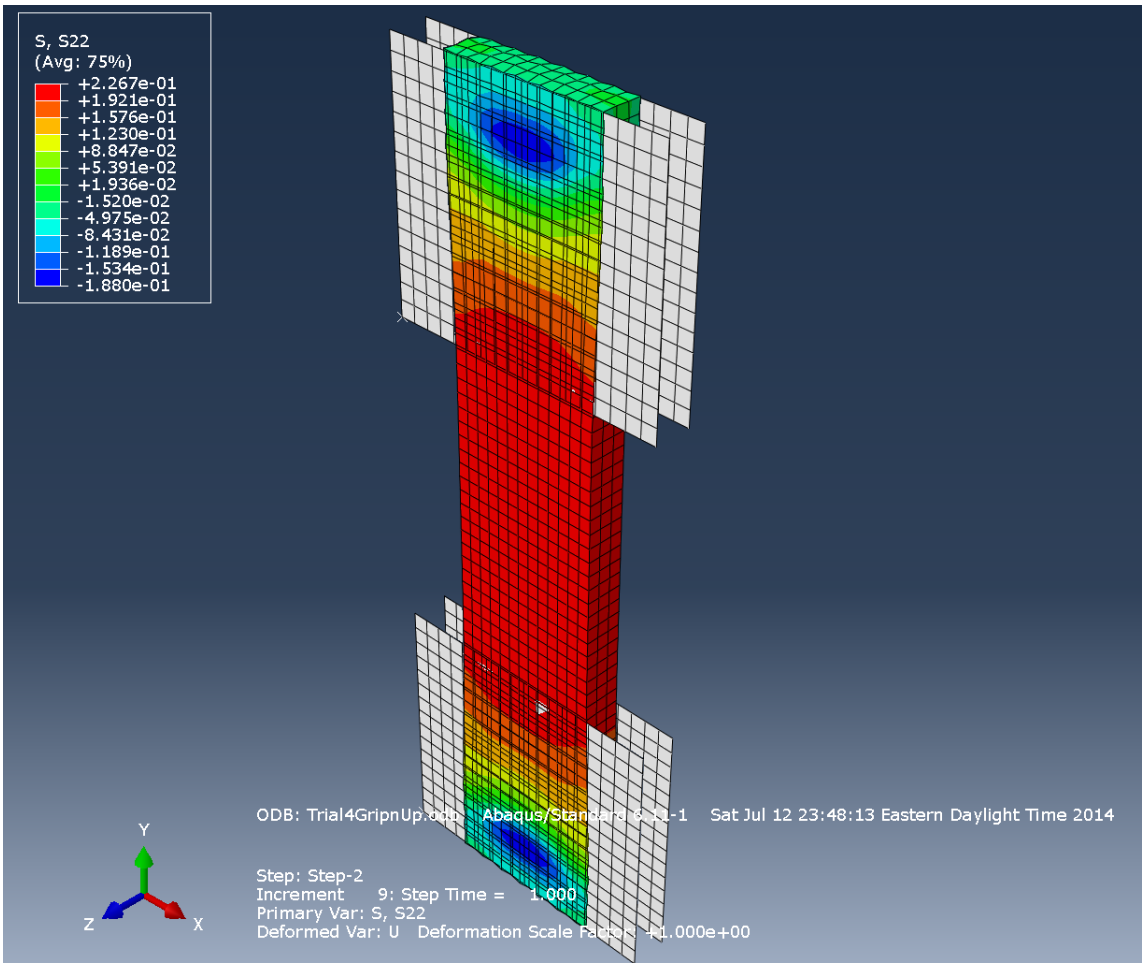

Figure 5.4 Stress S22 in draw direction at small tensile strain

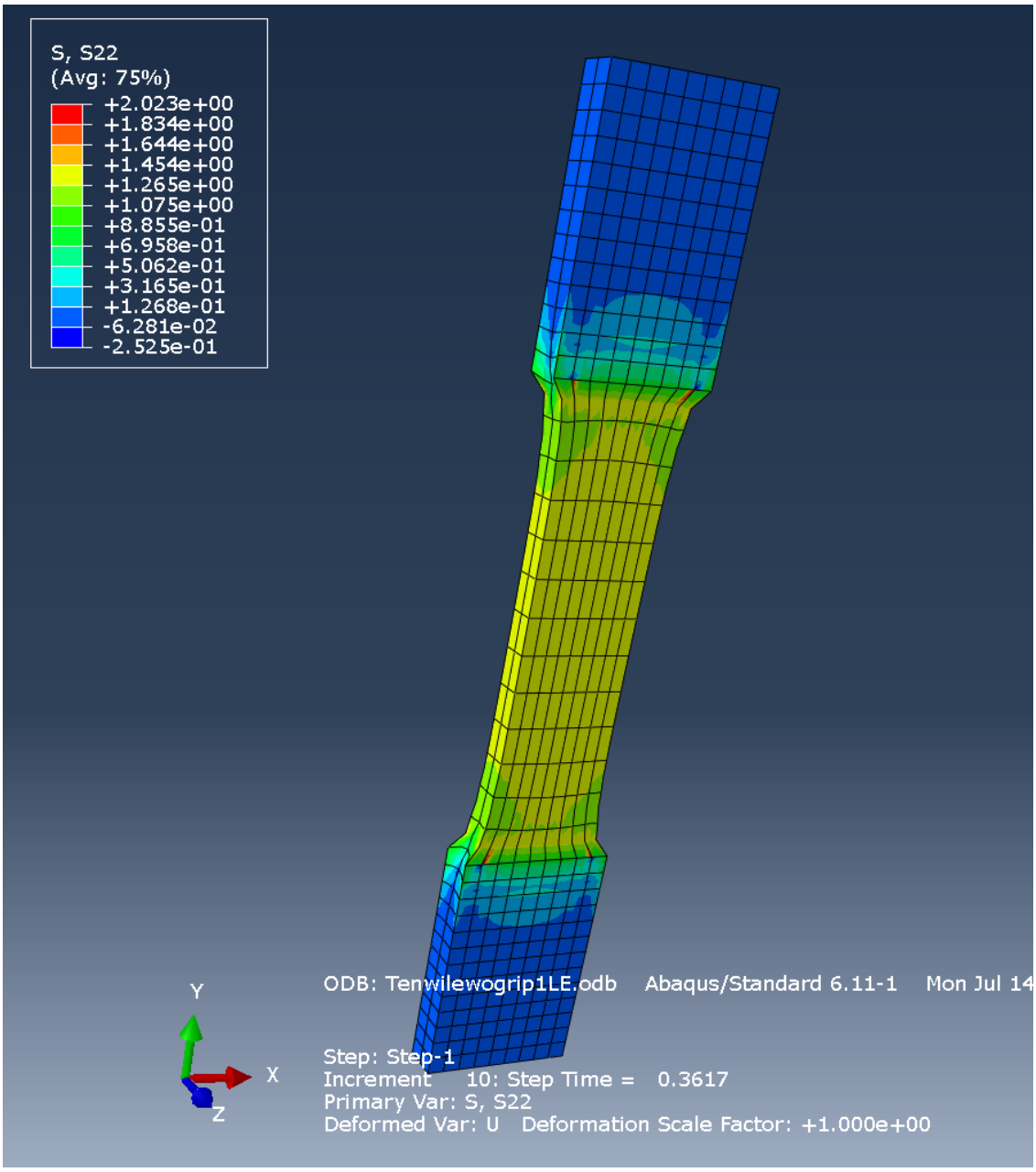

Figure 5.5 Stress in draw direction at higher tensile strains after replacement of grip model with suitable boundary conditions

5.2.3 Tensile Testing Procedure

The environmental chamber was equilibrated at testing temperature for one hour as done for the compression tests. Post equilibration, the tensile specimen was loaded in to the chamber and gripped at the bottom using the lower pneumatic grip. The specimen was then allowed to equilibrate in the chamber to allow it to attain the uniform test temperature. After this, the upper grips were lowered onto the specimen and gripped so that the distance between the grips was equal to the gauge length so that the portion of the specimen between the upper and lower grips were subject to tension during the course of the experiment.

For the tension tests, though the assumption that the specimen volume was constant as done for the compression tests holds good, slipping at the grips would prevent accurate computation of cross section area and hence true stress. Also, true strain rate had to be increased as draw ratio increased, which would exceed the maximum speed capability of the head of the machine at 8.5 mm/s (This has been discussed in Chapter 2 on compression tests). Hence, tension tests were conducted at a constant engineering strain rate as opposed to constant true strain rate which was used for the compression tests. Hence, unlike compression tests where the machine had to be programmed using the Profiler module, tensile testing only required the input of a constant displacement rate into the machine control software, Instron Bluehill. Also, all the simulations of the

Dupaix-Boyce model in tension have been performed using constant engineering strain rates.

5.3 Tensile Test Results

5.3.1 Temperature Dependence of Stress-Strain Characteristics

Figures 5.6 to 5.14 show the temperature dependence of the Engineering Stress vs Engineering Strain results obtained from the rectangular bars. Each figure shows different curves obtained by varying the temperature from 363K to 378K in steps of 5K at constant strain rate and IV. At all conditions, curves from 363K and 368 K show significant strain hardening once the engineering strain exceeds a particular value. It may be observed that this value is temperature and strain rate dependent. There is a drastic reduction in strain hardening as temperature further increases and becomes very small or is almost absent at 378K. The legend in these plots are of the form' Strain-rate(/s) Temperature(K) IV'.

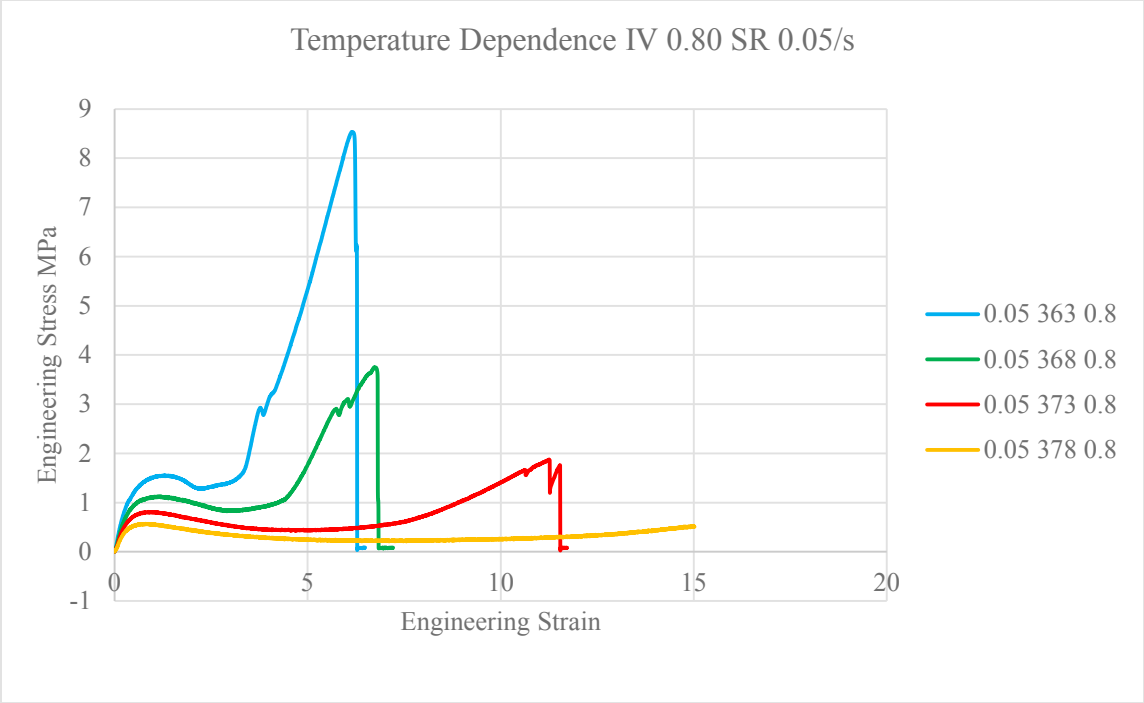

Figure 5.6 Temperature dependence of tension test results - IV 0.80 SR 0.05/s

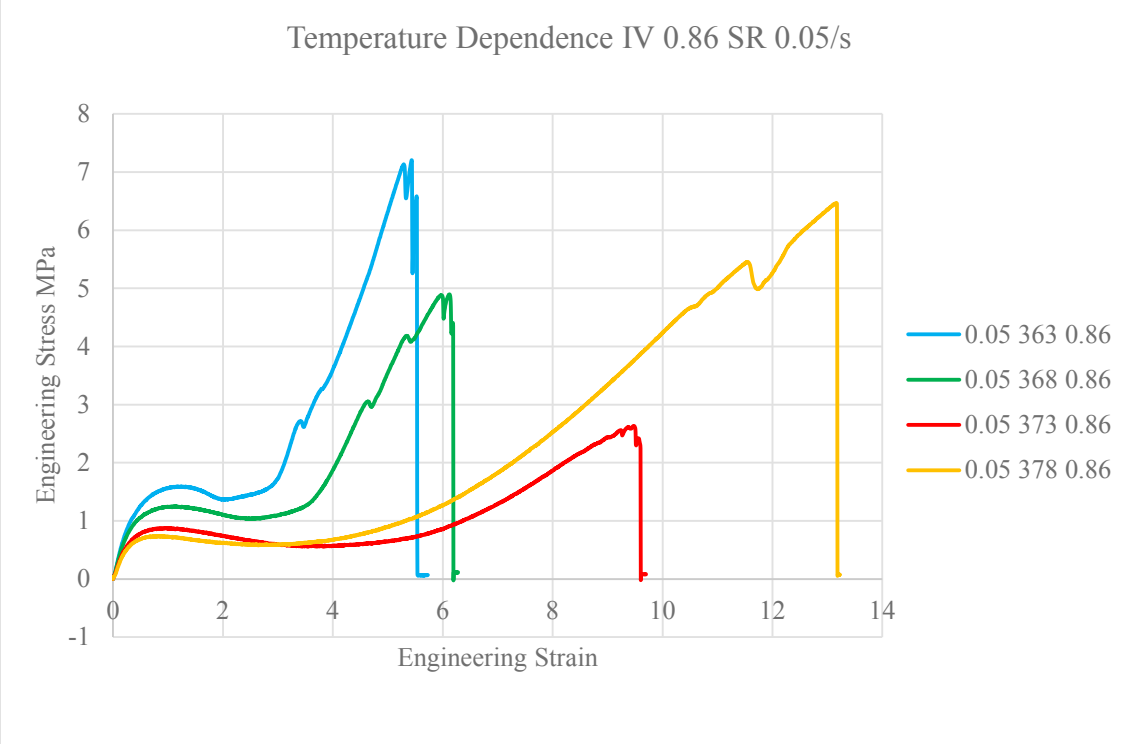

Figure 5.7 Temperature dependence of tension test results - IV 0.86 SR 0.05/s

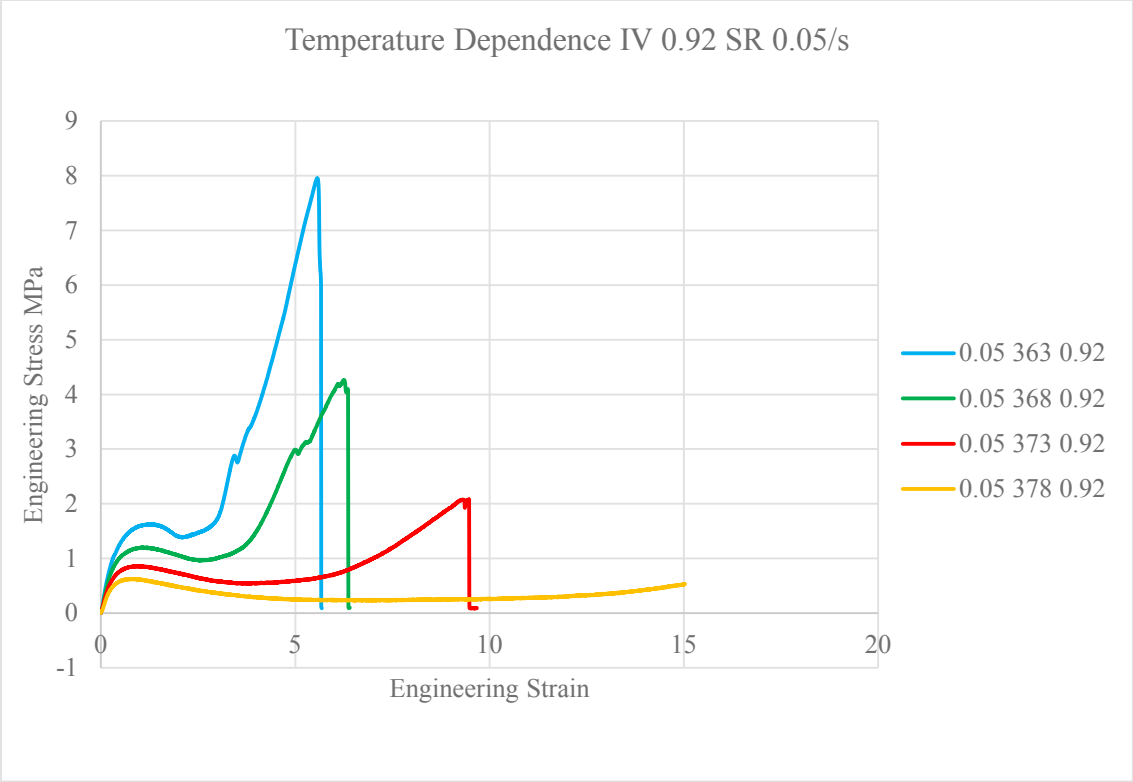

Figure 5.8 Temperature dependence of tension test results - IV 0.92 SR 0.05/s

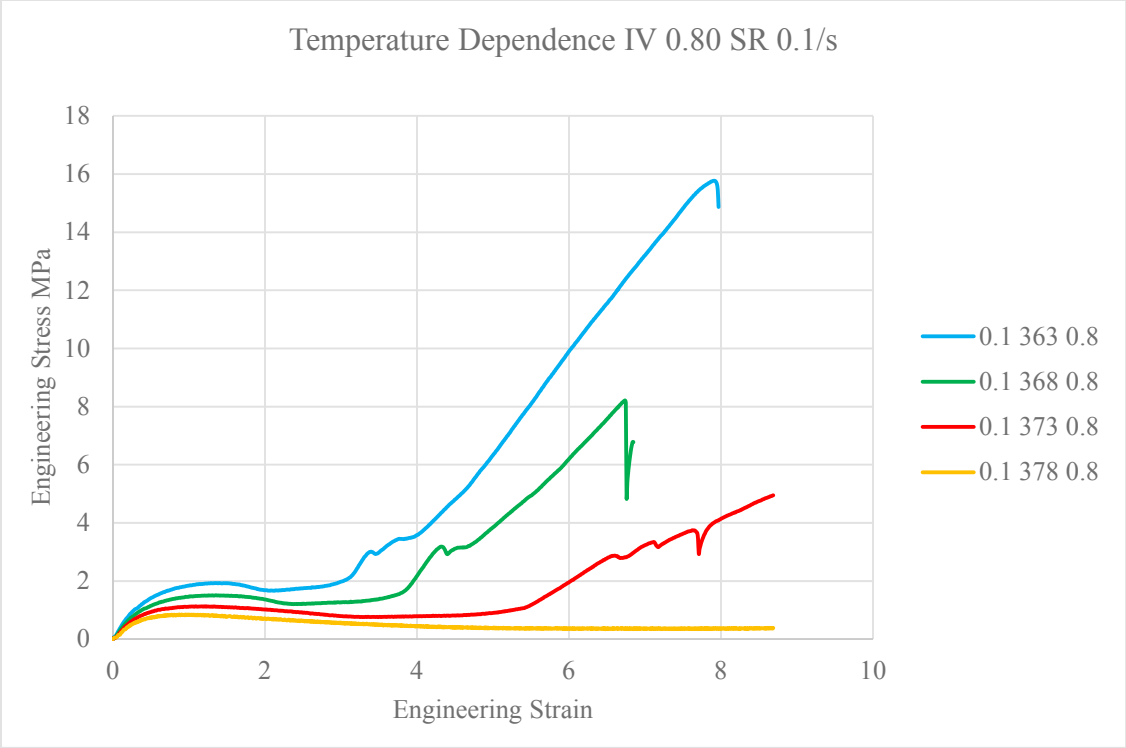

Figure 5.9 Temperature dependence of tension test results - IV 0.80 SR 0.1/s

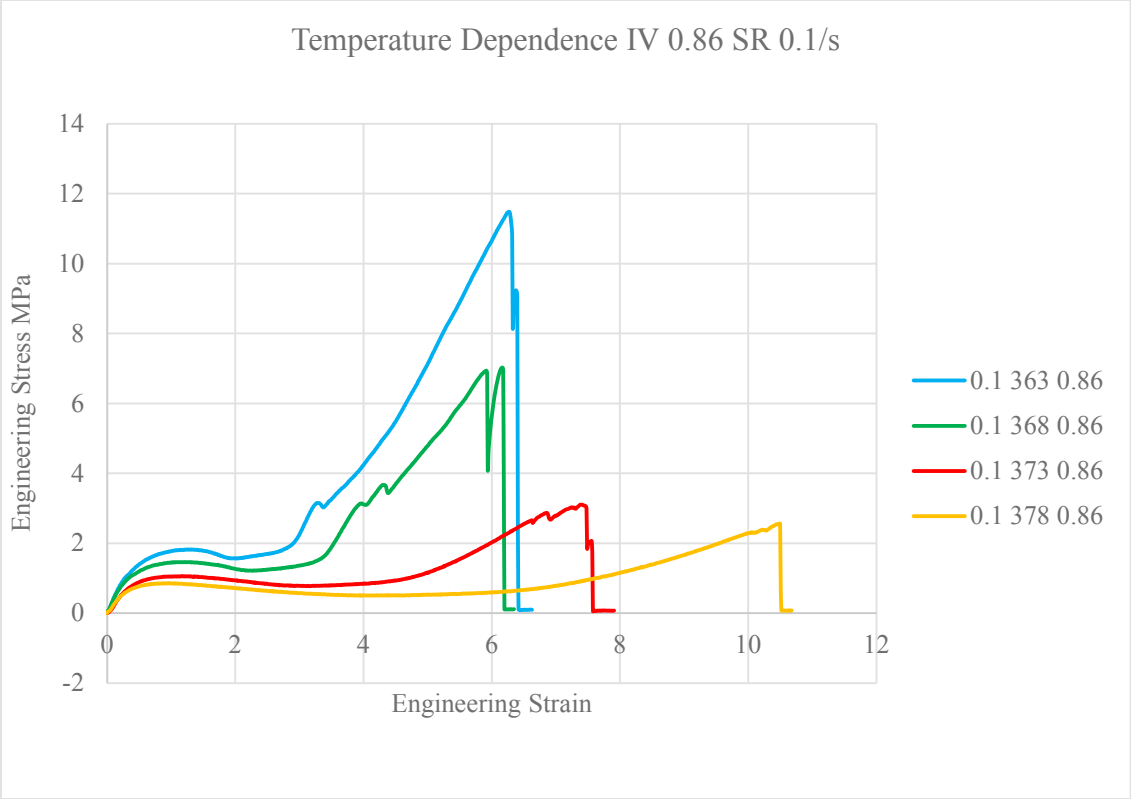

Figure 5.10 Temperature dependence of tension test results - IV 0.86 SR 0.1/s

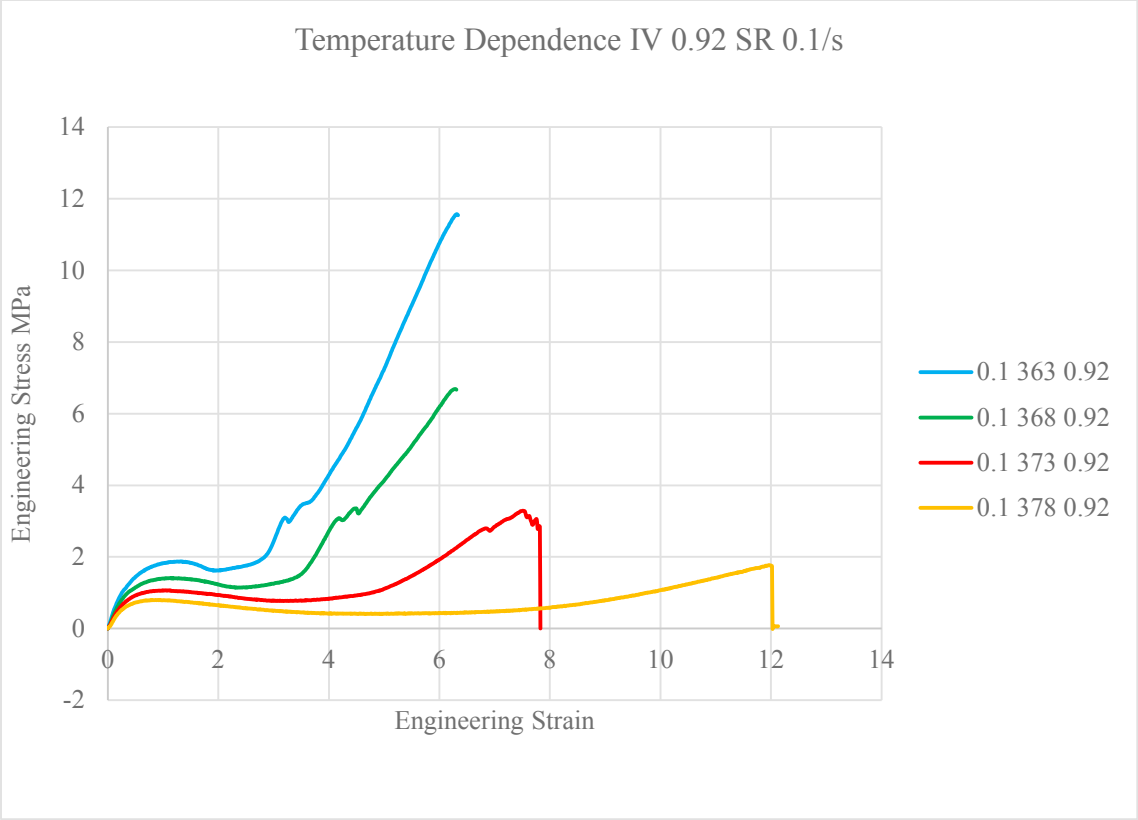

Figure 5.11 Temperature dependence of tension test results - IV 0.92 SR 0.1/s

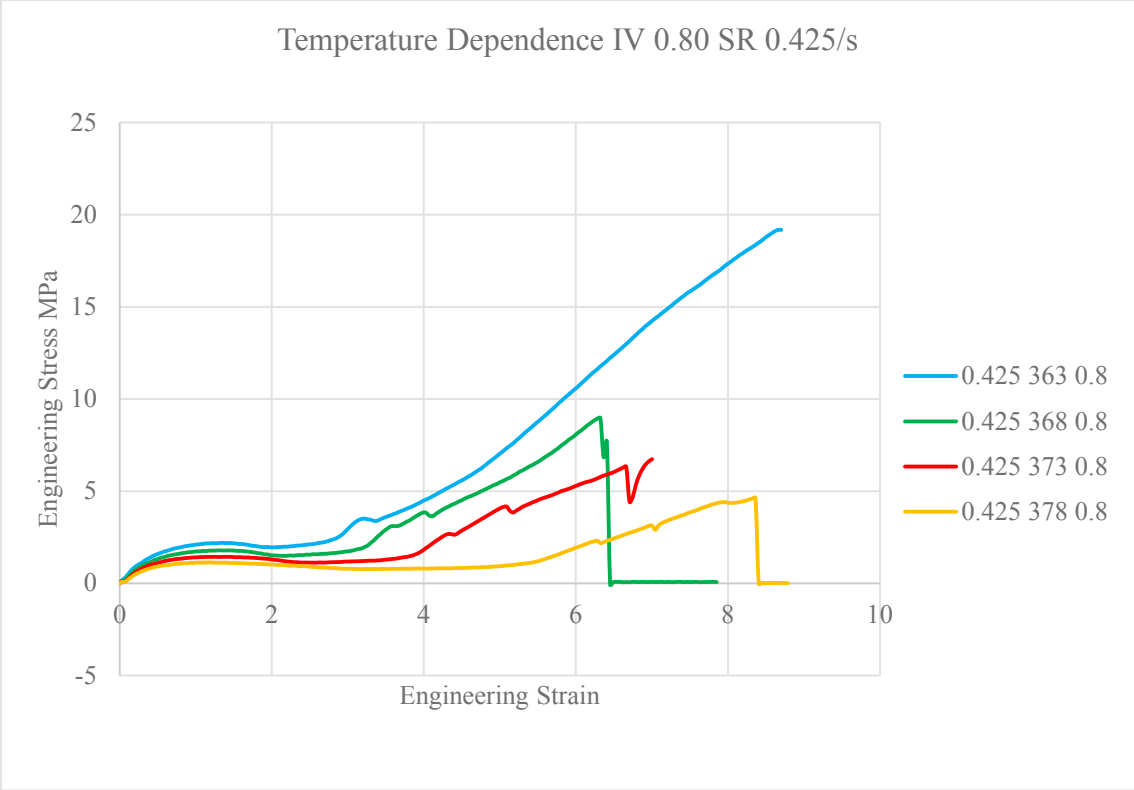

Figure 5.12 Temperature dependence of tension test results - IV 0.80 SR 0.425/s

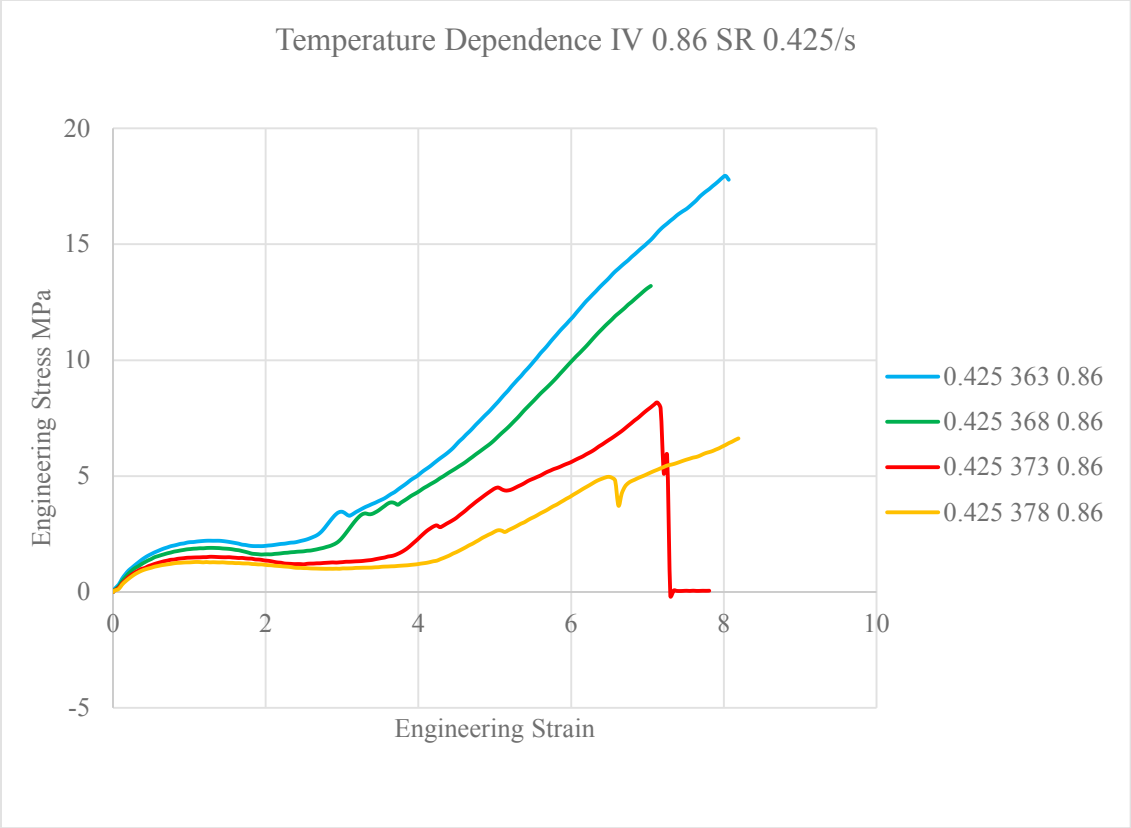

Figure 5.13 Temperature dependence of tension test results - IV 0.86 SR 0.425/s

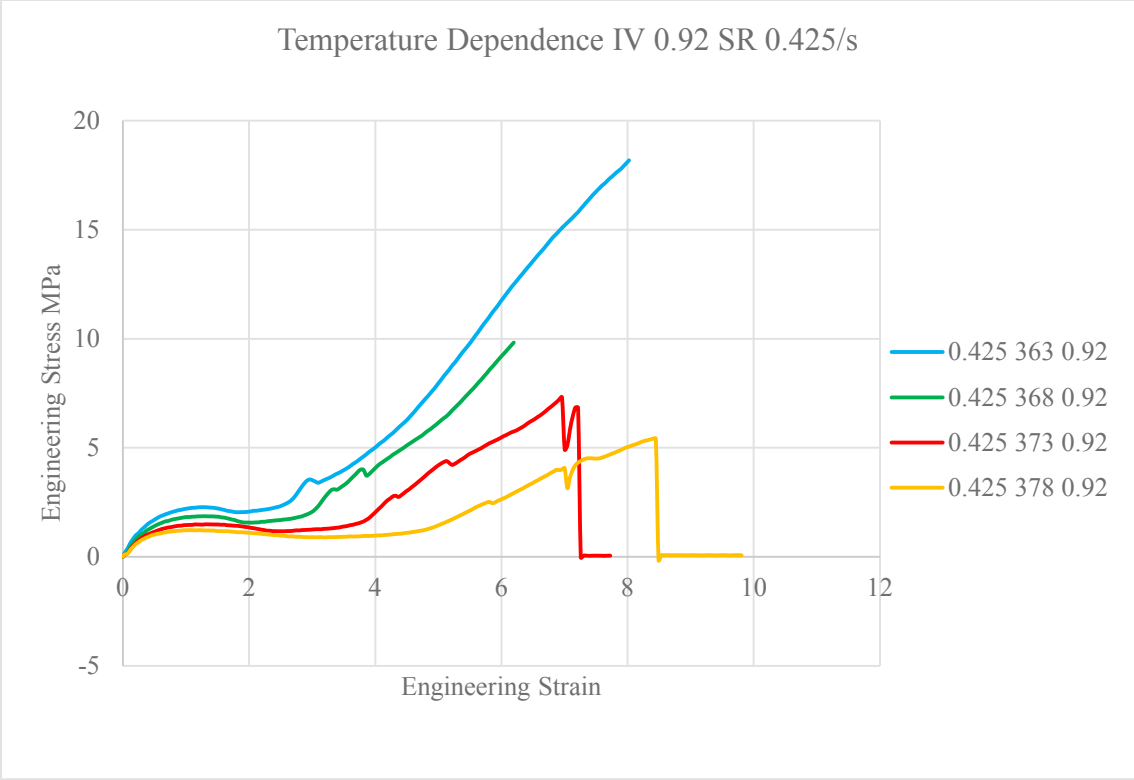

Figure 5.14 Temperature dependence of tension test results - IV 0.92 SR 0.425/s

5.3.2 Strain Rate Dependence of Stress-Strain Characteristics

Figures 5.15 to 5.26 show the engineering strain rate dependence of the Engineering Stress vs Engineering Strain results obtained from the rectangular bars. Each figure shows different curves obtained at three different strain rates at 0.05/s, 0.1/s and 0.425/s, with 0.425/s being the maximum limit of the machine at conditions of constant temperature and IV. Visco-elastic behavior of PET shows up here with stiffer properties being shown at higher strain-rate at constant conditions of temperature and IV.

It must be noted that the difference between the curves are small at 363K and 368K with increase in strain rate. However, as the temperature increases, the point where the dramatic strain hardening (hardening onset strain) is initiated becomes highly dependent on strain rate and temperature. At higher strain rates, the hardening onset strain occurs much earlier than at lower strain rates. This strain rate dependence becomes more significant at higher temperatures. Hence, at higher temperatures, the curves are much wider apart, with higher strain rate curves being much stiffer than the lower ones. This is apparent from figures 5.21 to 5.26.

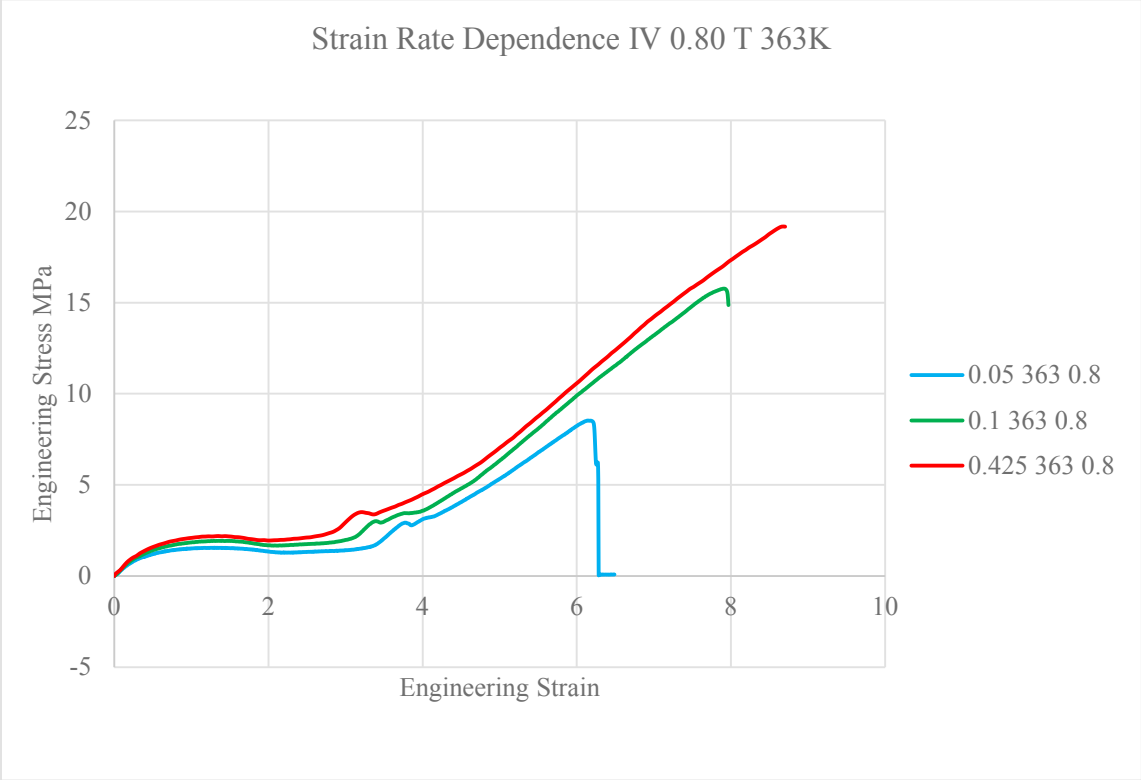

Figure 5.15 Strain Rate dependence of tension test results - IV 0.80 T 363K

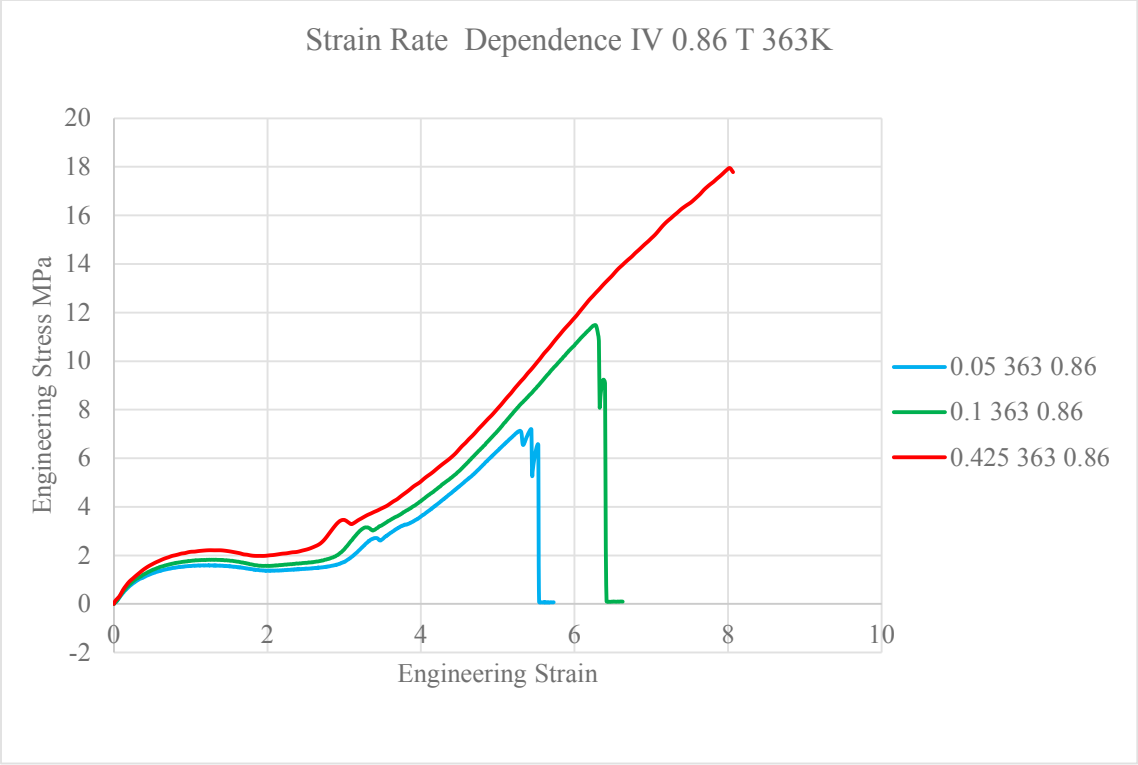

Figure 5.16 Strain Rate dependence of tension test results - IV 0.86 T 363K

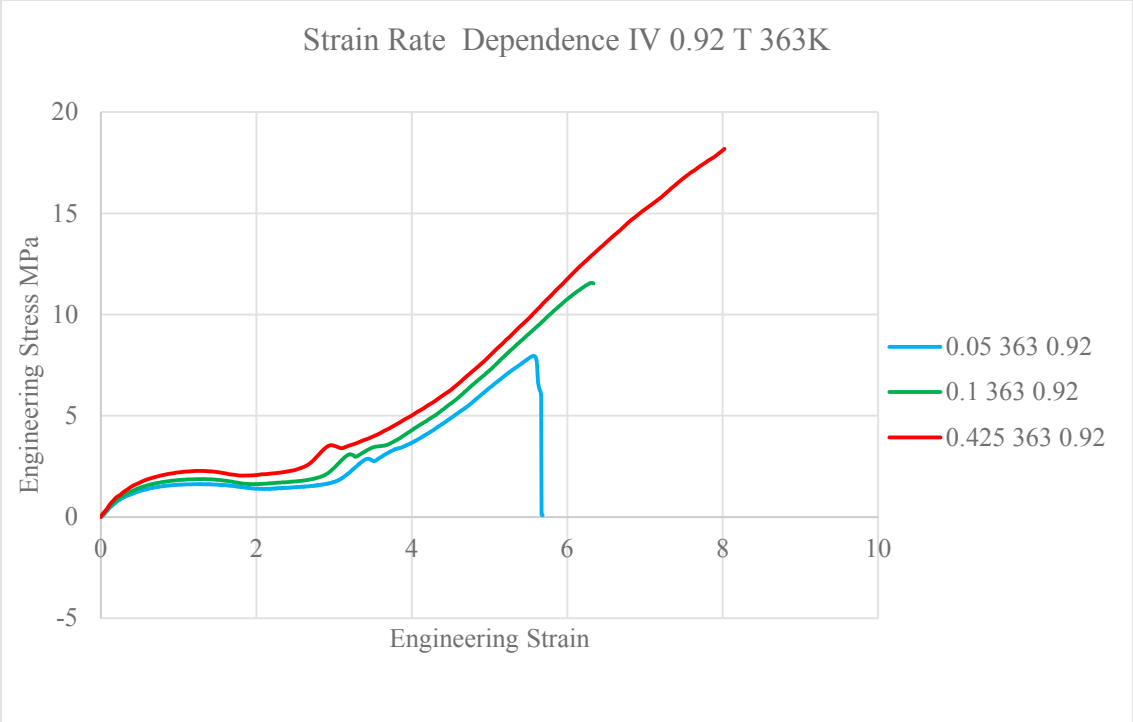

Figure 5.17 Strain Rate dependence of tension test results - IV 0.92 T 363K

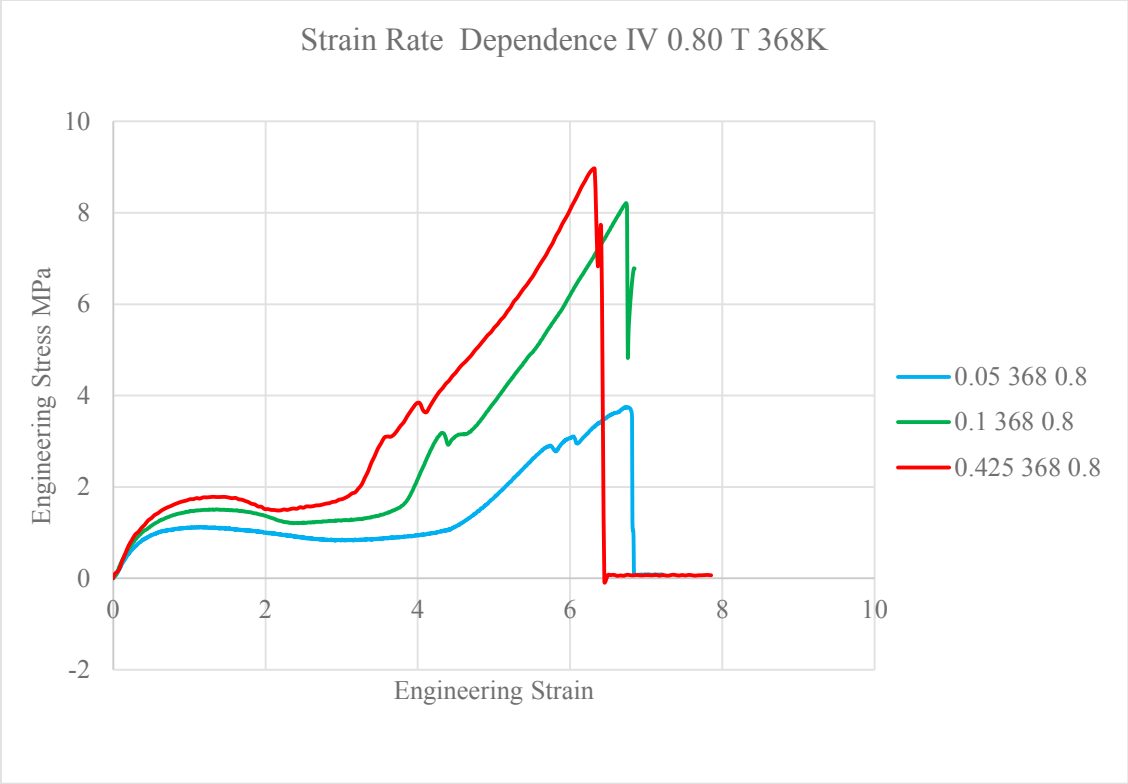

Figure 5.18 Strain Rate dependence of tension test results - IV 0.80 T 368K

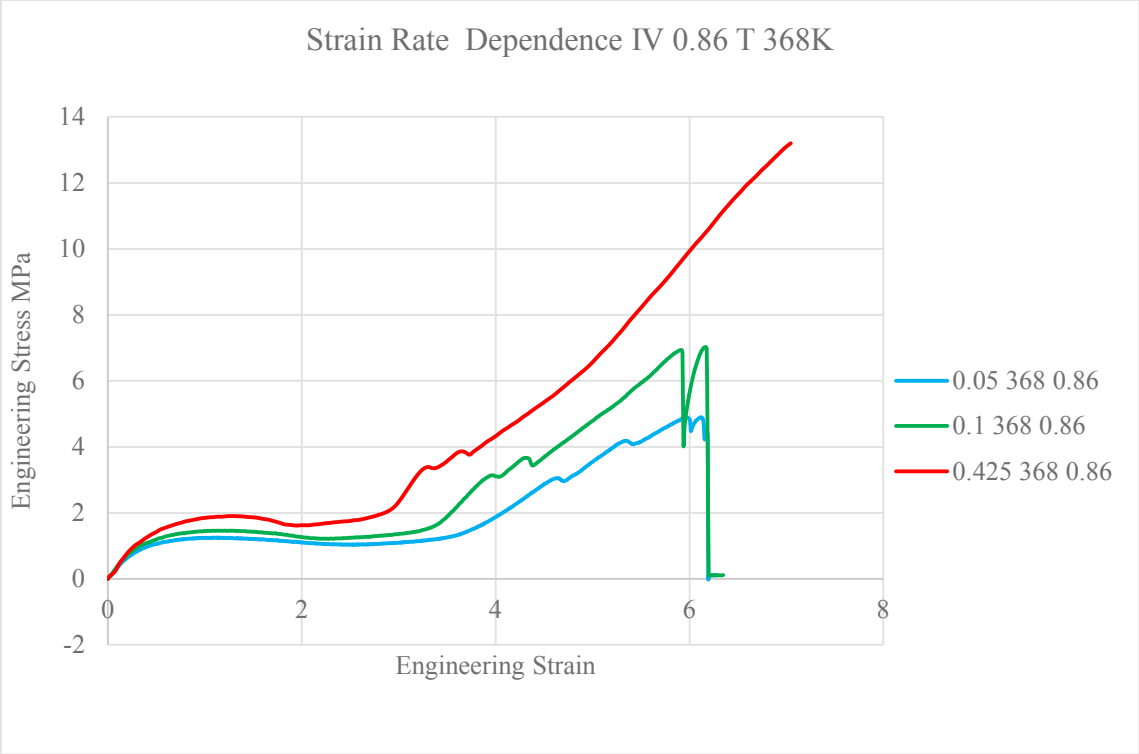

Figure 5.19 Strain Rate dependence of tension test results - IV 0.86 T 368K

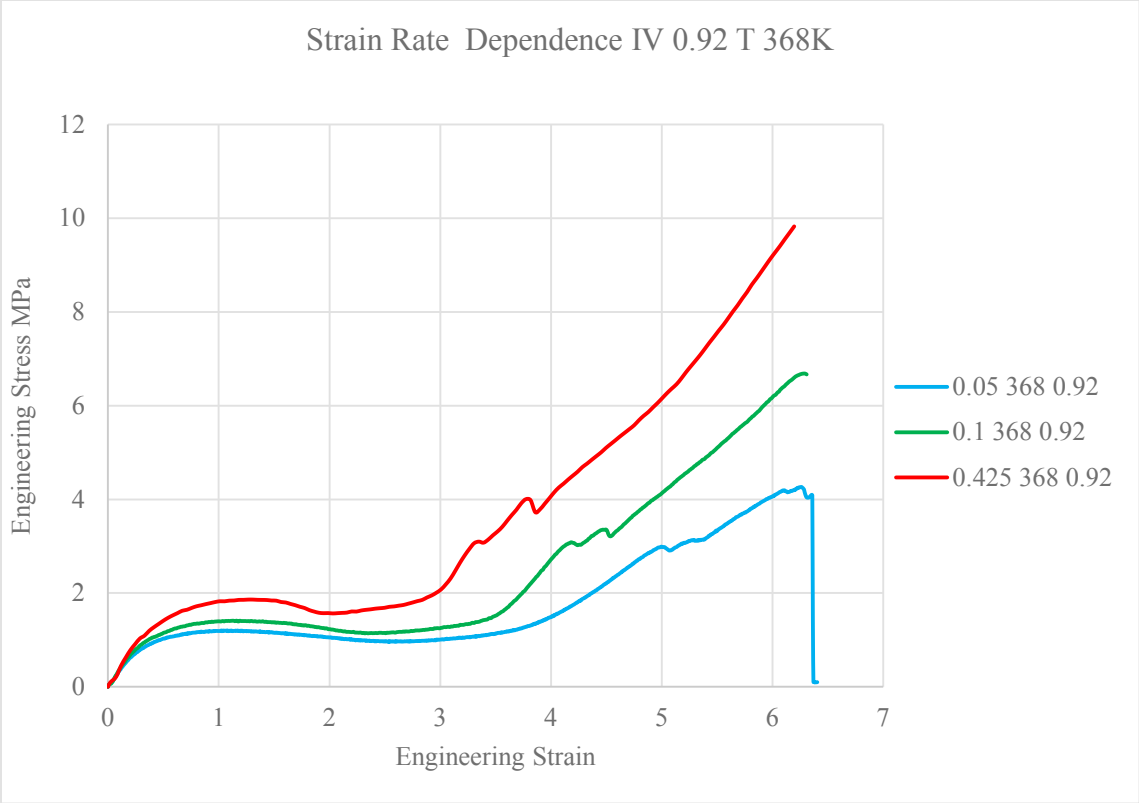

Figure 5.20 Strain Rate dependence of tension test results - IV 0.92 T 368K

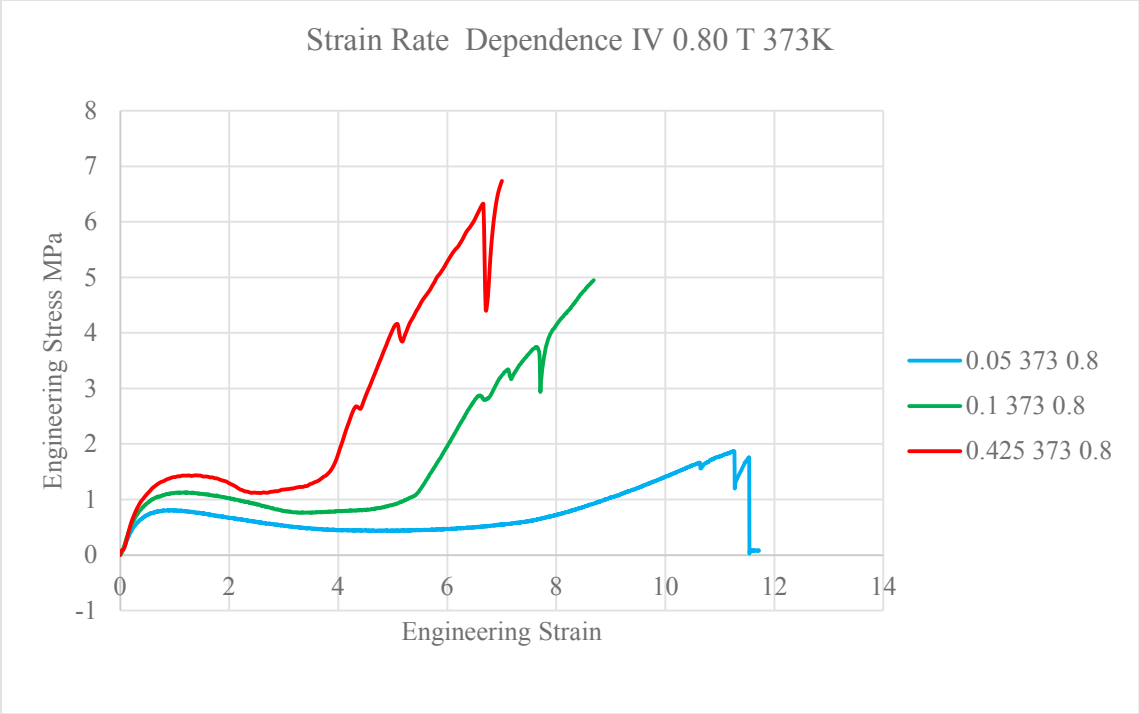

Figure 5.21 Strain Rate dependence of tension test results - IV 0.80 T 373K

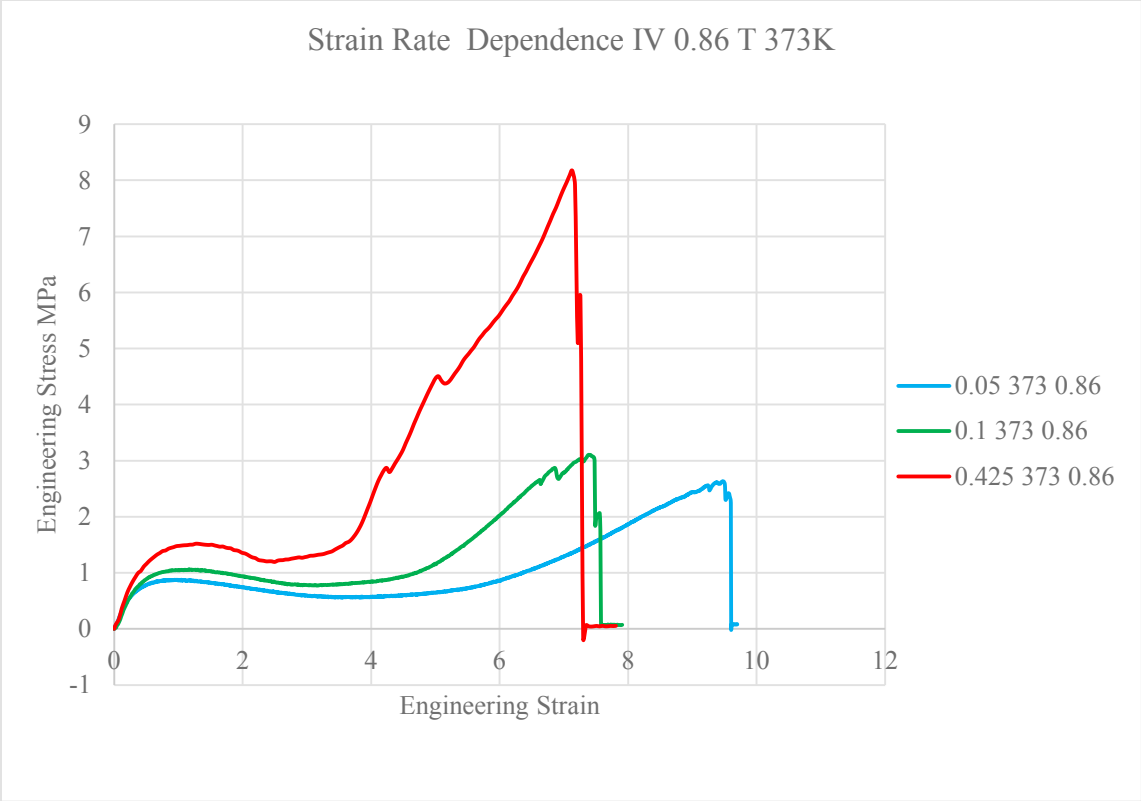

Figure 5.22 Strain Rate dependence of tension test results - IV 0.86 T 373K

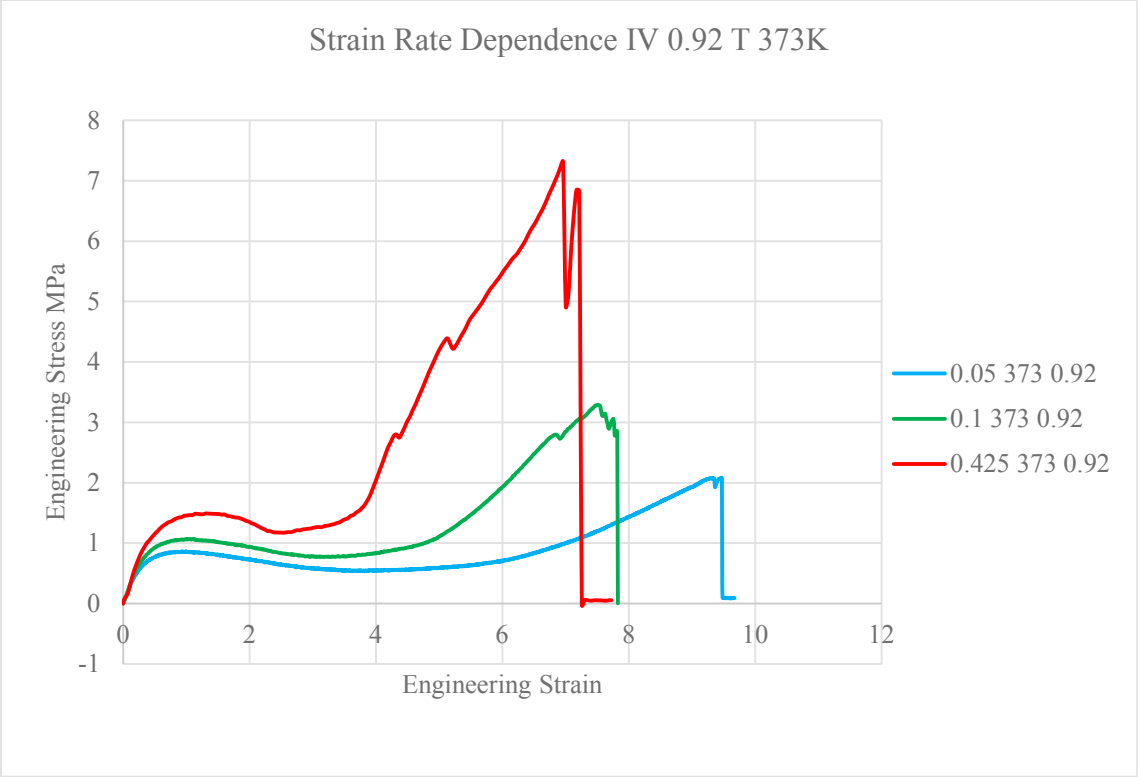

Figure 5.23 Strain Rate dependence of tension test results - IV 0.92 T 373K

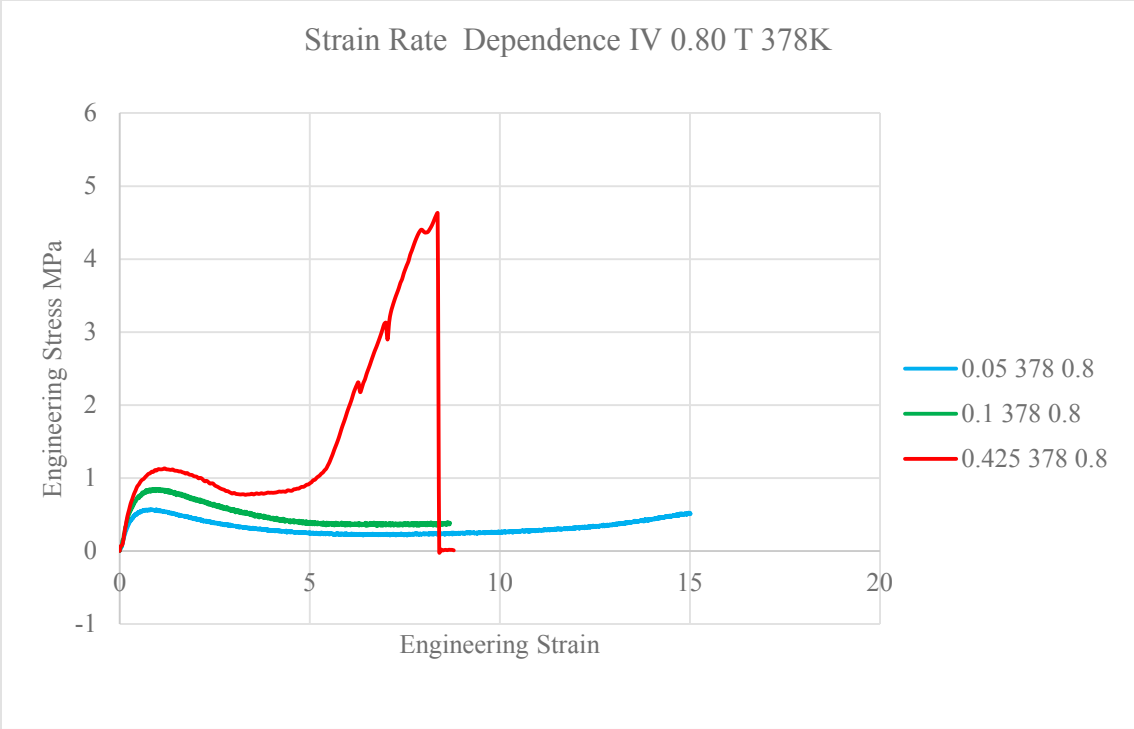

Figure 5.24 Strain Rate dependence of tension test results - IV 0.80 T 378K

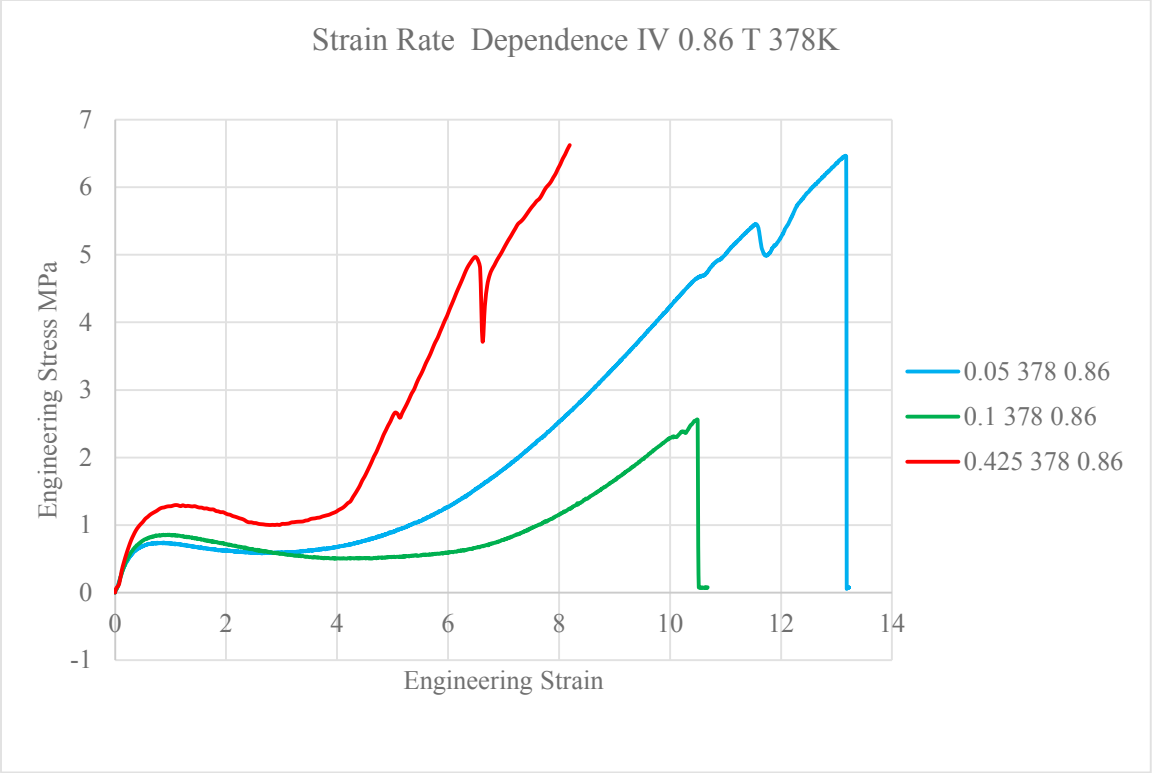

Figure 5.25 Strain Rate dependence of tension test results - IV 0.86 T 378K

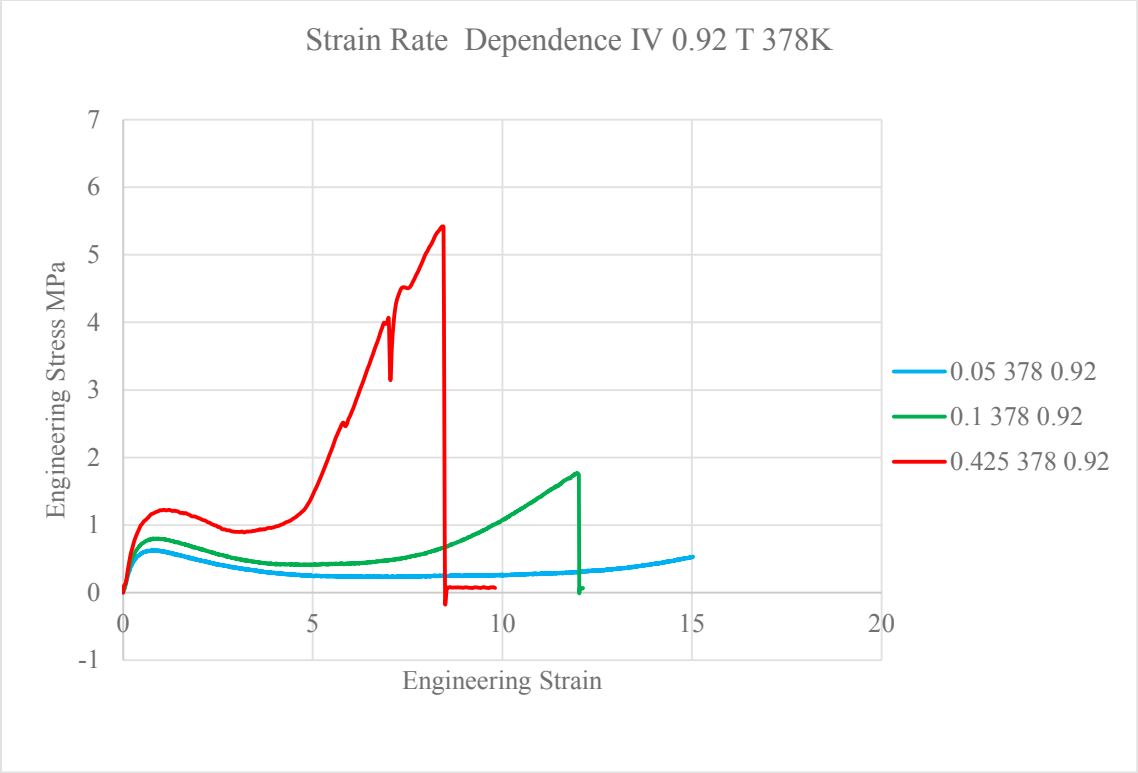

Figure 5.26 Strain Rate dependence of tension test results - IV 0.92 T 378K

5.3.3 IV Dependence of Stress-Strain Characteristics

Figures 5.27 to 5.38 show IV dependence of the experimental uniaxial tensile stress-strain curves. Though it is known that an increase in IV causes an increase in stiffness, in the obtained results, IVs 0.86 and 0.92 show very similar characteristics and are stiffer than IV 0.80. As temperatures increase, IV 0.86 shows slightly stiffer properties than IV 0.92, and this may be attributed to molding parameters. However, as an overall observation, it may be inferred that no significant IV dependence could be shown on the basis of these results.

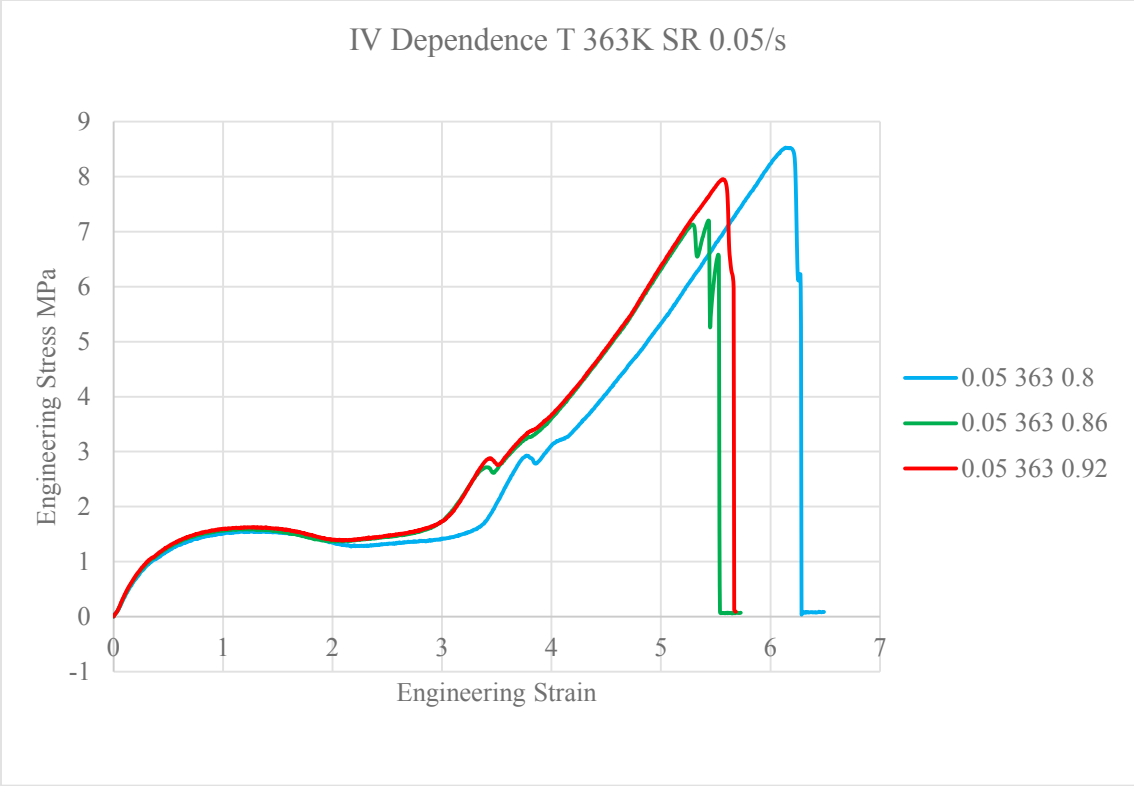

Figure 5.27 IV dependence of tension test results - T 363K SR 0.05/s

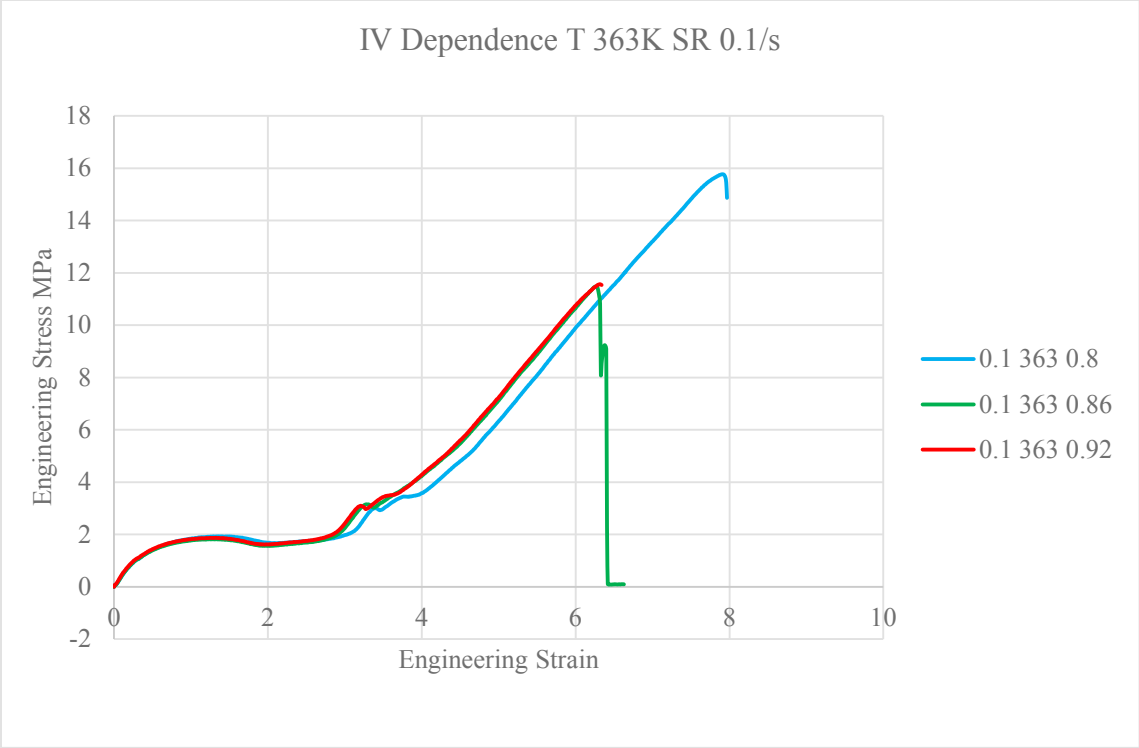

Figure 5.28 IV dependence of tension test results - T 363K SR 0.1/s

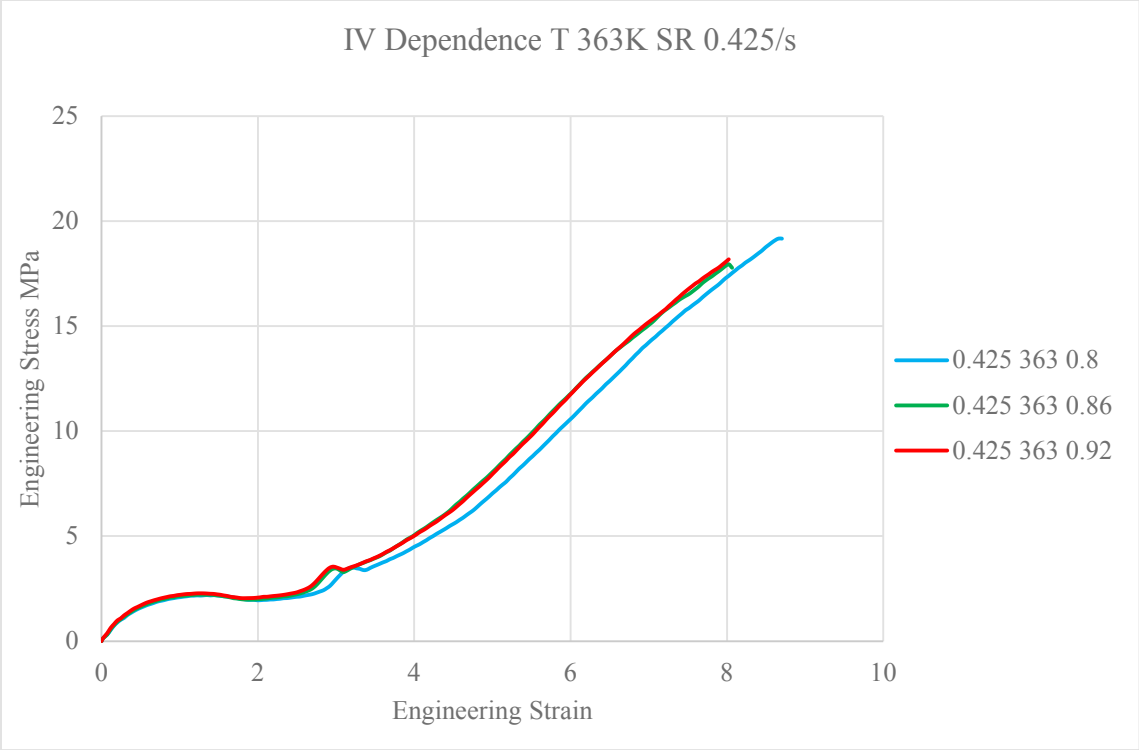

Figure 5.29 IV dependence of tension test results - T 363K SR 0.425/s

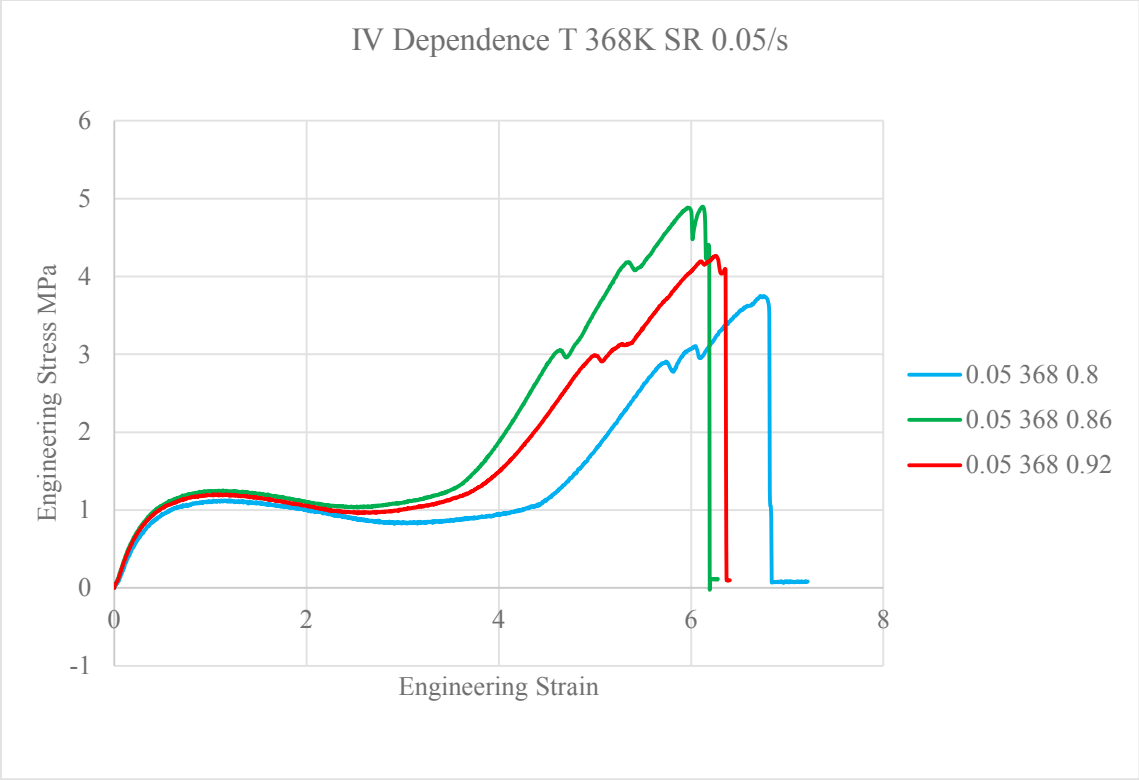

Figure 5.30 IV dependence of tension test results - T 368K SR 0.05/s

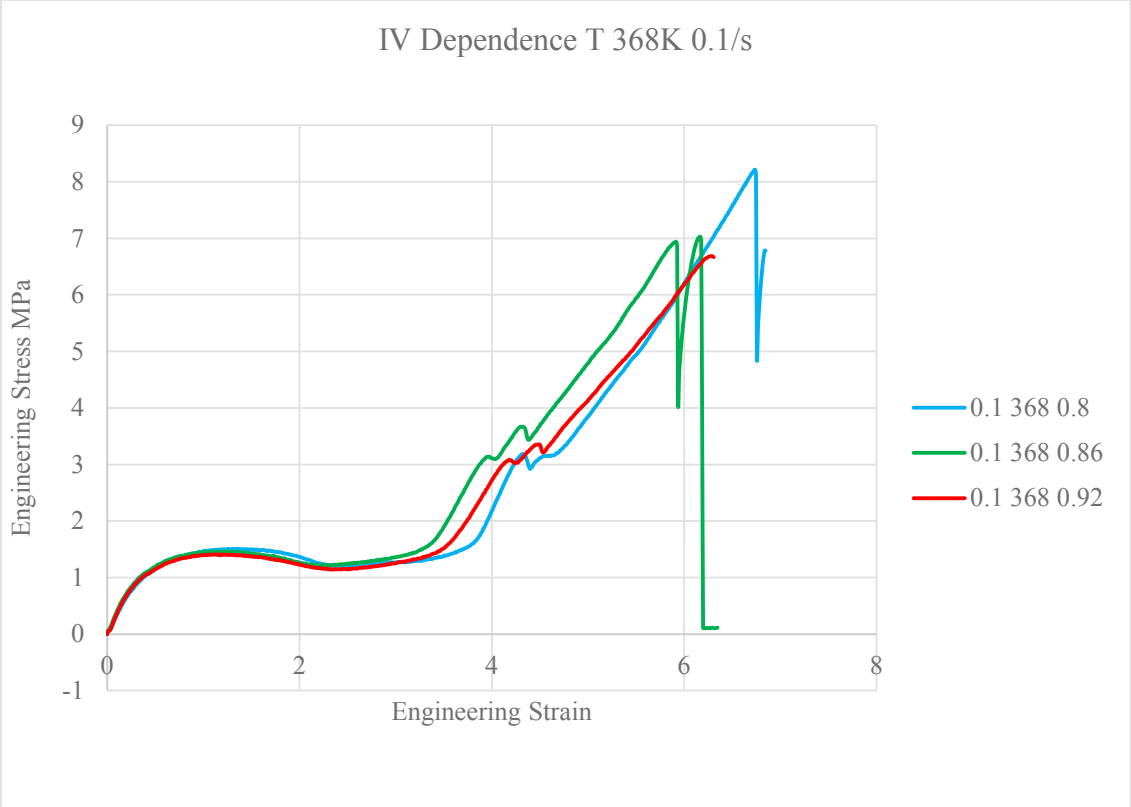

Figure 5.31 IV dependence of tension test results - T 368K SR 0.1/s

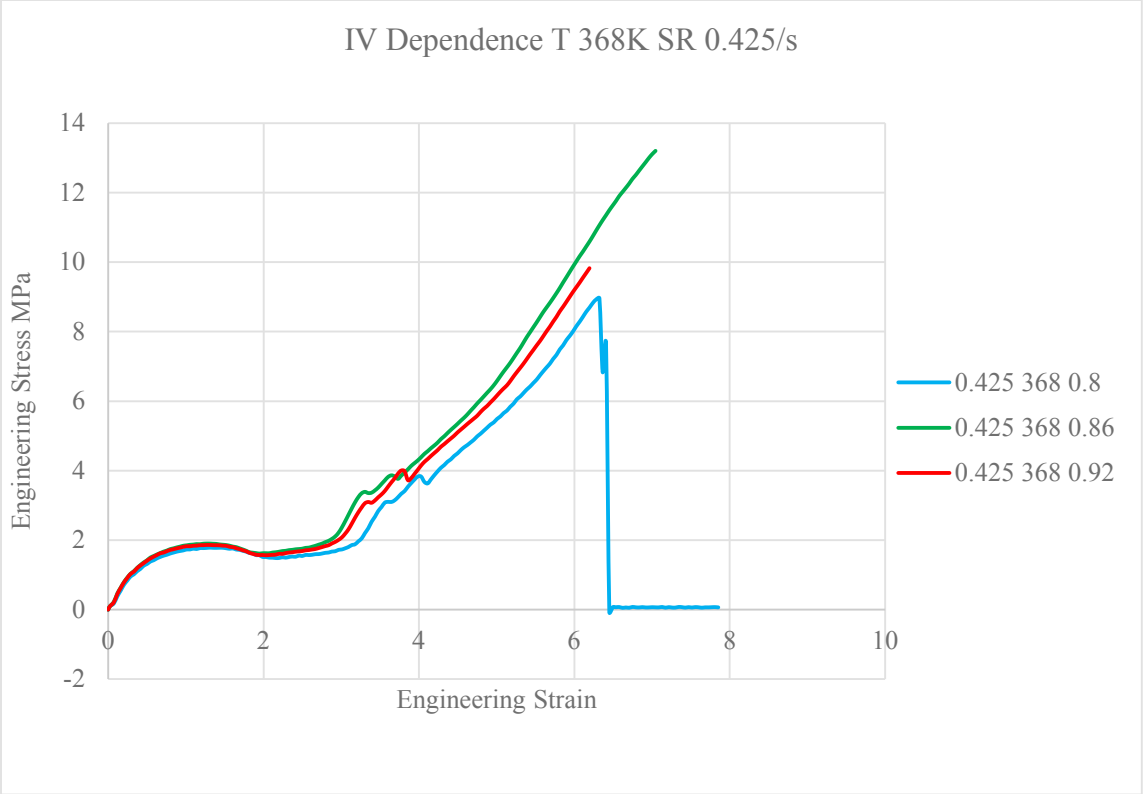

Figure 5.32 IV dependence of tension test results - T 368K SR 0.425/s

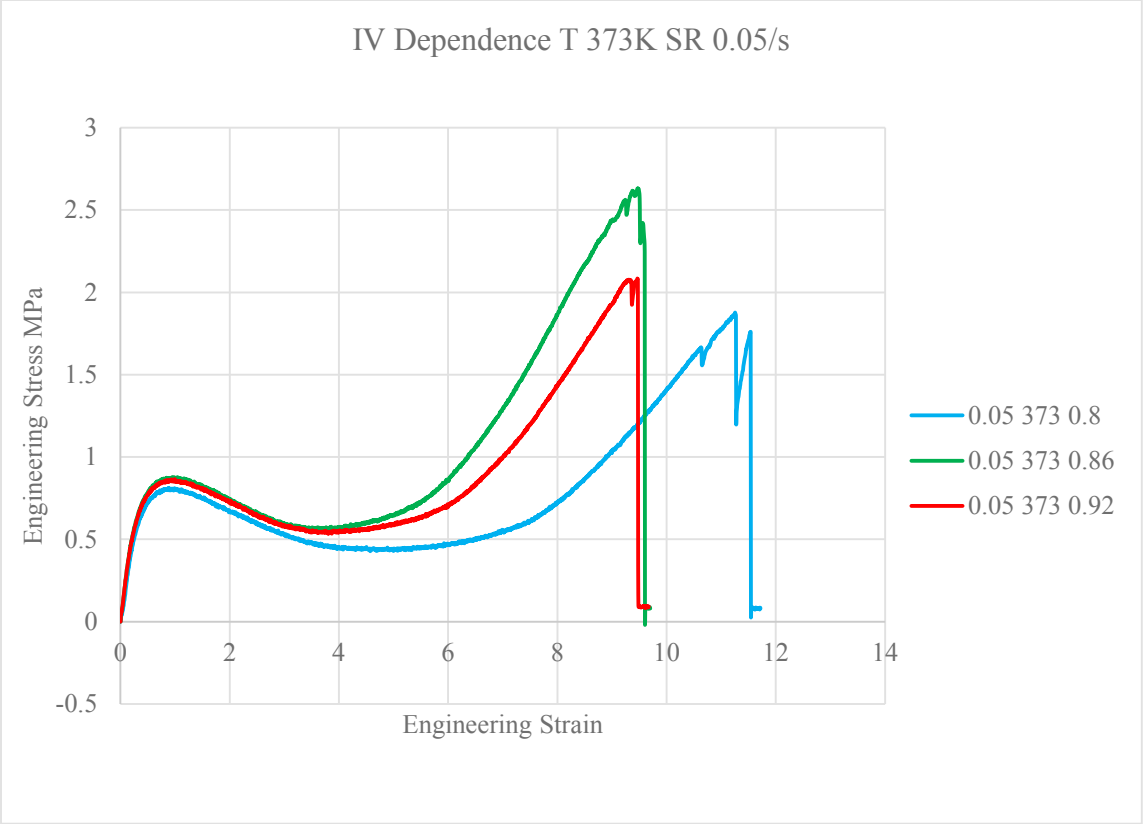

Figure 5.33 IV dependence of tension test results - T 373K SR 0.05/s

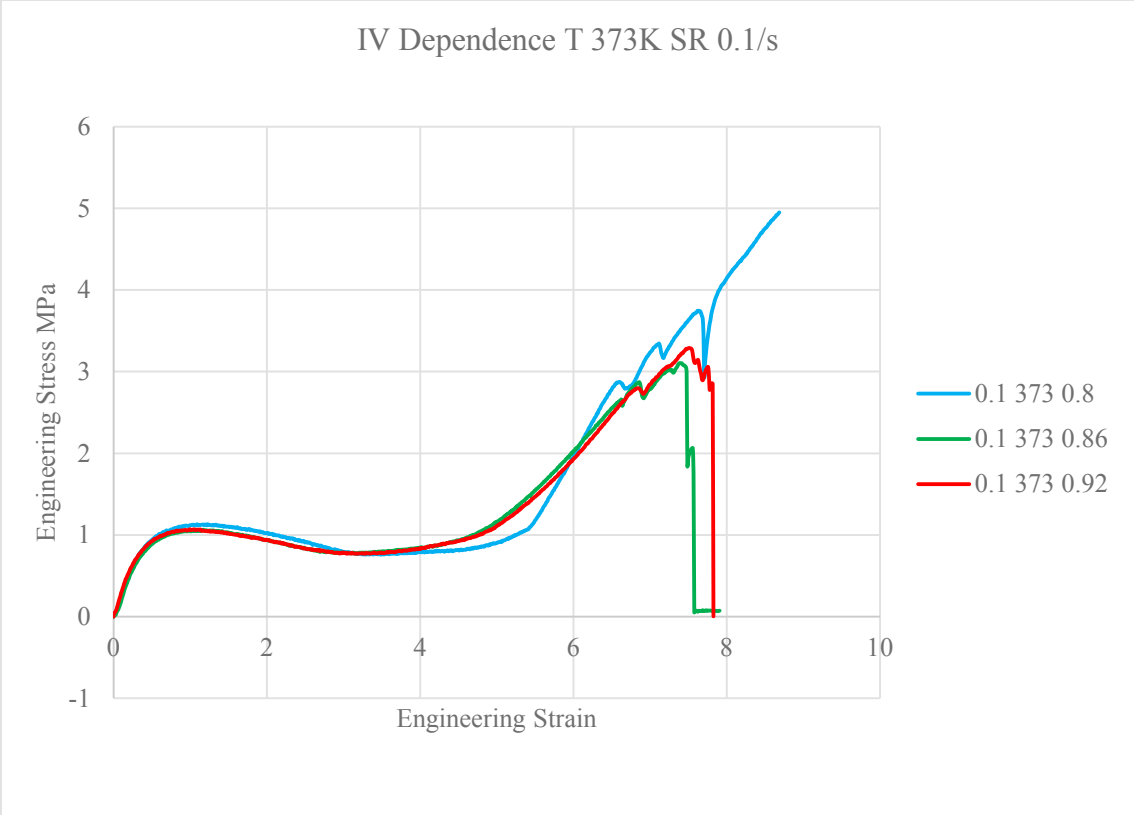

Figure 5.34 IV dependence of tension test results - T 373K SR 0.1/s

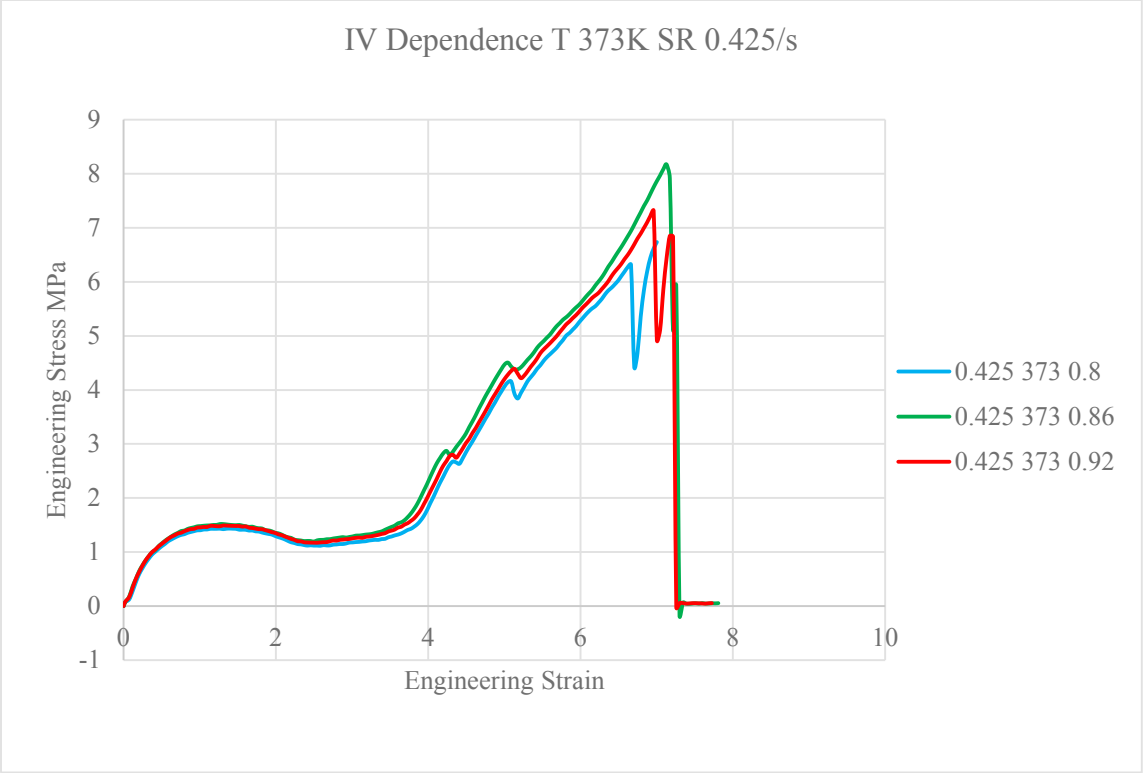

Figure 5.35 IV dependence of tension test results - T 373K SR 0.425/s

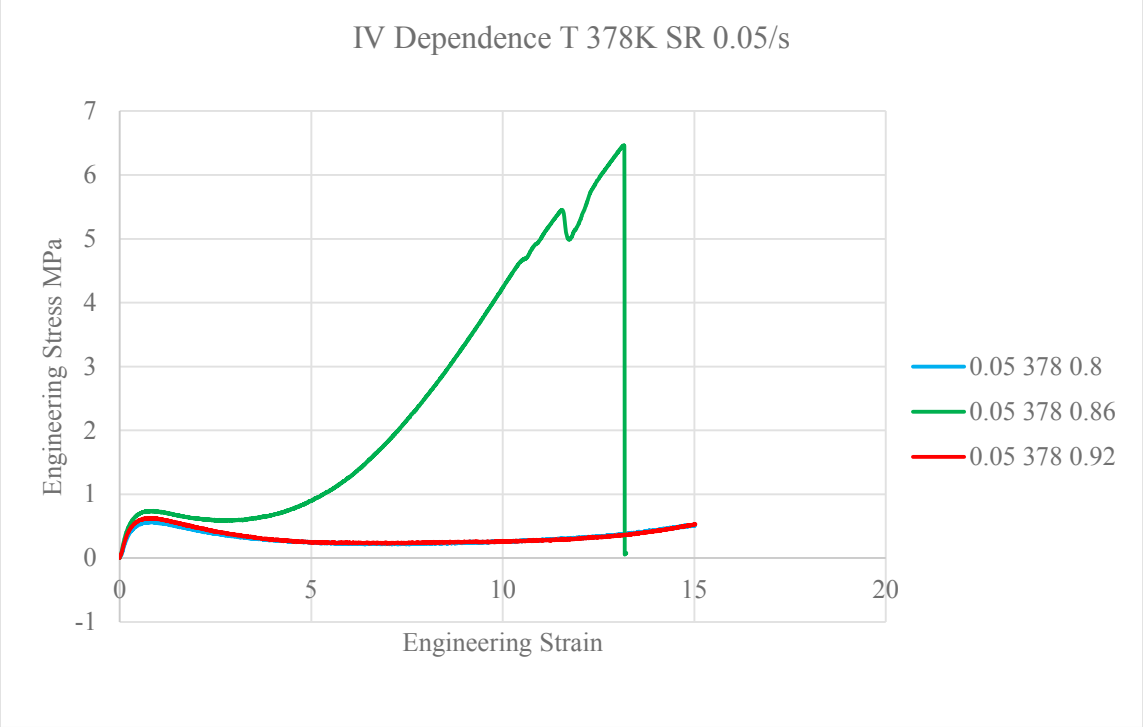

Figure 5.36 IV dependence of tension test results - T 378K SR 0.05/s

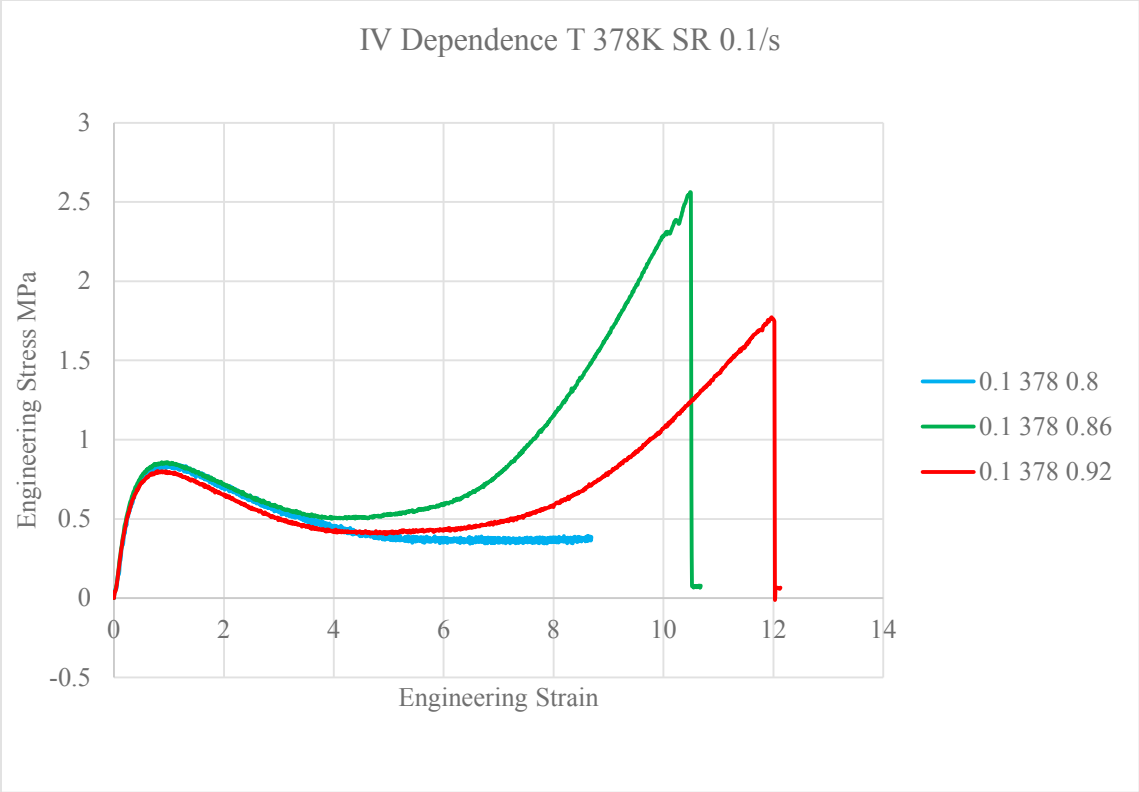

Figure 5.37 IV dependence of tension test results - T 378K SR 0.1/s

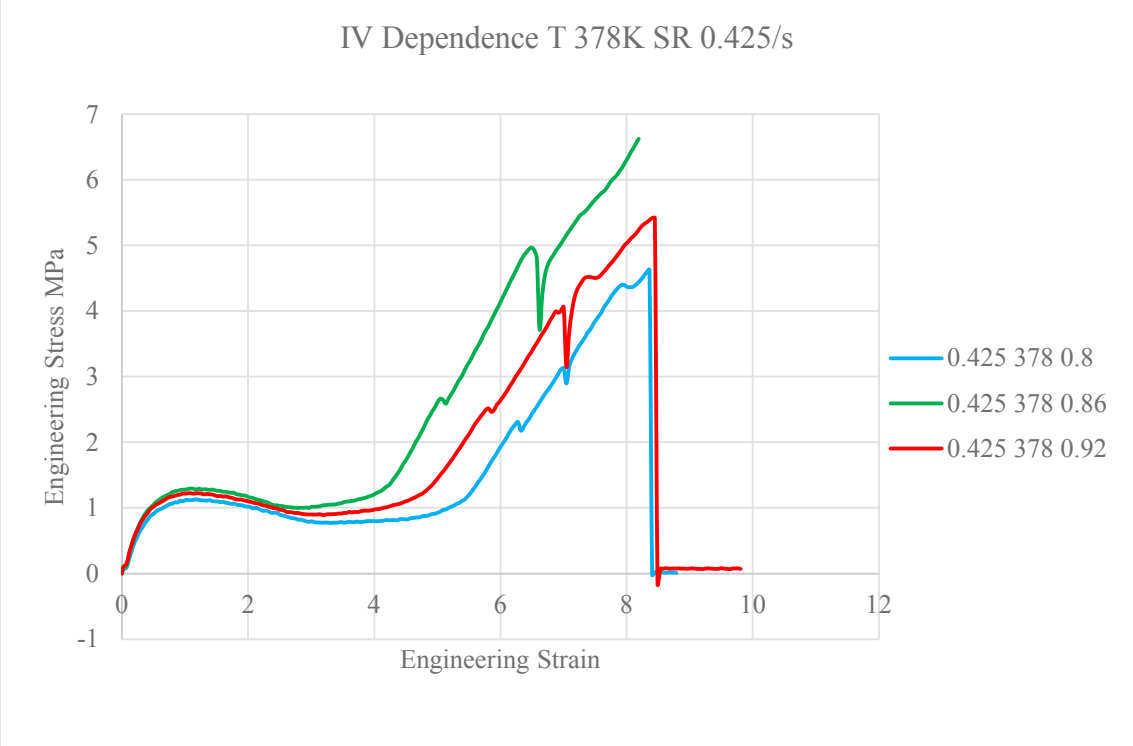

Figure 5.38 IV dependence of tension test results - T 378K SR 0.425/s

5.4 Tensile Test Results with DB Model

As with compression tests, the Dupaix-Boyce model was used to simulate uniaxial tensile tests. However, when the same constants used for uniaxial compression simulation were used in tensile simulation, the stress was considerably under-predicted by the model. Figure 5.39 shows the tensile simulation results with the same set of constants as used in compression. It can be observed that the stress levels predicted are very low.

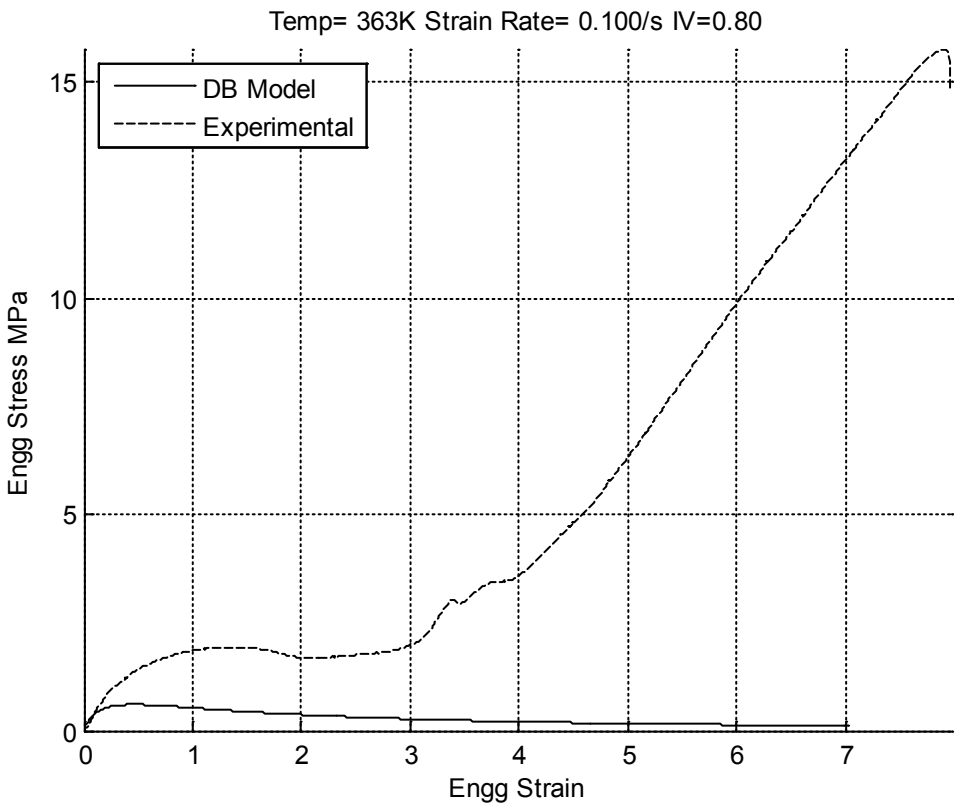

Figure 5.39 Tension simulation on DB model with same constants used as compression

Because of this, the model constants had to be changed to simulate tensile testing. Table 5.1 lists the constants used to fit both uniaxial compression and tension tests.

Table 5.1 DB Model constants for compression and tension

Model Constants	Symbol	Fits Compression	Fits Tensile	Unit
PROPS(1)	μ_{gl}	0.475E9	0.475E9	N/m^2
PROPS(2)	μ_r	0.42E7	0.42E7	N/m^2
PROPS(3)	$\Delta\theta$	23	23	K
PROPS(4)	X_g	-0.62E6	-0.62E6	N/m^2
PROPS(5)	ξ	3	3	K
PROPS(6)	ς	1.2263	1.2263	K
PROPS(7)	B	1E6	1.25E8	N/m^2
PROPS(8)	ΔG	2E12	2E12	1/s
PROPS(9)	$\dot{\gamma}_{0A}$	1.8E-19	1.8E-19	J
PROPS(10)	$nk\theta$	3E6	8.5E6	N/m^2
PROPS(11)	N	7	10	-na-
PROPS(12)	Q/R	5.335E3	5.210E3	K
PROPS(13)	D	3.2	2.46	$((N/m^2)^3 s)^{-1}$
PROPS(14)	$1/n$	4	6.67	-na-
PROPS(15)	α_c	5E-2	5E-2	rad

From table 5.1 which lists the constants for both tensile and compressive fits, it can be gathered that the major change is in PROPS(7), which is the temperature independent bulk modulus. It is increased by almost two orders of magnitude and imparts high stiffness to the elastic stress in Network I. This apart, small changes were made in other properties associated with Network N to provide better fits of simulation results to tensile data. Figure 5.40 onwards shows the simulated result with changed constants and experimental results. The fit in the initial stretches is much better, however, the curves diverge sharply after medium stretches, which might be attributed to strain induced crystallization. This is described in detail in chapter 8.

The DB model results for all strain rate and temperature conditions are plotted from figure 5.40. As mentioned earlier, beyond a strain rate and temperature dependent strain, the experimental curve hardens drastically, which is left uncaptured by the Dupaix-Boyce model.

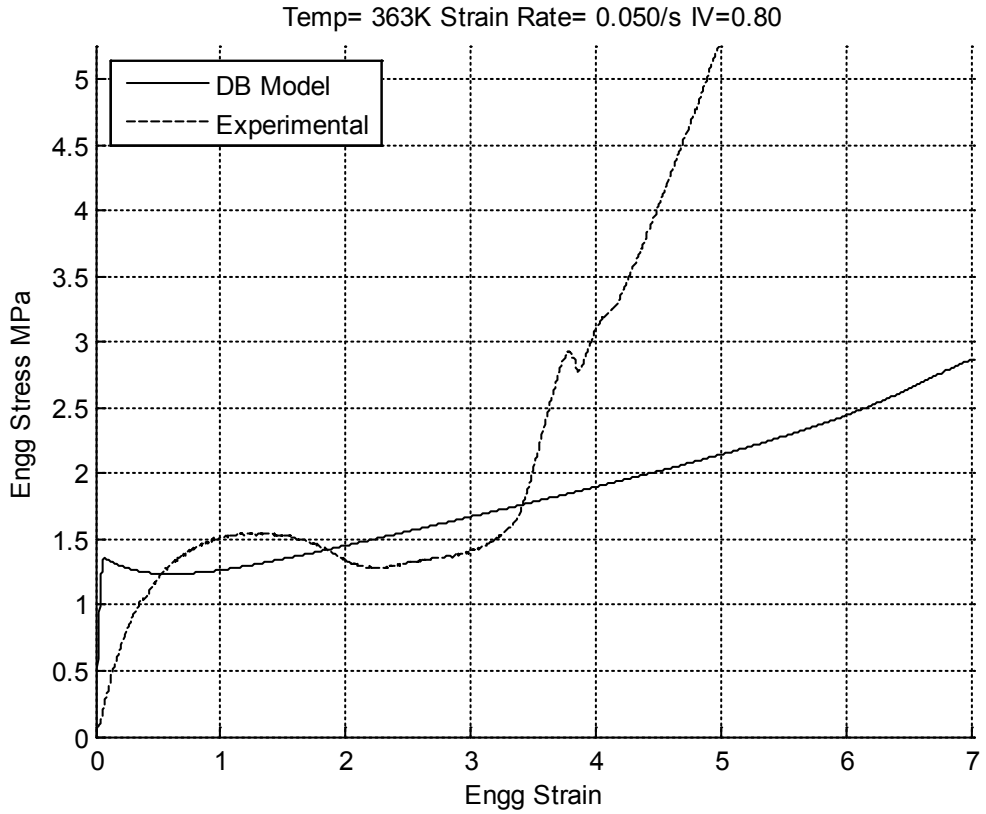

Figure 5.40 DB Model Fit - T 363K SR 0.05/s IV 0.80

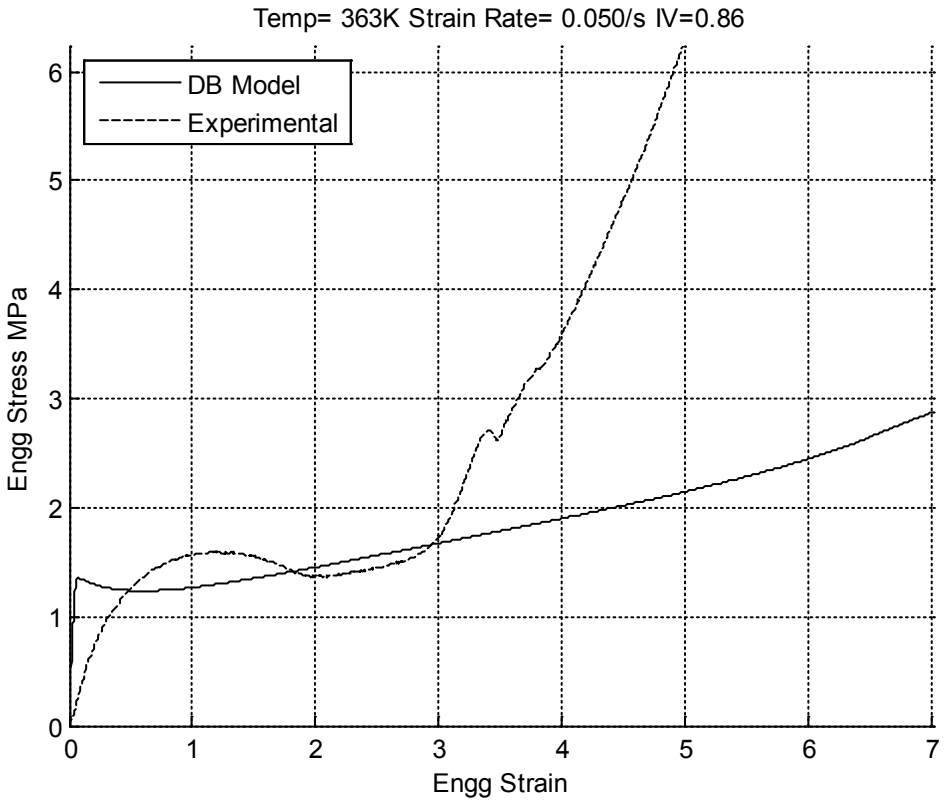

Figure 5.41 DB Model Fit - T 363K SR 0.05/s IV 0.86

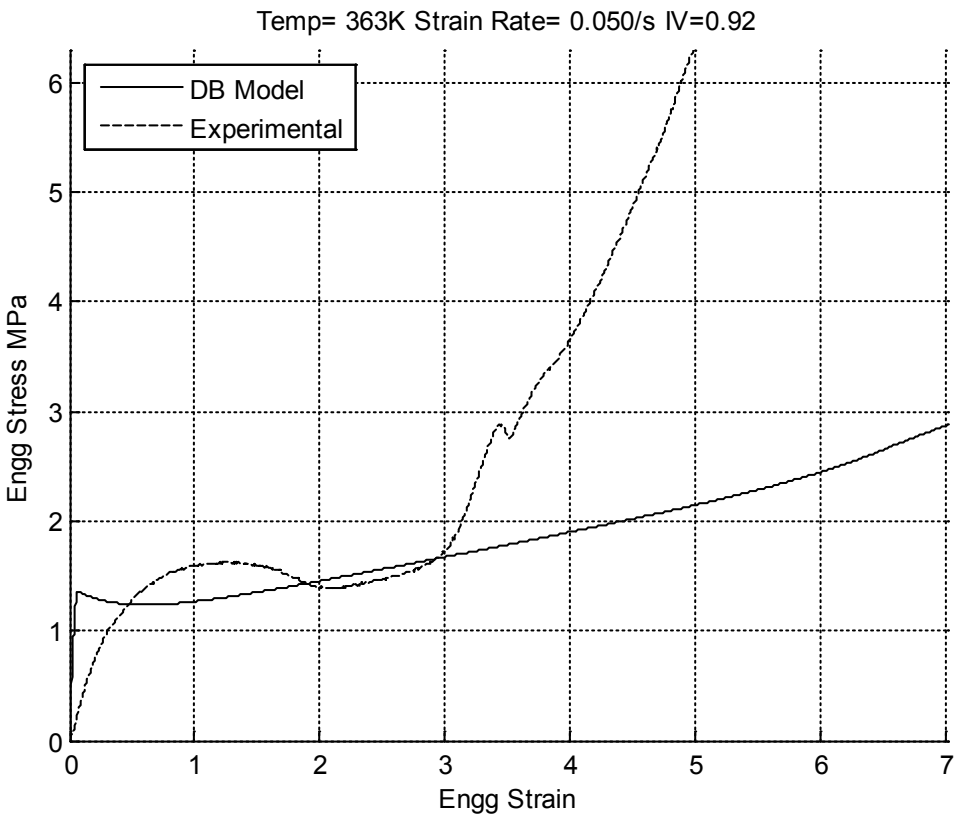

Figure 5.42 DB Model Fit - T 363K SR 0.05/s IV 0.92

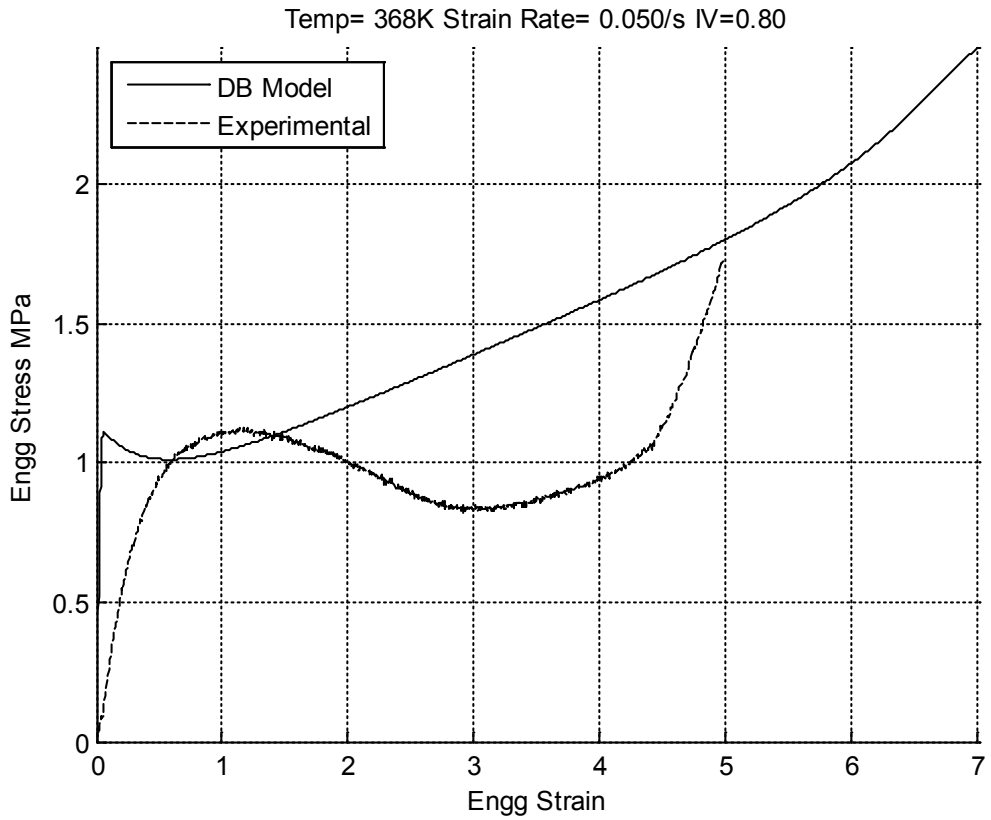

Figure 5.43 DB Model Fit - T 368K SR 0.05/s IV 0.80

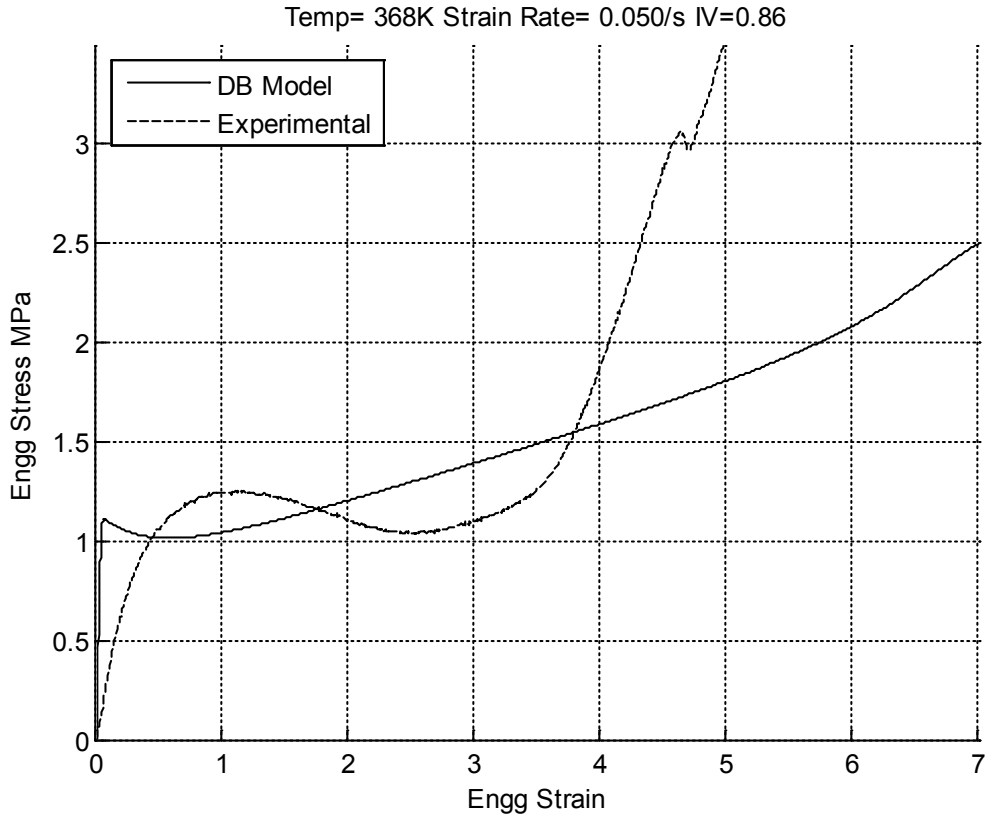

Figure 5.44 DB Model Fit - T 368K SR 0.05/s IV 0.86

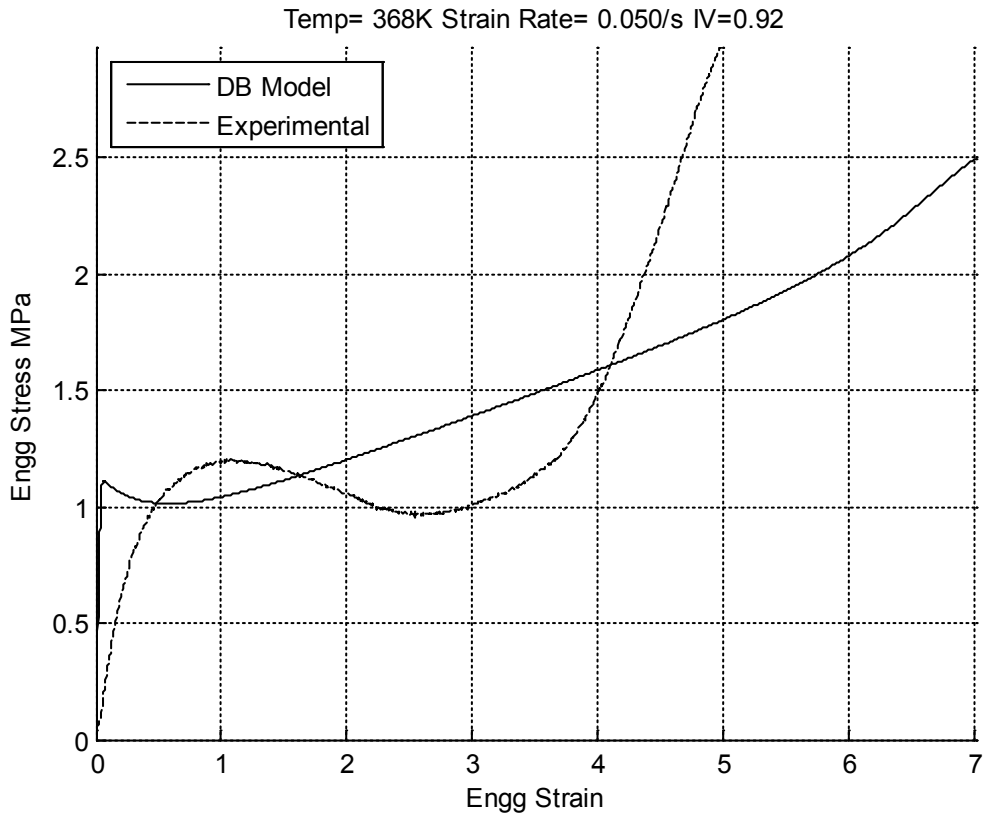

Figure 5.45 DB Model Fit - T 368K SR 0.05/s IV 0.92

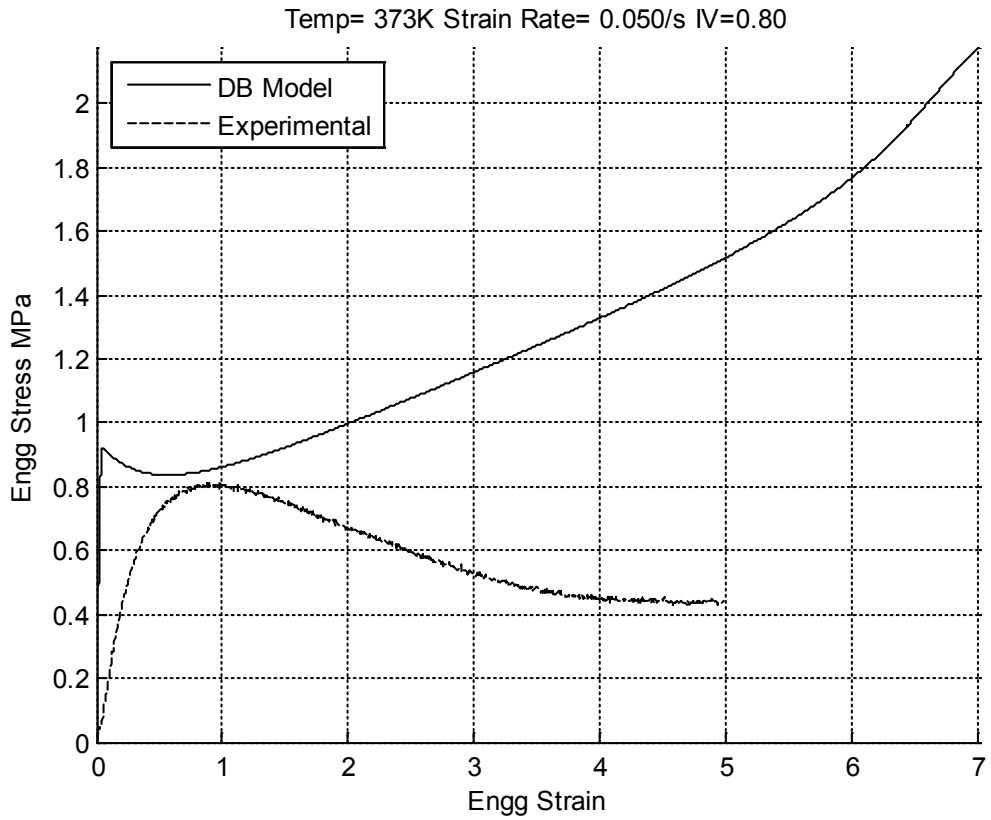

Figure 5.46 DB Model Fit - T 373K SR 0.05/s IV 0.80

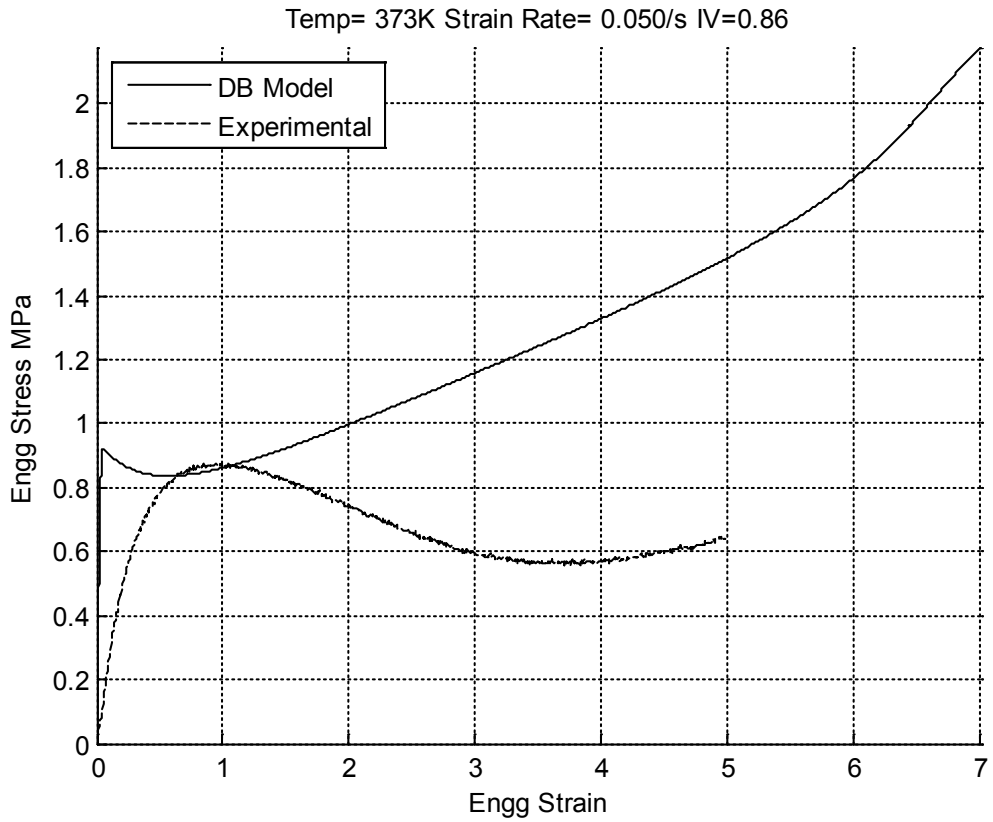

Figure 5.47 DB Model Fit - T 373K SR 0.05/s IV 0.86

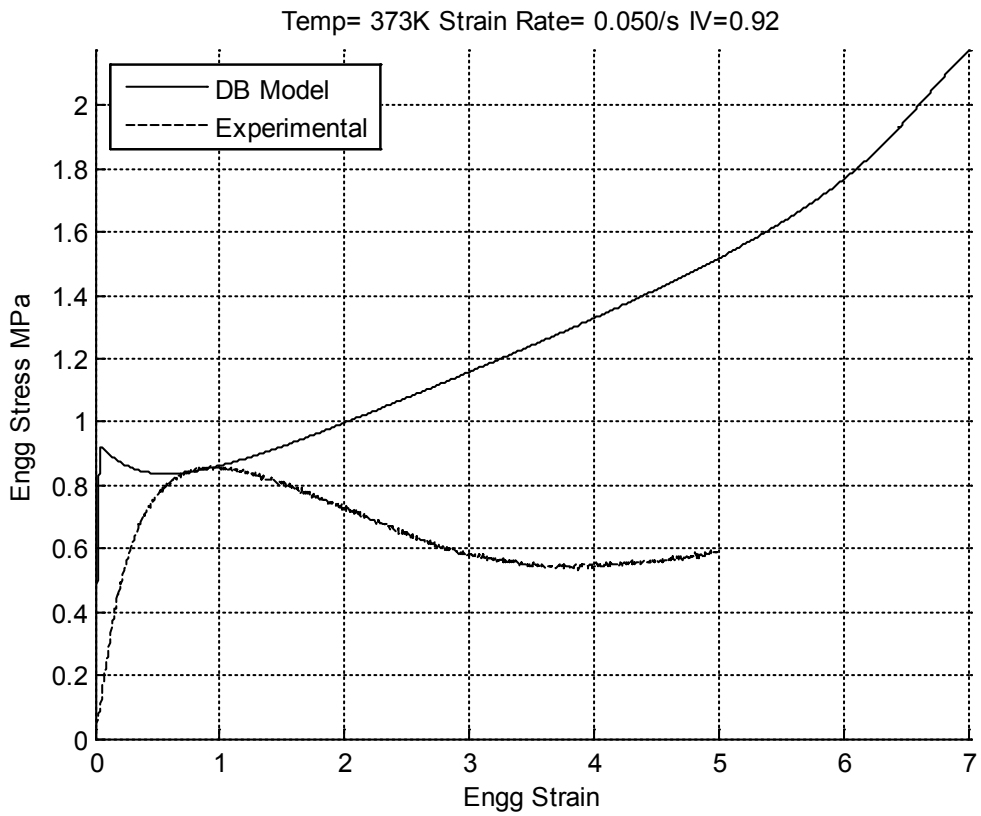

Figure 5.48 DB Model Fit - T 373K SR 0.05/s IV 0.92

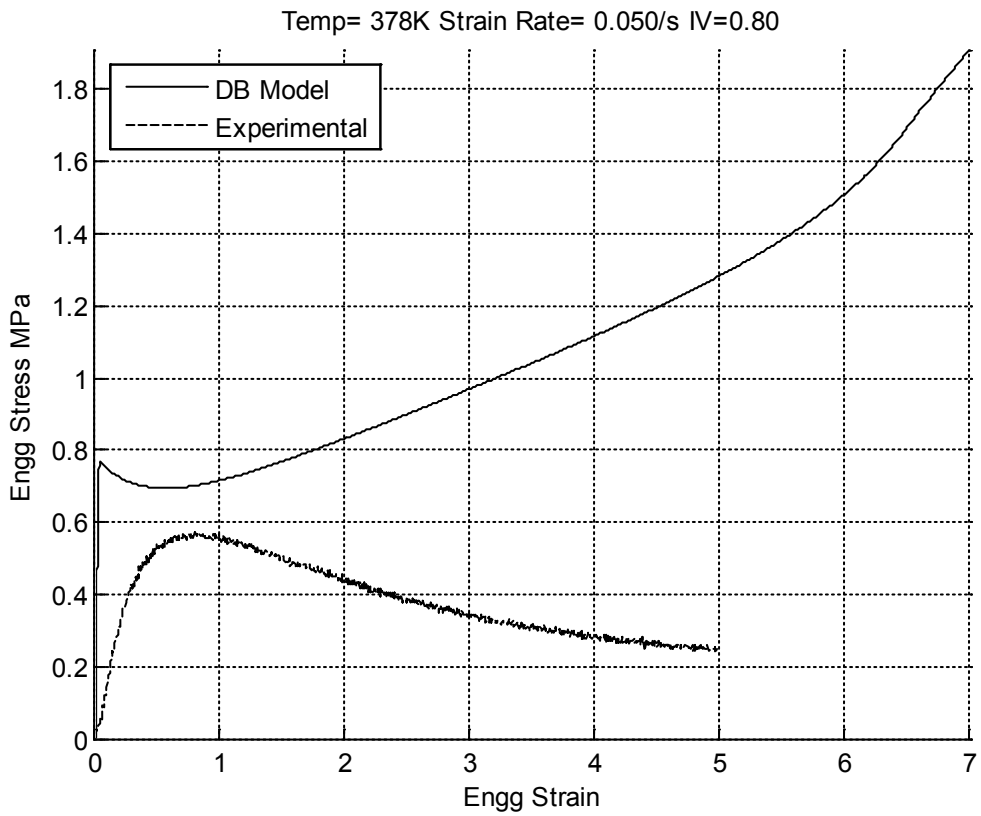

Figure 5.49 DB Model Fit - T 378K SR 0.05/s IV 0.80

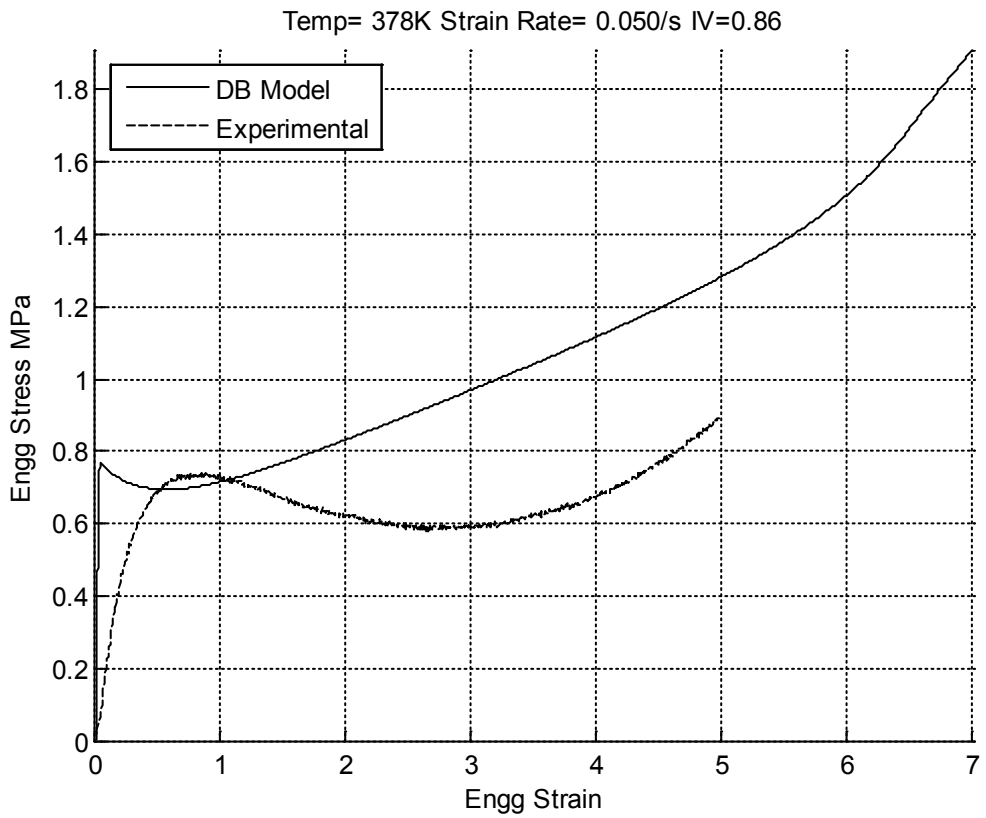

Figure 5.50 DB Model Fit - T 378K SR 0.05/s IV 0.86

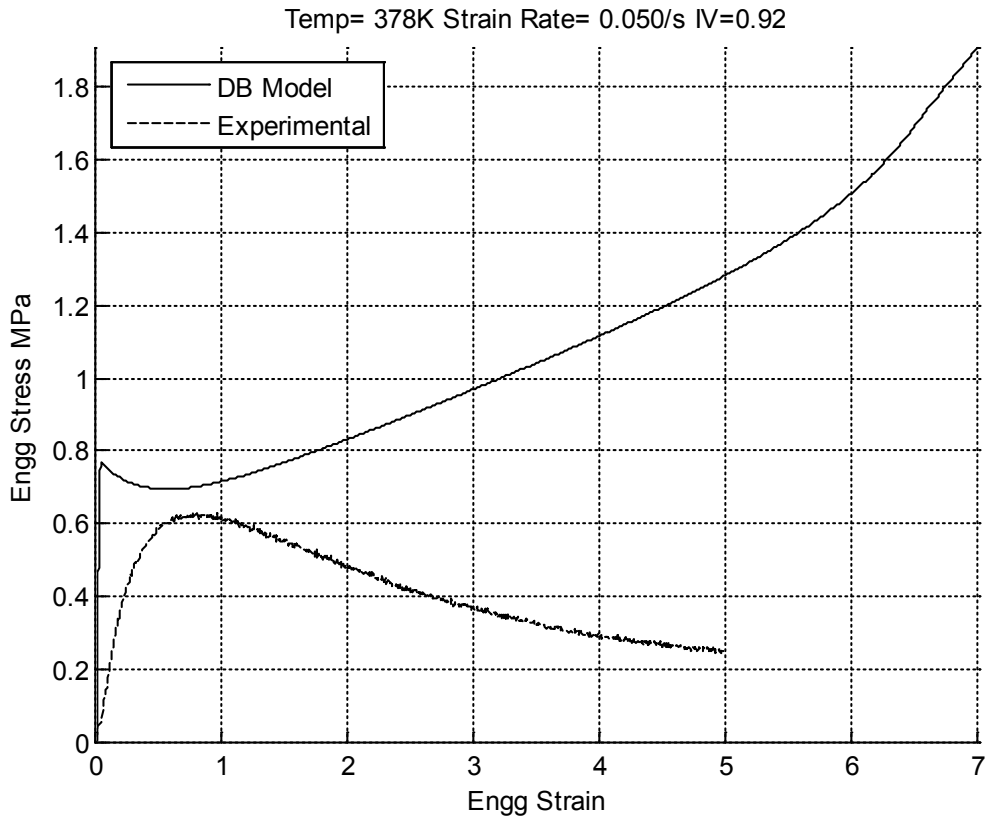

Figure 5.51 DB Model Fit - T 378K SR 0.05/s IV 0.92

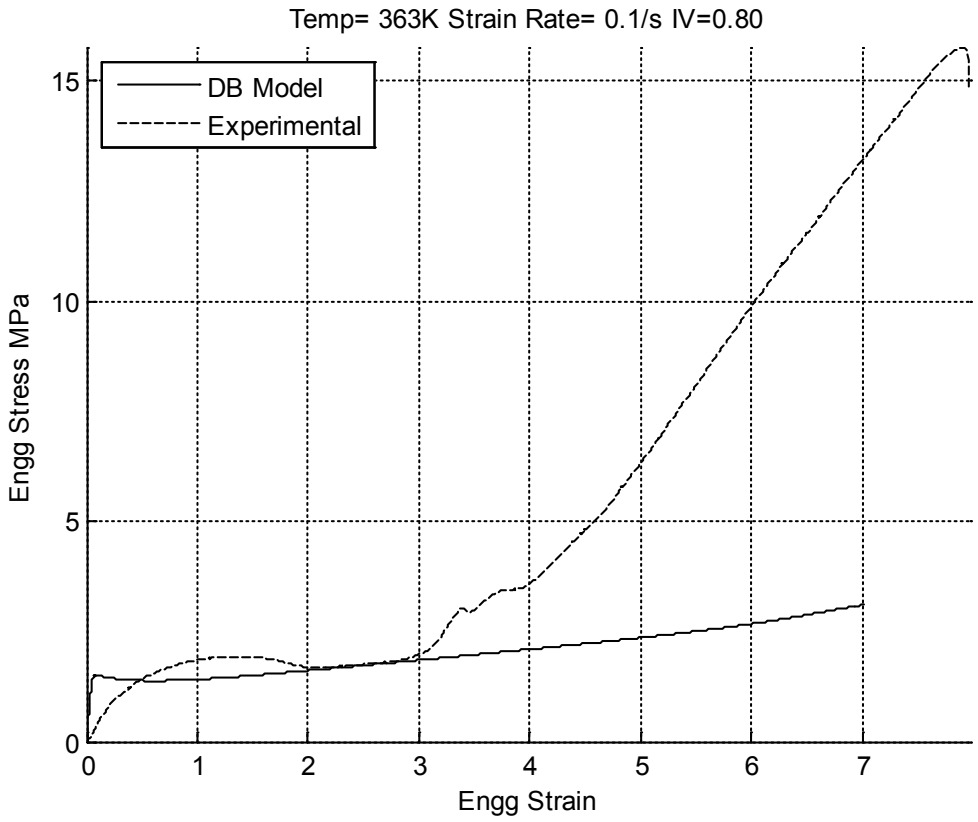

Figure 5.52 DB Model Fit - T 363K SR 0.1/s IV 0.80

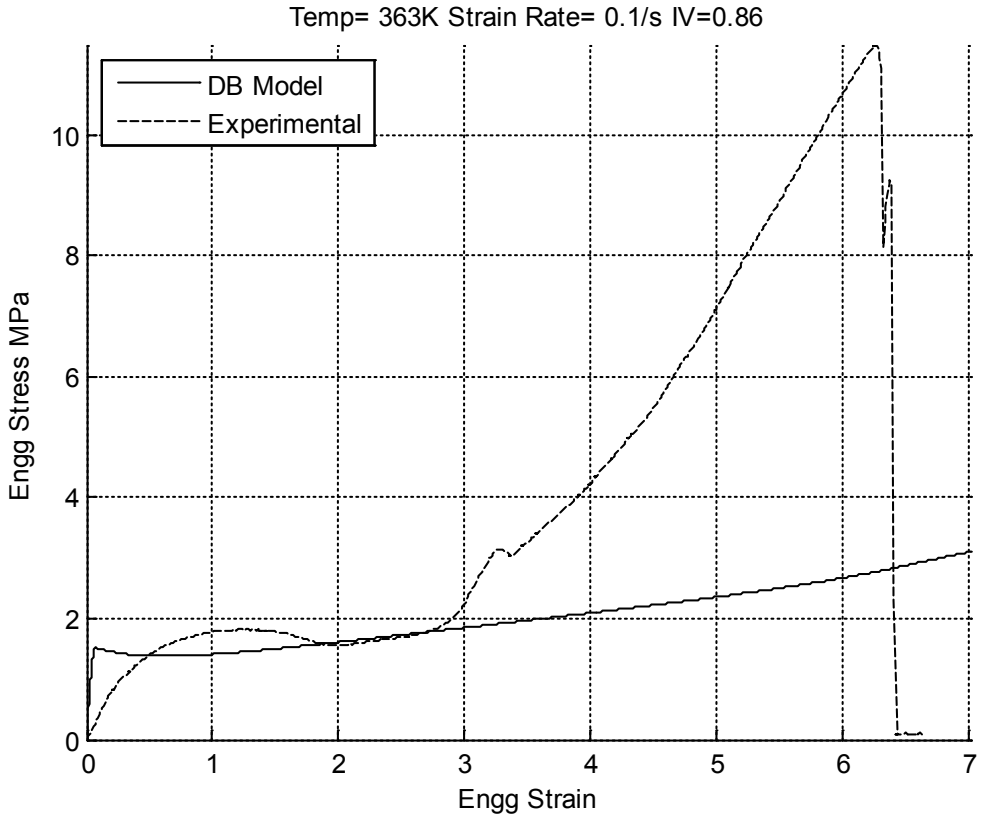

Figure 5.53 DB Model Fit - T 363K SR 0.1/s IV 0.86

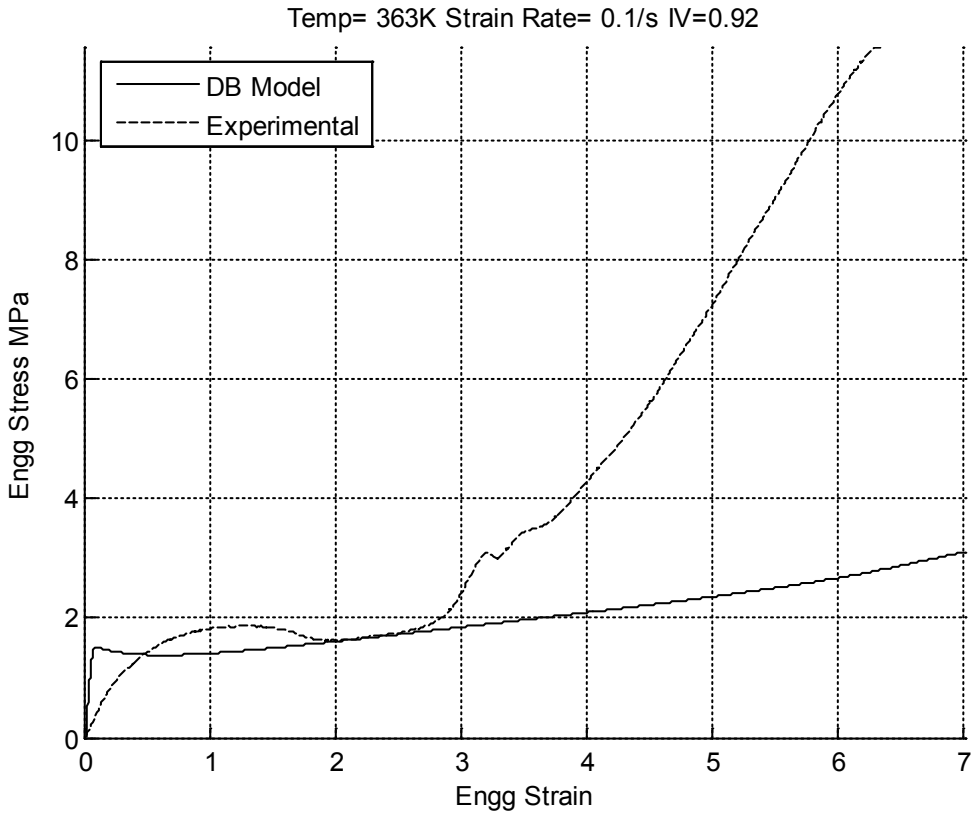

Figure 5.54 DB Model Fit - T 363K SR 0.1/s IV 0.92

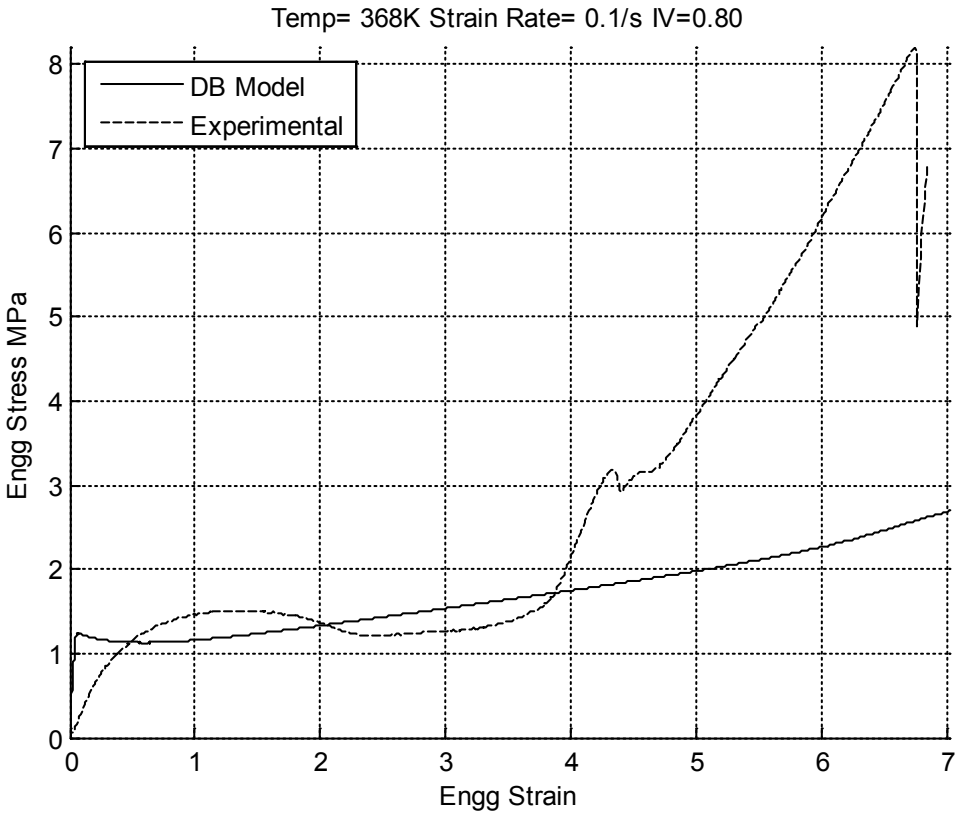

Figure 5.55 DB Model Fit - T 368K SR 0.1/s IV 0.80

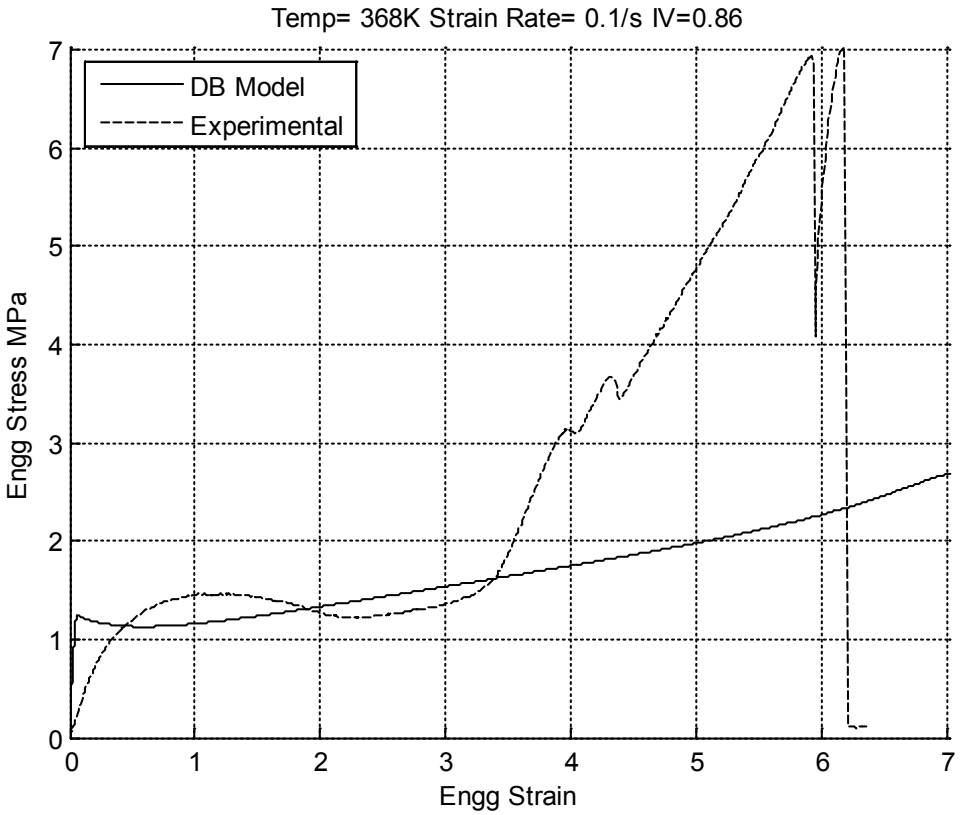

Figure 5.56 DB Model Fit - T 368K SR 0.1/s IV 0.86

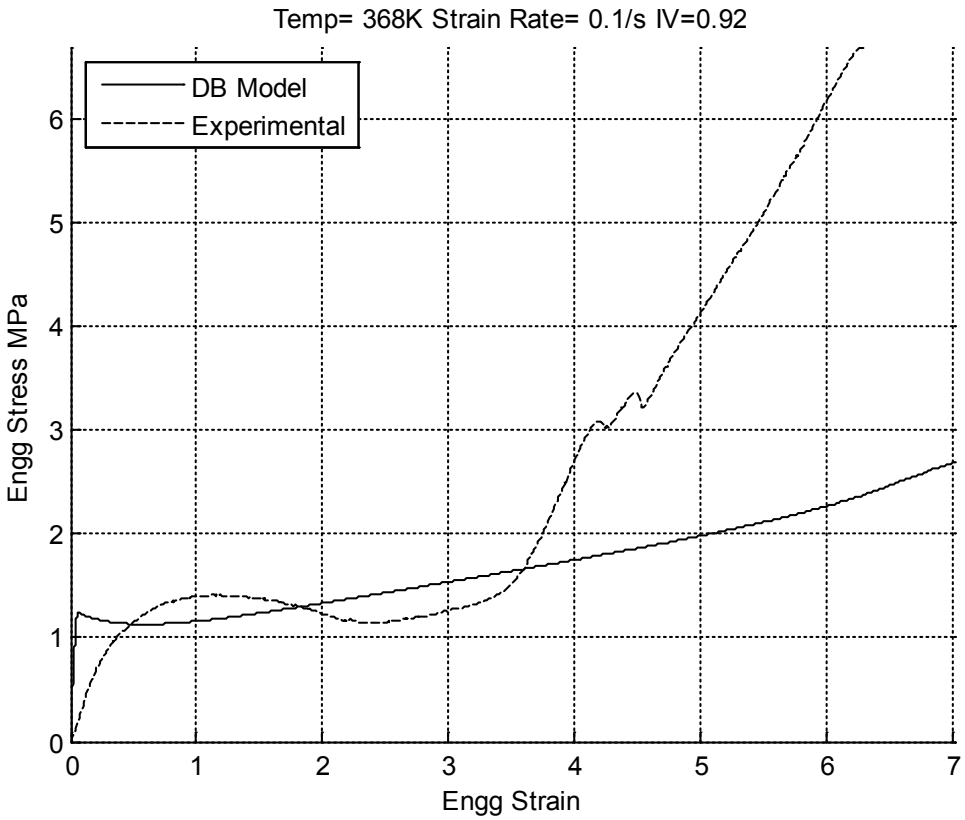

Figure 5.57 DB Model Fit - T 368K SR 0.1/s IV 0.92

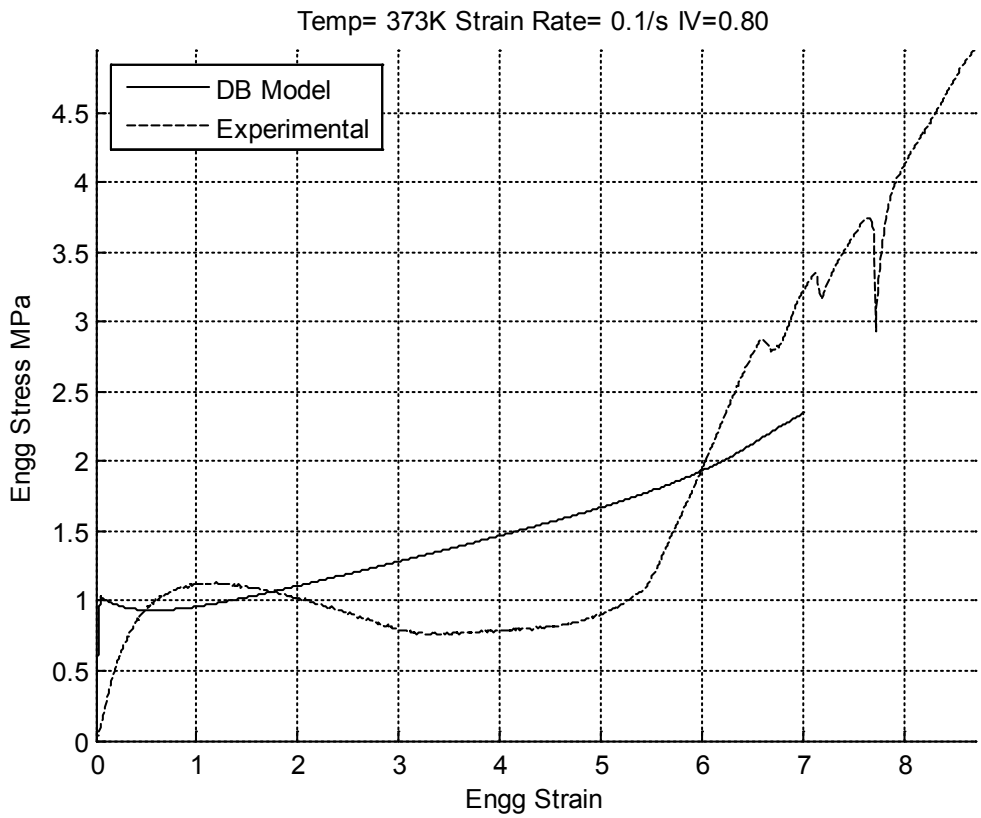

Figure 5.58 DB Model Fit - T 373K SR 0.1/s IV 0.80

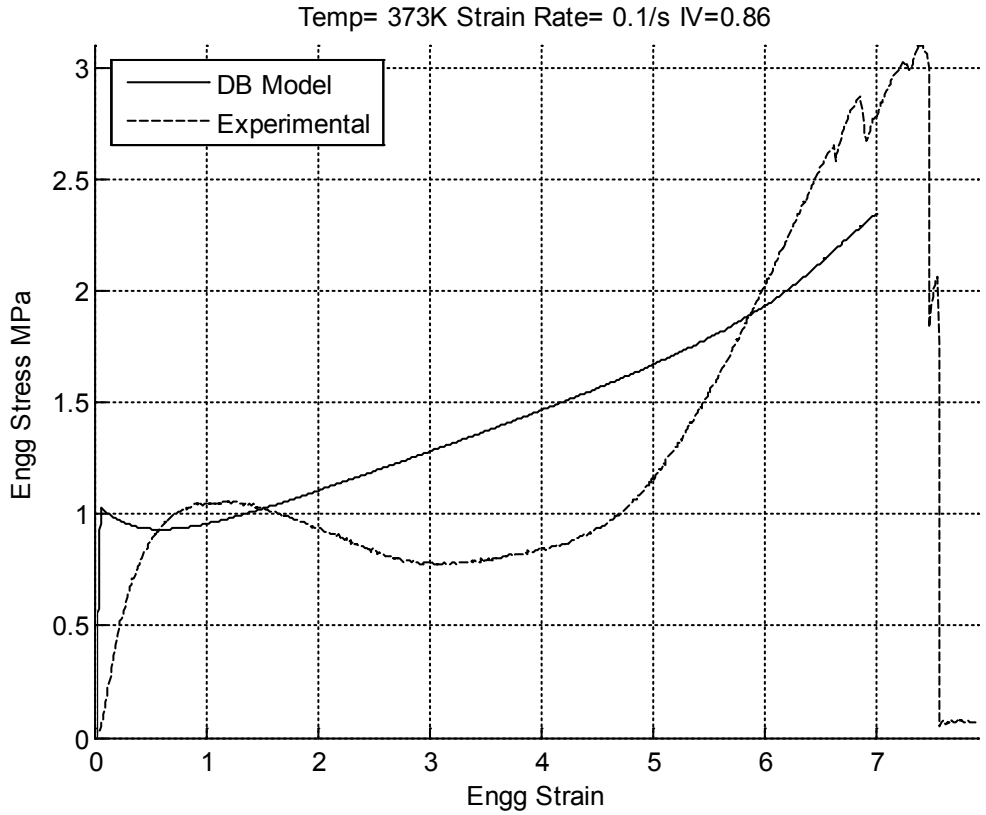

Figure 5.59 DB Model Fit - T 373K SR 0.1/s IV 0.86

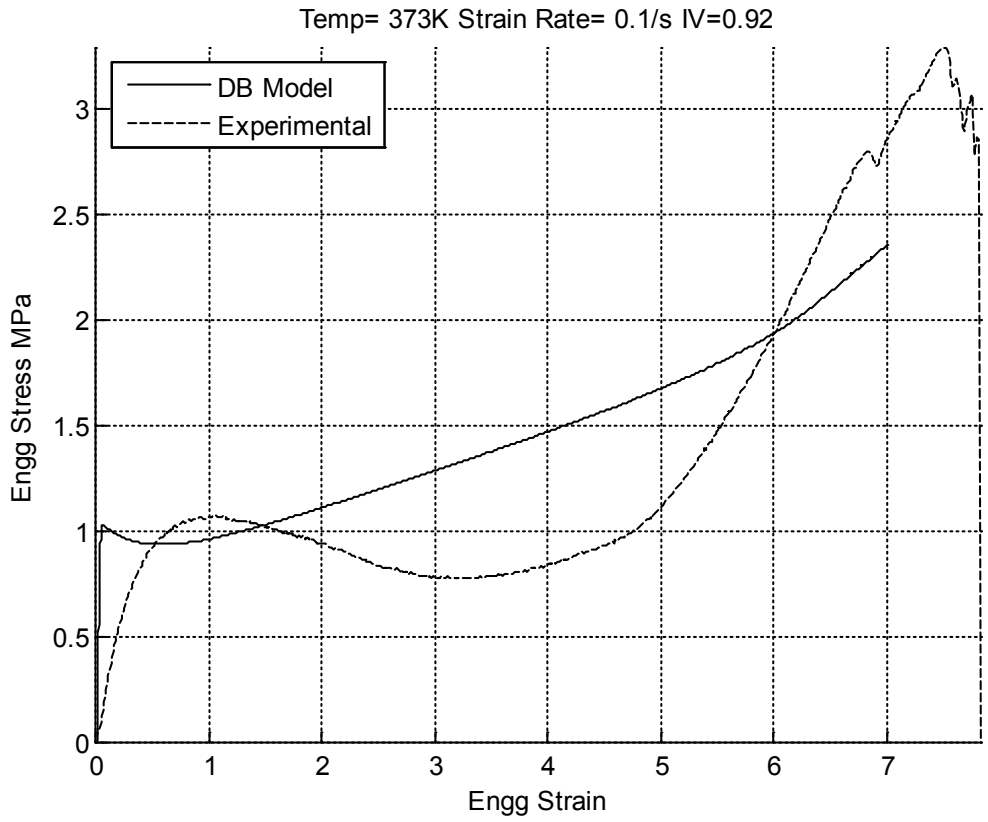

Figure 5.60 DB Model Fit - T 373K SR 0.1/s IV 0.92

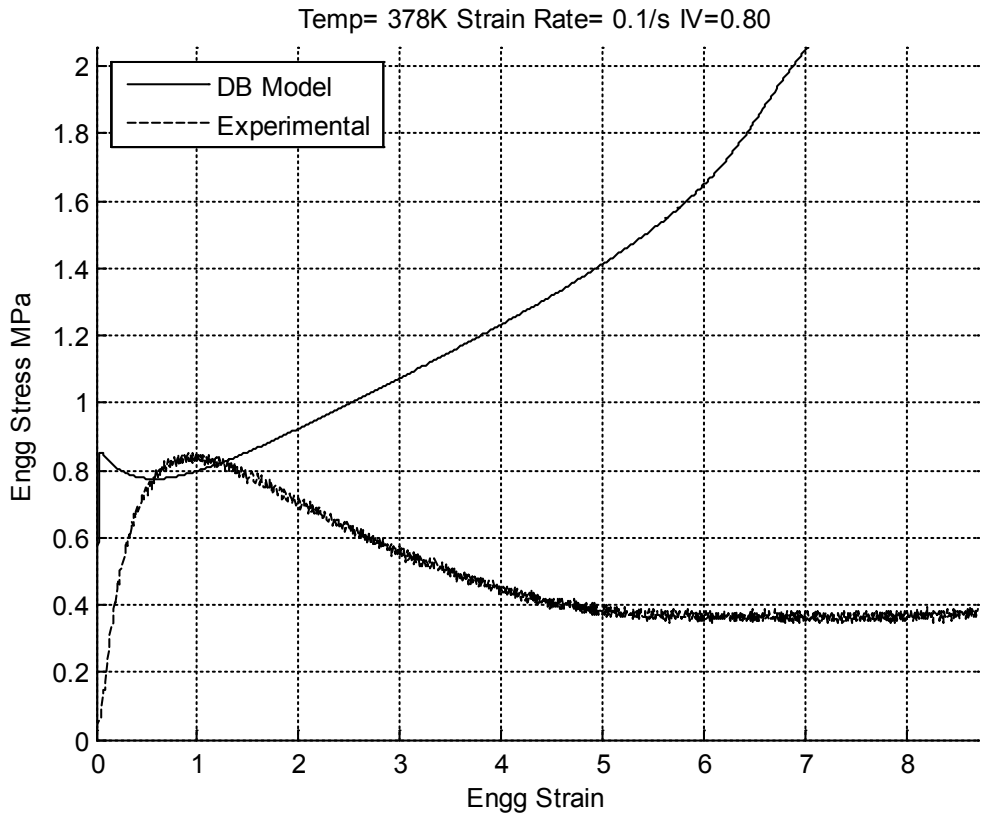

Figure 5.61 DB Model Fit - T 378K SR 0.1/s IV 0.80

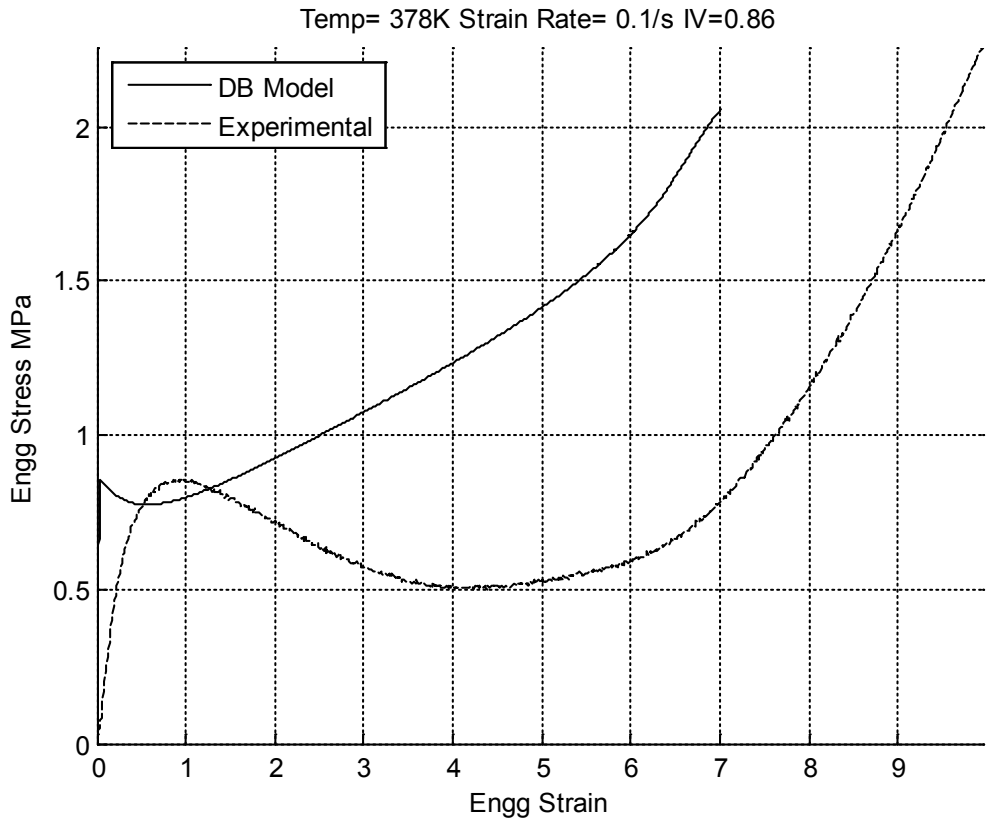

Figure 5.62 DB Model Fit - T 378K SR 0.1/s IV 0.86

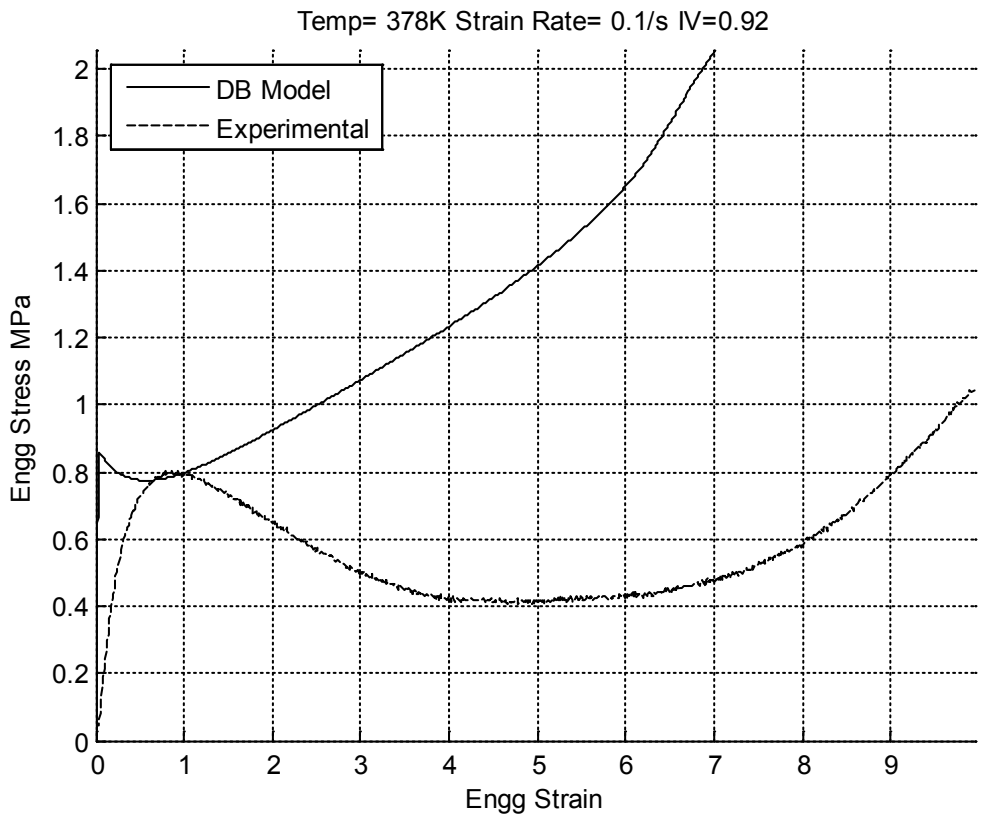

Figure 5.63 DB Model Fit - T 378K SR 0.1/s IV 0.92

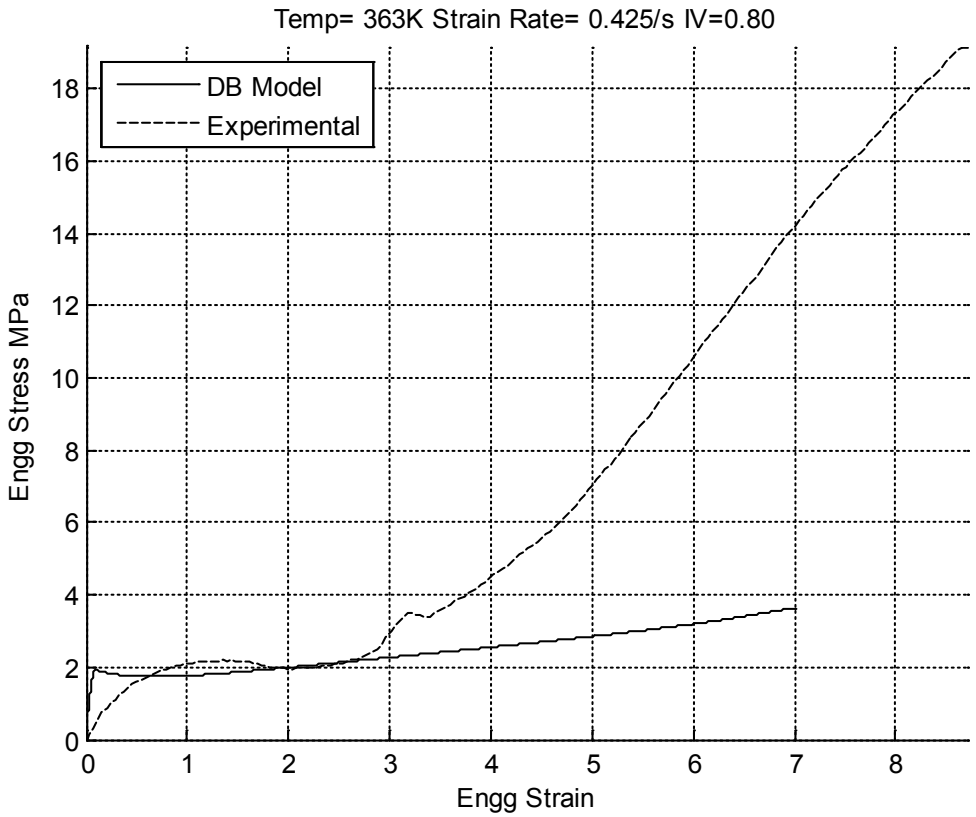

Figure 5.64 DB Model Fit - T 363K SR 0.425/s IV 0.80

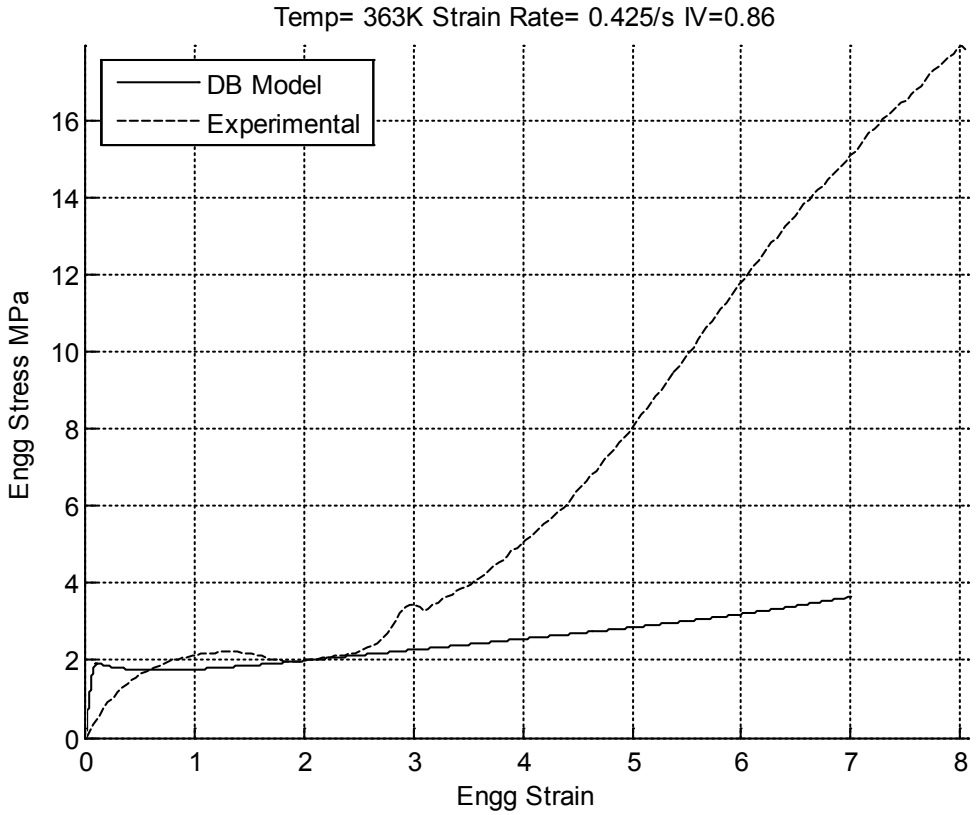

Figure 5.65 DB Model Fit - T 363K SR 0.425/s IV 0.86

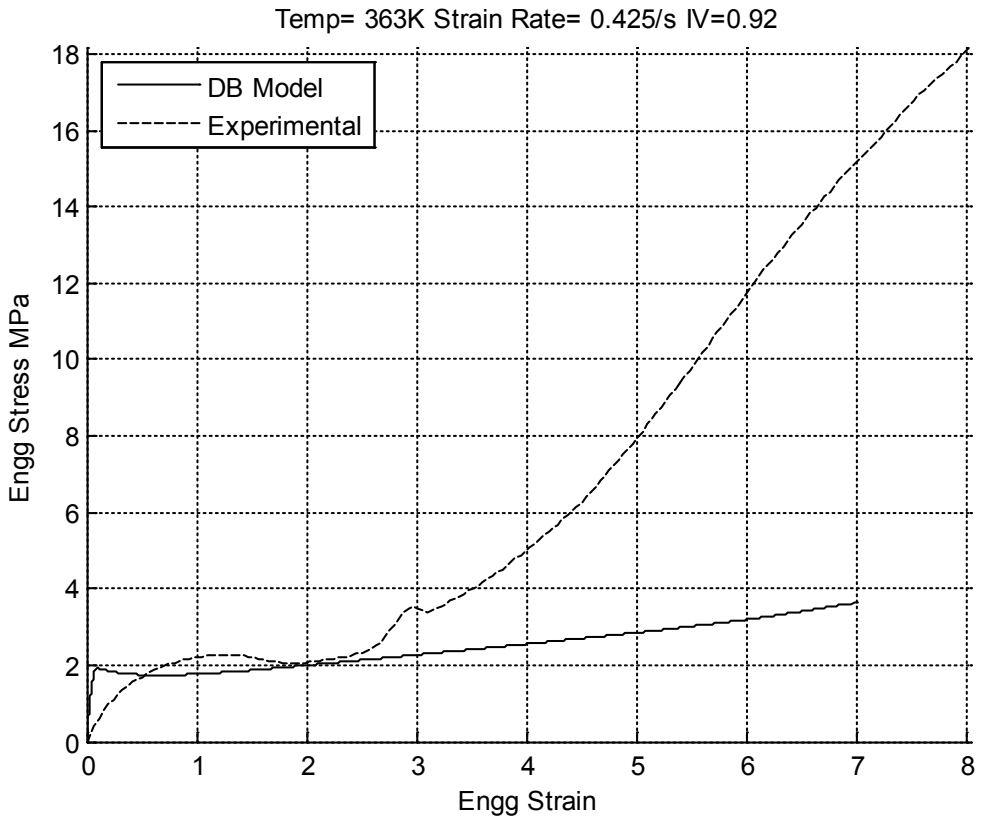

Figure 5.66 DB Model Fit - T 363K SR 0.425/s IV 0.92

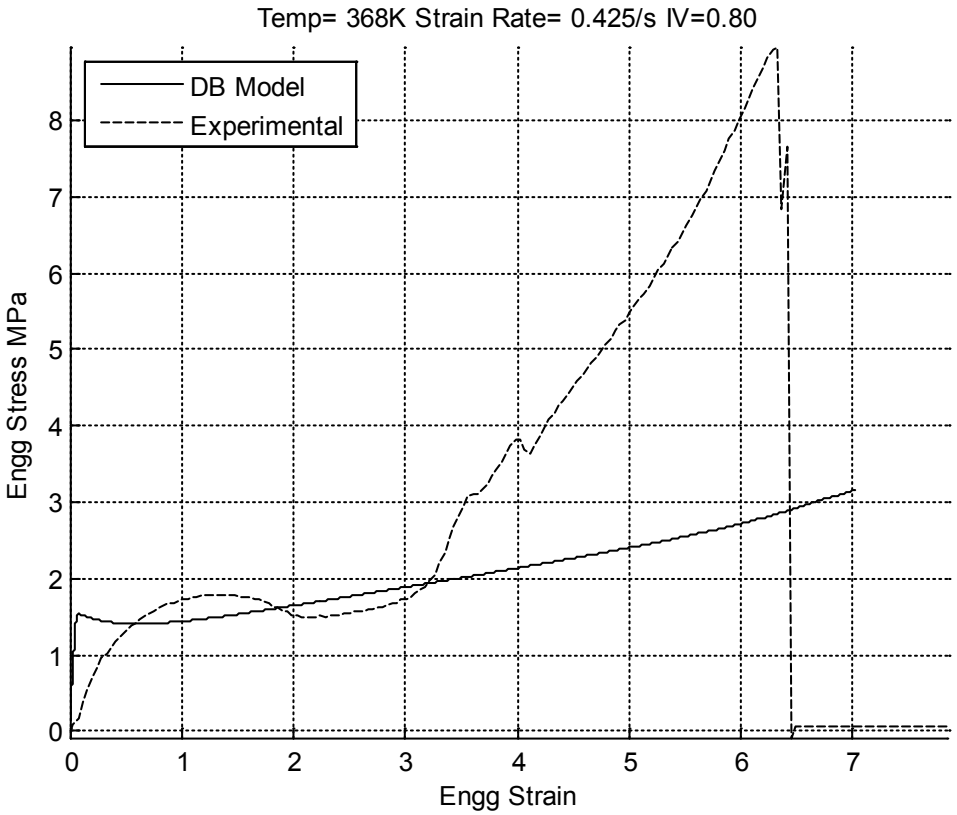

Figure 5.67 DB Model Fit - T 368K SR 0.425/s IV 0.80

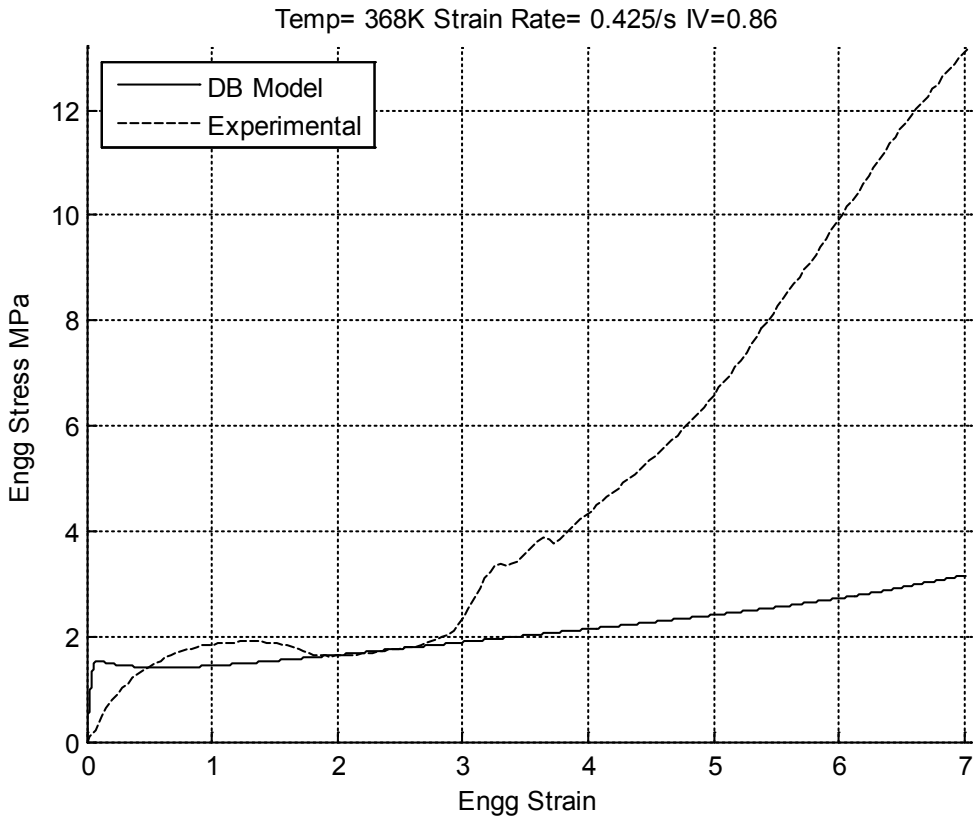

Figure 5.68 DB Model Fit - T 368K SR 0.425/s IV 0.86

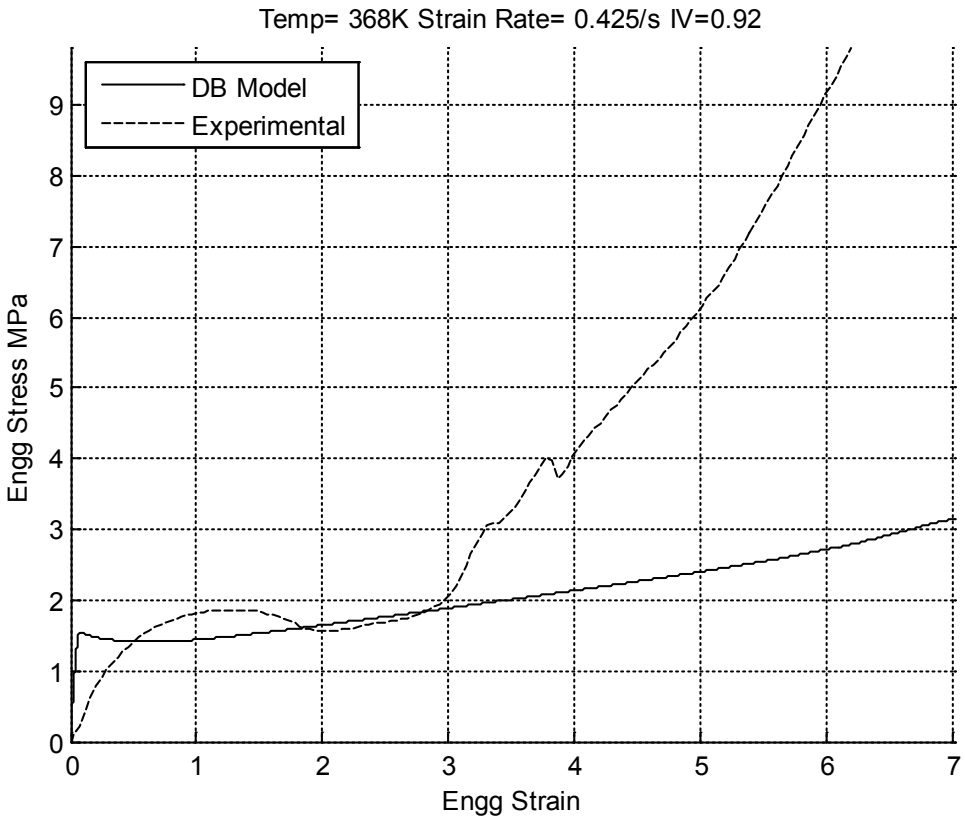

Figure 5.69 DB Model Fit - T 368K SR 0.425/s IV 0.92

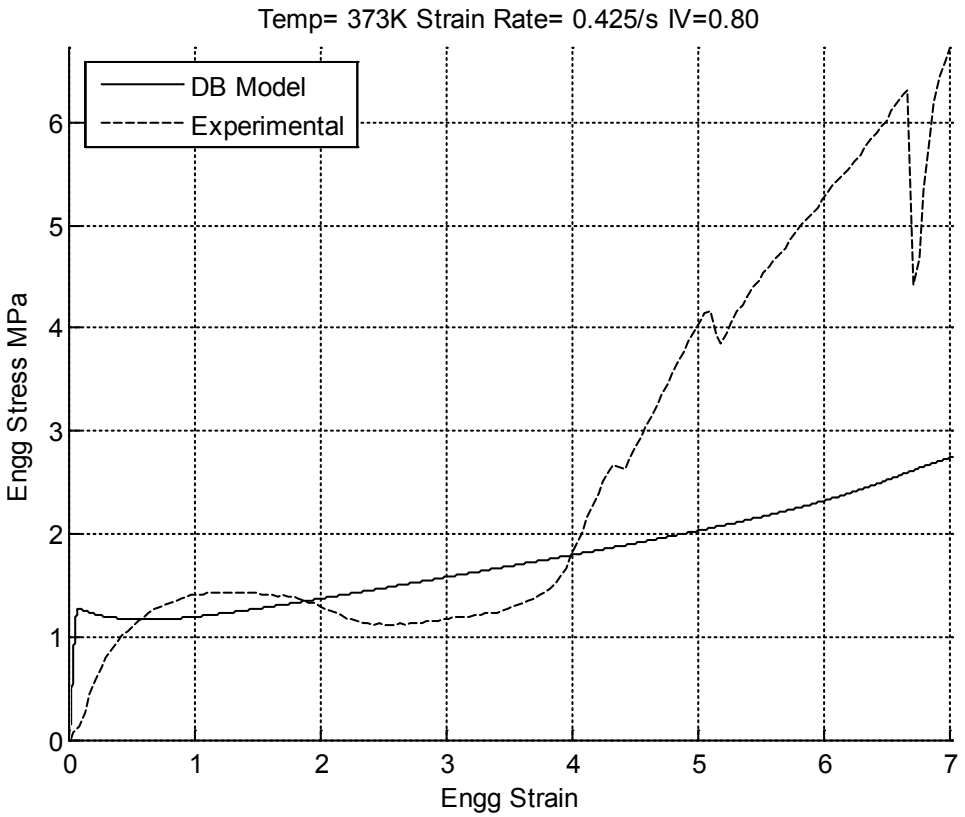

Figure 5.70 DB Model Fit - T 373K SR 0.425/s IV 0.80

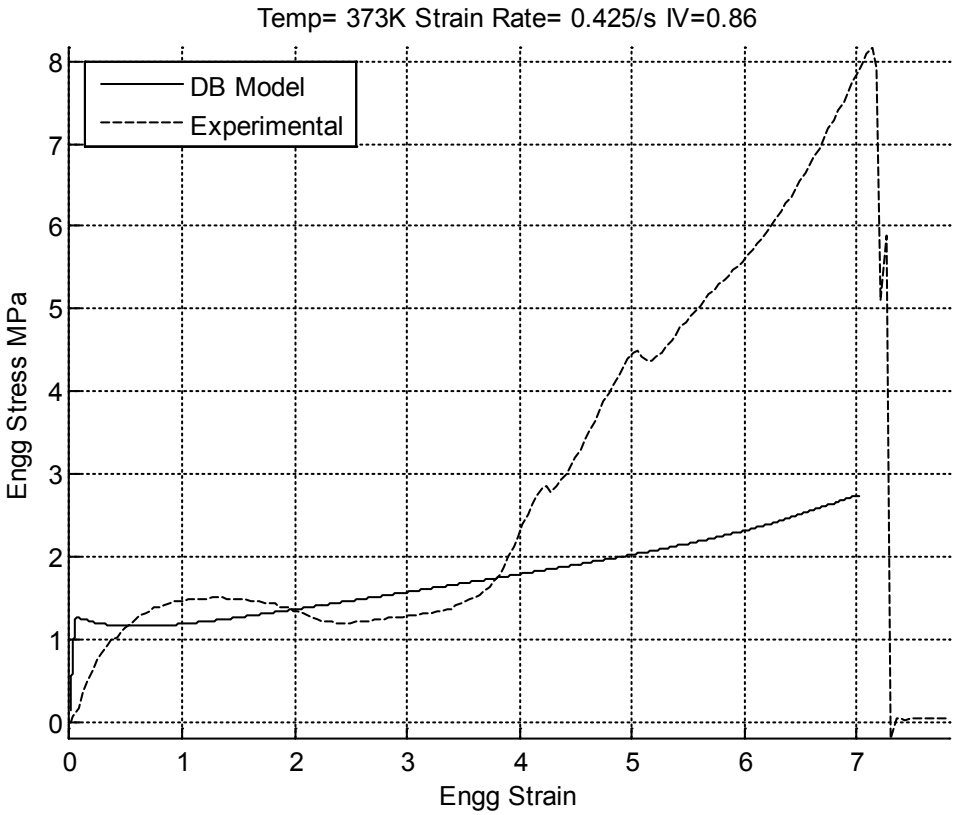

Figure 5.71 DB Model Fit - T 373K SR 0.425/s IV 0.86

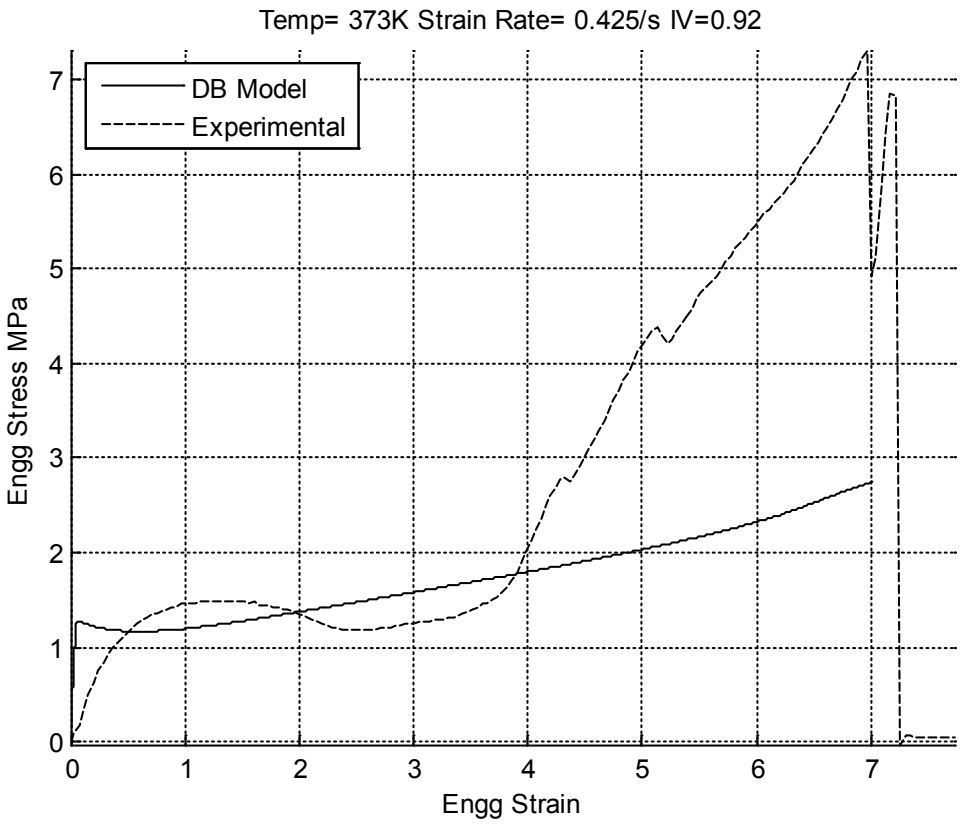

Figure 5.72 DB Model Fit - T 373K SR 0.425/s IV 0.92

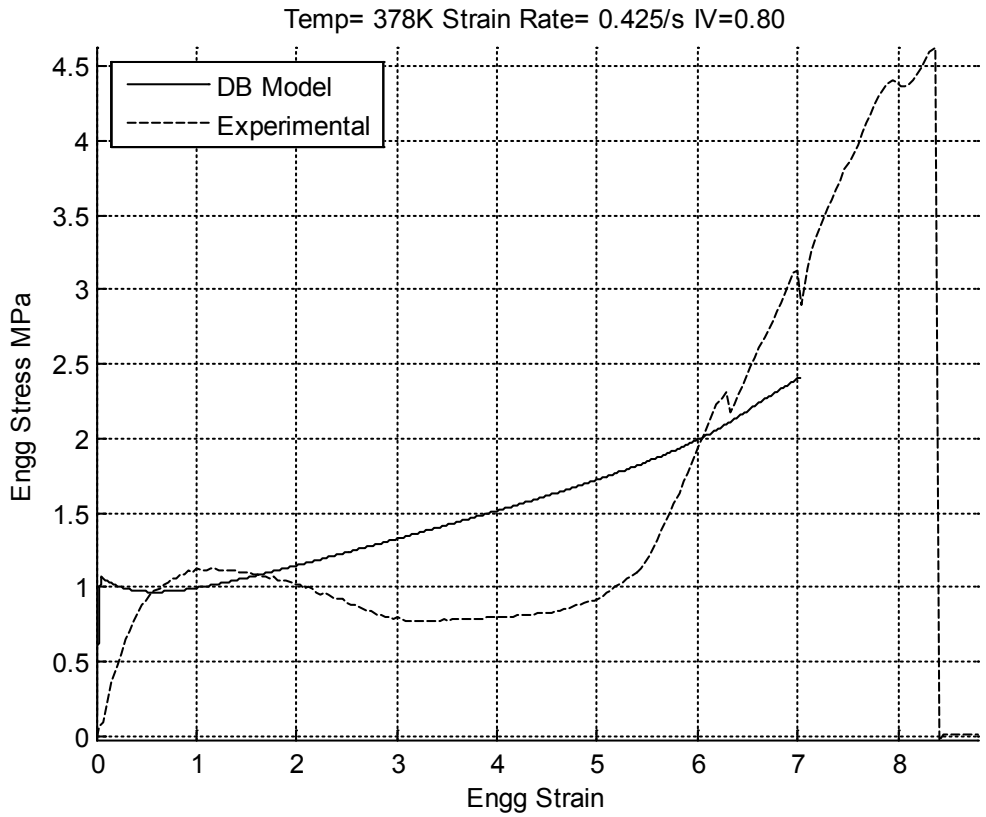

Figure 5.73 DB Model Fit - T 378K SR 0.425/s IV 0.80

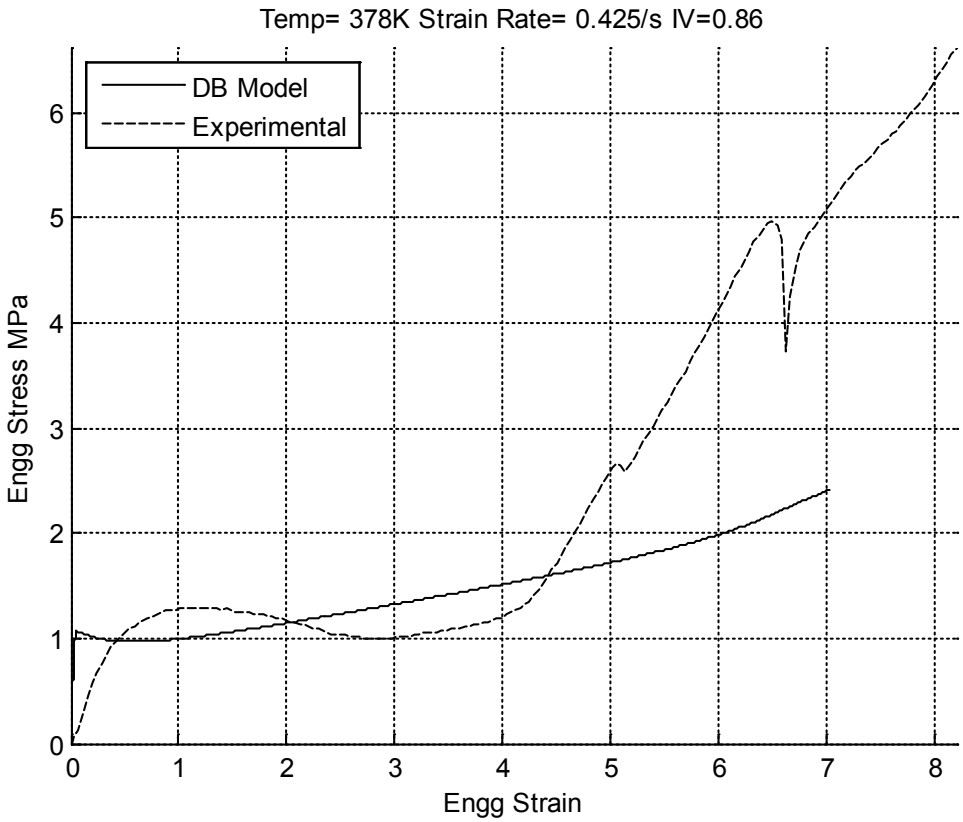

Figure 5.74 DB Model Fit - T 378K SR 0.425/s IV 0.86

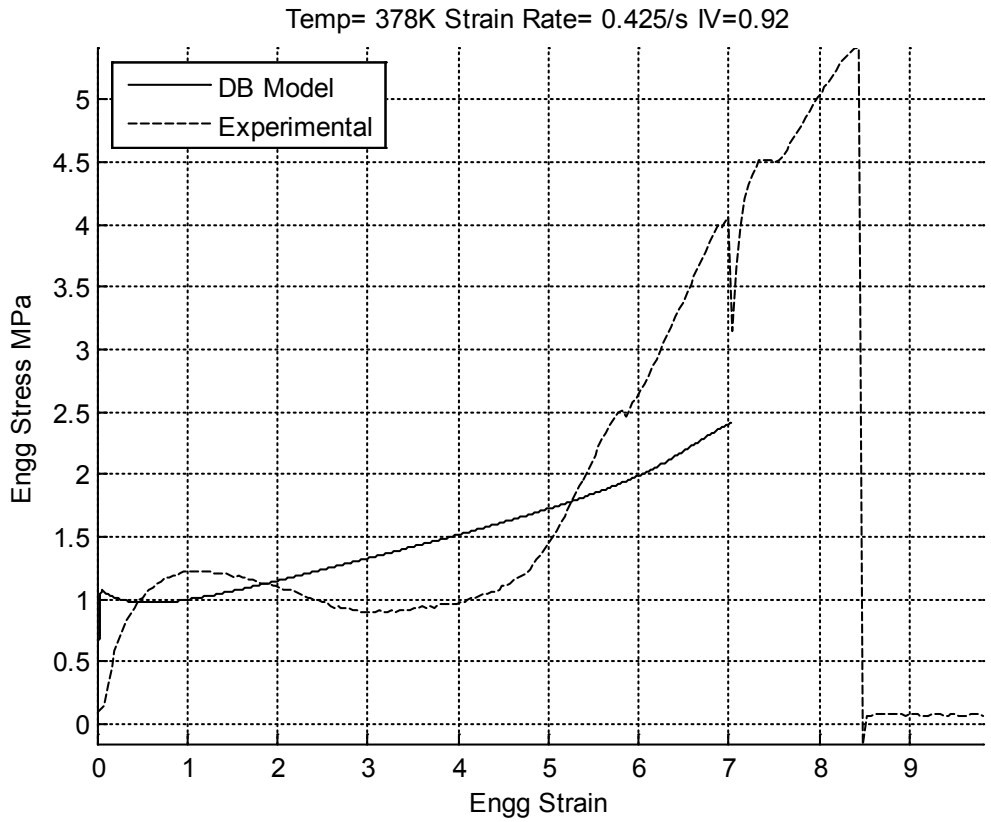

Figure 5.75 DB Model Fit - T 378K SR 0.425/s IV 0.92

5.5 Conclusion

This chapter described the uniaxial tensile tests conducted to obtain data to test the Dupaix-Boyce model. It can be seen that the tensile curves obtained showed similar temperature and strain rate dependence as observed from the compression curves. In addition to this, in medium stretches, there was a sudden onset of strain hardening which caused stress to increase steeply per unit increase in stretch. The onset of this hardening was found to be dependent on temperature and strain rate. Increase in temperature from

363K increased this onset stretch and at 383K this stretch was mostly beyond the maximum tensile stretch of the experiments. Increase in strain rate reduced the onset stretch, and at very small strain rates, the onset of strain hardening was completely absent. This observation could be related to stain induced crystallization. Simulated results from the current Dupaix-Boyce model could not capture this strain hardening in tension. An attempt was made to algebraically capture and incorporate this hardening in the crystallization module. This is described in Chapter 8. Also, plots showing the fit of the Dupaix-Boyce model for tension with crystallization for the above plotted conditions of temperature, strain rate and IV are provided in Chapter 8.

Chapter 6: Comparison of Compressive and Tensile test results

6.1 Introduction

The results obtained from uniaxial compression tests on circular discs and uniaxial tension tests on small rectangular bars have been discussed in previous chapters. The purpose of this chapter is to compare test results from both uniaxial compression and tension tests.

6.2 Issues in comparison of compressive and tensile test results

Though a comparison of true stress obtained from both types of tests with respect to strain invariants at similar conditions of temperature and strain-rate would be ideal, similar strain-rate conditions were not possible to be set up for the tests.

Compression tests were conducted at a constant true strain-rate where the displacement rate would decrease as the specimen length decreases during compression. However tension tests were conducted at a constant engineering strain-rate because of the maximum velocity capability of the machine head at 8.5 mm/s. Usage of a constant true strain rate for tensile tests required an increasing displacement rate along with the length

of the specimen during test, which would exceed the limit of 8.5mm/s at large tensile strain.

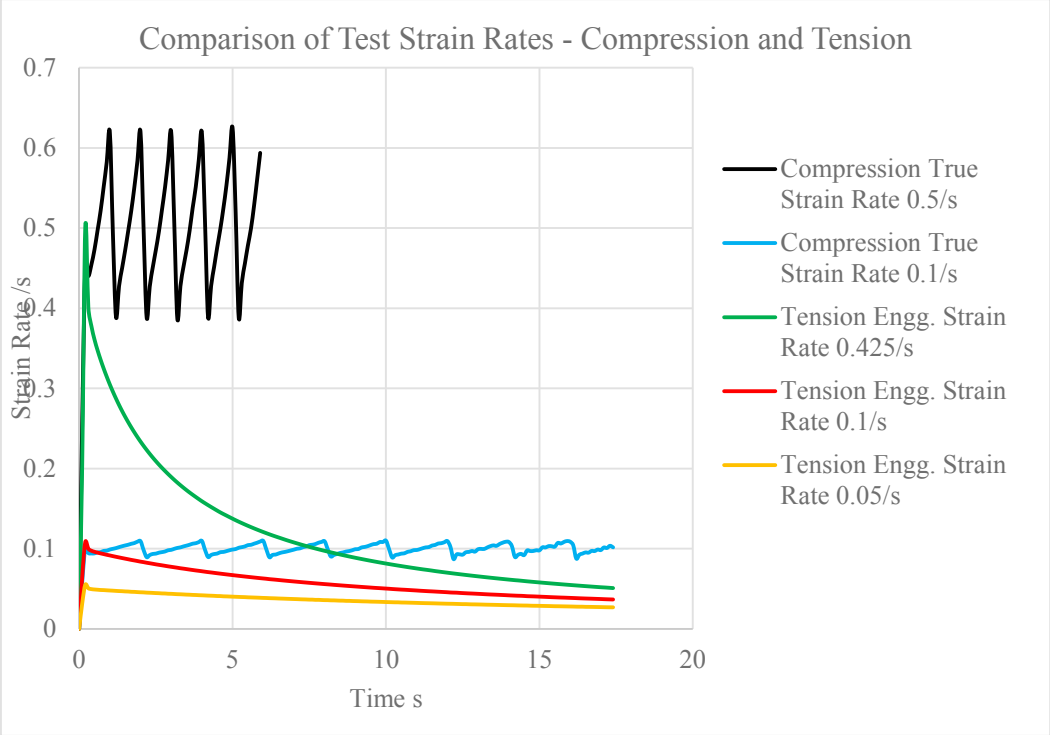

Figure 6.1 True Strain-Rate comparison for tension and compression tests

Figure 6.1 plots compressive and tensile true strains with respect to time. It can be seen that since the tensile tests were carried out at a constant engineering strain rate, the true strain starts at the engineering strain rate and falls logarithmically to very small values at large strain.

So, a direct comparison of tensile and compressive tests was not possible. Furthermore, if a constant engineering strain rate was used for compression and tension tests, the true

strain rates would diverge even more. However, since the compression data at a true strain rate of 0.1/s matches with tensile data at the engineering strain rate of 0.1/s in the small deformation region and tensile data at the engineering strain rate of 0.425/s in the mid-deformation region, these three test results were taken to be compared.

6.3 Experimental Results Comparison

6.3.1 True Stress vs True Strain

Figures 6.2 to 6.7 show the plot of True Stress vs True Strain for compression at true strain-rate (TSR) 0.1/s and tension at engineering strain-rates (ESR) 0.1/s and 0.425/s. As discussed earlier, a one-to-one comparison between the tension and compression curves would not be proper because of variable true strain-rate in tensile tests. However, since Tensile test with ESR 0.1/s has a true strain close to 0.1/s in the beginning of the test and ESR 0.425/s in the mid-deformation region, these two tensile results are compared with the compression data at TSR 0.1/s.

It can be inferred from the figure 6.2 and onwards that the true stress vs true strain plots are very similar for the tensile and compressive tests and are almost overlaid on each other. Tensile true stresses are slightly lower than compressive true stress as the true strain reaches a magnitude close to 1, which may be attributed to the fact that the tensile true strain rates start to fall well below the compressive true strain at those points.

The point where the tensile and compressive true stresses diverge significantly can be considered to be the crystallization onset point for the tensile tests. This point signifies the onset of drastic strain hardening, observed only in tensile tests and as suggested earlier could be attributed to strain-induced crystallization.

This point of significant strain hardening is seen to be dependent on tensile strain rate and usually occurs at a true-strain of about 1.3 at 363K. As temperature increases, this point shifts to higher true-strains, and at 373K is seen to occur close to a true-strain of 1.5-1.6, which is the point where the compression test reaches maximum compression.

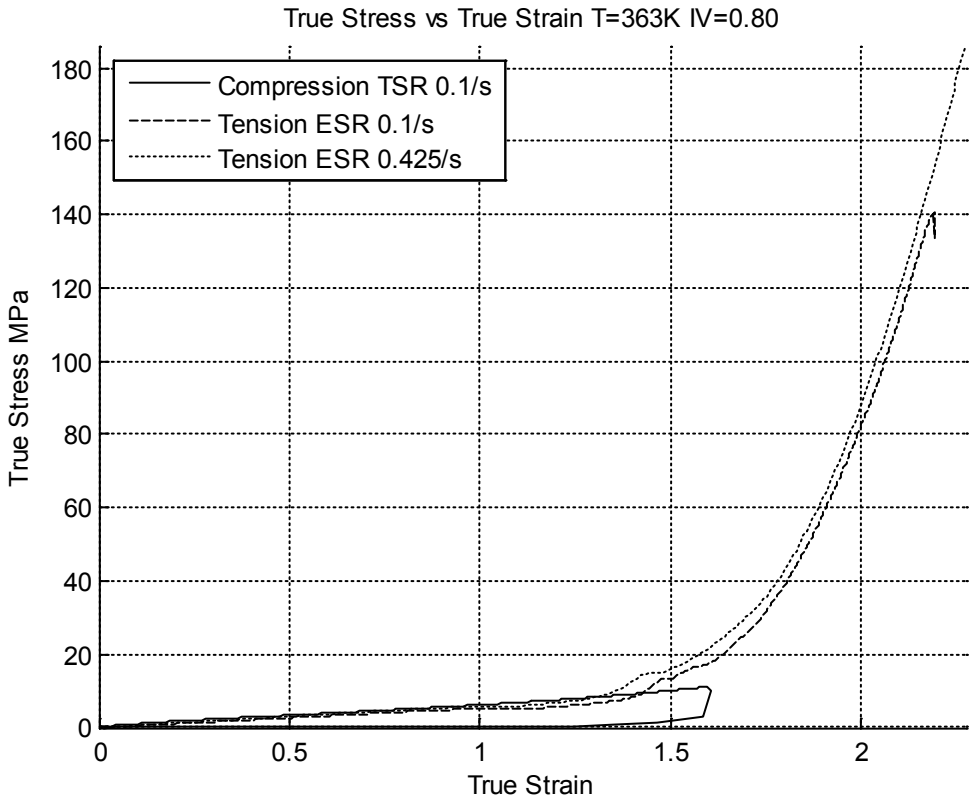

Figure 6.2 True Stress vs True Strain T=363K IV=0.80

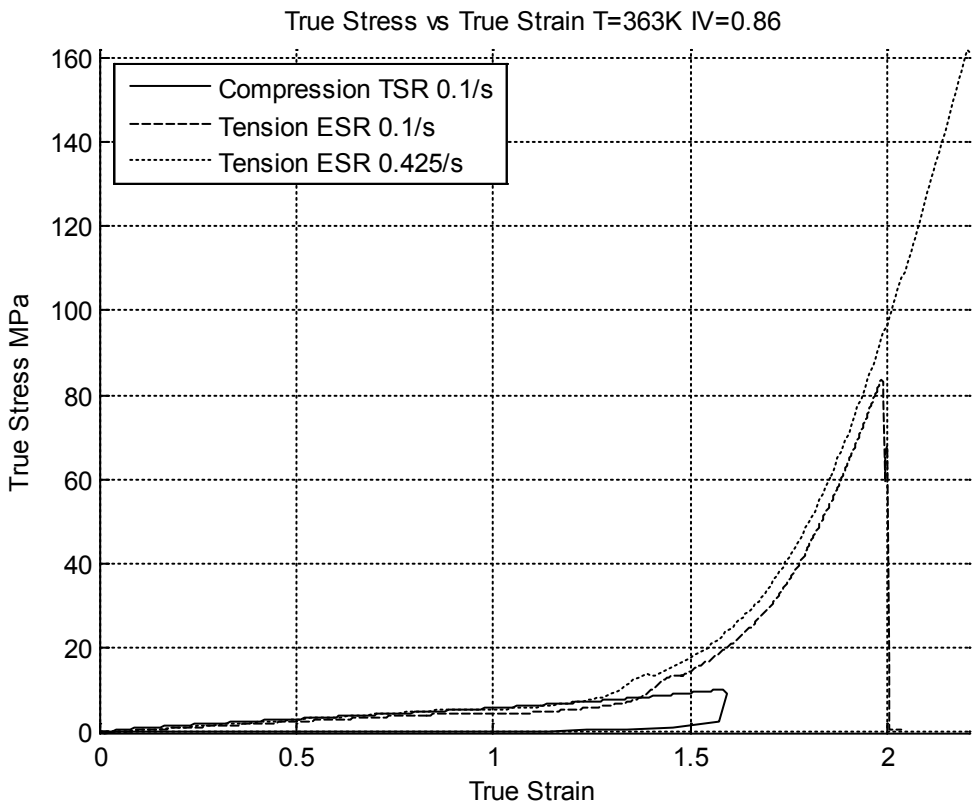

Figure 6.3 True Stress vs True Strain T=363K IV=0.86

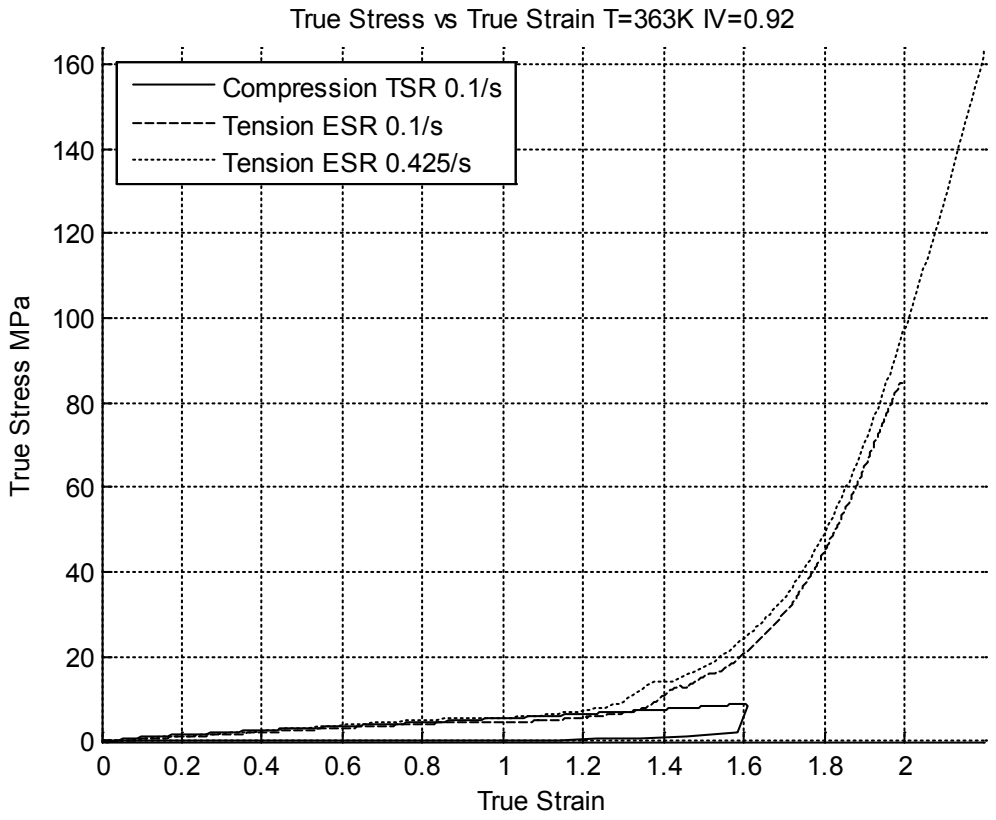

Figure 6.4 True Stress vs True Strain T=363K IV=0.92

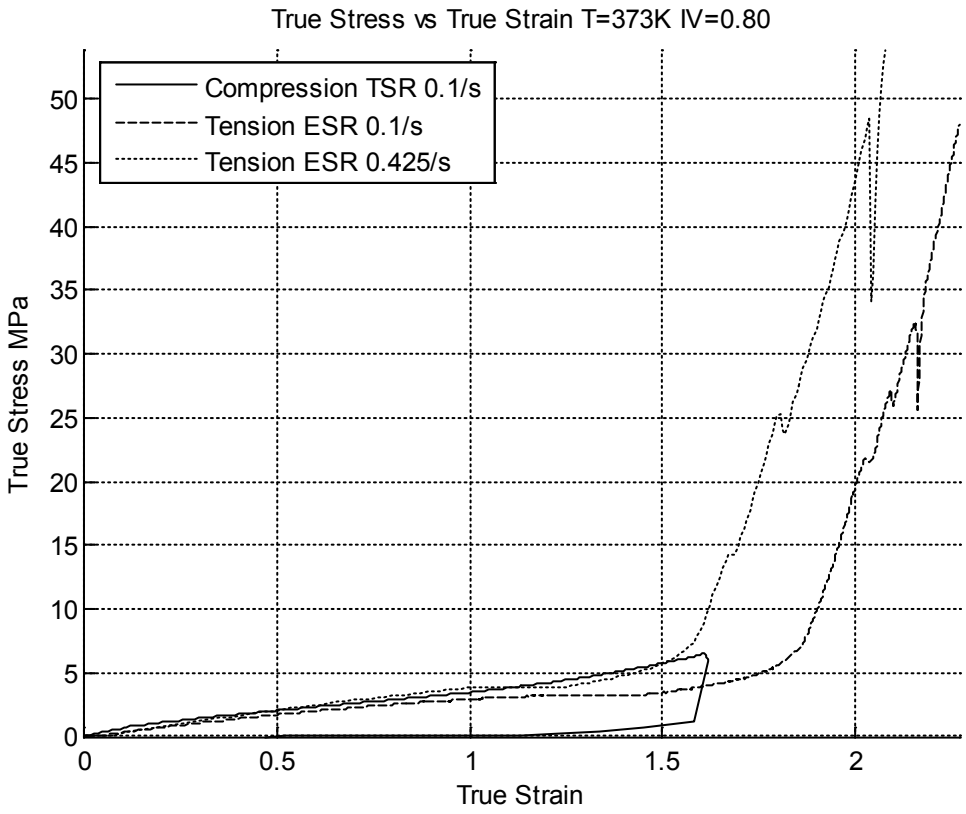

Figure 6.5 True Stress vs True Strain T=373K IV=0.80

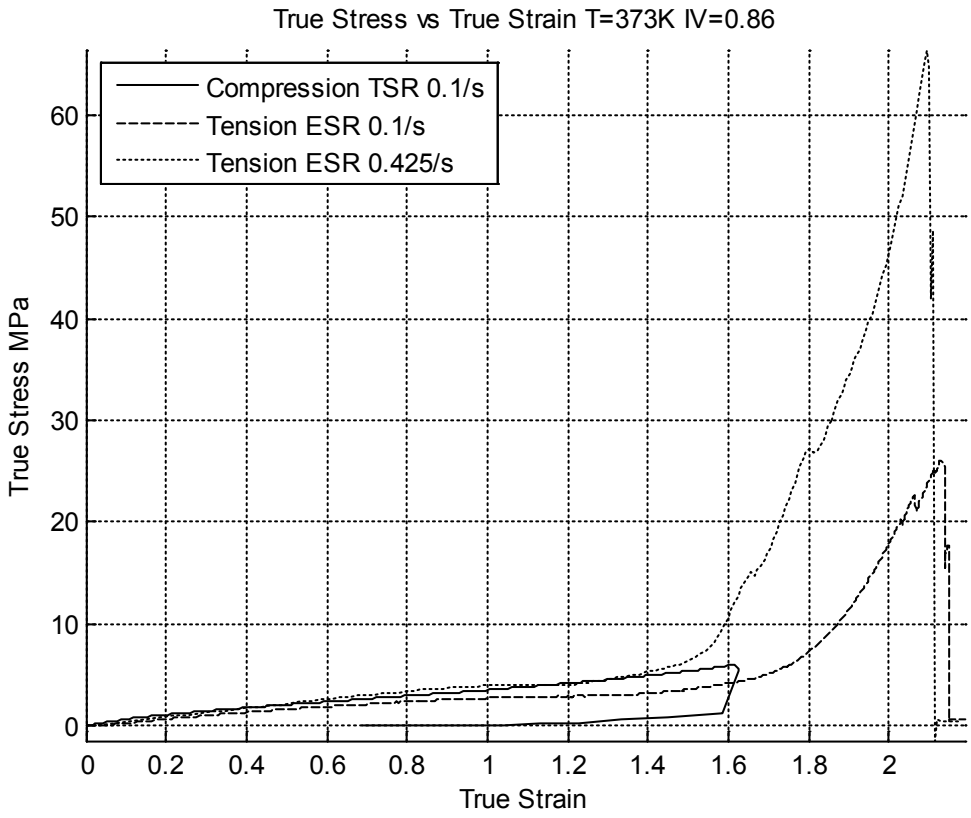

Figure 6.6 True Stress vs True Strain T=373K IV=0.86

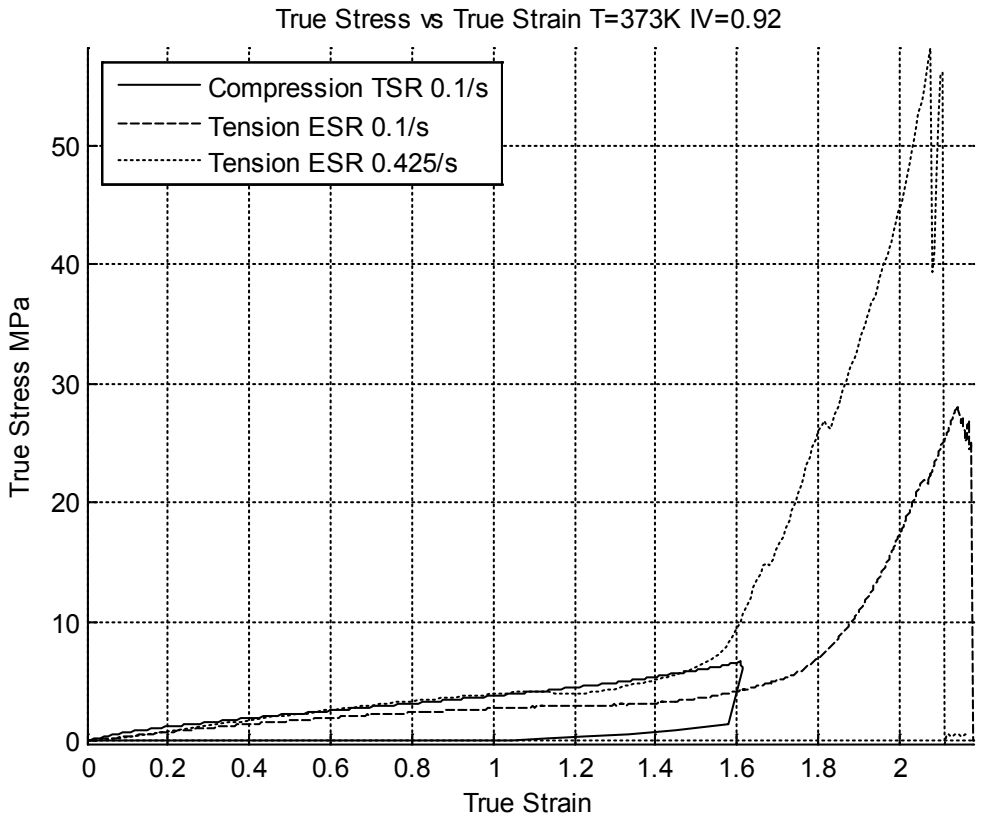

Figure 6.7 True Stress vs True Strain T=373K IV=0.92

6.3.2 True Stress vs First Stretch Invariant

Figures 6.8 to 6.13 show the variation true-stress with respect to the first stretch invariant for the compression and tensile tests. Assuming incompressibility, the first invariant would be smaller along the stretch axis for compressive data and higher for tensile data. Nevertheless, these plots are provided to provide a reference-independent look on the comparison of tensile and compressive experimental data. If S_{11}, S_{22} and S_{33} are the

diagonal elements of the principal stretch tensor, the first invariant is the trace of the principal stretch tensor given by

$$I_1 = S_{11} + S_{22} + S_{33}$$

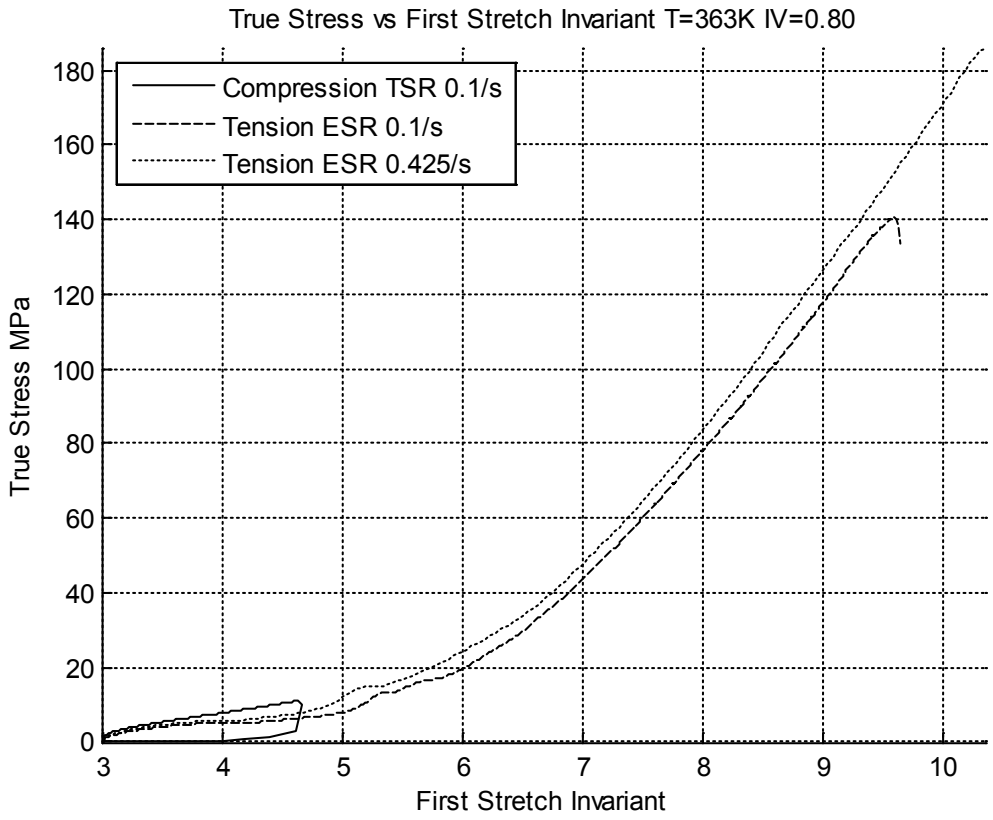

Figure 6.8 True Stress vs First Stretch Invariant T=363K IV=0.80

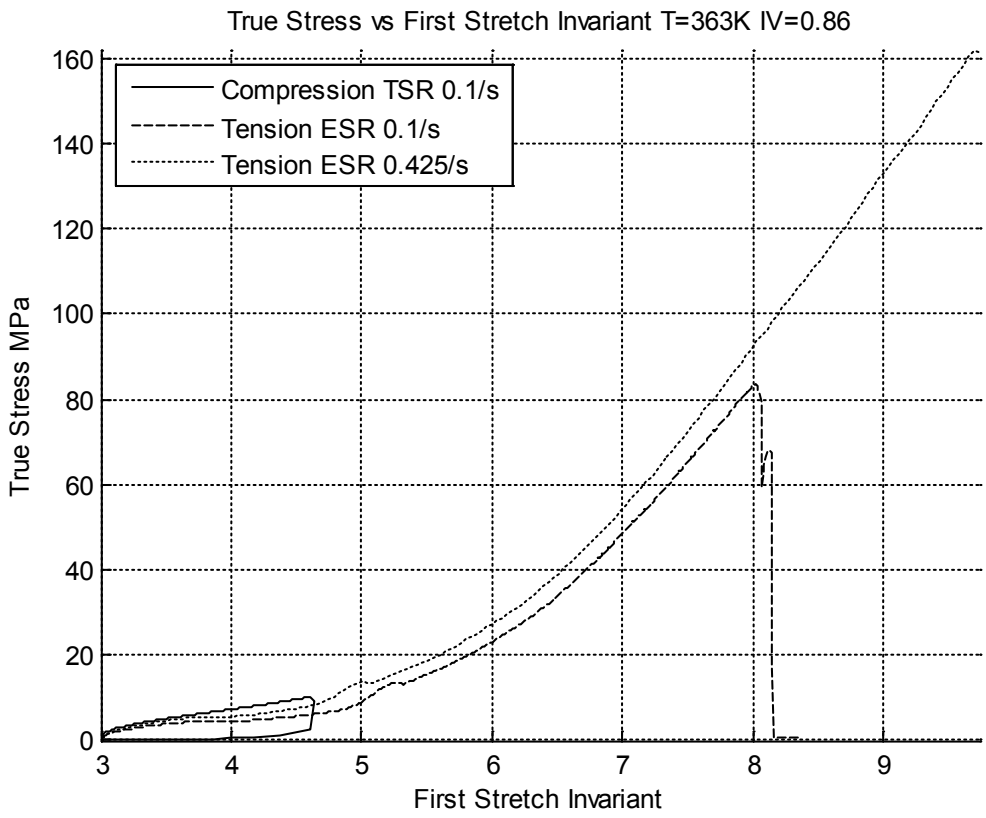

Figure 6.9 True Stress vs First Stretch Invariant T=363K IV=0.86

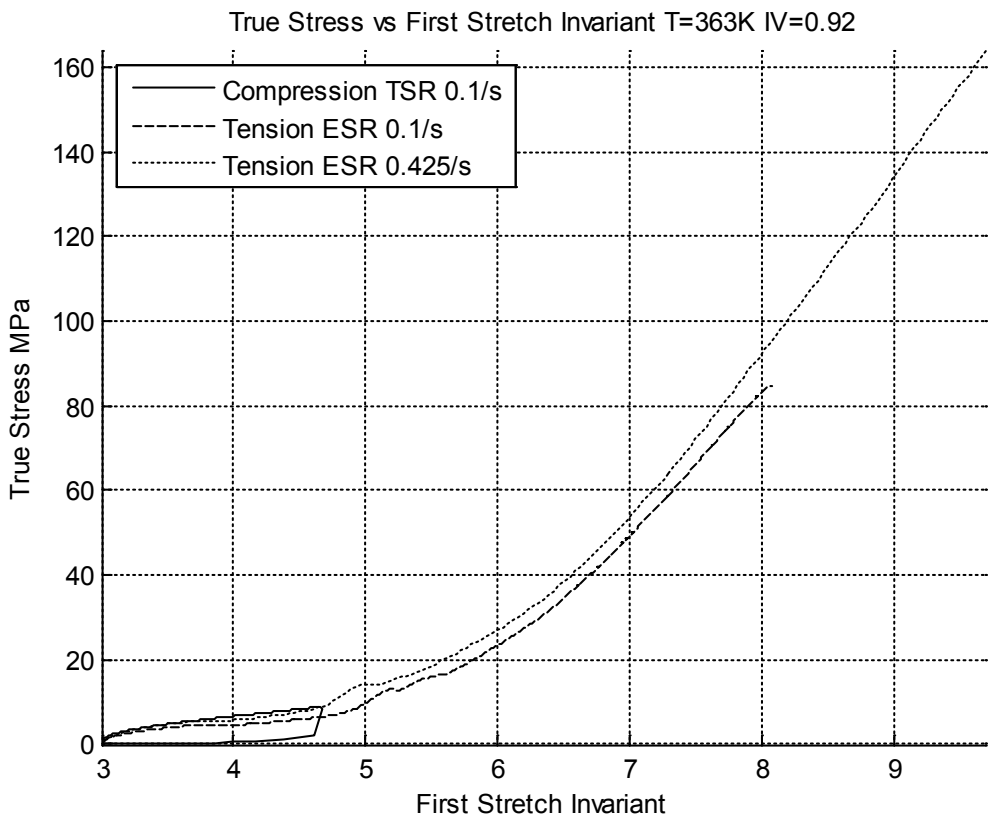

Figure 6.10 True Stress vs First Stretch Invariant T=363K IV=0.92

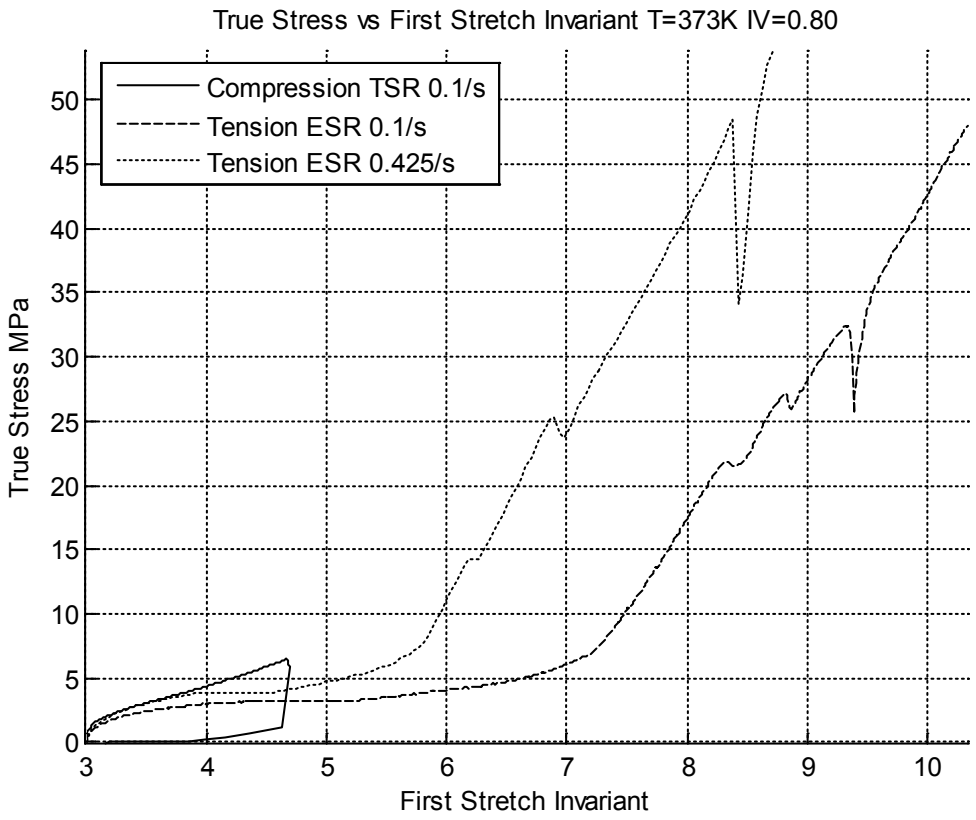

Figure 6.11 True Stress vs First Stretch Invariant T=373K IV=0.80

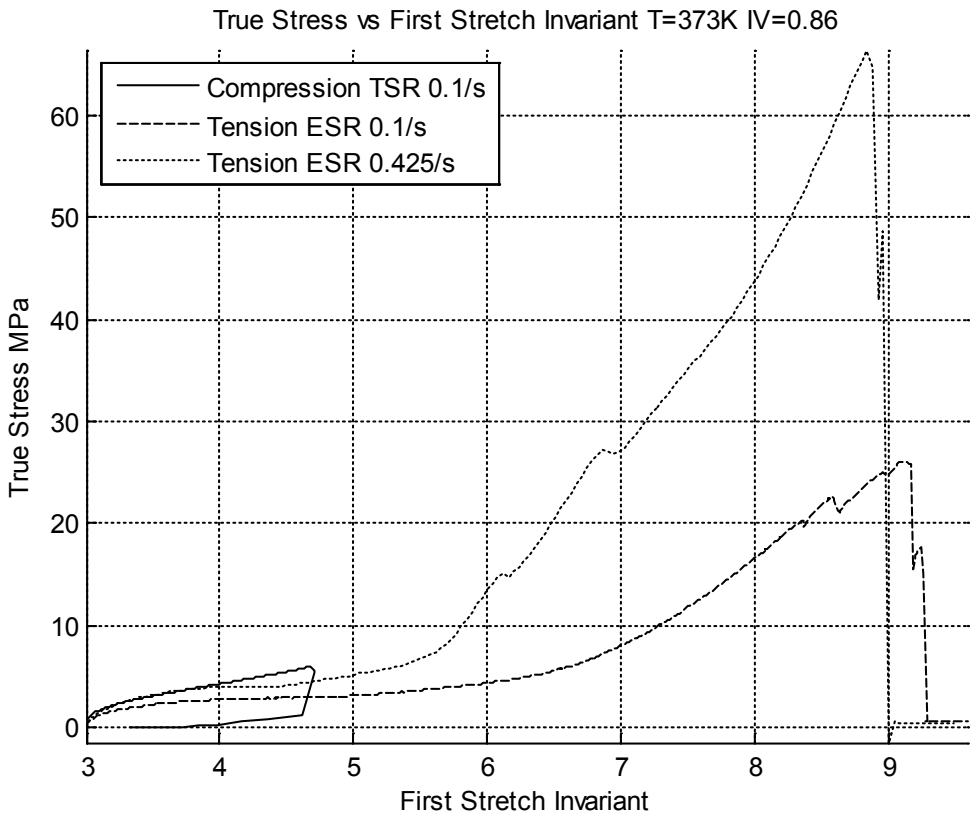

Figure 6.12 True Stress vs First Stretch Invariant T=373K IV=0.86

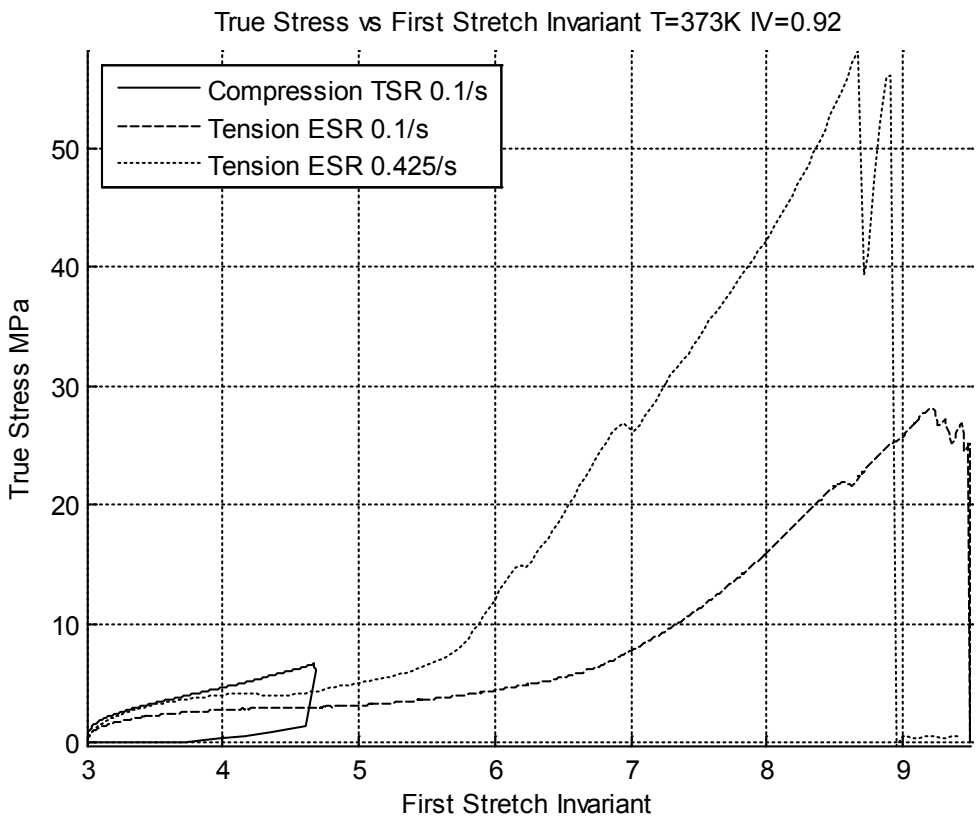

Figure 6.13 True Stress vs First Stretch Invariant T=373K IV=0.92

6.3.3 True Stress vs Second Stretch Invariant

Figures 6.14 to 6.19 show the variation in true-stress with respect to the second stretch invariant for the compression and tensile tests. Assuming incompressibility, the second invariant would be larger along the stretch axis for compressive data and smaller for tensile data. These plots provide a reference-independent look on the comparison of tensile and compressive experimental data. If S_{11}, S_{22} and S_{33} are the diagonal elements of the principal stretch tensor, the second invariant is obtained from the formula

$$I_2 = S_{11}S_{22} + S_{22}S_{33} + S_{33}S_{11}$$

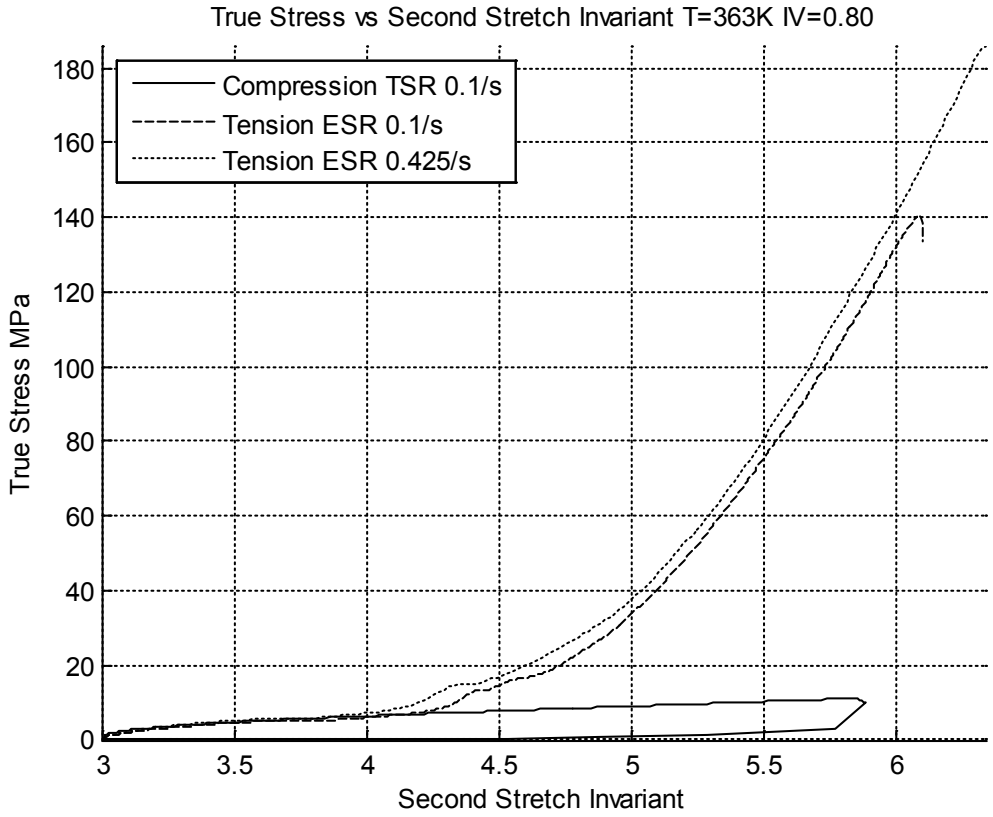

Figure 6.14 True Stress vs Second Stretch Invariant T=363K IV=0.80

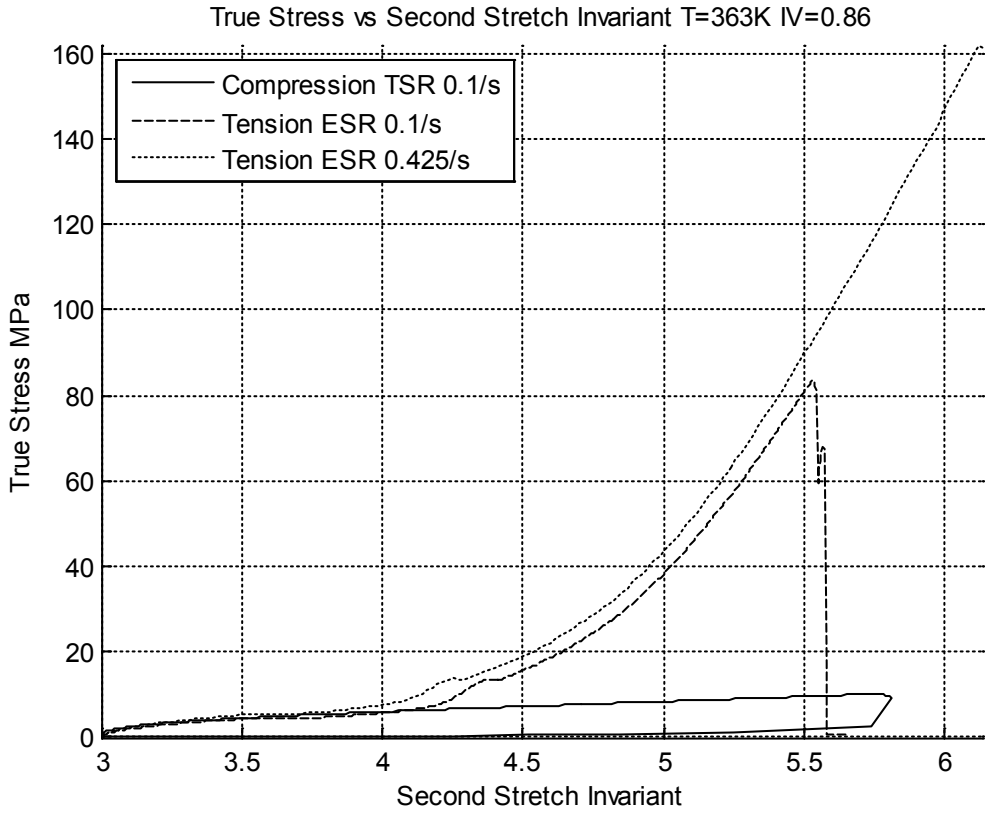

Figure 6.15 True Stress vs Second Stretch Invariant T=363K IV=0.86

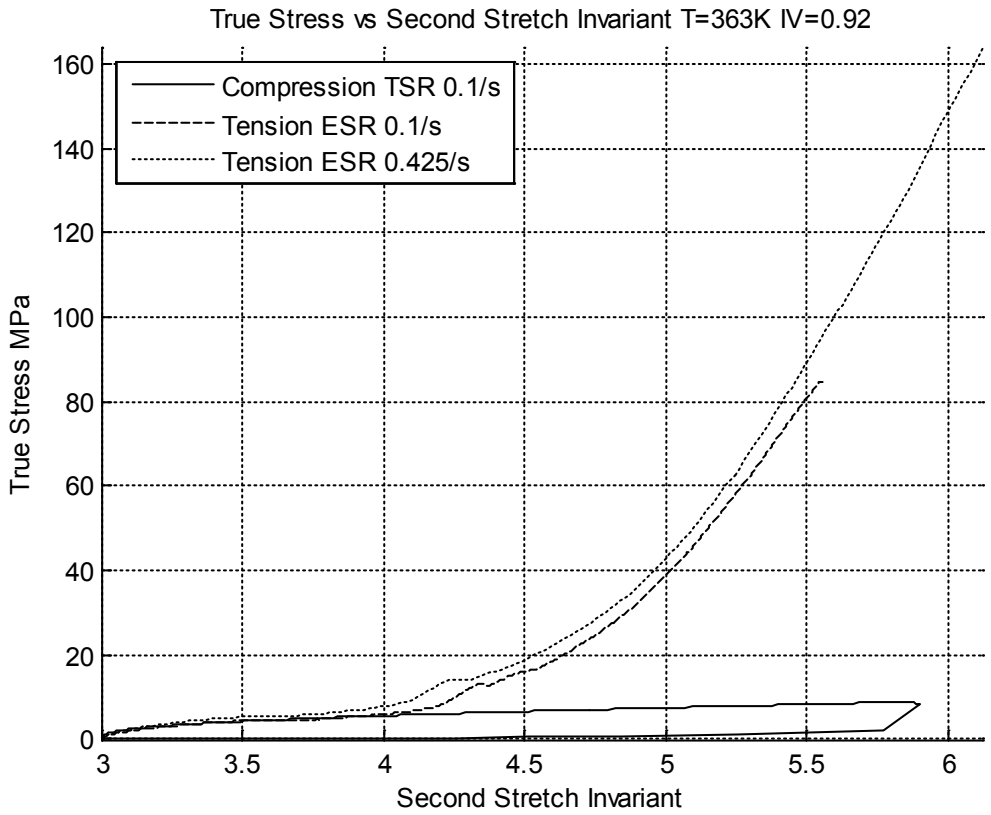

Figure 6.16 True Stress vs Second Stretch Invariant T=363K IV=0.92

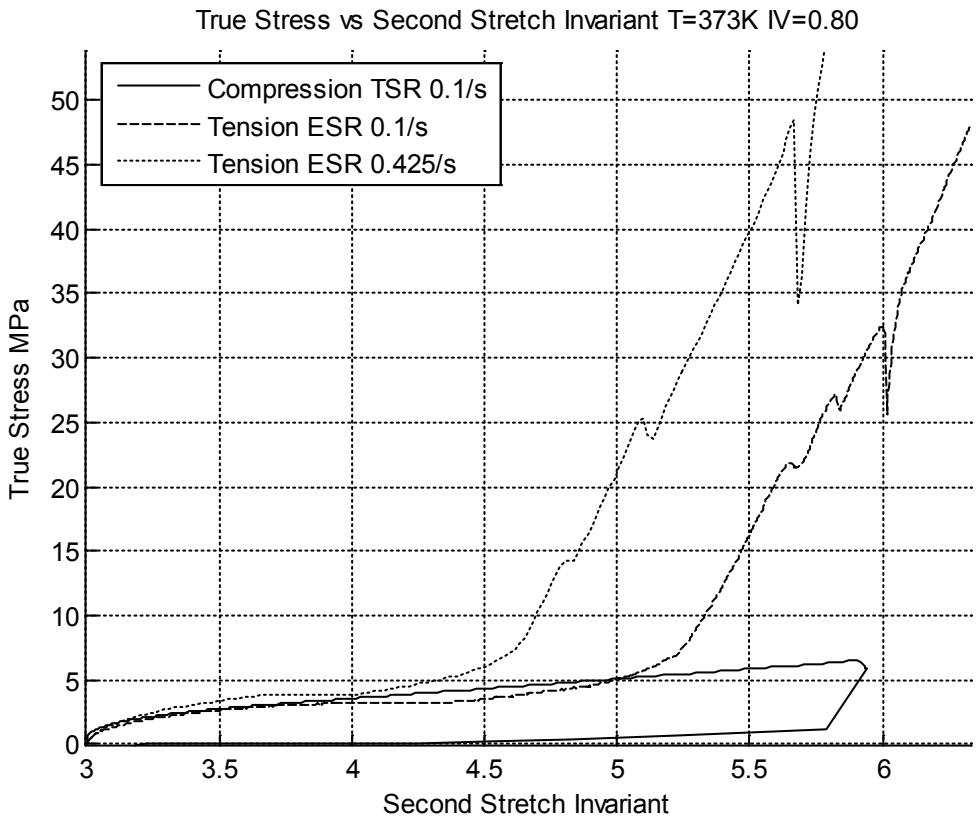

Figure 6.17 True Stress vs Second Stretch Invariant T=373K IV=0.80

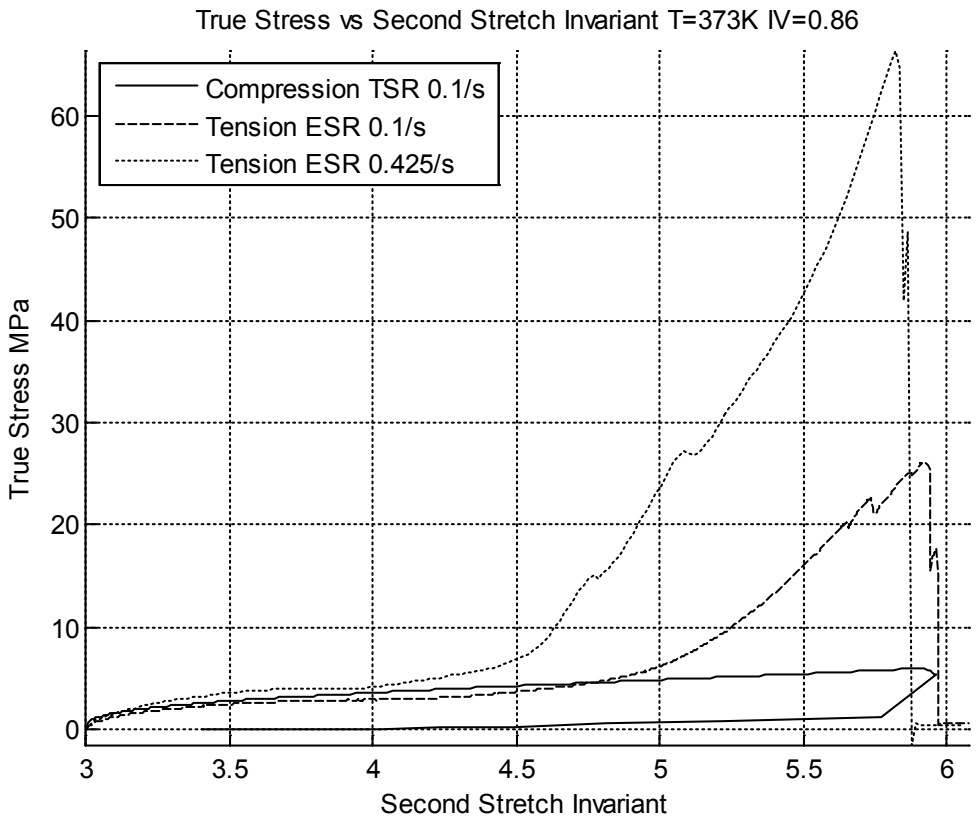

Figure 6.18 True Stress vs Second Stretch Invariant T=373K IV=0.86

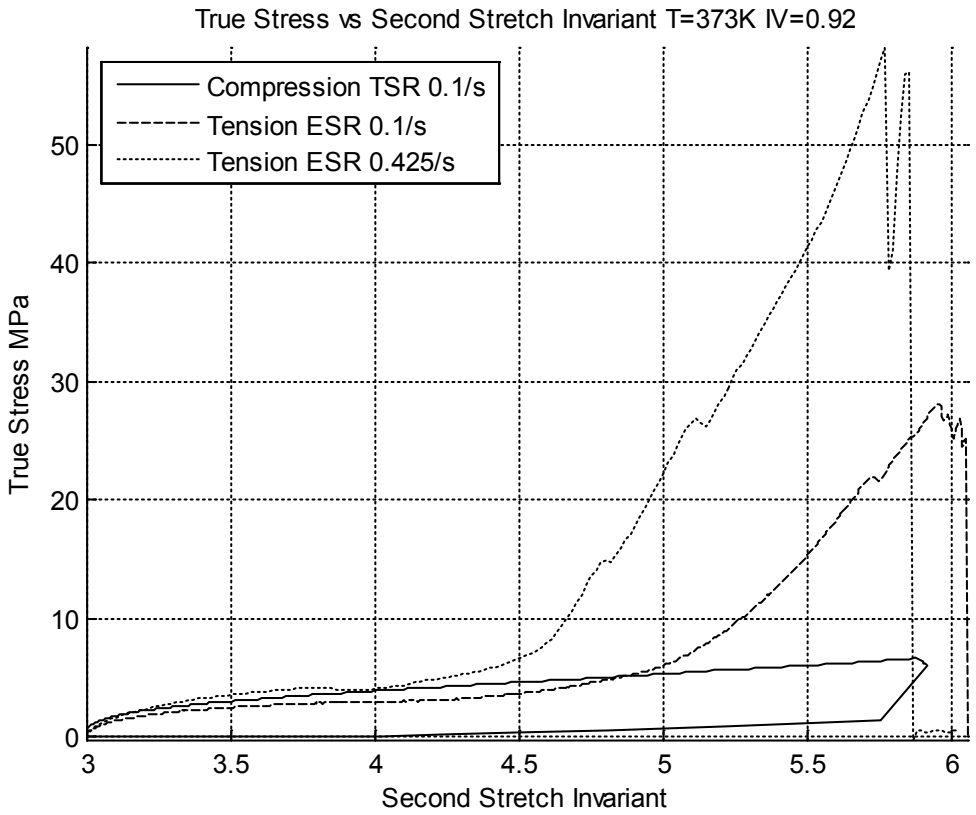

Figure 6.19 True Stress vs Second Stretch Invariant T=373K IV=0.92

In order to check whether the final true compressive strain was small to not cause the onset of crystallization, compression tests were repeated for a few samples of 0.80 IVs to reach higher final true strains. However, the curves from these tests simply followed the trend of the original compressive tests, i.e., no sudden strain hardening during compression was observed. This can be seen in figures 6.20 for 363K and 6.21 for 373K. This suggested the existence of a mechanism which finds tension to be favorable for the onset of crystallization and not compression.

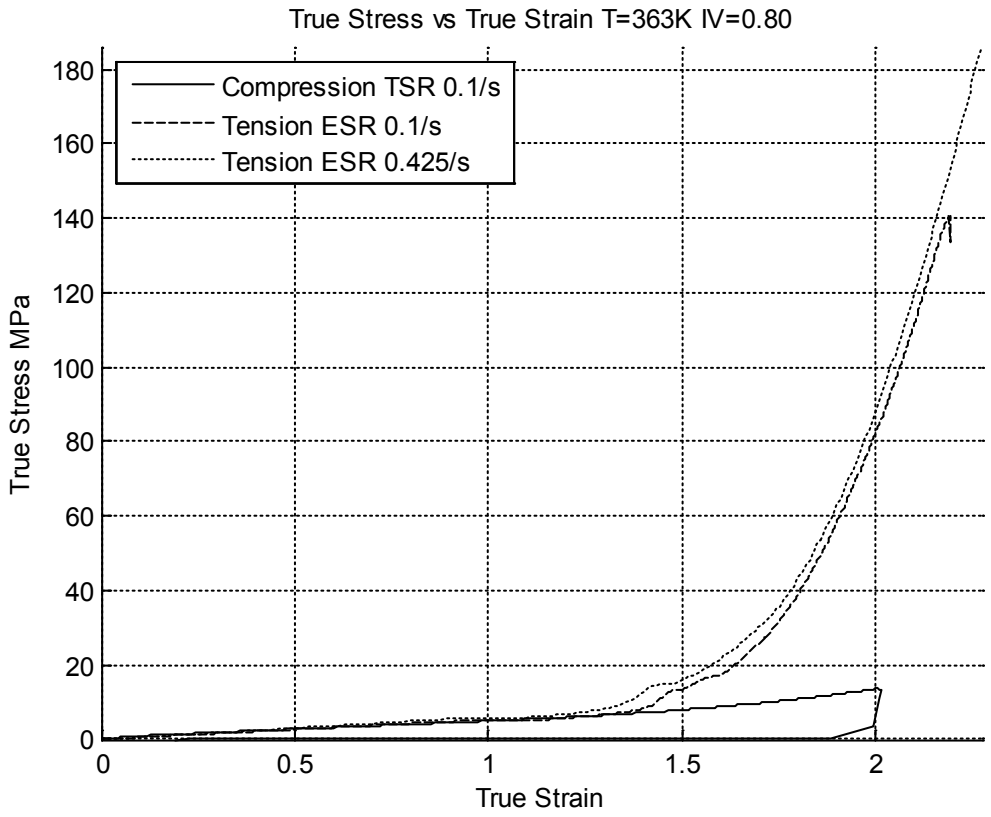

Figure 6.20 True Stress vs True Stress T=363K IV=0.80 – Higher compressive strain

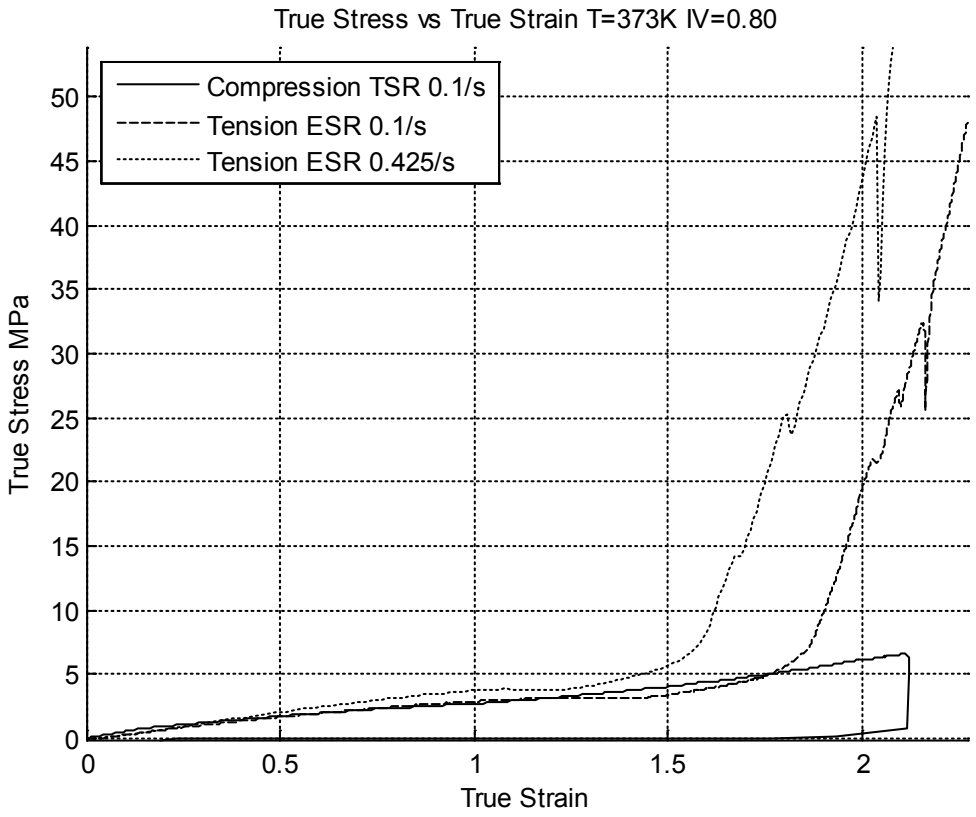

Figure 6.21 True Stress vs True Stress T=373K IV=0.80 – Higher compressive strain

The following figures plot true strain versus the invariants.

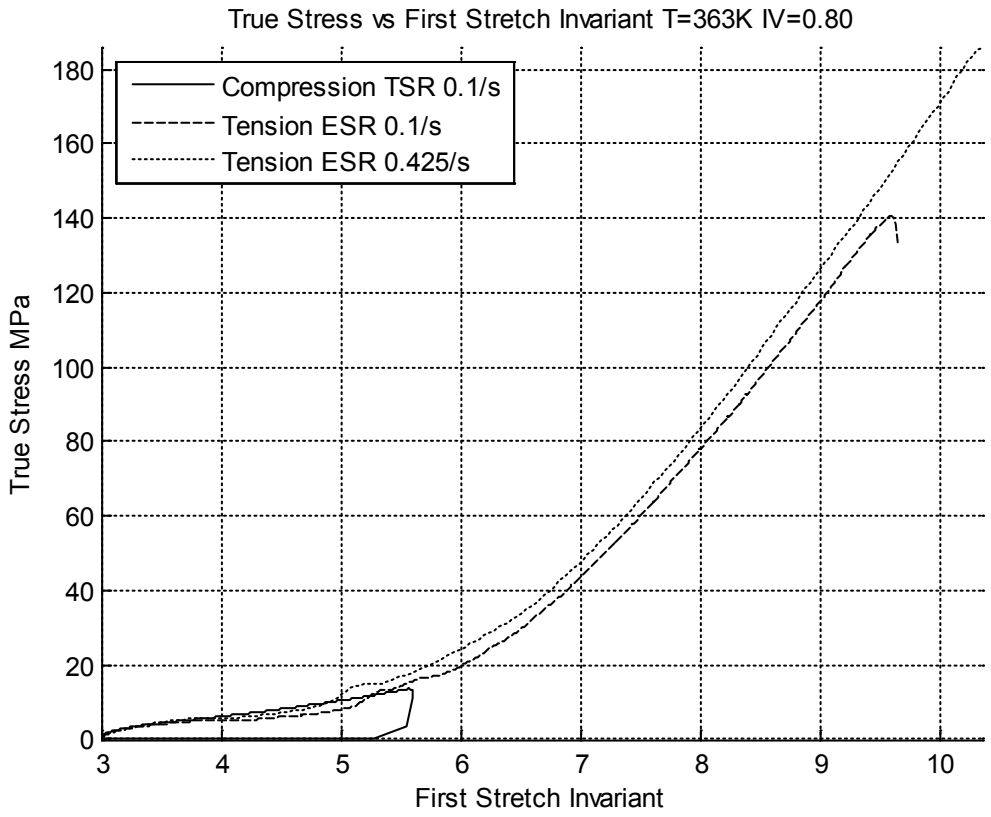

Figure 6.22 True Stress vs First Stretch Invariant T=363K IV=0.80 – Higher compressive strain

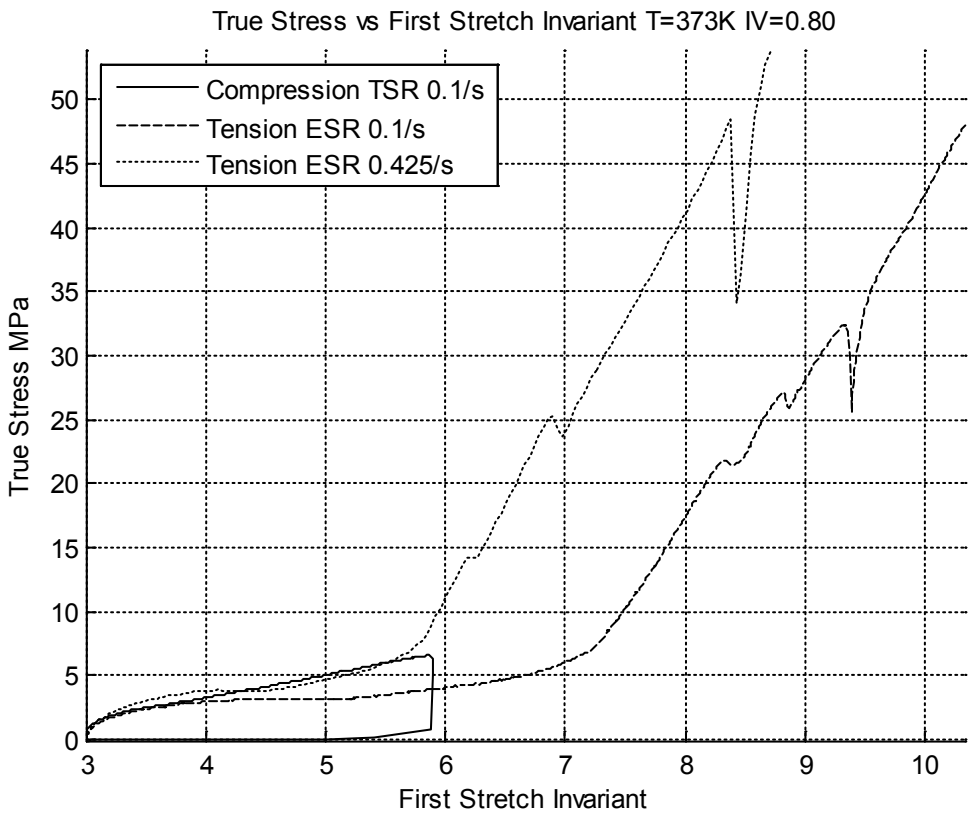

Figure 6.23 True Stress vs First Stretch Invariant T=373K IV=0.80 – Higher compressive strain

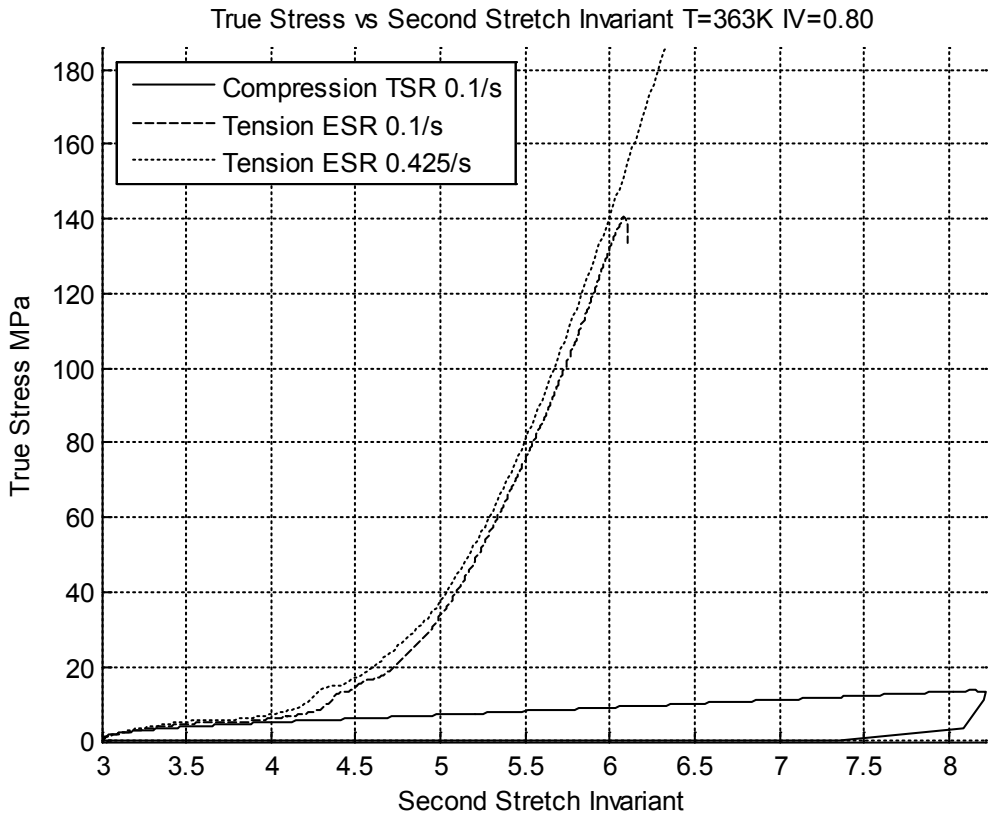

Figure 6.24 True Stress vs Second Stretch Invariant T=363K IV=0.80 – Higher compressive strain

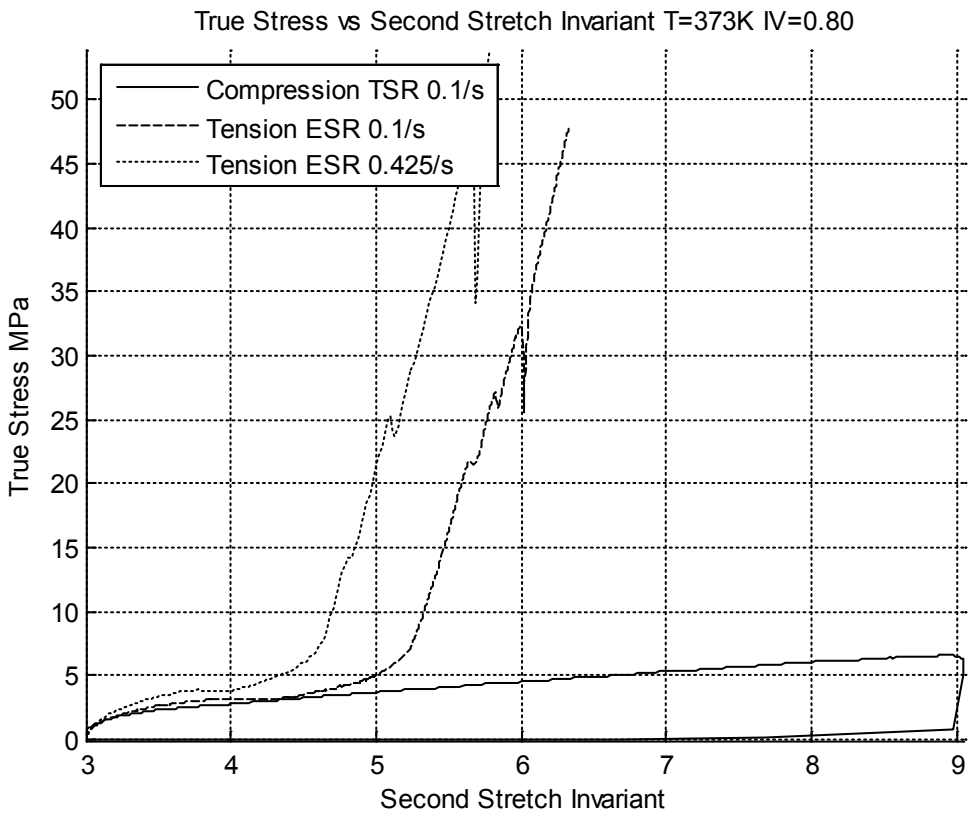

Figure 6.25 True Stress vs Second Stretch Invariant T=373K IV=0.80 – Higher compressive strain

It is apparent from figures 6.20 to 6.25 that while true stress vs true strain and true stress vs invariants trends remain similar for tensile and compressive tests initially, there is a sudden onset of strain-hardening that could be observed only for tensile tests. The tension and compression curves match up well until the crystallization point.

6.4 Conclusion

This chapter compared true stress with respect to true strain and the first and second stretch invariants for comparison of tensile and compressive experimental data. By comparison, it could be concluded that the tensile and compressive tests provided similar magnitudes of stress at the initial stretches. However, beyond a temperature and strain dependent medium stretch level, tensile experiments show a sudden onset of high strain hardening leading to very high stress levels. This observation is absent in compressive tests, which suggests the occurrence of crystallization only in tensile testing. This conclusion necessitated the development of a mathematical model for crystallization to be included for tensile testing simulation in the Dupaix-Boyce model.

Chapter 7: The Elasto-Visco-Plastic (EVP) Constitutive Model

7.1 Introduction

This chapter describes the Elasto-Visco-Plastic (EVP) constitutive model (Mir, Benrabah and Thibault, 2007), which has been used to characterize PET for comparison with the Dupaix-Boyce constitutive model in this work. This model is built on the assumption that elastic strain is very small in a polymer undergoing stretch-blow molding in comparison to plastic strain, which is very large relatively. This plastic strain also depends on the strain rate, hence the model is primarily visco-plastic. This visco-plastic part is modeled as a three-dimensional implementation of the G'Sell-Jonas law (G'Sell et al, 1979) with the inclusion of both hardening and softening phenomena.

7.2 Description

As described in the introduction, the EVP model is an implementation of the G'Sell-Jonas model in three-dimensions. The G'Sell-Jonas model is a uniaxial visco-plastic model and is represented by the following relation

$$\sigma_0(\varepsilon, \dot{\varepsilon}, T) = Ke^{\frac{a}{T}}(1 - e^{-w\varepsilon})e^{h_g\varepsilon^2}\dot{\varepsilon}^m$$

This model is temperature and rate dependent as inferred from the presence of variables T (Temperature), $\dot{\varepsilon}$ (Strain rate) and ε (Final strain). K, m, a and w are model constants. h_g is the hardening modulus and captures strain hardening observed in polymers at large strain.

Some polymers exhibit loss of stress once stress reaches a peak. This phenomenon is called strain-softening and is observed in PET (Dupaix and Boyce, 2005). This is not accounted for in the model. The G'Sell-Jonas model is generalized to 3D and a parameter representing strain-softening is included. It is based on the von-Mises yield criterion and is independent of hydrostatic pressure and material orientation. The constitutive equation consists of the following relation

$$J_2(p, \dot{p}, T) = Ke^{\frac{a}{T}}(1 - e^{-wp})e^{(h_g p^2 - h_f p)}\dot{p}^m$$

J_2 is the von Mises stress and p is the equivalent visco-plastic strain given by the relation

$$\dot{p} = \sqrt{\frac{3}{2}\dot{\varepsilon}^{vp} : \dot{\varepsilon}^{vp}}$$

Where the operator ":" describes the double dot product or the scalar product of two tensors, returning a scalar. As described in the G'Sell-Jonas model, h_g is the hardening modulus and captures strain hardening. In addition, the softening modulus h_f in included to model strain softening and $\dot{\varepsilon}^{vp}$ is the visco-plastic strain tensor.

The rate of total mechanical strain tensor is assumed to be composed additively of the elastic and visco-plastic rate of strain tensors given by the relation

$$\dot{\varepsilon} = \dot{\varepsilon}^{e} + \dot{\varepsilon}^{vp}$$

Rate of elastic strain $\dot{\varepsilon}^{e}$ is related to the rate of second order stress $\dot{\sigma}$ by the fourth order elasticity tensor H built using the constants λ and μ using standard continuum mechanics formulae.

$$\dot{\sigma} = H : \dot{\varepsilon}^{e}$$

The following expressions relate the rate of visco-plastic strain tensor $\dot{\varepsilon}^{vp}$ to von Mises stress J_2 and deviatoric stress S.

$$\dot{\varepsilon}^{vp} = \frac{3}{2J_2}\dot{p}S$$

$$J_2 = \sqrt{\frac{3}{2}S : S}$$

The deviatoric stress tensor S is computed by subtracting the hydrostatic stress, which is given by the trace of the stress tensor σ divided by 3, from the diagonal elements of the stress tensor σ.

$$S = \sigma - \frac{trace(\sigma)}{3}$$

7.3 EVP Model fits for experimental data

7.3.1 Uniaxial Compression Fits

This section shows the fit of the EVP model to compression tests at temperatures 363K and 373K and strain rates 0.1/s and 1/s. The fits were done manually. For the fits that

could be obtained, though the compression process was captured accurately, the unloading part was not. Refer Figure 7.1 where the unloading curve deviates significantly from the compression curve.

This model also required refitting of constants to accurately capture different temperature and strain rate conditions. The hardening modulus, hg, had to be changed from that for 363K to fit curves at 373K. Refer to tables 7.1 and 7.2 for the constants used in the fit.

Table 7.1 EVP Model constants for temperature 363K

Model constant	Value
K	1.0882E-8
a	6869.7704
w	5000
hg	35.202
hf	0.2206
m	0.18661

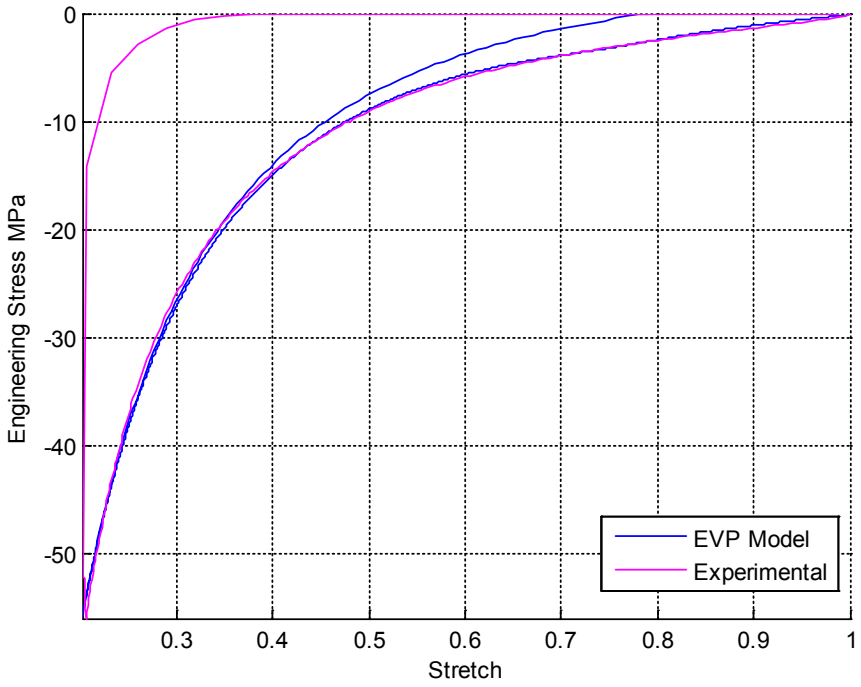

Figure 7.1 Experimental and EVP model fit at 363K 0.1/s

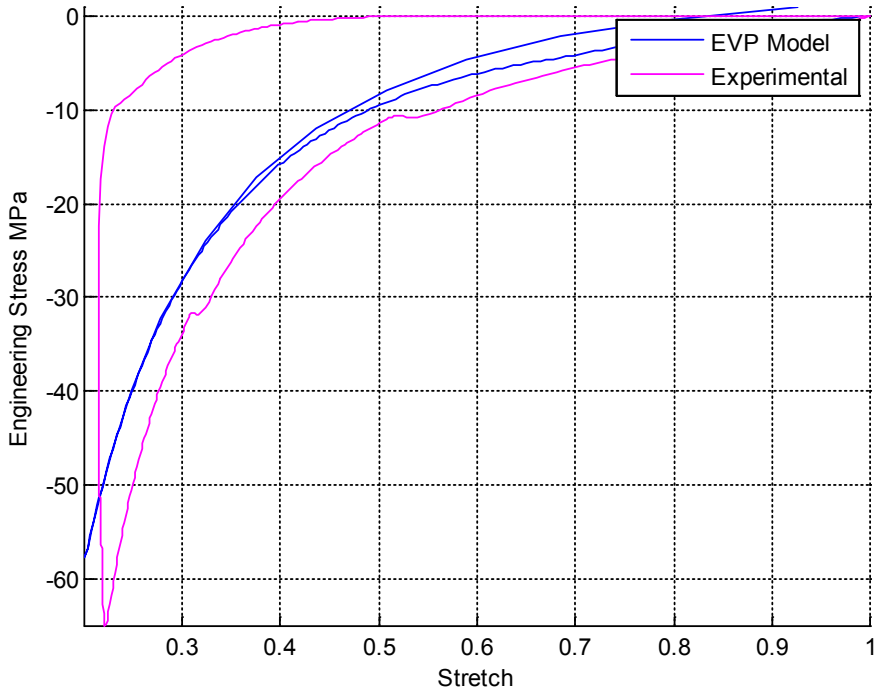

Figure 7.2 Experimental and EVP model fit at 363K 1/s

Table 7.2 EVP Model constants for temperature 373K

Model constant	Value
K	1.0882E-8
a	6869.7704
w	5000
hg	9.8202
hf	0.2206
m	0.18661

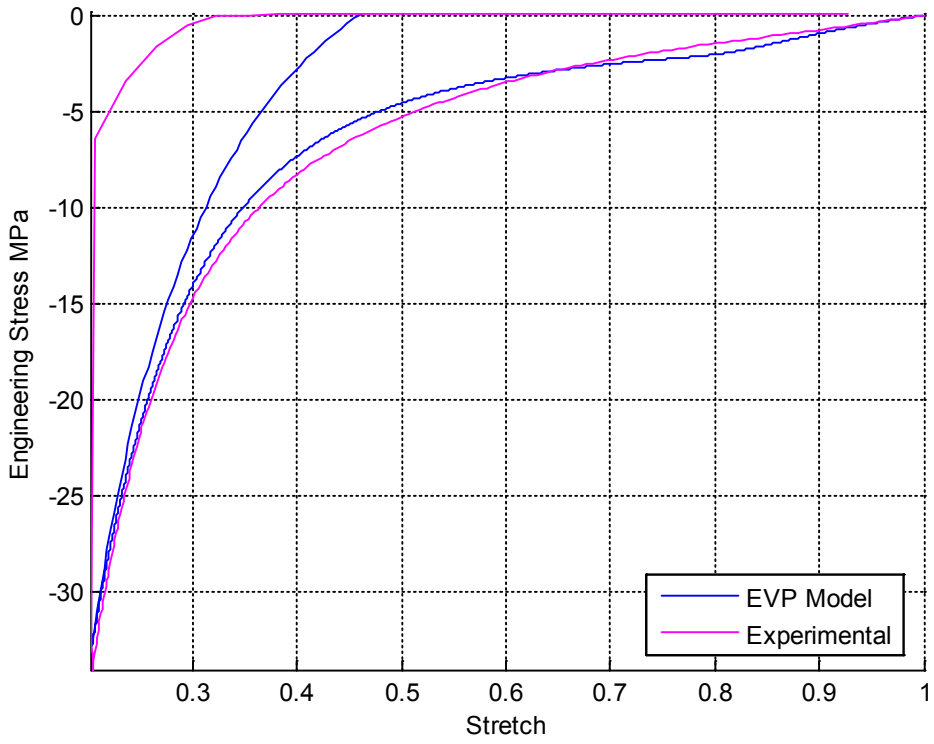

Figure 7.3 Experimental and EVP model fit at 373K 0.1/s

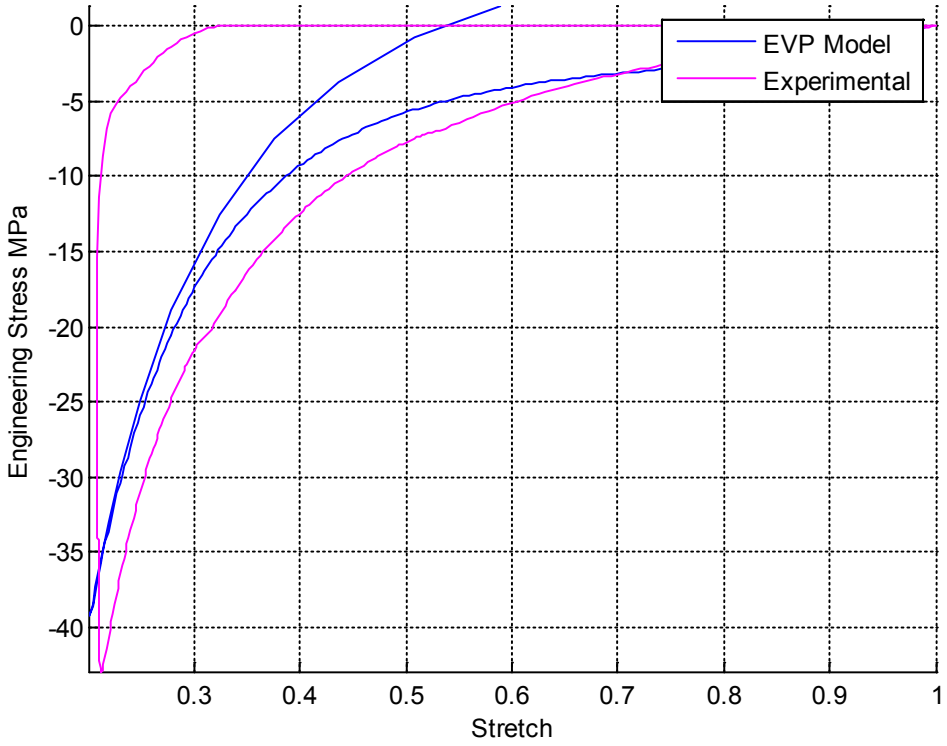

Figure 7.4 Experimental and EVP model fit at 373K 1/s

7.3.2 Uniaxial Tension Fits

Figures 7.5 and 7.6 compare experimental and EVP model results for tension tests. The model constants are the same as used for compression tests, given in tables 7.1 and 7.2. It can be seen that there is a close agreement between experimental and EVP model results up to a small value of stretch beyond which there is unprecedented strain hardening not captured by the model which is similar to results obtained from the Dupaix-Boyce model without crystallization in tension testing. The EVP model is used in blow molding simulation. It is available in the software that was used by the sponsor, Blow-view. The

EVP model also can be modified by inclusion of crystallinity to capture the upturn in the stress-strain curve. However details about this change was not available to explore in more detail.

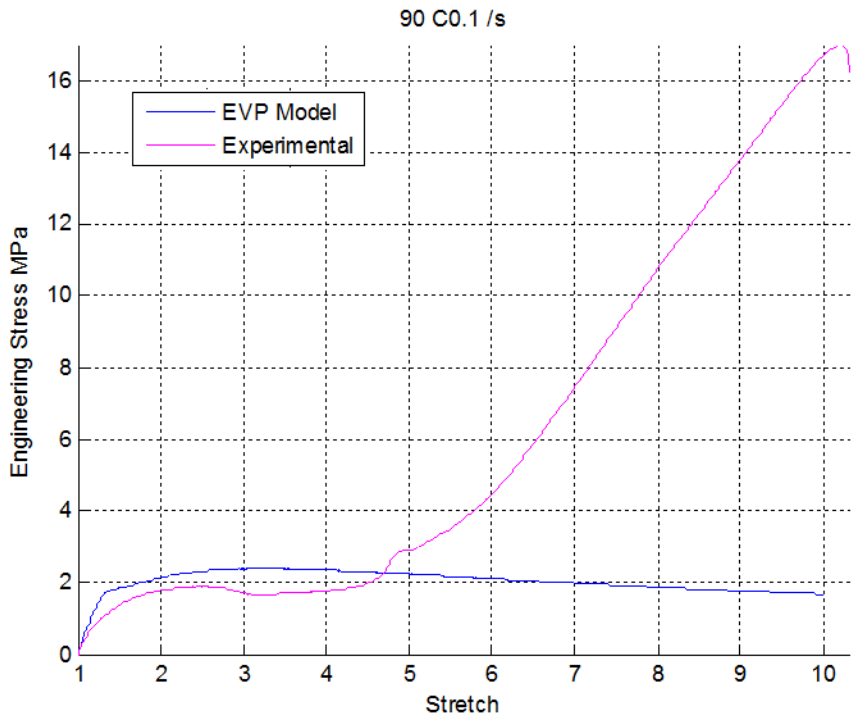

Figure 7.5 Tensile experimental and EVP model fit at 363K 0.1/s, Constants as in Table 7.1

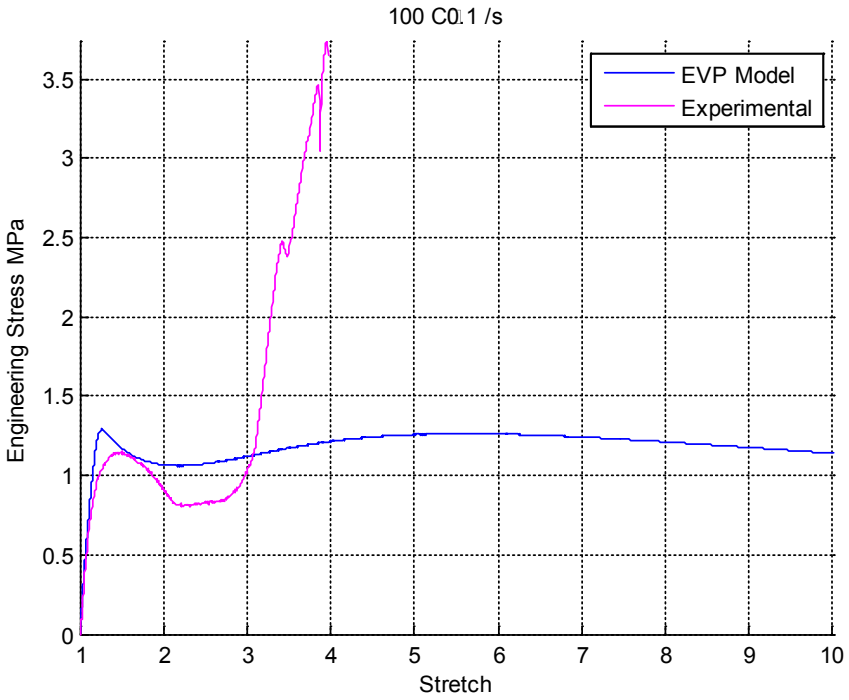

Figure 7.6 Tensile experimental and EVP model fit at 373K 0.1/s, Constants as in Table 7.2

7.4 Comparison of Dupaix-Boyce and EVP Models

It has been shown in this chapter that the EVP model has provided good fits for the compression part of compression tests. However, the relaxation part is not captured properly for the given material (Figure 7.1 – 7.4). Also, the EVP model required a minor change of constants to fit for other test conditions like different temperatures and strain rate. This is in contrast to the Dupaix-Boyce model, which has captured both compression and relaxation with fair accuracy.

In tension tests, both Dupaix-Boyce and EVP models fail to capture sudden significant strain hardening observed in medium stretch levels and both require some modifications to capture the same. However, since the Dupaix-Boyce model can be related to the physics of the polymer deformation problem, it has been easier to target modifications to sections of the model by physically relating to crystallization mechanisms. This has been done in implementing the Crystallization Module to the Dupaix-Boyce model.

The EVP model is much more empirical in nature and hence, while being lighter to code and run, implementing changes to it to capture physical phenomenon like crystallinity would offer some more challenges. This has not been done in this thesis. The main purpose here has been to study an alternate model and discuss how it compares to the main model of this work, i.e., the Dupaix-Boyce model.

7.5 Conclusion

The EVP model has been fitted to experimental data and the results have been studied in this chapter. Though being simple and light compared to the Dupaix-Boyce model, the EVP model fails to fit unloading in spite of accurately capturing compression. This might be a disadvantage in blow molding simulations where the unloading behavior is important to predict final stress. In addition, the model requires minor change of constants to simulate different test conditions. These factors show that the Dupaix-Boyce model might be better suited to serve blow molding applications.

Chapter 8: Incorporation of Crystallization

8.1 Introduction

As described in the previous chapters, a sudden onset of strain hardening was observed at a moderate stretch level of around 4 to 7 during uniaxial tension tests. This did not occur during compression and also could not be captured by the Dupaix-Boyce model which predicted compression well. This suggested the occurrence of a phenomenon only in tensile conditions and was considered to be associated with strain induced crystallization. In this chapter, algebraic functions to describe the onset of crystallization are added to the Dupaix-Boyce model to capture this phenomenon that was observed during tensile testing.

8.2 Crystallization Modeling Approach

The main effect of crystallization was to increase the stiffness of the polymer, thus causing a higher increase in stress per unit strain. In order to do this, stiffness of the material had to progressively increase with the onset of strain-induced crystallization. There were multiple options to do this in the model and the options considered are explained in the following sections.

Figure 8.1 shows tensile stress-strain properties obtained from samples crystallized after a long period of crystallization in the heated environment chamber at 0.1/s. As can be seen, there is a huge increase in the material's initial stiffness as well as a huge increase in yield stress. It can also be observed that the slope of the normal sample at 363K after the crystallization onset stretch matches with the slopes on the fully crystallized specimens.

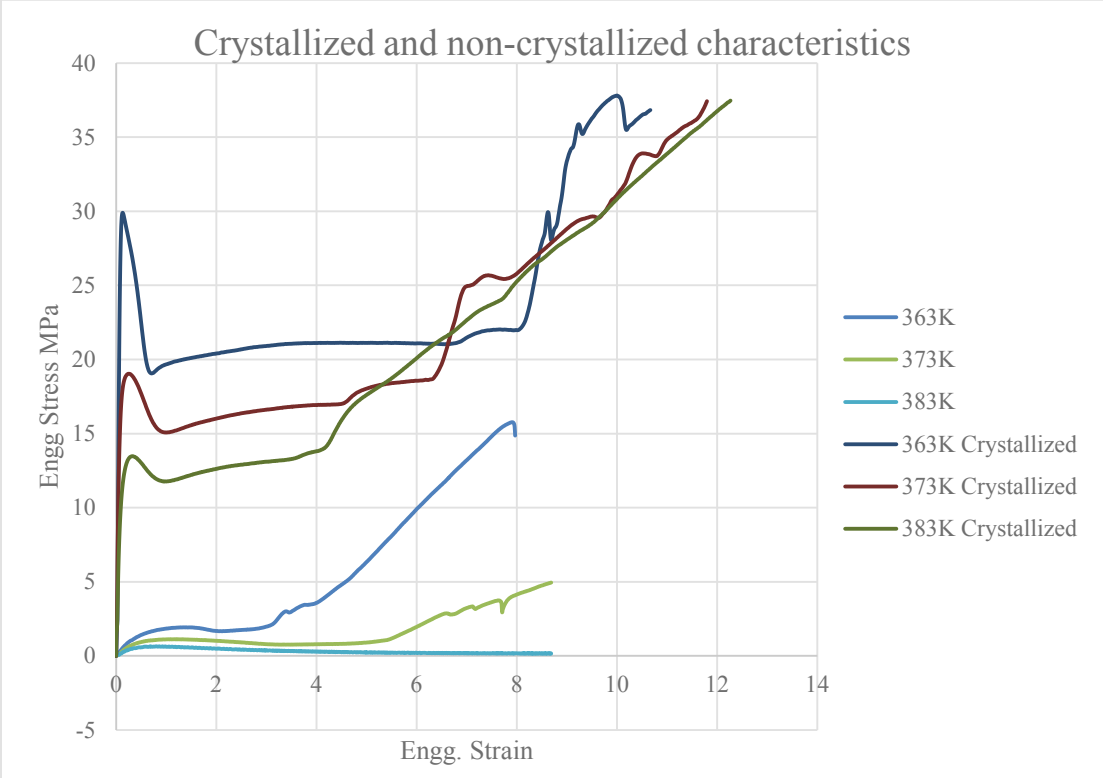

Figure 8.1 Stress Strain characteristics with crystallized and non-crystallized specimens at 0.1/s

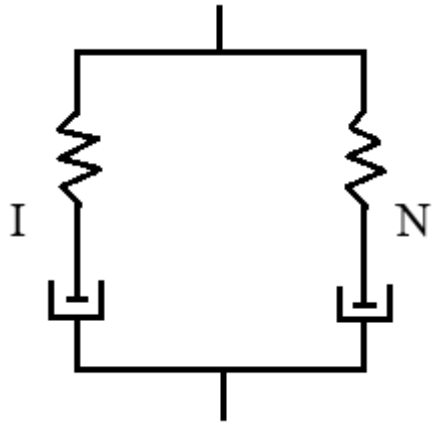

Figure 8.2 Existing DB Model schematic

8.2.1 Dupaix-Krishnan Model

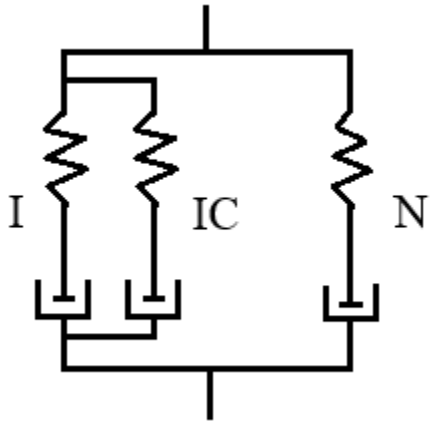

Figure 8.3 Dupaix-Krishnan model schematic

The Dupaix-Krishnan model is similar to the Dupaix-Boyce model with an additional network modeled in parallel with the Networks I and N. This additional network IC represents the intermolecular resistance in the crystallized polymer in a similar way to

Network I and uses the same model constants as Network I but with the exception that a much larger value is used for the Temperature Independent Bulk Modulus. This model also uses a method to calculate percentage of crystallinity in the sample using an equation based on the non-isothermal version of the Avrami equation (Doufas et al. 2000). The degree of transformation from amorphous to crystalline y is a number between 0 and 1 and is defined by the equation

$$\dot{y} = mK_{av}(\theta)(-\ln(1-y))^{\frac{m-1}{m}}(1-y)\exp(\xi\frac{tr(T)}{\mu_c})$$

And

$$K_{av}(\theta) = 1.47 \times 10^3(\frac{4\pi Nu}{3\varphi_\infty})^{0.33} \times \exp(-\left(\frac{\theta-414}{47.33}\right)^2)$$

Where m is the Avrami exponent, ξ is the dimensionless parameter, μ_c is the shear modulus, T the Cauchy stress in Network I, $K_{av}(\theta)$ is the transformation rate function, θ is the absolute temperature, φ_∞ is the maximum possible crystallinity in the material and Nu is the density of nuclei in the initial amorphous phase.

So, the final fraction of crystallinity x is given by

$$x = \varphi_\infty y$$

The final stress due to intermolecular resistance is a linear combination of stresses due to network I and network IC stresses, derived using the method of mixtures using the formula

$$Stress_{intermolecular} = (1-x) \times Stress_I + x \times Stress_{IC}$$

The results obtained from this model at 363K and engineering strain rate of 0.1/s are shown in figure 8.4. The percentage of crystallization x is plotted in figure 8.5 with respect to engineering stress.

It can be seen that though this method provides an onset of strain hardening and stiffening, it under-predicts the stress at higher strains. This possibly suggests that crystallinity might require an adjustment to constants that affect plastic flow properties at high strains too, in addition to changing only the linear elastic portion of the model through the Bulk Modulus.

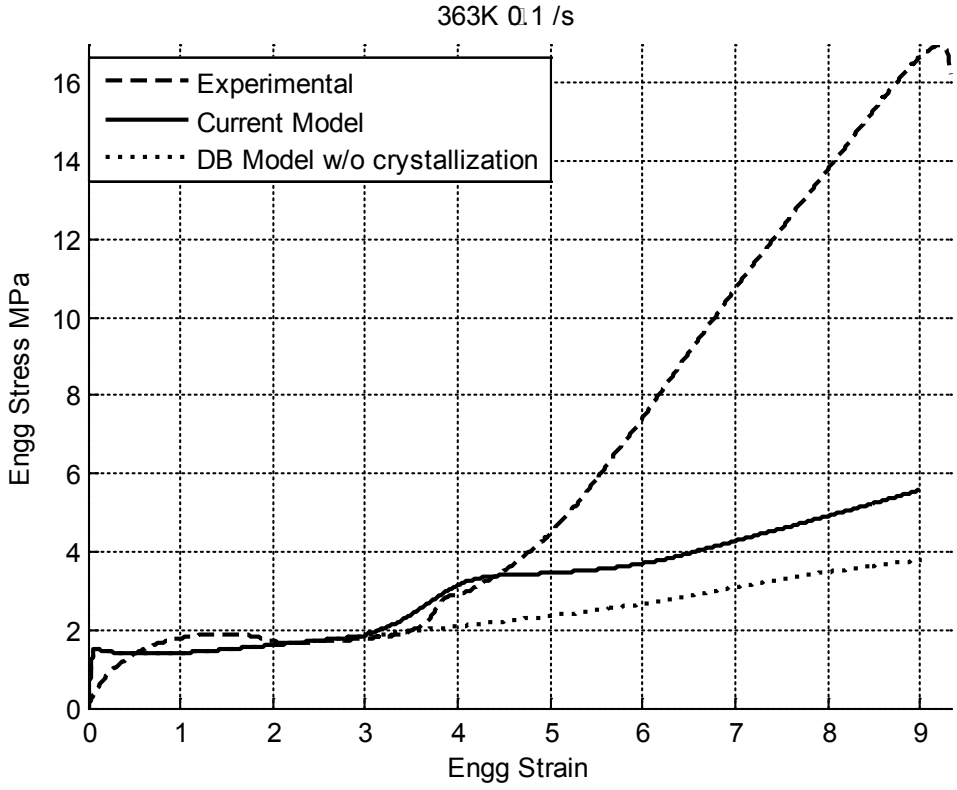

Figure 8.4 Dupaix-Krishnan model output

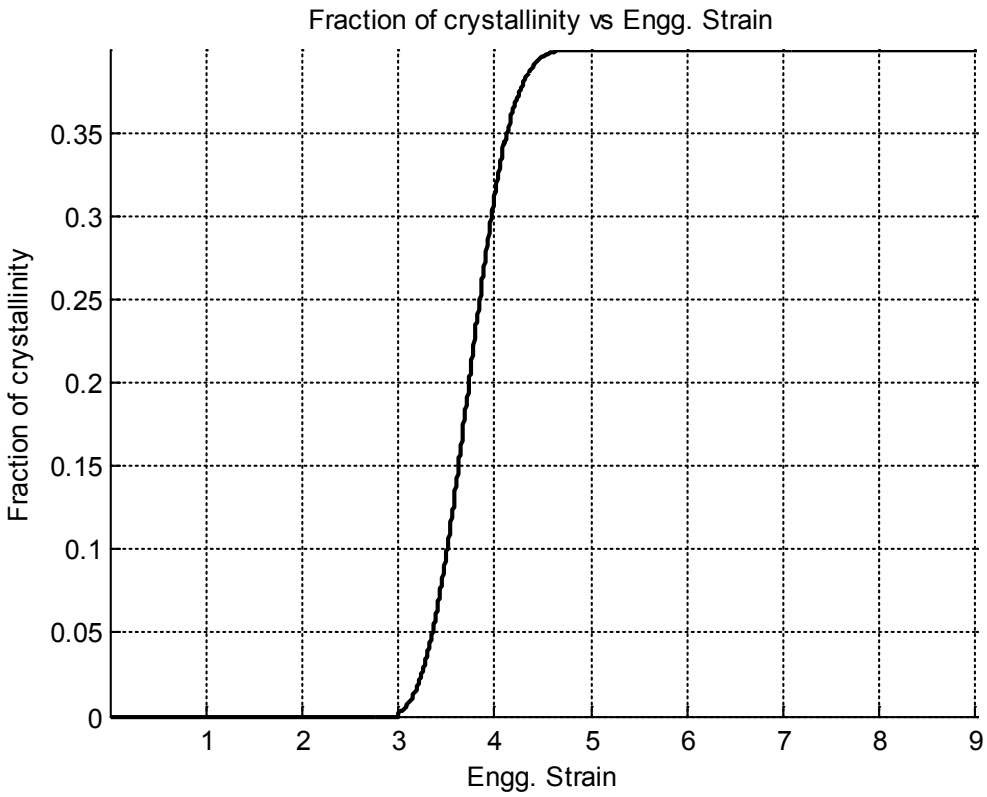

Figure 8.5 Crystallinity fraction vs Engg. Strain for Dupaix-Krishnan model

8.2.2 Dupaix-Krishnan Model with linear elastic crystallization

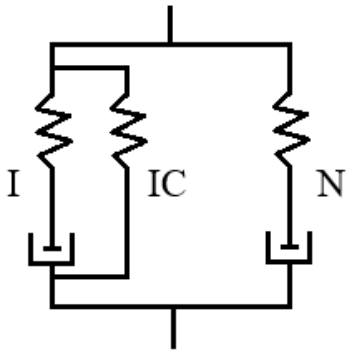

Figure 8.6 Dupaix-Krishnan model with linear elastic crystallization schematic

The crystallization branch, Network IC of the Dupaix-Krishnan model consists of a linear elastic component as well as a flow rule. It can be seen that this model tended to under-predict stress at large strains. To try to nullify this, the flow rule was eliminated from Network IC, thus creating a purely linear elastic parallel network in the Dupaix-Krishnan model. The other computation processes were identical to the Dupaix-Krishnan model, including the computation of the fraction of crystallinity. Figure 8.7 shows the result of this model for model constants identical to those used for the original Dupaix-Krishnan model plots in figures 8.4 and 8.5. It can be observed that the under-prediction in this case is lesser than the original Dupaix-Krishnan model, but is still significant.

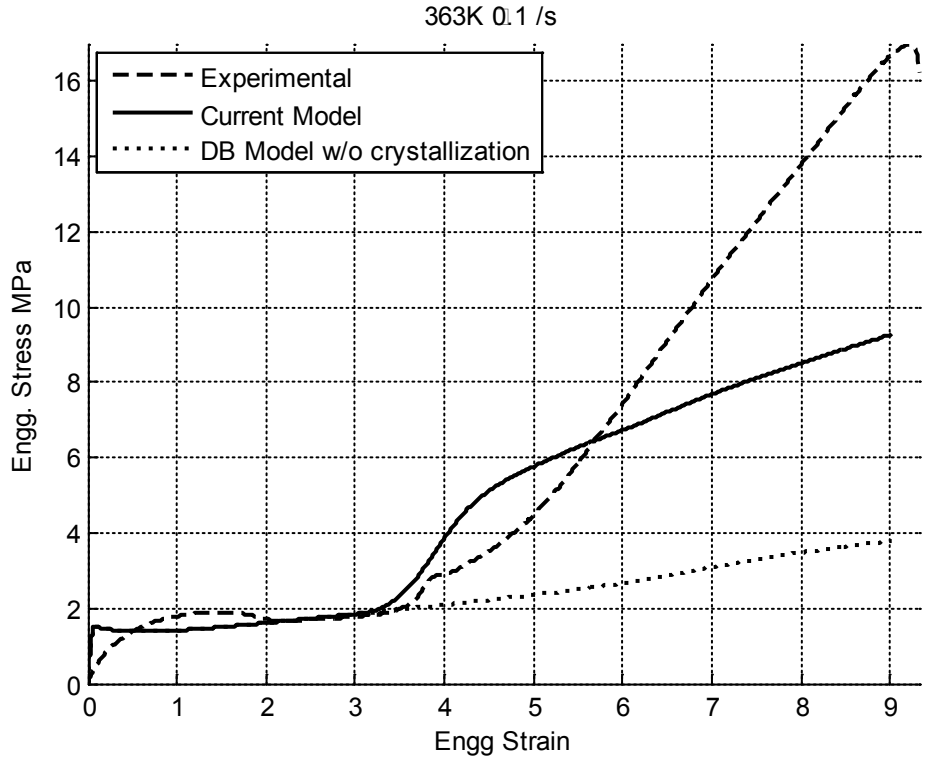

Figure 8.7 Dupaix-Krishnan Model with linear elastic crystallization output

8.2.3 Separate Crystallization networks for both Network I and Network N

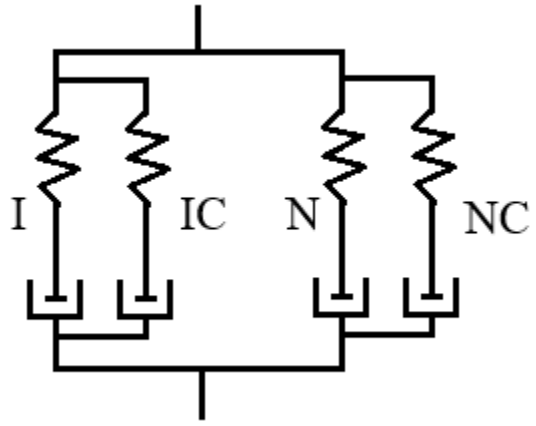

Figure 8.8 Separate crystallization for I and N schematic

The under-prediction of stress at higher strain levels necessitated the alteration of model constants that govern the plastic regions of both Network I and Network N. Because of this, a similar network but with altered constants to account for crystallization was added to both networks I and N. The net stress from each network is set up to be computed using a method similar to the one used in the Dupaix-Krishnan model based on a linear combination of the fraction of crystallinity using the method of mixtures.

Figure 8.9 shows the stress-strain characteristics obtained from the implementation of this setup. It can be observed that the model prediction is closer to the experimental data. This setup would also have the added advantage of the ability to tune each branch of the networks individually to obtain good fits of data. However, this method has the

disadvantage of using a larger number of state variables and having heavier computation requirements because of two additional network components, which is twice of that of the Dupaix-Boyce model. In addition, figure 8.9 suggests this method provides a curved stress-strain output at large strains, while the actual observed curve is linear.

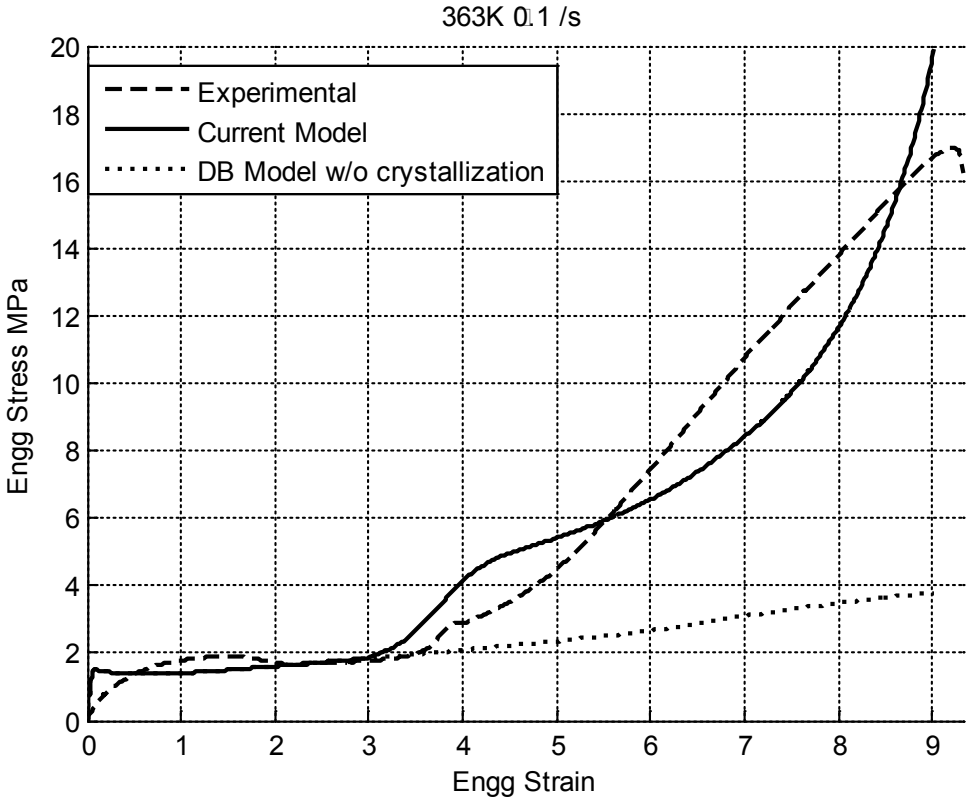

Figure 8.9 Separate Crystallization networks for both Network I and Network N output

Figure 8.10 shows the temperature dependence characteristics of this model setup. It can be seen that the fit is good only for one temperature case, at 363K (90ºC) and poor for the

rest. This model would also not capture the variation of the onset of crystallization with respect to temperature and strain rate.

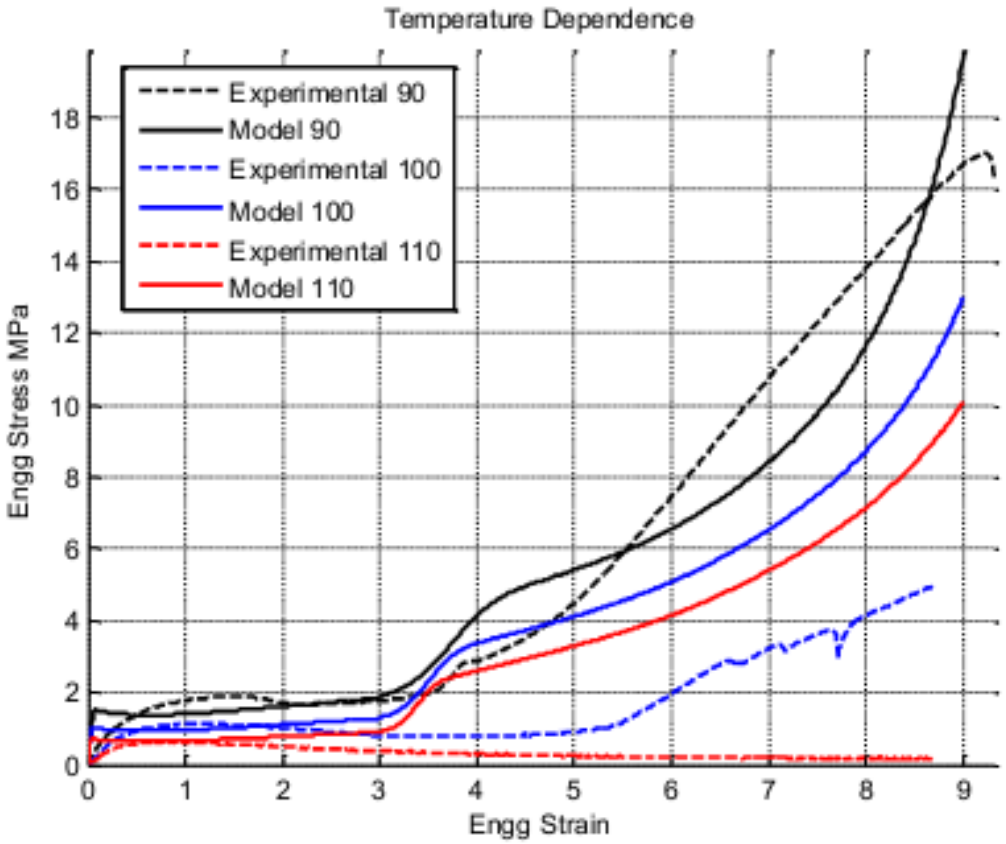

Figure 8.10 Temperature dependence - Separate Crystallization networks for both Network I and Network N output

8.2.4 Constant change on-the-fly

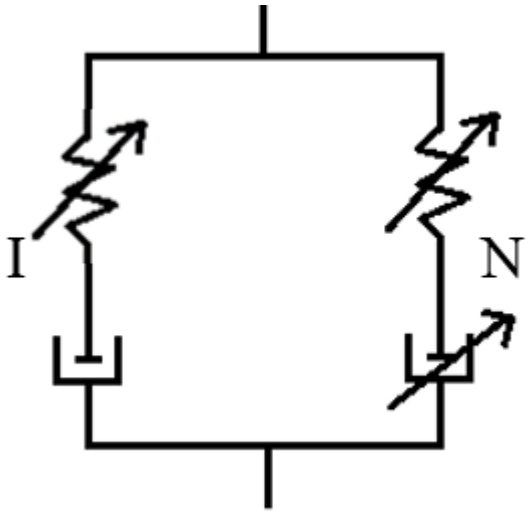

Figure 8.11 Constant change of the fly schematic

This method was setup to work by the variation of selected Dupaix-Boyce model constants over the drawing range with a linear change in the value of the constant per unit stretch. Four constants were chosen to be changed – Bulk Modulus (B), rubbery modulus ($nk\theta$), rigid links between entanglements (N), and flow cutoff angle (α_c). The equations governing the change of these constants with stretch are described in the next section. Figure 8.12 shows the fit obtained by this method. Since this method would provide individual control over each constant, it was chosen for further development.

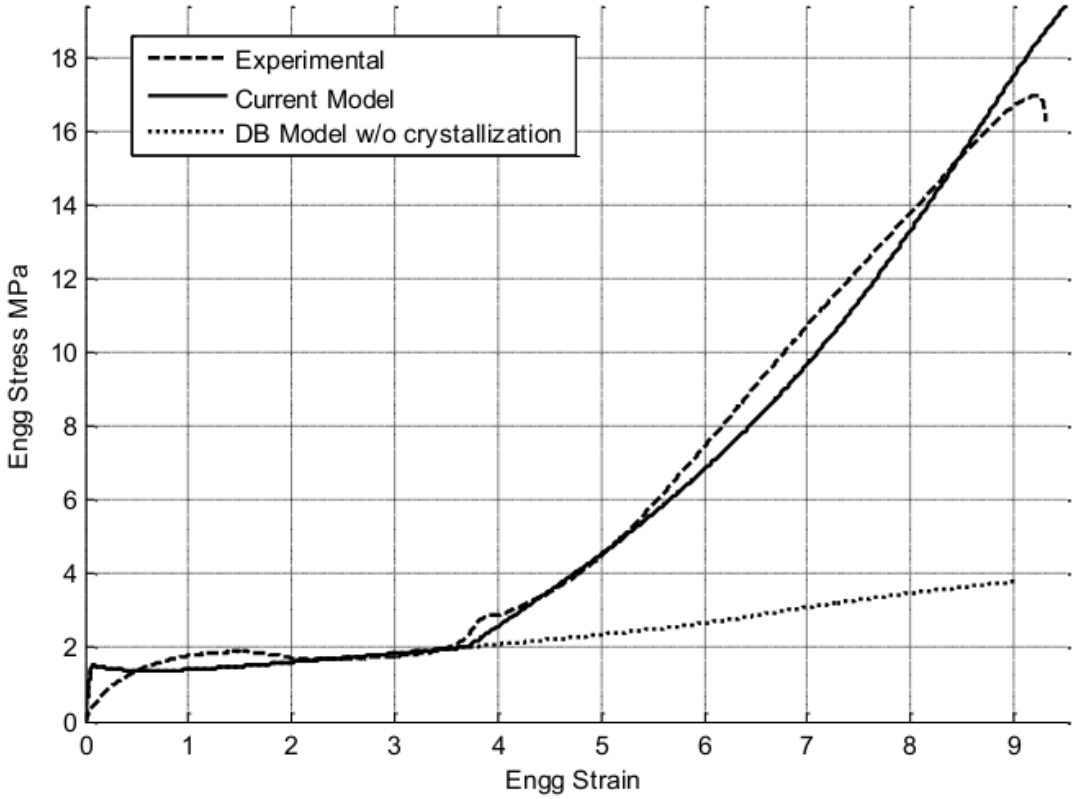

Figure 8.12 Constant change-on-the-fly output

8.3 Constant Change on the fly – Crystallization Module

Incorporation of constant change on the aforementioned properties required an understanding of the physical changes at the molecular level when strain induced crystallization occurs.

Firstly, crystallization causes an increase in material stiffness. This could be captured by an increase in the Bulk Modulus B (PROPS7) with increase in tensile stretch beyond crystallization onset. Secondly, crystallization is preceded by the formation nuclei, which

have the tendency to act similar to crosslinks (Chaari et al, 2003) between molecular chains. This is assumed to decrease the number of rigid links between entanglements, i.e. N (PROPS11). When this happens, chain density n has to increase. The product Nn is assumed to be a constant based on a principle of conservation of mass. Thus, the material constant $nk\theta$, i.e., the rubbery modulus (PROPS10) is increased to so as to keep Nn constant. Thirdly, the aforementioned entities are assumed to increase the minimum angle below which the plastic flow ceases in Network N. In other words, it makes the flow stop sooner than if there were no crystallization. In accordance to this, α_c is increased with stretch beyond crystallization onset.

The rate of change of these constants as mentioned above and the crystallization onset stretch itself, is dependent on strain rate and temperature. An algebraic fit based on time-temperature superposition was arrived at to determine the change of crystallization onset stretch and bulk modulus for a given condition of temperature and strain rate.

8.3.1 Equations for the crystallization module

Table 8.1 Experimental Crystallization Onset Stretch for IV 0.80

SR /s\Temp K	363	368	373	378	383
0.05	4.4	5.4	8.1	-	-
0.1	4	4.8	6.4	-	-
0.425	3.5	4.2	4.8	6.4	-

Table 8.2 Experimental Crystallization Onset Stretch for IV 0.86

SR /s\Temp K	363	368	373	378	383
0.05	4	4.7	6.5	-	-
0.1	3.9	4.4	5.8	7	-
0.425	3.4	4	4.7	5.4	-

Table 8.3 Experimental Crystallization Onset Stretch for IV 0.92

SR /s\Temp K	363	368	373	378	383
0.05	4	4.8	7	-	-
0.1	3.9	4.4	5.8	8.2	-
0.425	3.4	4	4.7	5.8	-

The following equations were arrived at using the time-temperature superposition form of equation given by

$$CRYSSTARTSHIFT = (TEMPCELSIUS - 105) * \frac{CRYWLFC1}{TEMPCELSIUS - 105 + CRYWLFC2}$$

Where CRYSSTARTSHIFT is the shift variable used in computation of CRYSSTARTSTRETCH, i.e., the crystallization onset stretch. Crystallization onset stretch was then computed using the equation

$$CRYSSTARTSTRETCH = -3.71 * (EDOT + CRYSSTARTSHIFT)^3 + 13.71 * (EDOT + CRYSSTARTSHIFT)^2 + 18.39 * (EDOT + CRYSSTARTSHIFT)^1 + 12.85$$

Where EDOT is the strain rate. CRYWLFC1 takes a value of -9 for IV 0.80 and -10 for IV 0.86 and 0.92 and CRYWLFC2 takes a value of 140 for IV 0.80 and 135 for IV 0.86 and 0.92 based on experimental data fit.

The following equation based on the time-temperature superposition form was used to compute the temperature and strain-rate dependent change of N (PROPS11)

Table 8.4 Prop11slope for different temperature and strain rates, all IVs

SR /s\Temp K	363	368	373	378	383
0.05	-1.3	-	-	-	-
0.1	-1.1	-1.3	-1.1	-	-
0.425	-1.1	-1.1	-1.1	-	-

$$PROP11SLOPESHIFT = (TEMPCELSIUS - 100) * \frac{PROP11WLFC1}{TEMPCELSIUS - 100 + PROP11WLFC2}$$

$$PROP11SLOPE = 1.5509 * (EDOT + PROP11SLOPESHIFT) - 2.6889$$

Where PROP11SLOPE is the change in PROPS11 per unit of stretch. The following equation provided the change per stretch of the other two constants.

$$PROP7SLOPE = 6E8$$

$$PROP15SLOPE = 0.2$$

It is to be noted that the change of PROPS7 and PROPS15 are constant with respect to temperature and strain rate because these provided a sufficiently close fit for experimental data.

Finally, the following equations provided the changed values of the constants.

$$B = PROPS(7) + PROP7SLOPE * (F(1,1) - CRYSSTARTSTRETCH)$$

$$N = PROPS(11) + PROP11SLOPE * (F(1,1) - CRYSSTARTSTRETCH)$$

$$nk\theta = PROPS(10) * \frac{PROPS(11)}{N}$$

$$\alpha_c = PROPS(15) + PROP15SLOPE * (F(1,1) - CRYSSTARTSTRETCH)$$

8.3.2 Implementation of the crystallization module

Figure 8.13 depicts the flowchart of the implementation of the crystallization module with the Dupaix-Boyce model. As of now, this module only supports the uniaxial tensile deformation mode. So, the following checks in the code of the material model, if passed, would trigger the crystallization module. These checks were, firstly, the deformation mode had to be uniaxial tensile. This could be checked by comparing the different elements of the deformation gradient tensor. Following this, crystallization onset stretch

was to be computed based on temperature and strain rate. Since only a small range of temperature and strain rate test data was available, the computed crystallization onset stretch could turn negative for certain temperature and strain rate conditions. So, a check was placed in the code to ignore crystallization if the onset stretch turned negative. Finally the third check was to determine if the tensile stretch was actually greater than the onset stretch, after which the crystallization module would be triggered.

Once these checks were cleared, the constants were changed with stretch based on the previously shown equations and stress computed by the Dupaix-Boyce model procedure.

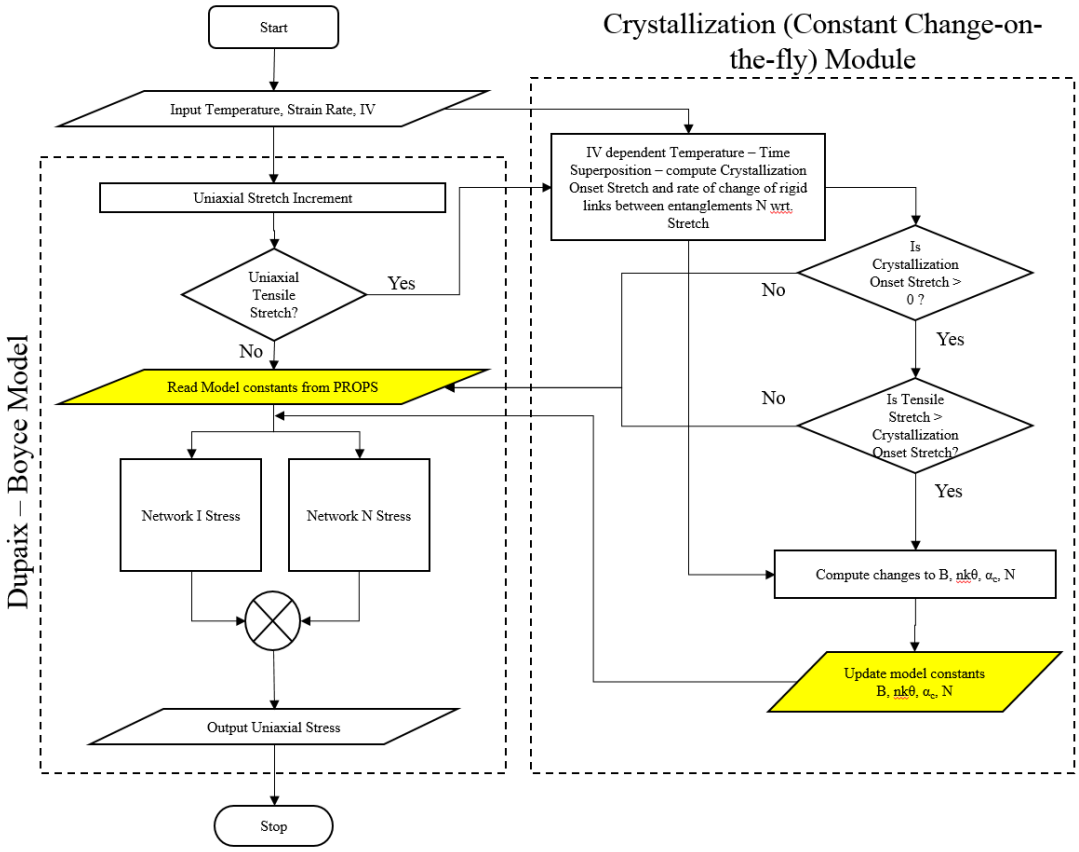

Figure 8.13 Crystallization module implementation logic

8.4 Tensile data fits for the Dupaix-Boyce model with the crystallization module

Figures 8.14 to 8.49 provide an overlay of the experimental data and DB model output with the crystallization module. It can be seen that the DB model closely predicts tensile stress in stiffer conditions, i.e., temperatures 363K and 368K and strain rates 0.425/s and majority of 0.1/s data. However, at softer conditions, i.e., temperatures 373K and above and strain rate of 0.05/s, it can be observed that the deviation of the model curves from

the experimental curves increases. This suggests the presence of other factors and non-linearity yet to be captured.

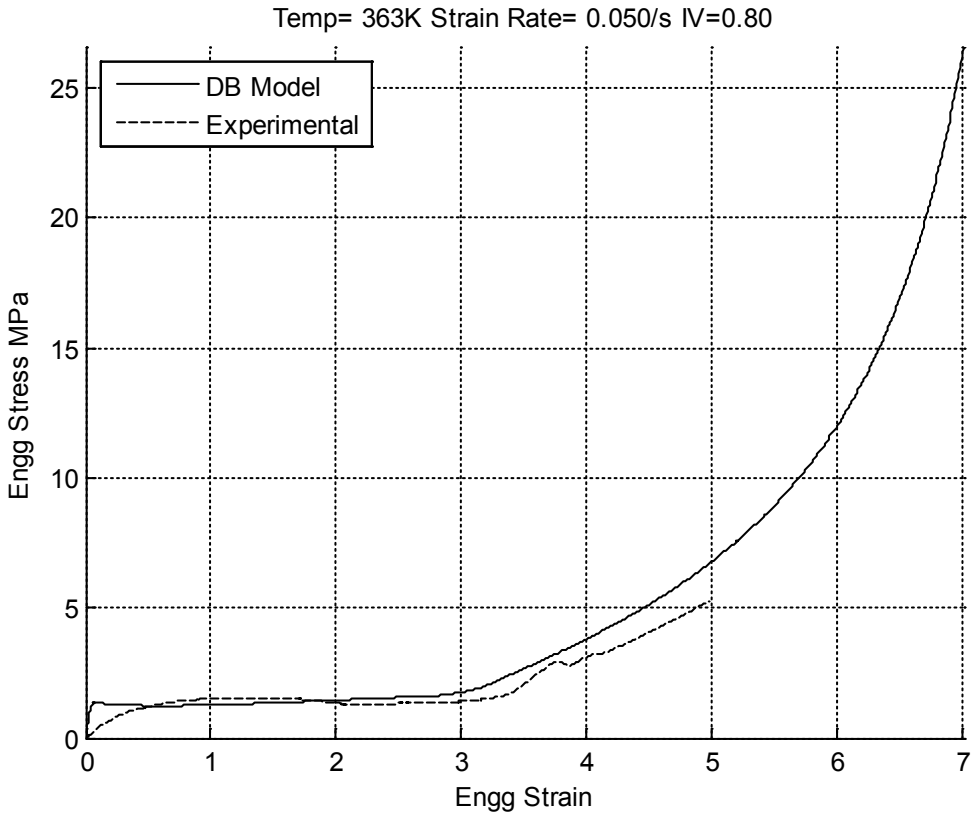

Figure 8.14 Dupaix-Boyce model with crystallization fit - 363K 0.05/s IV 0.80

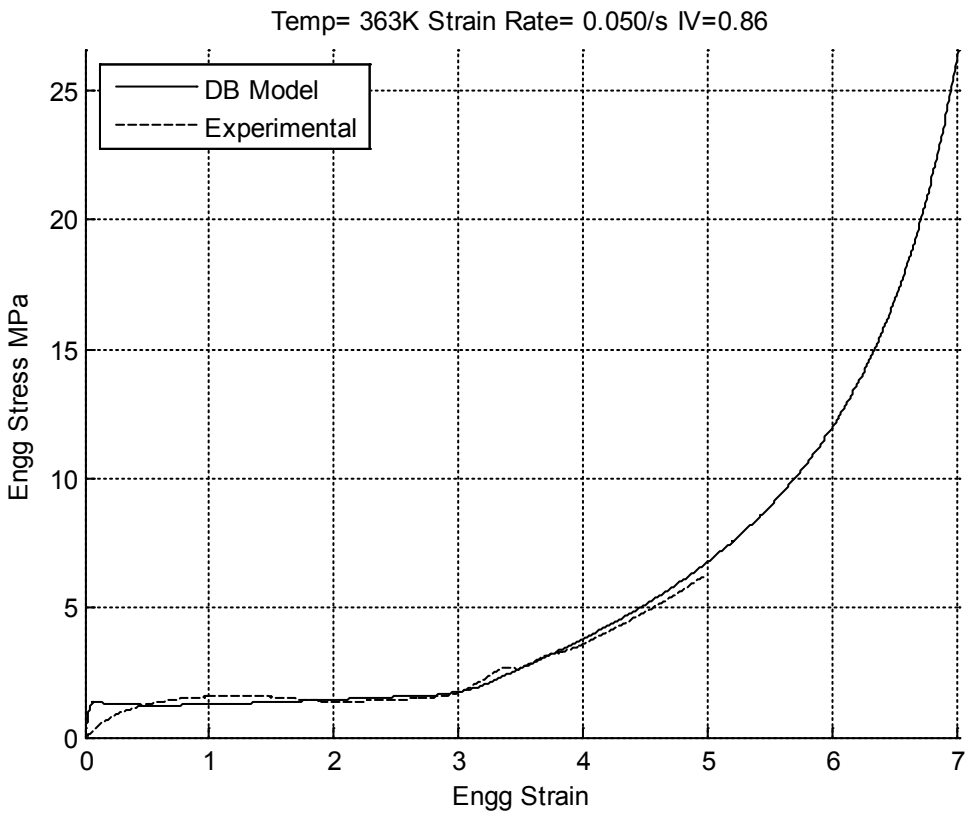

Figure 8.15 Dupaix-Boyce model with crystallization fit - 363K 0.05/s IV 0.86

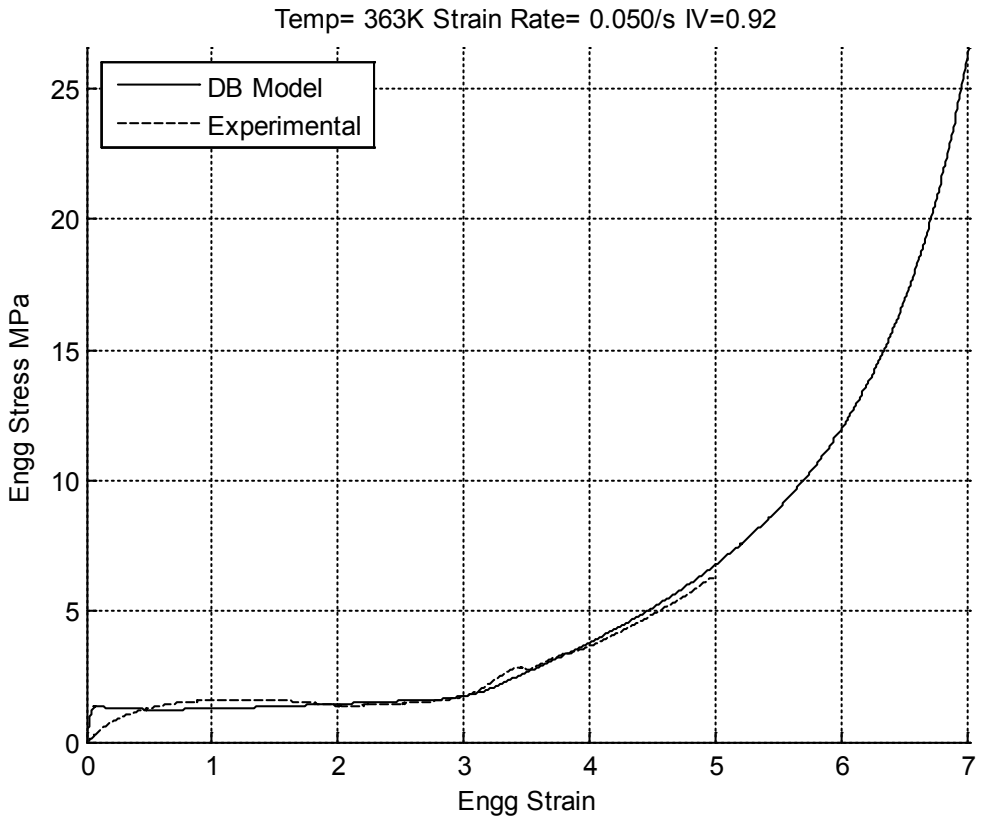

Figure 8.16 Dupaix-Boyce model with crystallization fit - 363K 0.05/s IV 0.92

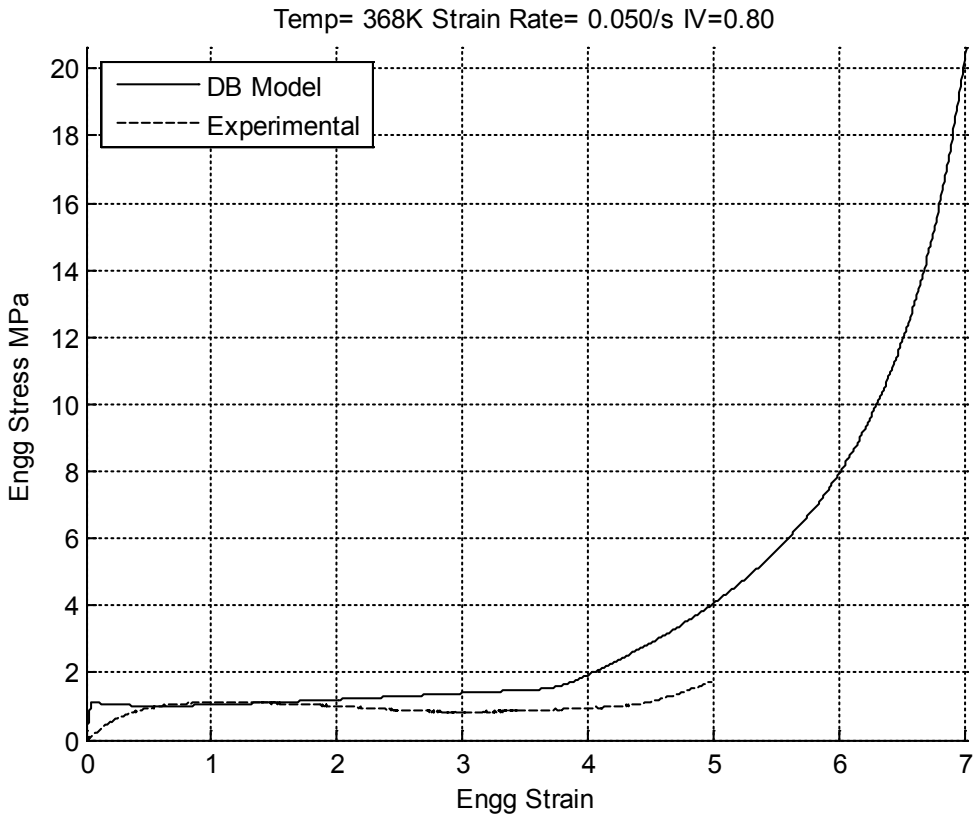

Figure 8.17 Dupaix-Boyce model with crystallization fit - 368K 0.05/s IV 0.80

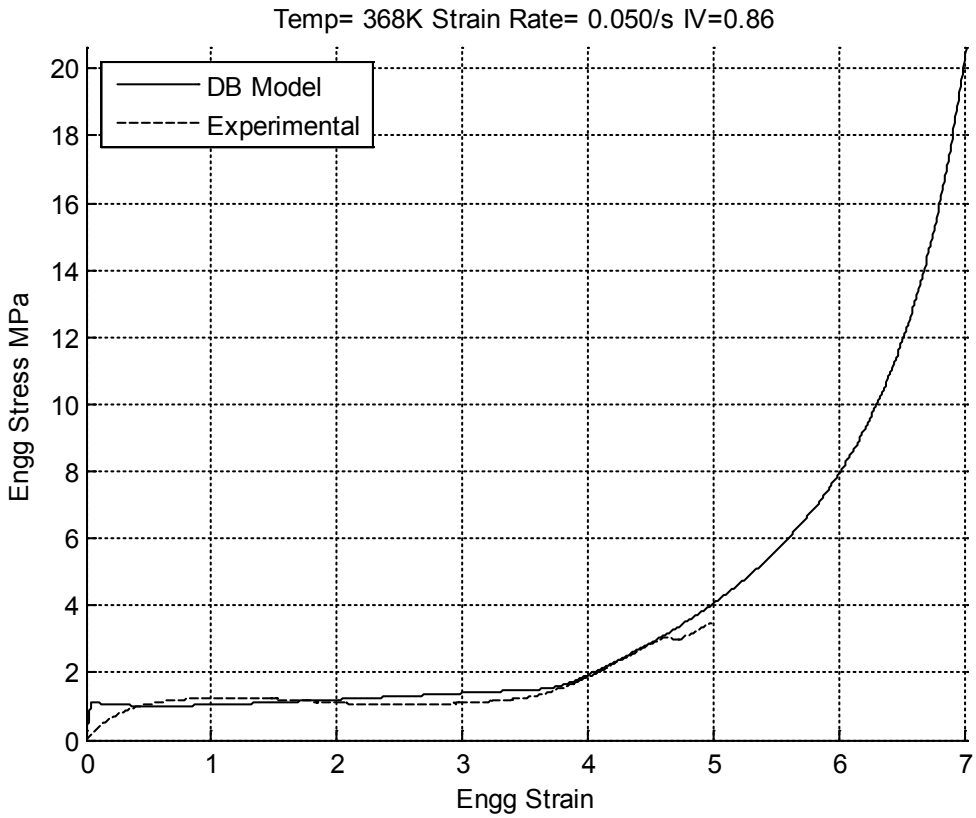

Figure 8.18 Dupaix-Boyce model with crystallization fit - 368K 0.05/s IV 0.86

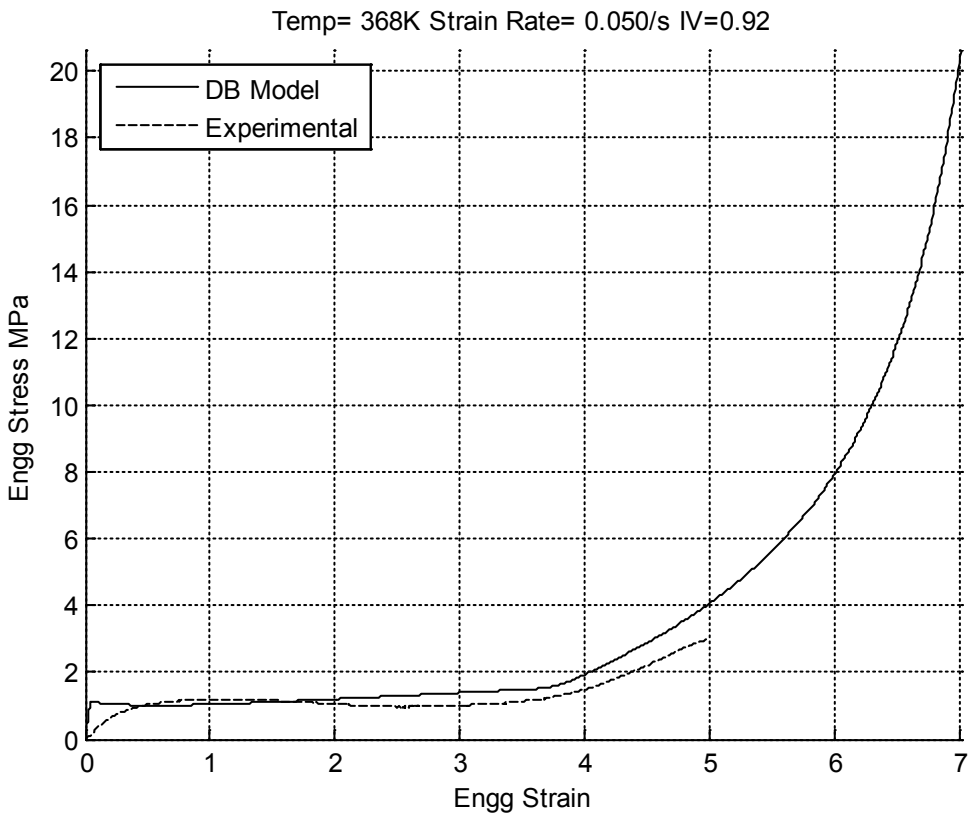

Figure 8.19 Dupaix-Boyce model with crystallization fit - 368K 0.05/s IV 0.92

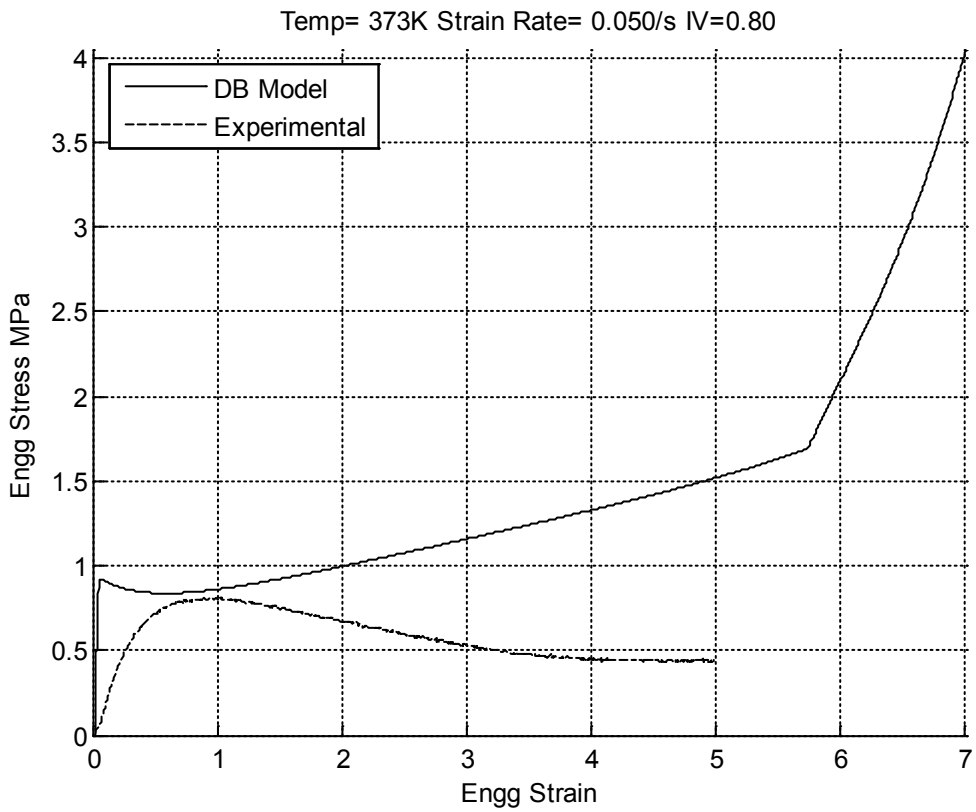

Figure 8.20 Dupaix-Boyce model with crystallization fit - 373K 0.05/s IV 0.80

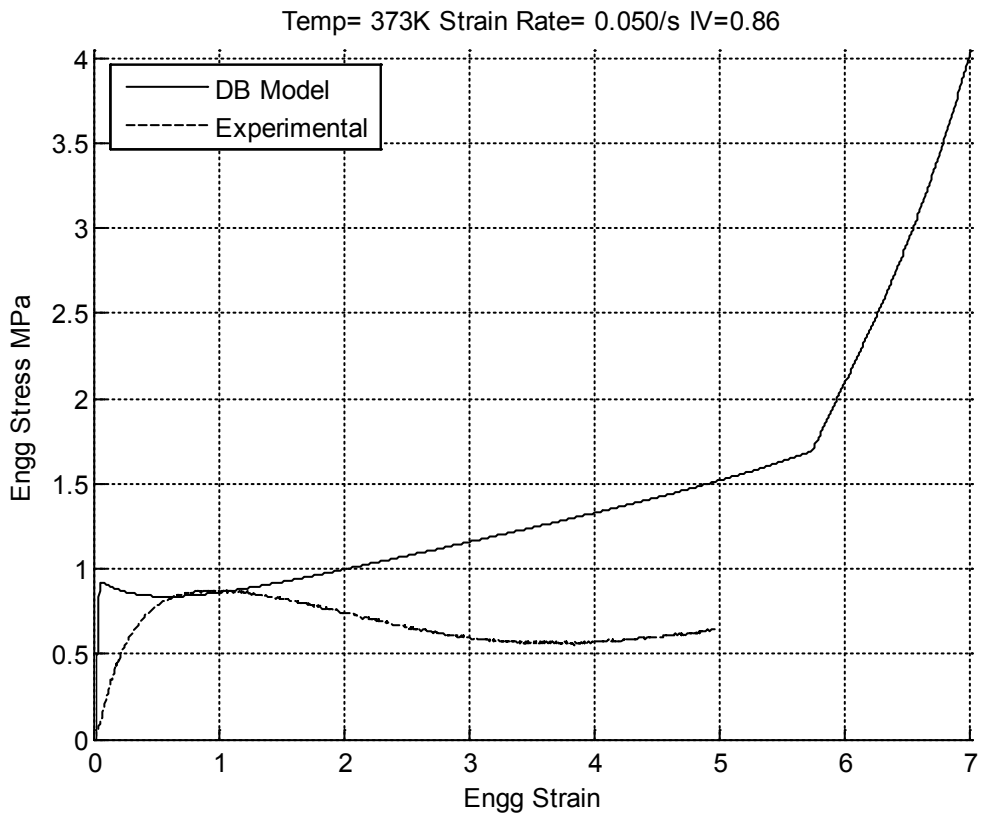

Figure 8.21 Dupaix-Boyce model with crystallization fit - 373K 0.05/s IV 0.86

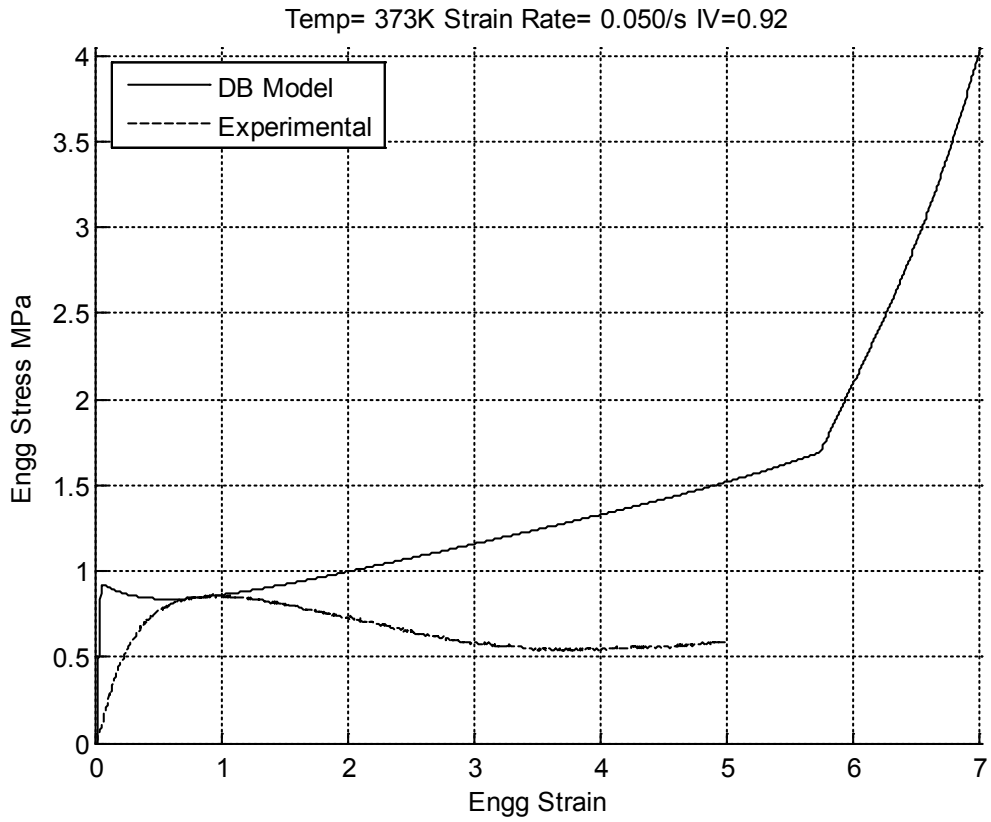

Figure 8.22 Dupaix-Boyce model with crystallization fit - 373K 0.05/s IV 0.92

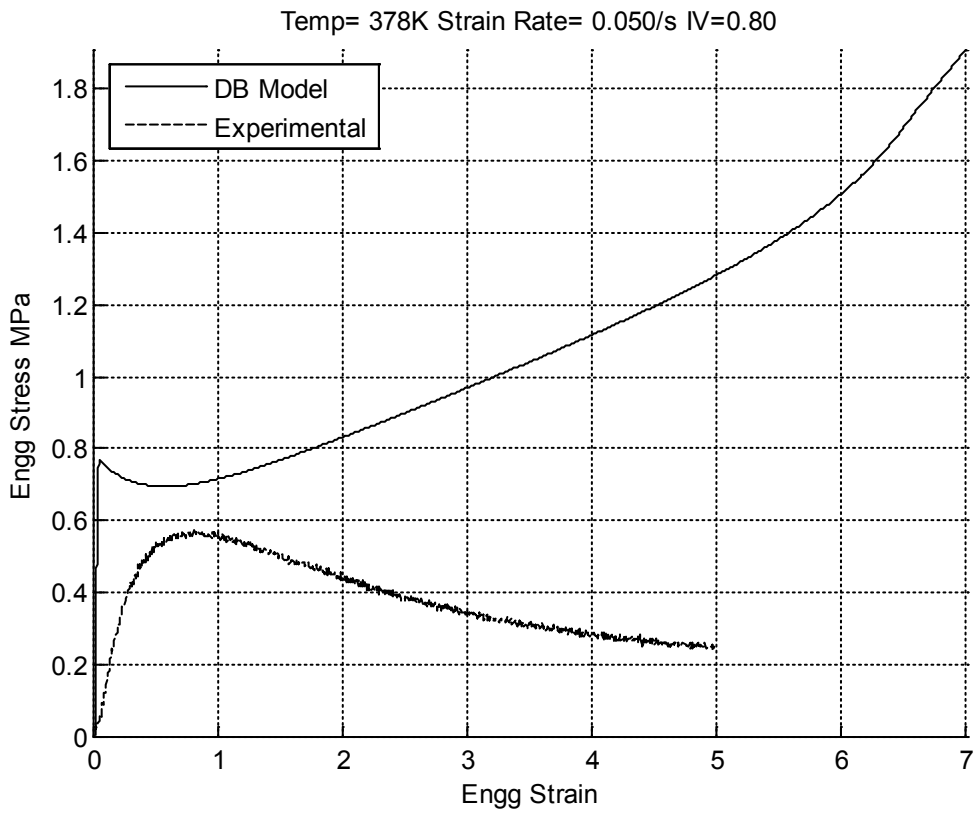

Figure 8.23 Dupaix-Boyce model with crystallization fit - 378K 0.05/s IV 0.80

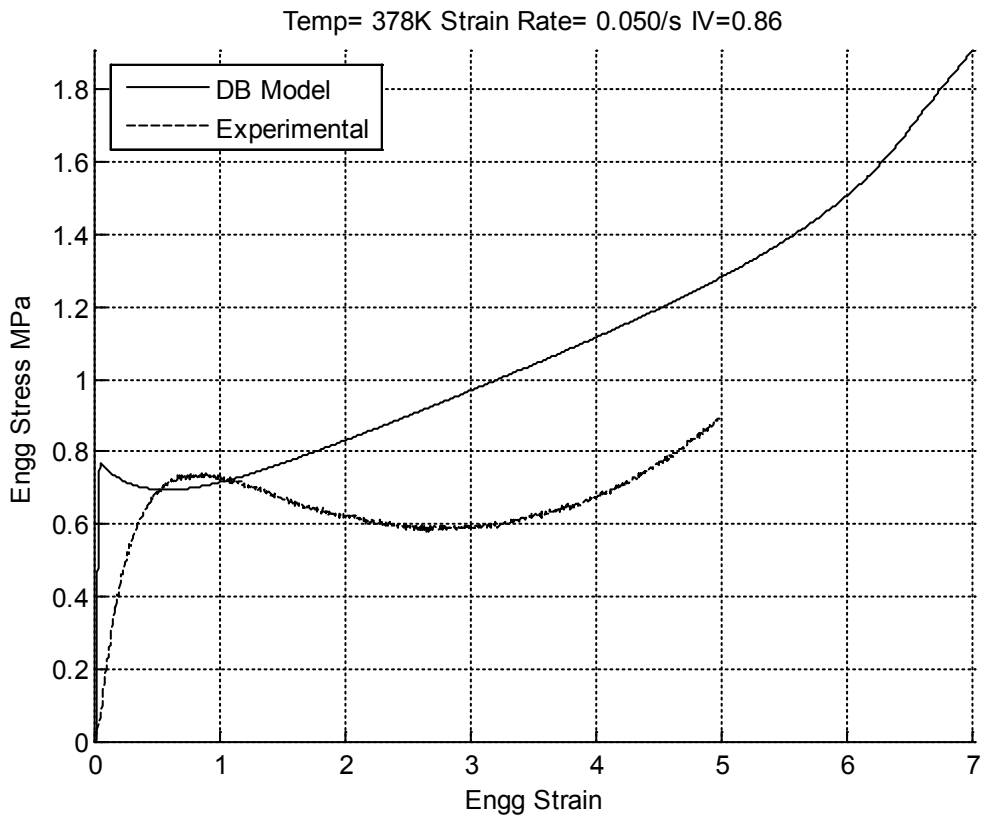

Figure 8.24 Dupaix-Boyce model with crystallization fit - 378K 0.05/s IV 0.86

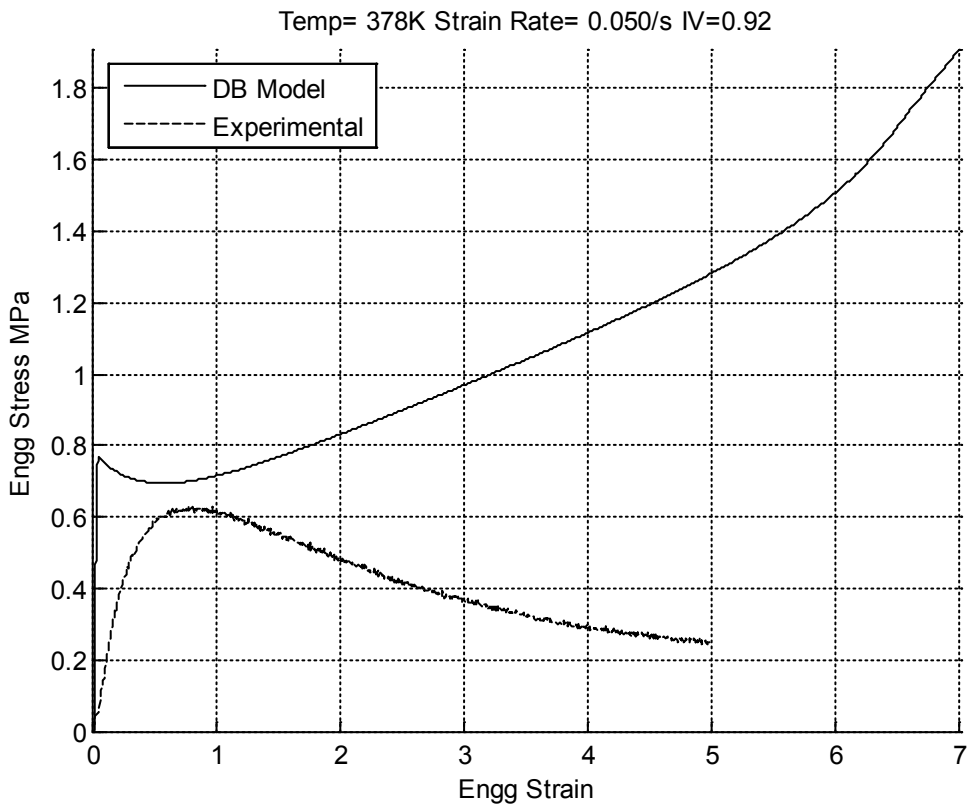

Figure 8.25 Dupaix-Boyce model with crystallization fit - 378K 0.05/s IV 0.92

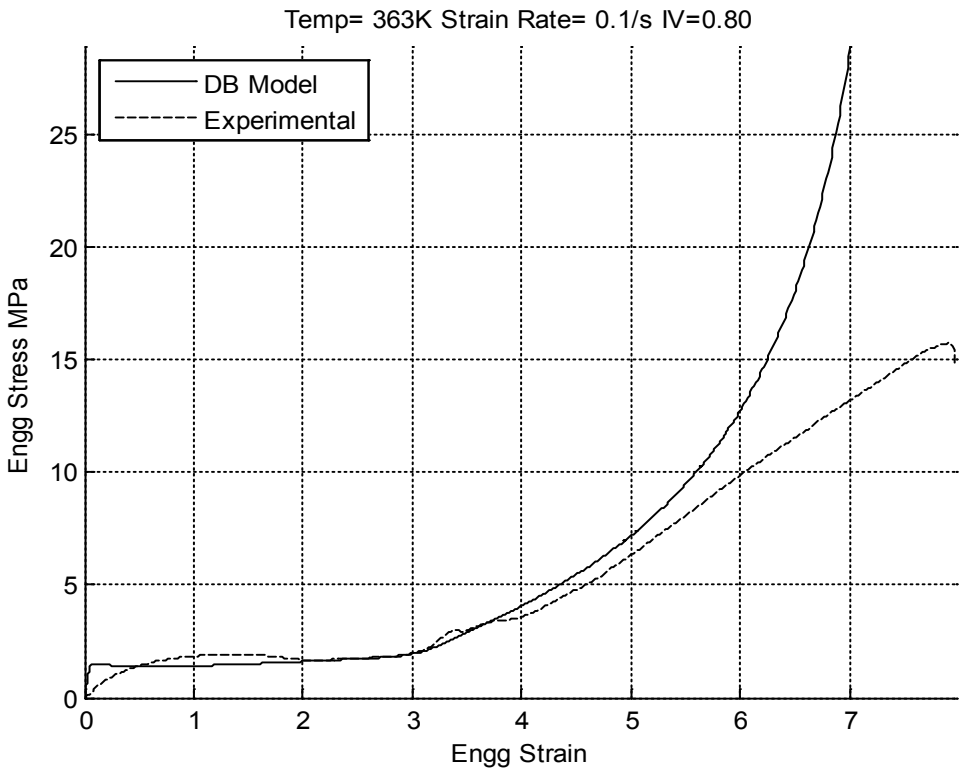

Figure 8.26 Dupaix-Boyce model with crystallization fit - 363K 0.1/s IV 0.80

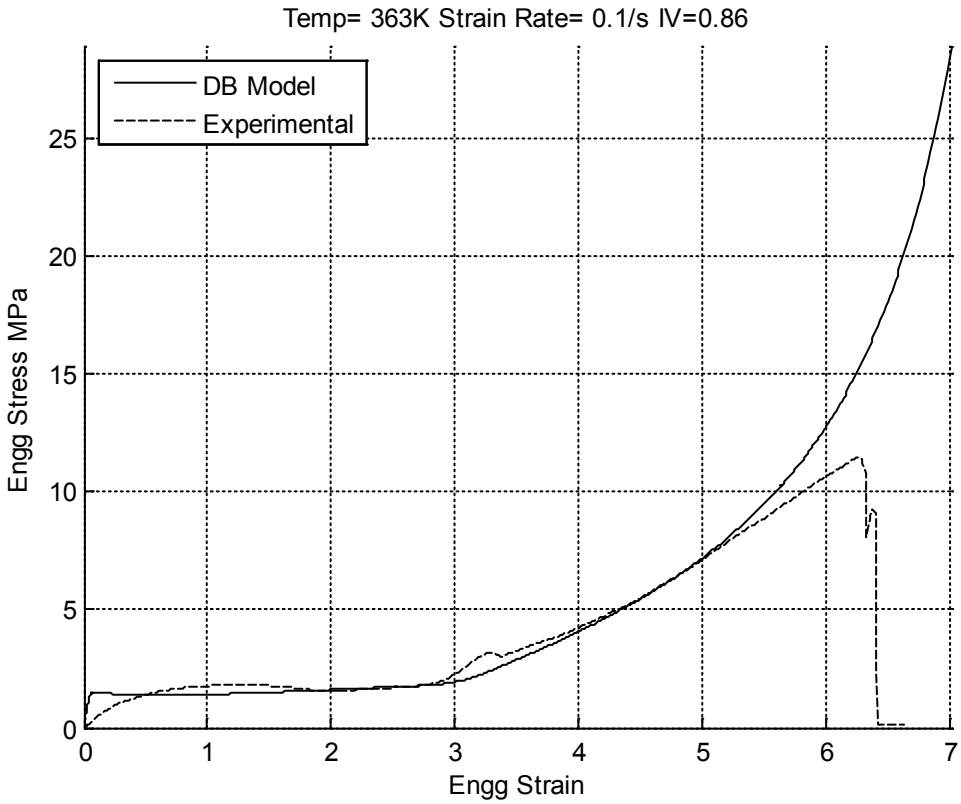

Figure 8.27 Dupaix-Boyce model with crystallization fit - 363K 0.1/s IV 0.86

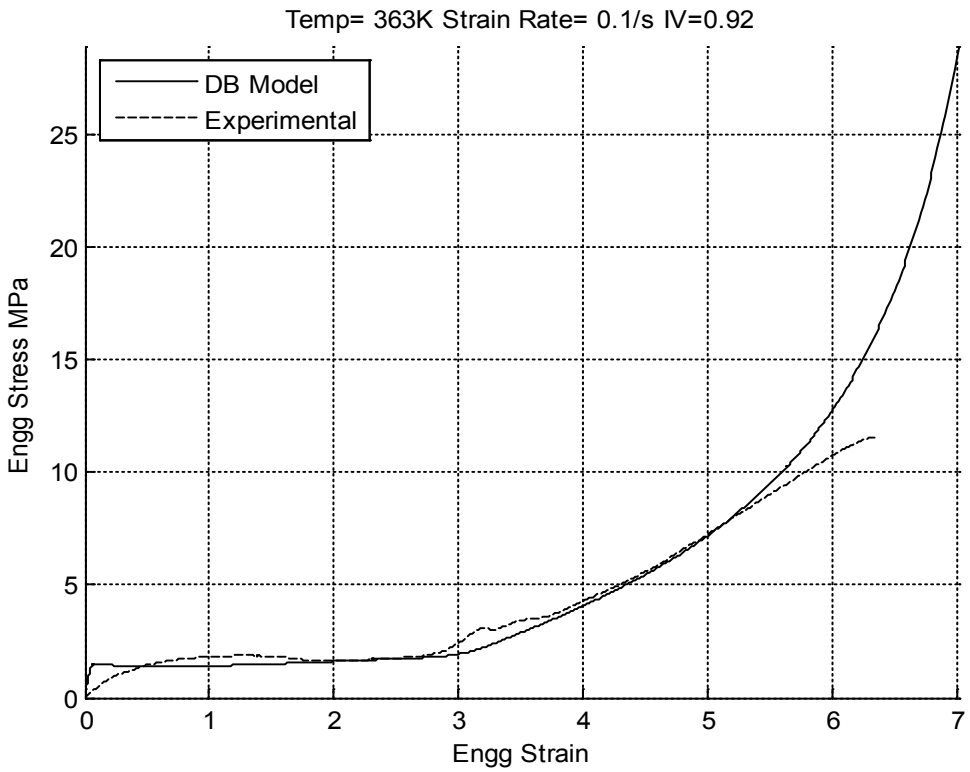

Figure 8.28 Dupaix-Boyce model with crystallization fit - 363K 0.1/s IV 0.92

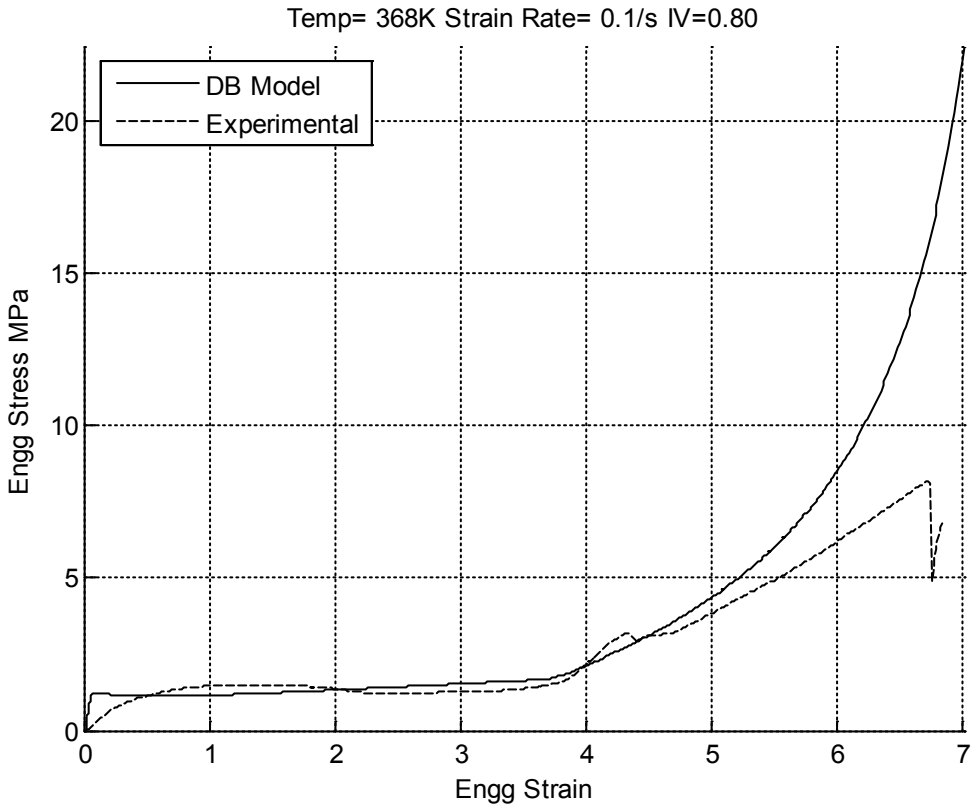

Figure 8.29 Dupaix-Boyce model with crystallization fit - 368K 0.1/s IV 0.80

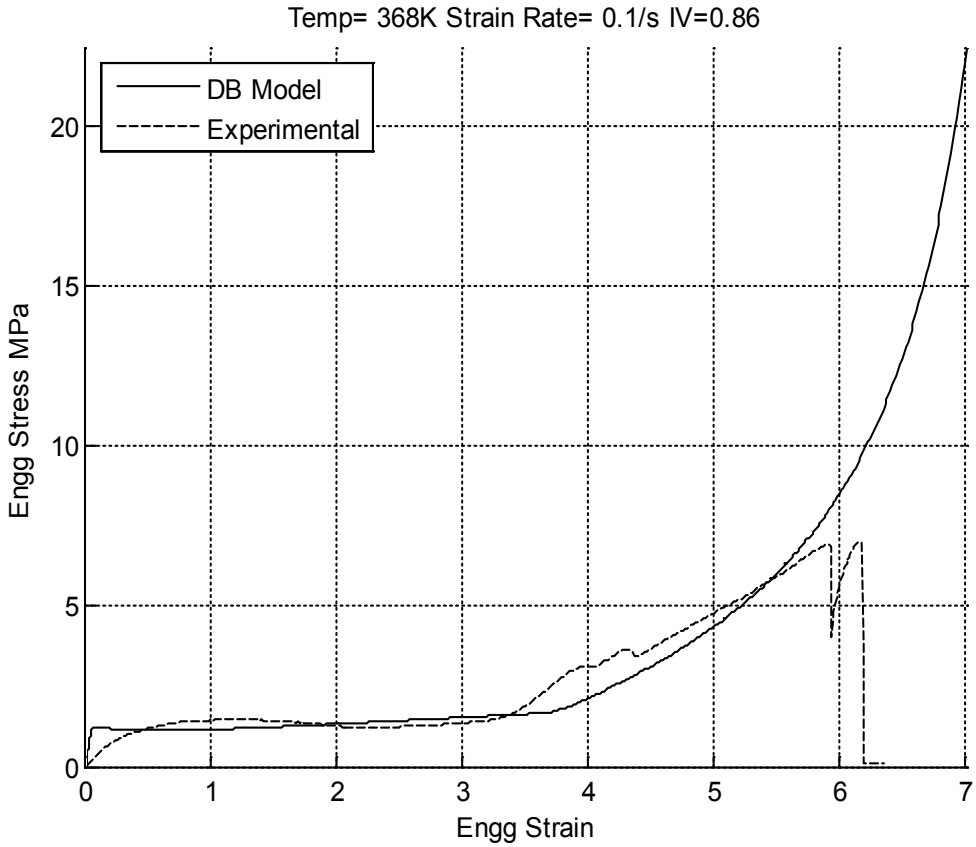

Figure 8.30 Dupaix-Boyce model with crystallization fit - 368K 0.1/s IV 0.86

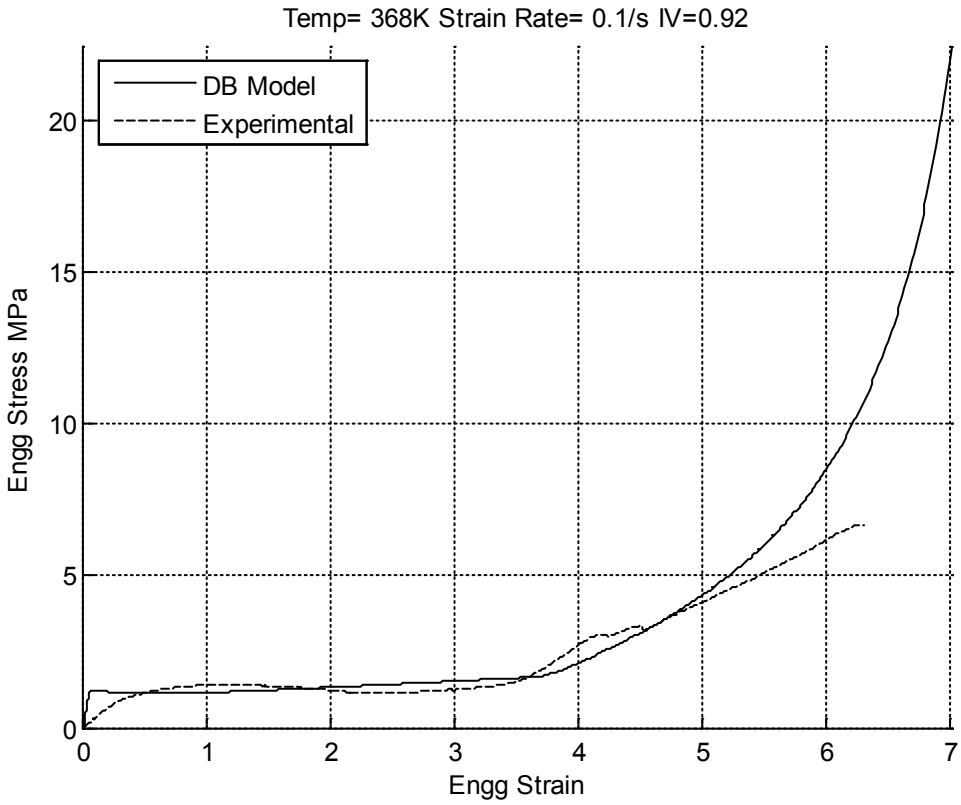

Figure 8.31 Dupaix-Boyce model with crystallization fit - 368K 0.1/s IV 0.92

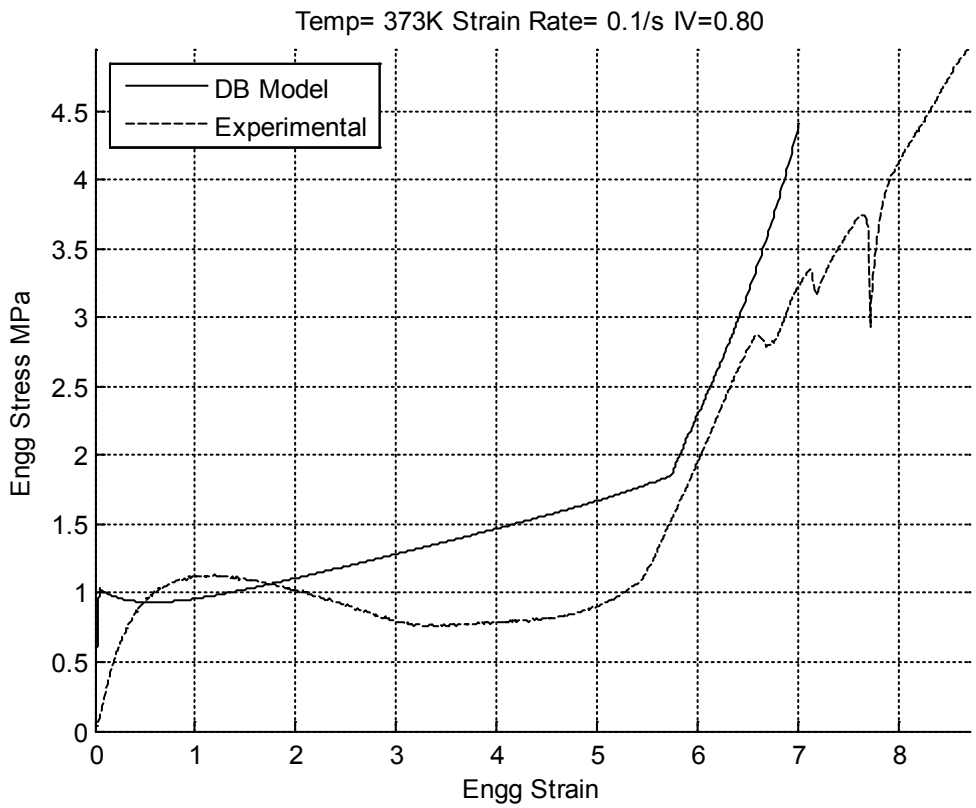

Figure 8.32 Dupaix-Boyce model with crystallization fit - 373K 0.1/s IV 0.80

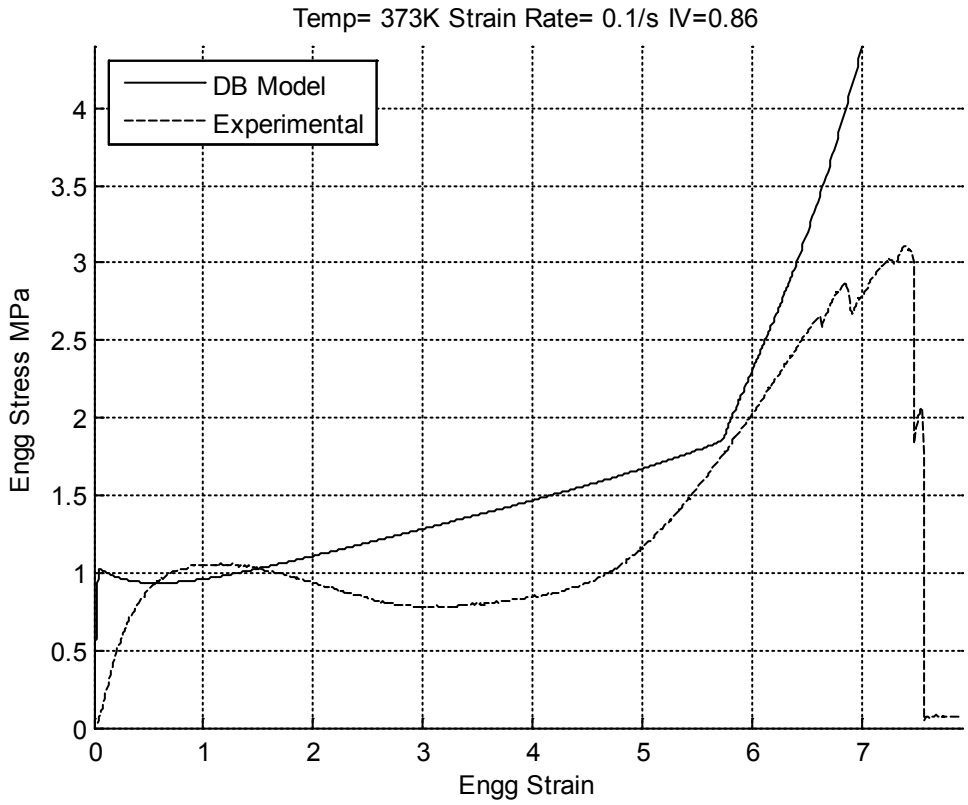

Figure 8.33 Dupaix-Boyce model with crystallization fit - 373K 0.1/s IV 0.86

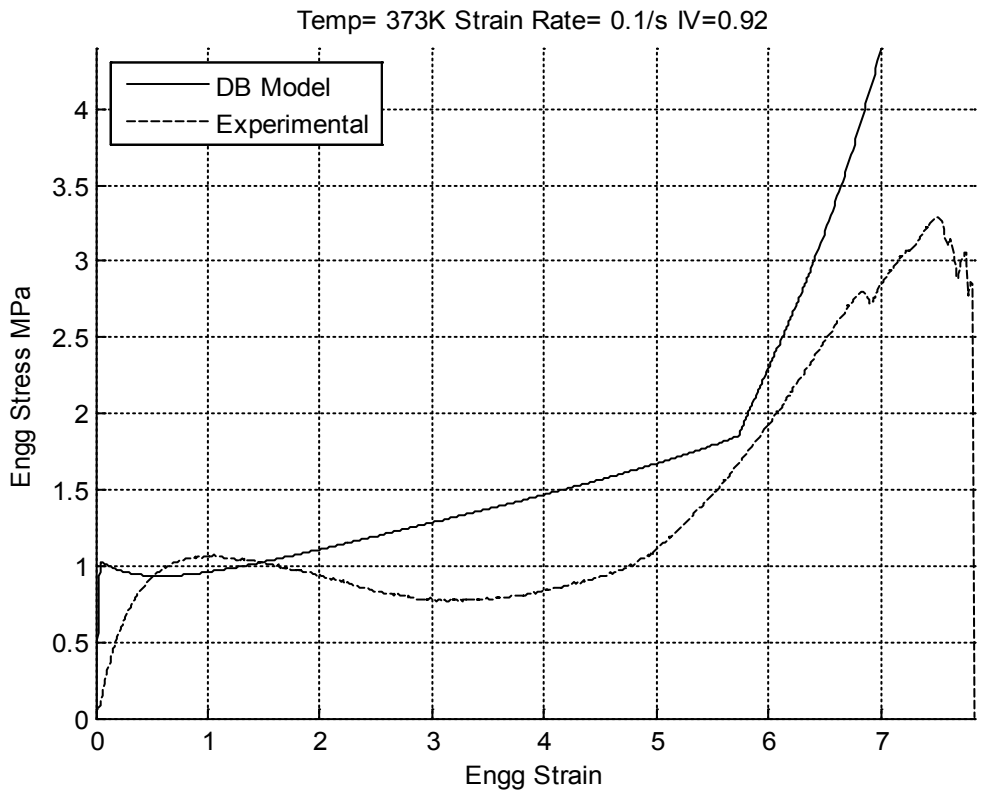

Figure 8.34 Dupaix-Boyce model with crystallization fit - 373K 0.1/s IV 0.92

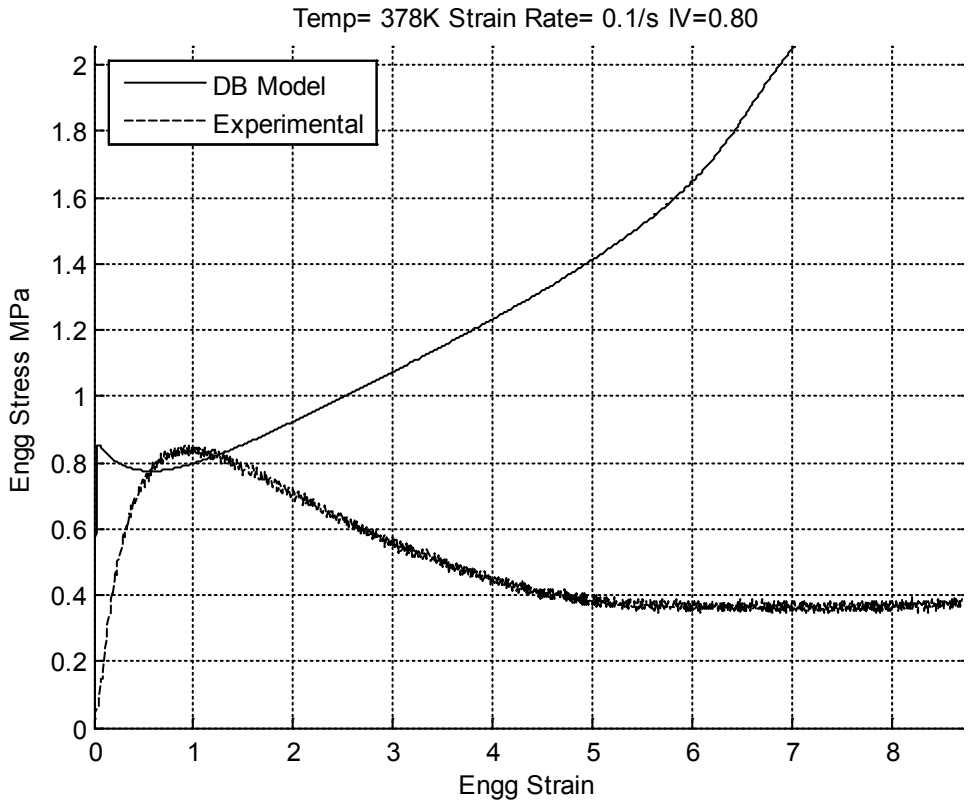

Figure 8.35 Dupaix-Boyce model with crystallization fit - 378K 0.1/s IV 0.80

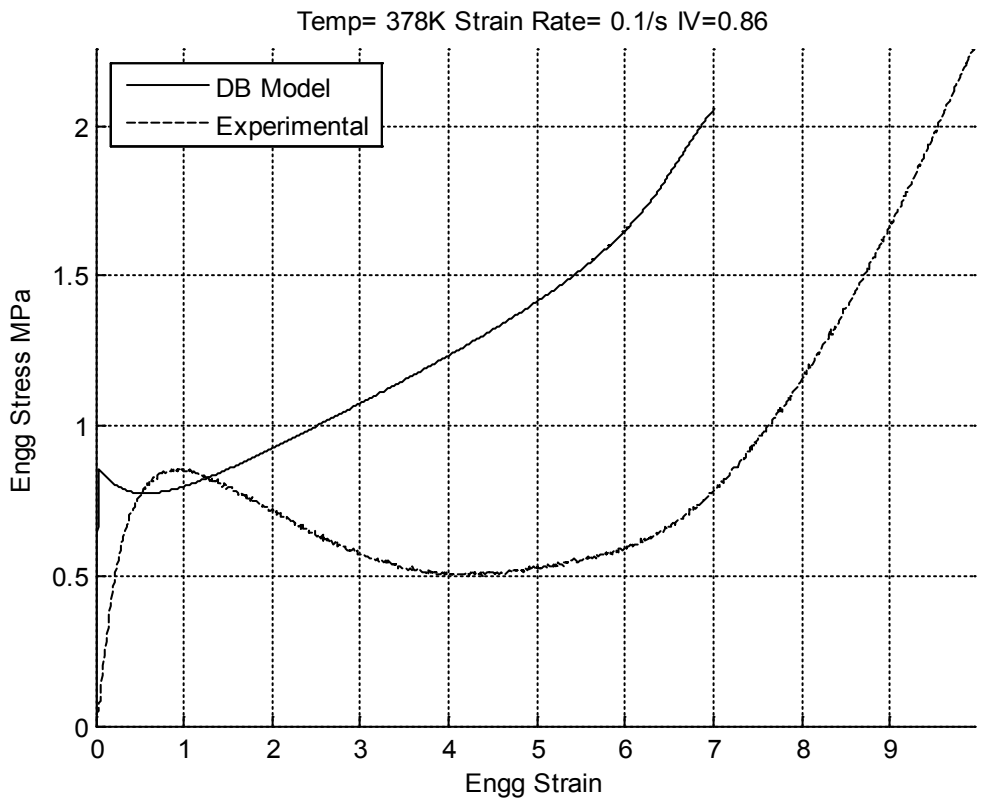

Figure 8.36 Dupaix-Boyce model with crystallization fit - 378K 0.1/s IV 0.86

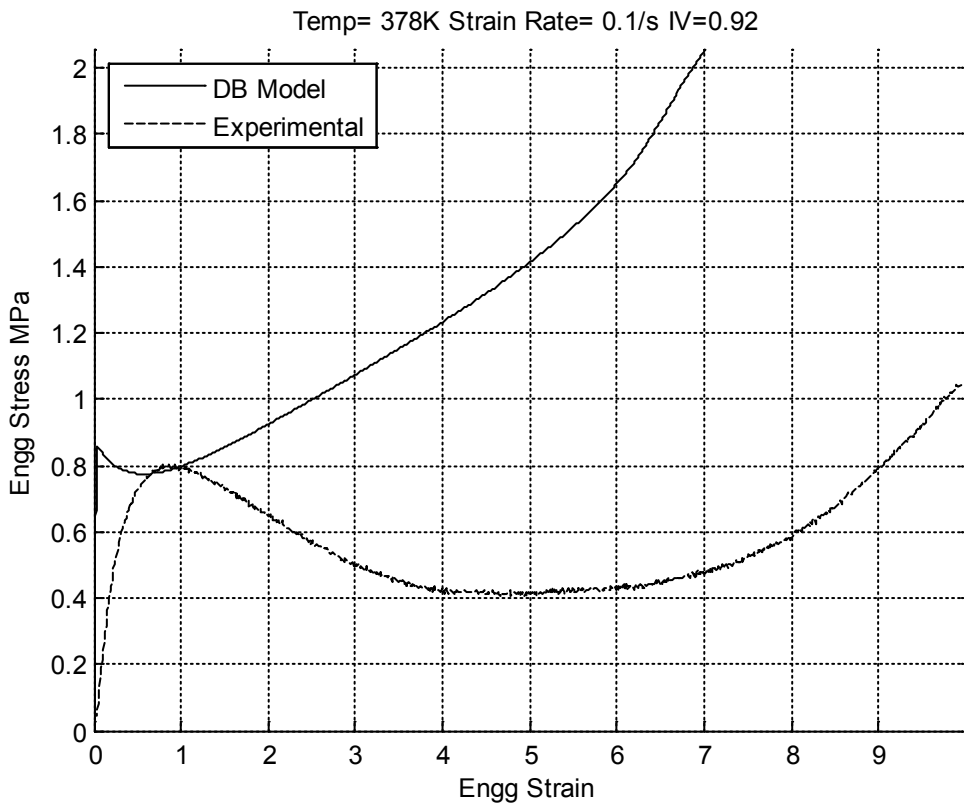

Figure 8.37 Dupaix-Boyce model with crystallization fit - 378K 0.1/s IV 0.92

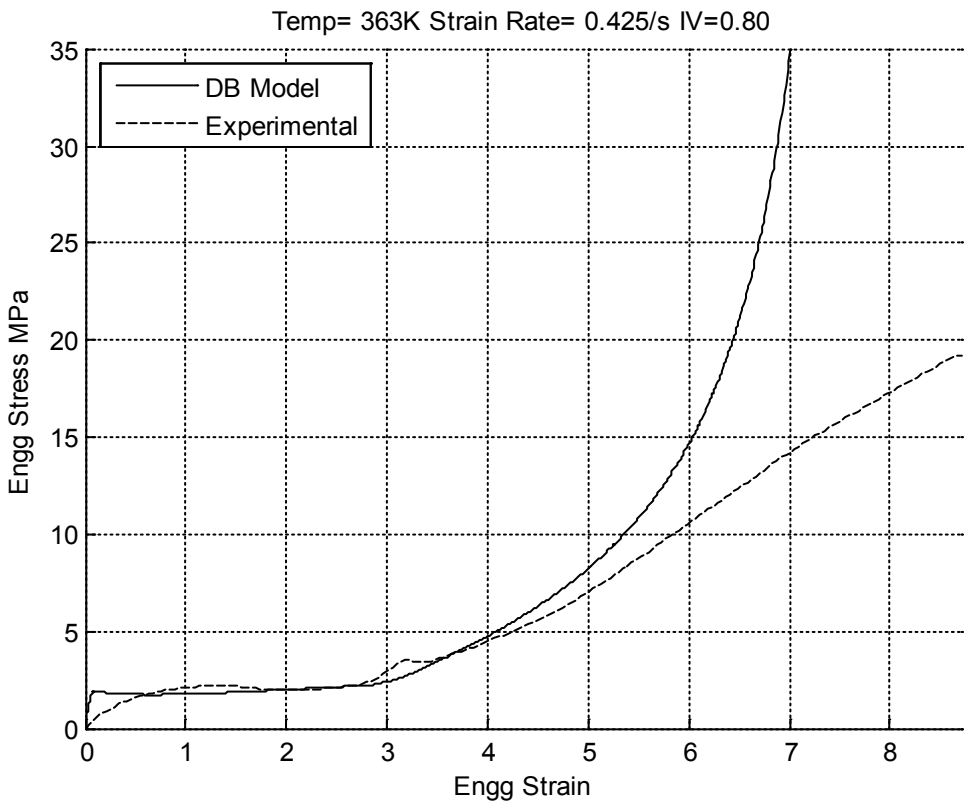

Figure 8.38 Dupaix-Boyce model with crystallization fit - 363K 0.425/s IV 0.80

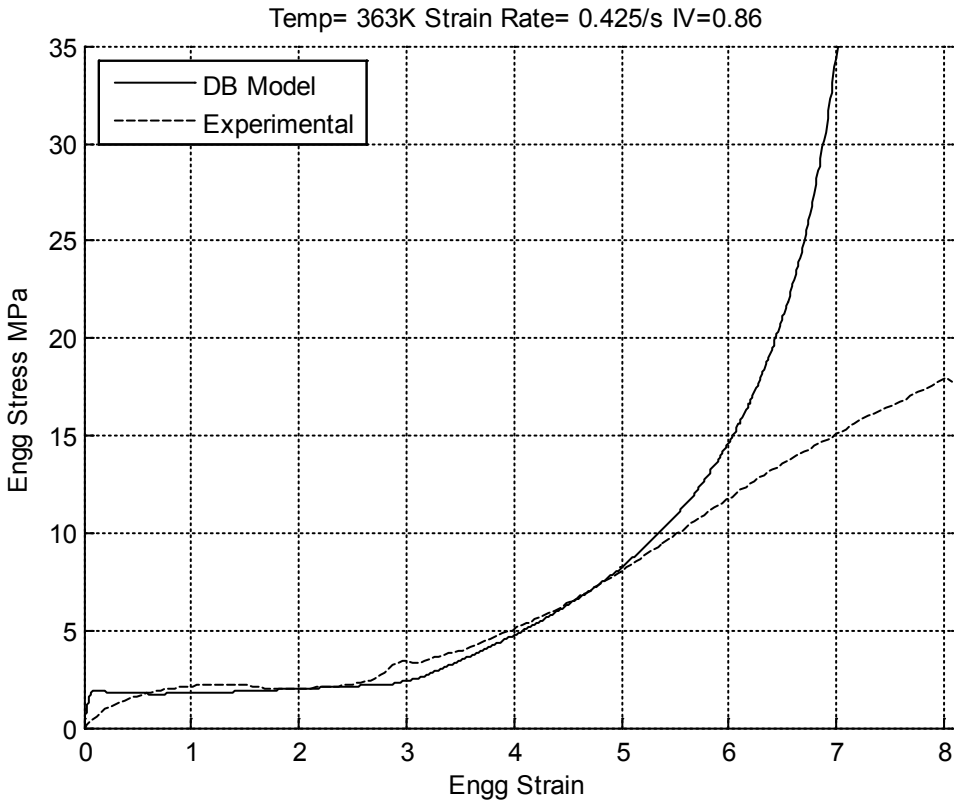

Figure 8.39 Dupaix-Boyce model with crystallization fit - 363K 0.425/s IV 0.86

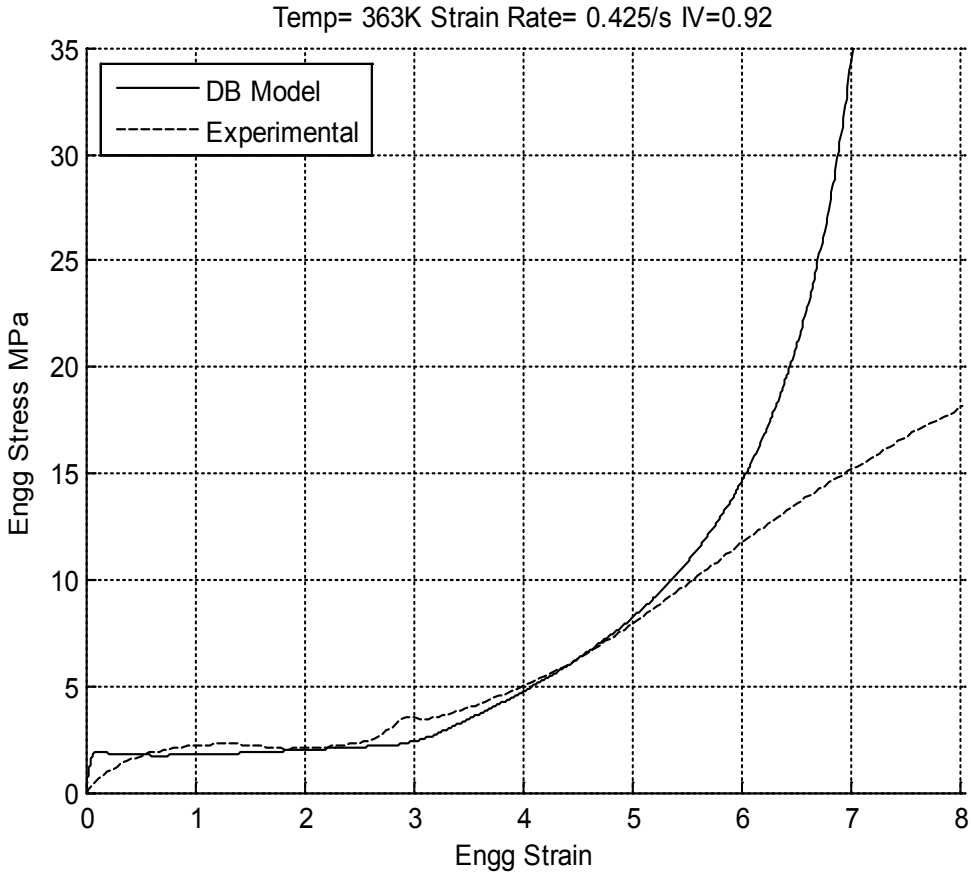

Figure 8.40 Dupaix-Boyce model with crystallization fit - 363K 0.425/s IV 0.92

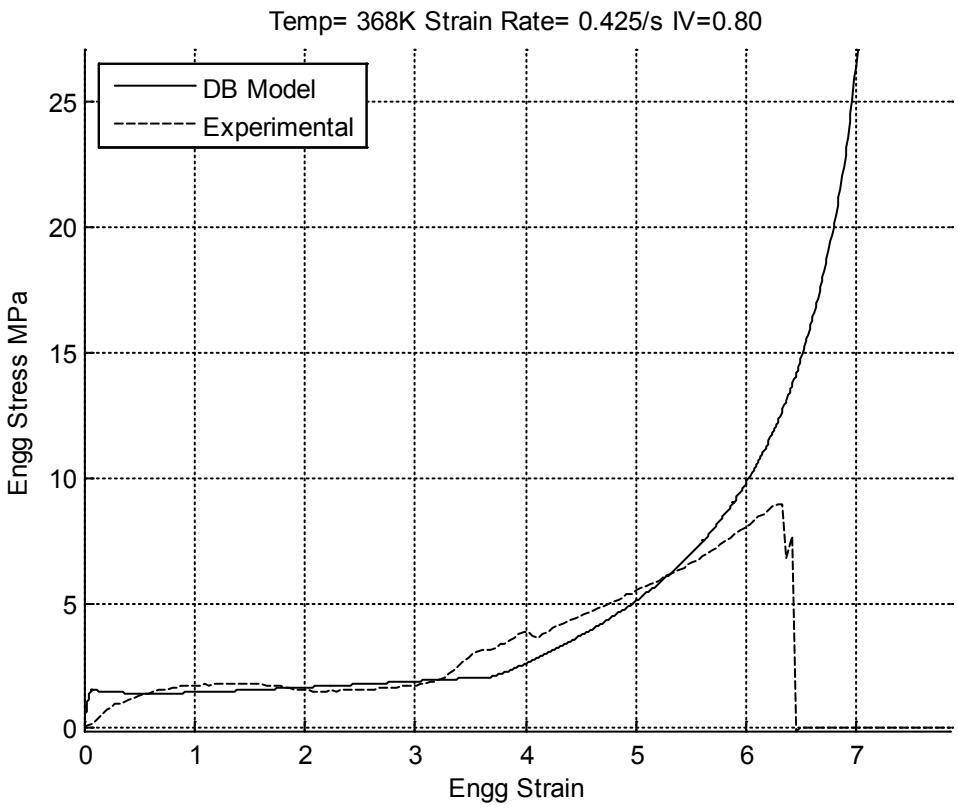

Figure 8.41 Dupaix-Boyce model with crystallization fit - 368K 0.425/s IV 0.80

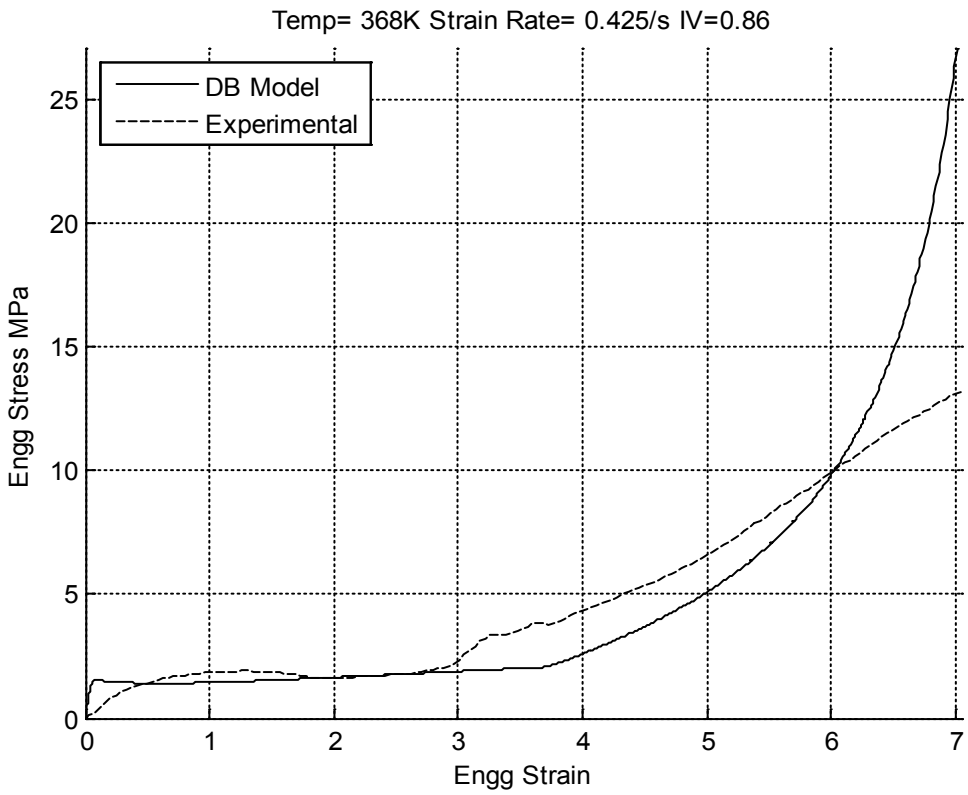

Figure 8.42 Dupaix-Boyce model with crystallization fit - 368K 0.425/s IV 0.86

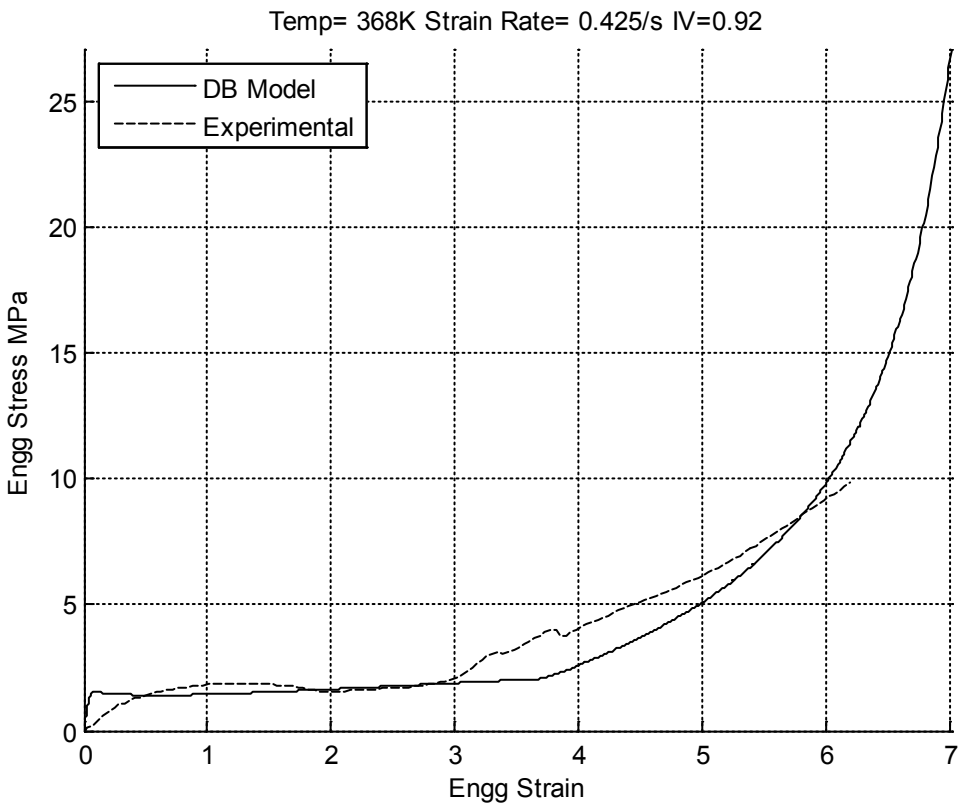

Figure 8.43 Dupaix-Boyce model with crystallization fit - 368K 0.425/s IV 0.92

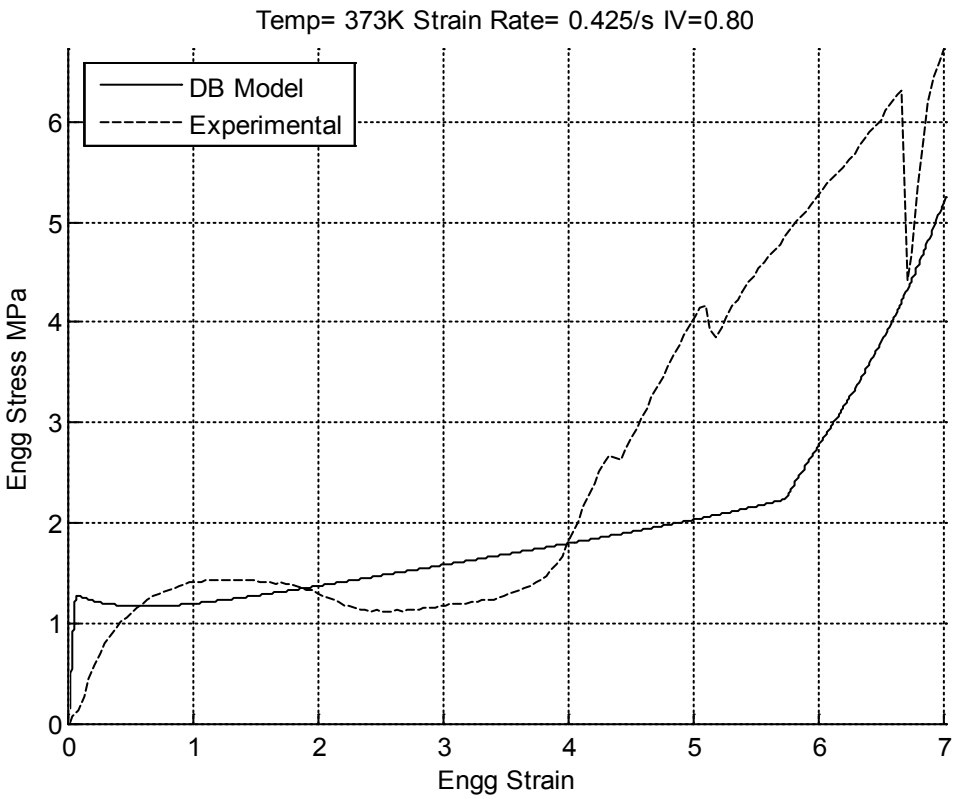

Figure 8.44 Dupaix-Boyce model with crystallization fit - 373K 0.425/s IV 0.80

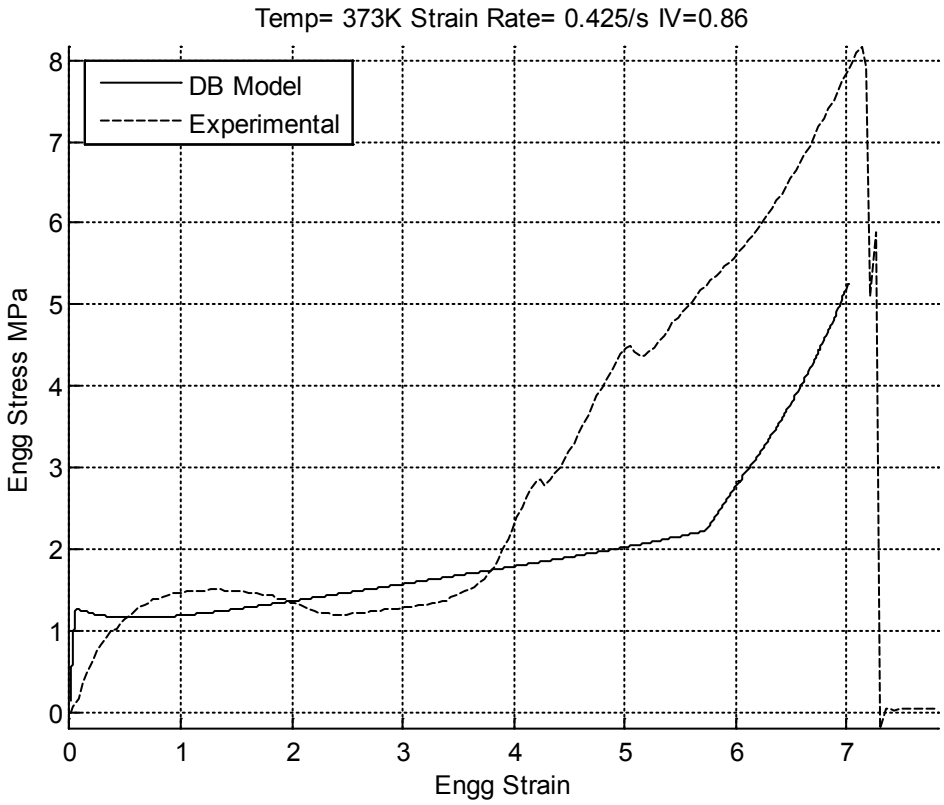

Figure 8.45 Dupaix-Boyce model with crystallization fit - 373K 0.425/s IV 0.86

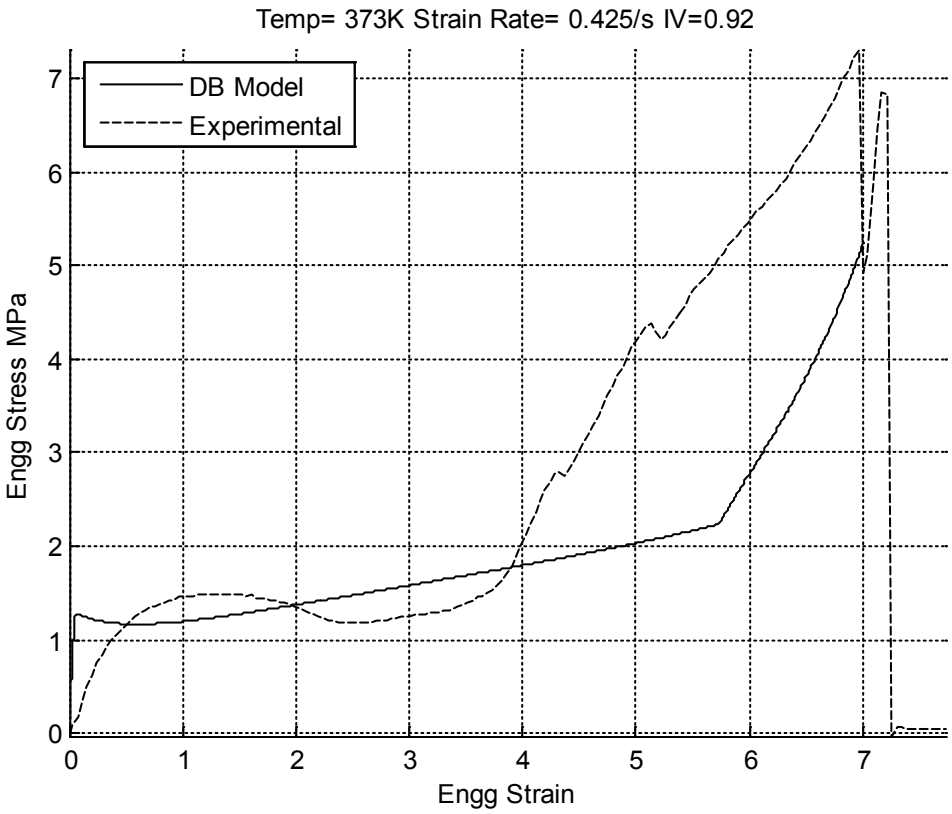

Figure 8.46 Dupaix-Boyce model with crystallization fit - 373K 0.425/s IV 0.92

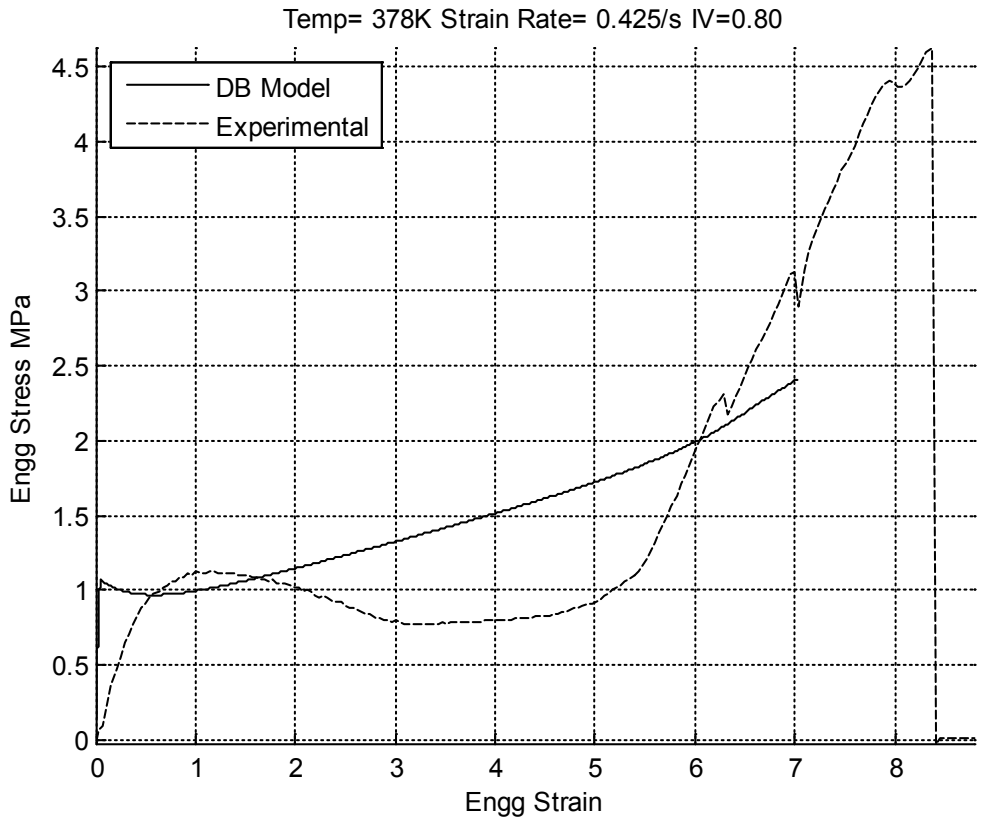

Figure 8.47 Dupaix-Boyce model with crystallization fit - 378K 0.425/s IV 0.80

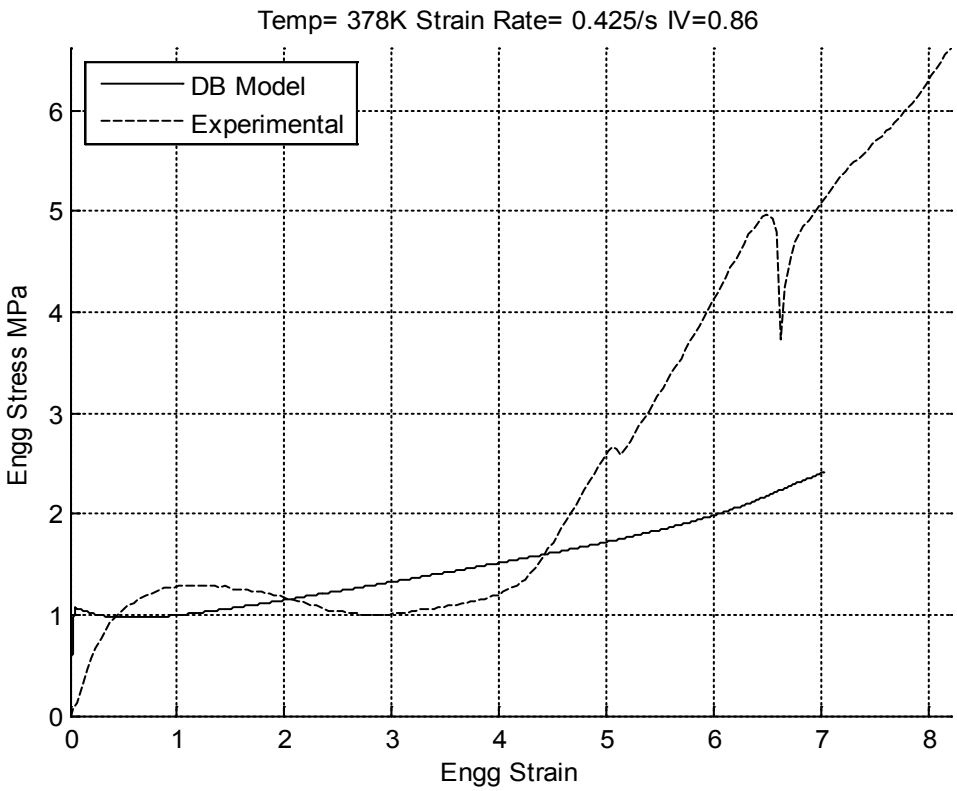

Figure 8.48 Dupaix-Boyce model with crystallization fit - 378K 0.425/s IV 0.86

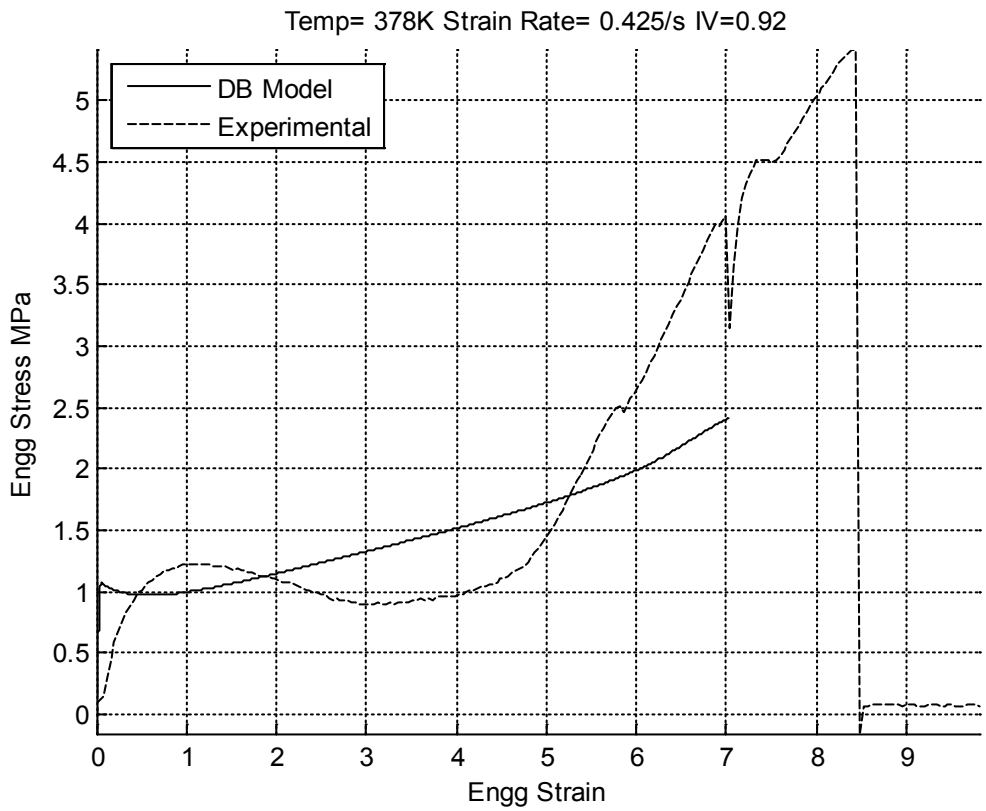

Figure 8.49 Dupaix-Boyce model with crystallization fit - 378K 0.425/s IV 0.92

8.5 Conclusion

This chapter discussed the development and implementation of the crystallization module. It could be seen from the result plots that this module allowed a close prediction of stress by the Dupaix-Boyce model under stiffer conditions of lower temperature and higher strain rates. However, at softer conditions of higher temperature and lower strain rates, there is some deviation of the predicted stress from the actual stress. Also, this method now addresses only uniaxial tensile tests and the fits for other modes of

deformation are left for future work. There are limitations with respect to the temperature and strain rate range within which the current setup of this module works. Extension of this range by the use of a more generalized method is also for the subject of future work.

Chapter 9: Conclusion and future work

9.1 Conclusion

The primary purpose of this thesis was to implement a constitutive material model of PET for use in finite element blow molding simulation. Since PET mechanical behavior is temperature, strain-rate and IV dependent, PET preforms of different IVs were sourced from the sponsors and cut into cylindrical hollow specimens for uniaxial compression tests. The compression stress-strain curves from these specimens showed inconsistent strain softening (dips) at moderate strains which was then determined to be caused by the instability of the hollow specimens in buckling and the caving in of the walls of the cylinder into the center during compression.

Tests were repeated with non-hollow specimens which were cut from injection molded specimens. These test results were consistent. As with previously published literature, stiffening was observed with increasing strain-rate and decreasing temperature. Though increasing IV (related to molecular weight) increases viscous behavior and hence stiffness, this was not significant from test results obtained across different IVs. The Dupaix-Boyce (DB) model was fit to compression data. It accurately captured the

temperature and strain-rate dependence of the stress strain curves in uniaxial compression.

Tests were repeated in uniaxial tension but at constant engineering strain rate unlike compression tests which were performed at constant true strain rate primarily because of testing machine limitations. These test results also showed temperature, strain rate and IV dependence similar to what was observed in compression tests. When the Dupaix-Boyce model was used to simulate uniaxial tension, it under-predicted the stress-strain curve. So, fitting of tension tests required some changes to the model constants, most significantly to the temperature independent bulk modulus. The new constants fit only the initial part of the tension test curves well. The experimental stress-strain curves showed a sudden onset of drastic strain hardening at medium strain levels. This strain hardening could not be captured by the Dupaix-Boyce model. The main reason for this hardening was assumed to be crystallization, primarily because the slope of the stress-strain curve in the hardening region was similar to that observed in crystallized specimens.

True stress vs true strain and true stress vs stretch invariant plots from the uniaxial compression and tension tests showed similar trends until the beginning of the aforementioned strain hardening region. This hardening increased the stress only for the tensile test results and was completely absent in the compression test results. The onset of this strain hardening and the slope of the curve after hardening were dependent on temperature and strain-rate. Increase of temperature and decrease of strain rate pushed the

onset of this hardening to higher strains and decreased the slope of the stress-strain curve post the onset of hardening.

A modification was proposed to the Dupaix-Boyce model which allowed the change of certain model constants during the deformation itself, governed by certain criteria. A time-temperature superposition based equation was derived to describe the temperature and strain-rate dependent strain of onset of strain hardening (called the crystallization onset strain). Similarly, changes to the model constants per unit stretch were derived and implemented. The modified model predicted well the tension test results including the strain hardening at stiffer conditions (temperatures of 363K to 373K and strain rates of 0.1/s to 0.425/s). At higher temperatures and lower strain rates the model tended to over-predict stress.

These simulations were also performed with the Elasto-Visco-Plastic (EVP) model and the results compared with the DB model. The EVP model captured the compression phase of the stress-strain characteristics well but failed to predict the stress in unloading accurately. While the EVP model required minor changes in constants to capture temperature and strain rate dependence, it simulated the initial portion of the tension test curves with the same set of constants unlike the DB model. Just like the DB model, it failed to capture the drastic strain hardening caused by crystallization in tension.

9.2 Future work

The modification of the Dupaix-Boyce model as of now has some disadvantages and still requires work. These modifications are based on the idea of changing the Dupaix-Boyce model constants to make the behavior stiffer, thus simulating crystallization. As of now, the framework governing the change of constants has been derived algebraically from curve fits to the test data. A physically based approach is required to implement this idea more gracefully. As said earlier, the modified model over-predicts stress at softer conditions. A better understanding of temperature and strain-rate effects on crystallization is required to overcome this problem. In addition, since the constant change equations are based on algebraic curve fits, the results obtained from the model in temperatures and strain-rates that fall beyond the range from which data has been collected is questionable without verification. Finally, this change to the Dupaix-Boyce model has been validated only for uniaxial tension tests. The behavior under other strain-states remains unknown and must be analyzed. A physically based model would be better equipped to deal with varying strain states, which ultimately is essential for a robust model for use in finite element simulation.

References

Adams, A. M., Buckley, C. P. and Jones, D. P. (2000), "Biaxial Hot Drawing of Poly (ethylene terephthalate): Measurements and Modeling of Strain Stiffening," Polymer 41(2), 771-786

Arruda, E. M. and Boyce, M. C. (1993), "A Three dimensional Constitutive Model for the Large Stretch Behavior of Rubber Elastic Materials," J. Mech. Phys. Solids, 41(2), 389-412

Arruda, E. M. and Boyce, M. C. (1993b), "Evolution of Plastic Anisotropy in Amorphous Polymers during Finite Straining," Int. J. Plasticity, 9(6), 697-720

Ashford, E., Bachmann, M. A., Jones, D. P. and MacKerron, D. H. (2000),"The prediction of orientation and crystallinity in drawn poly(ethylene terephthalate)," Trans IChemE, 78 A, 33-37

ASTM International, "Standard Test Method for Tensile Properties of Plastics", Designation: D638-10

Bergström, J. S. and Boyce, M. C. (1998), "Constitutive Modeling of the Large Strain Time-dependent Behavior of Elastomers," J. Mech. Phys. Solids, 46(5), 931-954

Blundell, D. J., MacKerron, D. H., Fuller, W., Mahendrasingham, A., Martin, C., Oldman, R. J., Rule, R. J., and Riekel, C. (1996),"Characterization of strain-induced crystallization of Poly(ethylene terephthalate) at fast draw rates using synchrotron radiation," Polymer 37(15), 3303-3311

Blundell, D. J., Mahendrasingam, A., Martin, C., Fuller, W., MacKerron, D. H., Harvie, J. L., Oldman, R. J., Riekel, C. (2000), "Orientation prior to crystallization during drawing of PET," Polymer 41, 7793-7802

Boyce, M. C., Socrate, S. and Llana, P. G. (2000), "Constitutive Model for the Finite Deformation Stress-Strain Behavior of Poly (ethylene terephthalate) above the Glass Transition," Polymer, 41(6), 2183-2201

Buckley, C. P. and Jones, D. C. (1995),"Glass-rubber constitutive model for amorphous polymers near the glass transition," Polymer 36(17), 3301-3312

Buckley, C. P., Jones, D. C., and Jones, D. P. (1996),"Hot-drawing of poly(ethylene terephthalate) under biaxial stress: application of a three-dimensional glass-rubber constitutive model," Polymer 37(12), 2403-2414

Chaari, F., Chaouche, M. and Doucet, J. (2003),"Crystallization of poly(ethylene terephthalate) under tensile strain: crystalline development versus mechanical behavior," Polymer 44, 473-479

Chandran, P. and Jabarin, S (1993a), "Biaxial orientation of poly(ethylene terephthalate," Advances in Polymer Technology, 12(2), 119-132

Chandrasekaran, G. (2008)"Material characterization and modeling of strain induced crystallization in PET above the glass transition temperature," M.S. Thesis, The Ohio State University

de Gennes, P. G. (1979), Scaling Concepts in Polymer Physics, Cornell University Press, Ithaca, New York

Doufas, A. K., McHugh, A. J. and Miller, C. (2000), "Simulation of Melt Spinning including Flow Induced Crystallization Part I. Model Development and Predictions," J. Non-Newtonian Fluid Mech., 92, 27-66

Dupaix, R.B (2003), "Temperature and Rate De pendant Finite Strain Behavior of Poly(ethylene terephthalate) and Poly(ethylene terephthalate)-glycol above the Glass Transition Temperature," Ph. D. Thesis, MIT

Dupaix, R.B and Boyce, M.C. (2005), "Finite strain behavior of poly(ethylene terephthalate) (PET) and poly(ethylene terephthalate)-glycol (PETG)," Polymer, 46, 4827–4838

Dupaix, R.B and Boyce, M.C. (2007), "Constitutive modeling of the finite strain behavior of amorphous polymers in and above the glass transition," Mech. of Materials, 39, 39-52

Dupaix, R.B and Krishnan, D. (2006), "A Constitutive Model for Strain-Induced Crystallization in Polyethylene terephthalate (PET) during Finite Strain Load-Hold Simulations," Journal of Engg. Mat. And Tech., 128, 28-33

G'Sell, C. and Jonas, J. J. (1979),"Determination of the plastic behavior of solid polymers at constant true strain rate," Journal of Materials Science, 14(1979), 583-591

Haward, R. N. and Thackray, G. (1968), General Proceedings of the Royal Society, 302, 453

Jabarin, S. A. (1992),"Strain-induced crystallization of poly(ethylene terephthalate," Polymer Engineering and Science, 32(18), 1341-1348

Jabarin, S. A., "Orientation studies of poly(ethylene terephthalate)," Polymer Engineering and Science, 24(5), 376-384

Krishnan, D. (2005), "A Constitutive Model for Strain-induced Crystallization in PET including Finite Element Analysis of Reheat Stretch Blow-molding," M.S. Thesis, The Ohio State University

Lee, E. H. (1969), "Elastic- Plastic Deformation at Finite Strains," J. App. Mech., 36(3), 1-6

Llana, P. G. and Boyce, M. C. (1999), "Finite Strain Behavior of Poly (ethylene terephthalate) above the Glass Transition Temperature," Polymer, 40, 6729-6751

Mahendrasingam, A., Martin, C., Fuller, W., Blundell, D. J., Oldman, R. J., Harvie, L. J., MacKerron, D. H., Riekel, C. and Engström, P. (1999), "Effect of Draw Ratio and Temperature on the Strain Induced Crystallization of Poly(ethylene terephthalate) at Fast Draw Rates," Polymer, 40(20), 5553-5565

Mir, H., Thibault, F. and DiRaddo, R. (2011),"Modelling behavior of PET for stretch and micro-blow moulding applications using an elasto-visco-plastic material model," International Polymer Processing, 2, 173-181

Misra, A. and Stein, R. S. (1979),"Stress-induced crystallization of poly(ethylene terephthalate)," Journal of Polymer Science: Polymer Physics Edition, 17, 235-237

Mooney, M. (1940), Journal of Applied Physics, 11, 582

Ogden, R.W. (1972)," Large Deformation Isotropic Elasticity - On the Correlation of Theory and Experiment for Incompressible Rubberlike Solids", Proceedings of the Royal Society A, 326(1567), 565-584

Palm, G. and Dupaix, R. B (2006), "Large Strain Mechanical Behavior of Poly(methyl methacrylate)(PMMA) Near the Glass Transition Temperature," Journal of Engg. Mat. and Tech., 128, 559-563

Rivlin, R. S. (1948), "Large Scale Deformations of Isotropic Materials for Further Developments of the General Theory", Philosophical Transactions of the Royal Society of London, 241(835), 379-397

Treloar, L. R. G. (1943), Transactions of the Faraday Society, 39, 241

Zaroulis, J. S. and Boyce, M. C. (1997), "Temperature, Strain rate , and Strain state Dependence of the Evolution in Mechanical Behavior and Structure of PET with Finite Strain Deformation," Polymer, 38(6), 1303-1315

Appendix A: Dupaix-Boyce Model UMAT Flow

The program flow logic for the Dupaix-Boyce model is described in the following section.

The intermolecular interaction (Network I) is identified as 'Network A' and the network resistance (Network N) is identified as 'Network B' in the code. Hence, in the section below, variables and function names with the suffix A belong to Network I and those with the suffix B belong to Network N, which were described in Chapter 3. The logic behind the crystallization module is fully described in Chapter 8 and is hence not repeated here.

A.1 Simulation Procedure

To simulate a particular strain state, the Deformation Gradient tensor F at the current time step is input to the UMAT function, which uses the different variables stored as state variables to compute and return the Cauchy Stress tensor T and the updated state variables for that time step. Newton-Raphson iteration is performed by varying the strain-state dependent non-specified elements of F to obtain T which satisfies the equilibrium and boundary conditions pertaining to the strain-state. Once the converged solution is

obtained from the iteration, the next time increment the corresponding change applied to F before repeating the entire process again. The inner workings of the UMAT function is described in the following sections.

A.2 State variables for the UMAT

The following variables are mandatory:

Plastic deformation gradient for Network A F_A^p and Network B F_B^p

Rate of change of plastic deformation gradient for Network A $\dot{F}_A^p$ and Network B $\dot{F}_B^p$

Plastic shear strain rate for Network A $\dot{\gamma}_A^p$ and network B $\dot{\gamma}_B^p$

Note: Other variables may be used as state variables for analysis/plotting purposes in ABAQUS. 4 more variables are to be set as mandatory state variables if the crystallization module is used.

A.3 UMAT process

Glass transition temperature is a function of plastic shear strain rate $\dot{\gamma}_A^p$ and PROPS 5-6 ξ, ς given by

$\theta_g = 350K + \xi \ln(\dot{\gamma}_A^p) + \varsigma$ if $\dot{\gamma}_A^p$>8.66e-5, else $350K$ (1)

Shear modulus μ is temperature dependent and is computed as a function of model constants 1-4, temperature θ and the glass transition temperature θ_g.

$$\mu = \frac{1}{2}(\mu_{gl} + \mu_r) - \frac{1}{2}(\mu_{gl} - \mu_r)\tanh(\frac{5}{\Delta\theta}(\theta - \theta_g) + X_g(\theta - \theta_g) \quad (2)$$

Using Shear modulus μ and Bulk modulus B (PROPS(7)), Youngs modulus E, Lame's constants λ, μ and Poisson's ratio ν are computed using standard formulae.

Shear resistance $s = 0.15\mu$ (3)

The UMAT function contains the following sub-functions:

NewA

This subroutine computes the Cauchy stress T_A due to inter-molecular interactions (Network A) in the Dupaix-Boyce model.

Input(at time t): time t, time increment dt, deformation gradient F, plastic deformation gradient F_A^p, rate of Plastic Stretch tensor $\dot{F}_A^p$, plastic shear strain rate $\dot{\gamma}_A^p$, shear resistance s, PROPS(8) ΔG, PROPS(9) $\dot{\gamma}_{0A}$, Temperature θ, Lame's constants λ and μ

Output(at time $t + dt$): plastic deformation gradient F_A^p, rate of Plastic Stretch tensor $\dot{F}_A^p$, plastic shear strain rate $\dot{\gamma}_A^p$, Cauchy stress T_A

Elapla

This subroutine uses the time increment dt, Stretch tensor F_A, Plastic Stretch tensor F_A^p and Rate of Plastic Stretch tensor $\dot{F}_A^p$ from the previous time step to compute Elastic F_A^e and Plastic F_A^p stretch tensors and Left Cauchy-Green deformation tensor B_A for the current step.

Input: $dt,\ F_A, F_A^p, \dot{F}_A^p$

Output: F_A^p, F_A^e, B_A

Equations involved:

$$F_A^p = (F_A^p + \dot{F}_A^p * dt)/\det(F_A^p + \dot{F}_A^p * dt)^{0.33} \quad (4)$$

$$F_A^e = F F_A^{p^{-1}} \quad (5)$$

$$B_A = F_A^e F_A^{e^T} \quad (6)$$

Astress

This subroutine uses the Left Cauchy-Green deformation tensor B_A and the elastic constants $\lambda,\ \mu$ to compute Kirchoff stress σ_A

Input: $B_A, \lambda,\ \mu$

Output: σ_A

Equations Involved:

$$\sigma_A = \mathcal{L}^e[\ln(V_A^e)] \quad (7)$$

Where $\mathcal{L}^e$ is the fourth-order elastic tensor constructed with elastic constants $\lambda,\ \mu$. $\ln(V_A^e)$ is the Hencky Strain derived from principal stretches obtained from the square root of the eigenvalues of B_A, . The Kirchoff stress is transformed to the frame of B_A, using the eigenvectors of B_A, .

Finally, Cauchy stress T_A is computed from Kirchoff stress σ_A as

$$T_A = \sigma_A/\det(F_A^e) \quad (8)$$

Deviat

This subroutine computes normalized deviatoric stress N_A from the Cauchy stress T_A.

Input: T_A

Output: N_A, τ_A

Equations involved:

$$\tau_A = [\frac{1}{2} T_A' T_A']^{1/2} \quad (9)$$

$$N_A = \frac{1}{\sqrt{2}\tau_A} T_A' \quad (10)$$

Where T_A' is the deviatoric component of the Cauchy stress T_A.

The plastic shear strain rate $\dot{\gamma}_A^p$ is computed from the equation

$$\dot{\gamma}_A^p = \dot{\gamma}_{0A}[-\frac{\Delta G\left(1-\frac{\tau_A}{s}\right)}{k\theta}] \quad (11)$$

The rate of change of plastic deformation gradient tensor $\dot{F}_A^p$ is computed from the equation

$$\dot{F}_A^p = F_A^{e^{-1}} \dot{\gamma}_A^p N_A F \quad (12)$$

NewB

This subroutine computes the stress due to network resistance (Network B) in the Dupaix-Boyce model.

Input(at time t): time increment dt, deformation gradient F, plastic deformation gradient F_B^p, rate of plastic stretch tensor $\dot{F}_B^p$, plastic shear strain rate $\dot{\gamma}_B^p$, PROPS(10) $nk\theta$,

PROPS(11) N, PROPS(12) Q/R, PROPS(13) D, PROPS(14) $1/n$, PROPS(15) α_c, Temperature θ

Output(at time $t + dt$): plastic deformation gradient F_B^p, rate of Plastic Stretch tensor $\dot{F}_B^p$, plastic shear strain rate $\dot{\gamma}_B^p$, Cauchy stress T_B

Elapla

This subroutine uses the time increment dt, Stretch tensor F_B, Plastic Stretch tensor F_B^p and Rate of Plastic Stretch tensor $\dot{F}_B^p$ from the previous time step to compute Elastic F_B^e and Plastic F_B^p stretch tensors and Left Cauchy-Green deformation tensor B_B for the current step.

Input: $dt,\ F_B, F_B^p, \dot{F}_B^p$

Output: F_B^p, F_B^e, B_B

Equations involved:

$$F_B^p = (F_B^p + \dot{F}_B^p * dt)/\det(F_B^p + \dot{F}_B^p * dt)^{0.33} \quad (13)$$

$$F_B^e = F F_B^{p^{-1}} \quad (14)$$

$$B_B = F_B^e F_B^{e^T} \quad (15)$$

Bstress

This subroutine uses the Arruda-Boyce Model and computes chain stretch $\bar{\lambda}_N$, the inverse Langevin function $\mathcal{L}^{-1}$ and finally outputs Kirchoff Stress due to Network B σ_B.

Input: $B_B, nk\theta, N$

Output: σ_B

Equations involved:

$$\bar{\lambda}_N = [\frac{1}{3}\ trace(B_B)]^{1/2} \tag{16}$$

$\mathcal{L}^{-1}(\frac{\bar{\lambda}_N}{\sqrt{N}})$ is computed using Newton-Raphson iteration, where $\mathcal{L}(x) = \coth(x) - 1/x$

$$\sigma_B = \frac{nk\theta}{3}\frac{\sqrt{N}}{\bar{\lambda}_N}\mathcal{L}^{-1}\left(\frac{\bar{\lambda}_N}{\sqrt{N}}\right)[B_B - \bar{\lambda}_N{}^2 I] \tag{17}$$

Cauchy stress is then computed as:

$$T_B = \sigma_B/\det(F_B^e) \tag{18}$$

Deviat

This subroutine computes normalized deviatoric stress N_B from the Cauchy stress T_B.

Input: T_B

Output: N_B, τ_B

Equations involved:

$$\tau_B = [\frac{1}{2}T_B'T_B']^{1/2} \tag{19}$$

$$N_B = \frac{1}{\sqrt{2\tau_B}}T_B' \tag{20}$$

Where T_B' is the deviatoric component of the Cauchy stress T_B.

Calcngdb

This subroutine computes the plastic shear strain rate $\dot{\gamma}_B^p$ for network B.

Input: $\tau_B, F, \frac{Q}{R}, D, \frac{1}{n}, \alpha_c, \theta$

Output: $\dot{\gamma}_B^p$

Equations involved:

α_{min} is computed from the principal stretches S_i of the total deformation gradient given by:

$$\alpha_i = \frac{\pi}{2} - \text{acos}\left(\frac{S_i}{\sqrt{S_1^2+S_2^2+S_3^2}}\right) \tag{21}$$

The principal stretches are computed from the Left Cauchy-Green deformation gradient of F.

$$C = (h\alpha_{min})^{1/n} \tag{22}$$

$$h = Dexp(-\frac{Q}{R\theta}) \tag{23}$$

$$\dot{\gamma}_B^p = (\frac{\frac{\alpha_{min}}{\alpha_c}-1}{\frac{\alpha_0}{\alpha_c}-1})C(\tau^B)^{1/n} \tag{24}$$

However, if $\frac{\alpha_{min}}{\alpha_c}$ is lesser than 1, $\dot{\gamma}_B^p$ is set to 0, ie, no slip.

Note: If the change in plastic shear strain rate $\dot{\gamma}_A^p$ and $\dot{\gamma}_B^p$ is significant in a time step, the code is setup to break that iteration and repeat with a cut back in time increment dt by a factor PNEWDT.

Output Cauchy stress is the sum of that due to Network A and Network B.

$$T = T_A + T_B \tag{25}$$

Note: The ABAQUS UMAT requires computation of Jacobians describing the ratio of change in stress to change in strain and temperature for Network A and the ratio of change in stress to change in strain for Network B. These functions are required by ABAQUS to run and don't have a role in the model as such and hence are not described here.

Appendix B: Numerical Integration of the Elasto-Visco-Plastic model

The numerical integration and simulation of the EVP model was done in a similar way to that of the DB model through the enforcement of strain-state equilibrium by the Newton-Raphson iteration. This is explained in Appendix A section A.1. The UMAT file, however was different, built using the equations described in Chapter 7. This is elaborated in the section below.

B.1 UMAT flow for the EVP Model

The following variables are used as the state variables for the UMAT: Stress σ, Strain ε, equivalent viscoplastic strain p, $\dot{p}$, change in stress Δσ and change in viscoplastic strain $\Delta\varepsilon^{vp}$.

1. The temperature dependent shear modulus is described using the same way as done in the DB model using the equation.

$$\mu = \frac{1}{2}(\mu_{gl} + \mu_r) - \frac{1}{2}(\mu_{gl} - \mu_r)\tanh(\frac{5}{\Delta\theta}(\theta - \theta_g) + X_g(\theta - \theta_g)$$

Where is the μ shear modulus, θ the temperature, μ_{gl} the glassy shear modulus, μ_r the rubbery shear modulus, $\Delta\theta$ the transition temperature interval, θ_g the glass transition temperature and X_g the slope after transition temperature.

2. Lame's constant λ are computed as

$$\lambda = K - \frac{2}{3}\mu$$

Where K is the bulk modulus.

3. The elasticity tensor H is built using the constants λ and μ using standard continuum mechanics formulae.
4. The change in strain $\Delta\varepsilon$ between the current time step and the previous time step is computed from the current and the previous Deformation Gradient F
5. The change in elastic strain is determined using additive decomposition

$$\Delta\varepsilon^e = \Delta\varepsilon - \Delta\varepsilon^{vp}$$

6. Change in stress is determined using the elasticity equation

$$\Delta\sigma = H\Delta\varepsilon^e$$

Stress σ in the current time step is determined by adding $\Delta\sigma$ to the stress from the previous time step in the state variable.

7. From stress σ the deviatoric S stress is computed as

$$S = \sigma - \frac{trace(\sigma)}{3}$$

8. Von Mises stress J_2 is computed using the formula

$$J_2 = \sqrt{\frac{3}{2}S:S}$$

9. $\dot{p}$ is determined from the equation that uses the EVP model constants described in Chapter 7. The value of p is taken from the aforementioned state variable.

$$\dot{p} = \left(\frac{J_2}{K e^{\frac{a}{T}} (1 - e^{-wp}) e^{(h_g p^2 - h_f p)}} \right)^{\frac{1}{m}}$$

10. The net change of p is computed from the time step length and the value of p is updated for the current time step.

$$\Delta p = \dot{p} * \Delta t$$

11. The net rate of change and change of viscoplastic strain is computed using the equation

$$\dot{\varepsilon}^{vp} = \frac{3}{2J_2} \dot{p} S$$

$$\Delta \varepsilon^{vp} = \dot{\varepsilon}^{vp} * \Delta t$$

12. The entire cycle is repeated for the next time step.

::End::